

# Topics in steady-state MRI sequences and RF pulse optimization

by

Hao Sun

A dissertation submitted in partial fulfillment  
of the requirements for the degree of  
Doctor of Philosophy  
(Electrical Engineering: Systems)  
in The University of Michigan  
2015

Doctoral Committee:

Assistant Research Scientist Jon-Fredrik Nielsen, Co-Chair  
Professor Jeffrey A. Fessler, Co-Chair  
Assistant Professor Laura Balzano  
Professor Douglas C. Noll

© Hao Sun 2015  

---

All Rights Reserved

For my mother, father, grandparents, and Jing Zhu

## ACKNOWLEDGEMENTS

I could not have done this work without the help and support from many people. First of all, I want to thank my co-advisors Jon-Fredrik Nielsen and Jeffrey A. Fessler. I feel so lucky that I contacted them when I first came to UM without an advisors, and I am deeply thankful that they granted me the opportunity to work in their groups. They provided me great guidance in my PhD life. Both of them are very knowledgeable in their field. Jon is an expert on MRI sequence and scanner programming. He brought me into the intriguing field of MR steady-state sequence, and helped me a lot in experiments. Jeff is an expert on optimization and image reconstruction, and he can always give me helpful answers whenever I have math related questions. They are great advisors not only because of their knowledge but also their attitude toward students. They always showed great interest in my research ideas. They were willing to sit down and discuss every project details with me. They are both rigorous, but always commented my work in positive way. Also, I truly appreciate the freedom they gave to me, so I could work on the projects I was interested in, and I could have one-month trip back to home every year, which means a lot to me and my family.

I would also want to thank Douglas C. Noll, who was not my official advisor, but provided me lots of help in many aspects. He financially supported me in many semesters. He showed great interest and provided lots of insightful suggestions to my work. Moreover, he made the fMRI lab such a great work place. Prof. Laura Balzano also deserve my gratitude for serving my dissertation committee and carefully reviewed my thesis.

The fMRI lab provided a great working and life environment for me, thanks to the terrific lab-mates and senior researchers. Feng Zhao has been my best friend in the lab. We liked to discuss almost everything, like research, course works, career plan, sports, traveling, and news from China, which made my working experience in the lab much more productive and pleasurable. Yash Shah, Alan Chu, Steve Allen, Matt Muckley, Kathleen Ropella, Sydney Williams are all nice, bright guys, and we had a lot of fun together. I want to thank Luis Hernandez for sharing his MRI knowledge and humor with us and invite us to his foosball party. Thank Scott Peltier for always

being approachable on scanner issues. Thank Keith Newnham, Ryan Smith, Chuck Nicholas, Ruth Halsey, Krisanne Litinas for their assistance on lab business. I also want to thank some senior members, Daehyun Yoon, Will Grissom, and Chun-yu Yip for their excellent work in pulse design.

I would also like to thank my colleagues in Jeff's imaging group. First, I thank Daniel Weller for his crucial contribution in my mini-max pulse design work, and his suggestions and encouragement before my first conference talk. Then, I thank Hung Nien for always being willing to answer my questions, and share interesting stories in life. Finally, I thank Sathish Ramani, Donghwan Kim, Mai Le, Gopal Nataraj, Michael Allison, Madison McGaffin, Jang Hwan Cho, Jung Kuk Kim, Young Song Kwon, Antonis Matakos, Stephen Schmitt, Lianli Liu, Jiabei Zheng for sharing their knowledge in image reconstruction problems and providing helpful comments in my presentations. I would also like to thank Ms. Becky Turanski and Ms. Rachel Yang Antoun for always being willing to help.

Outside my research labs, I am very fortunate to have so many friends who enriched my life in Ann Arbor. I want to thank Hong Li for persuading me to come to UM, driving me everywhere before I bought a car, discussing course works, playing games together. I also thank Qingsi Wang, Zhaoshi Meng, Shengtao Wang, Tianpei Xie, Yang Liu, Jingmin Zhang, Xiyu Duan, Chris Fink and many other friends for so much fun together.

Finally I owe my deepest gratitude to my mother, my father and my grandparents for their unconditional love and support that warms me all the time. As the only child in my family, I really wish I can spend more time with them in the future. I also want to thank my fiancée Jing Zhu, who has accompanied me through my highs and lows for more than 7 years, and brought me endless happiness and support.

*Hao Sun*  
*Ann Arbor, Michigan*  
*Feb 17, 2015*

# TABLE OF CONTENTS

DEDICATION . . . . .	ii
ACKNOWLEDGEMENTS . . . . .	iii
LIST OF FIGURES . . . . .	ix
LIST OF TABLES . . . . .	xviii
LIST OF APPENDICES . . . . .	xix
ABSTRACT . . . . .	xx
CHAPTER	
<b>I. Introduction</b> . . . . .	1
<b>II. Background</b> . . . . .	5
2.1 MRI Physics . . . . .	5
2.1.1 Spin and bulk Magnetization . . . . .	5
2.1.2 Three Magnetic Fields . . . . .	5
2.1.3 The Bloch Equation . . . . .	8
2.2 RF Pulse Design . . . . .	8
2.2.1 Excitation Pulse Design Problem . . . . .	8
2.2.2 Small-tip-angle Approximation . . . . .	9
2.2.3 Iterative Small-tip-angle RF Pulse Design . . . . .	11
2.3 Steady-state Imaging . . . . .	12
2.3.1 Phase Graph . . . . .	13
2.3.2 RF Spoiling . . . . .	13
2.3.3 Balanced Steady-state Sequence (bSSFP) . . . . .	14
2.4 Functional MRI . . . . .	15
2.4.1 Blood-oxygen-level-dependent (BOLD) . . . . .	15
2.4.2 bSSFP fMRI . . . . .	15

<b>III. Strategies for Improved 3D Small-tip Fast Recovery Imaging</b>	<b>17</b>
3.1 Introduction . . . . .	17
3.2 Theory . . . . .	18
3.2.1 Unspoiled STFR . . . . .	18
3.2.2 Steady-state Magnetization for a Spin Isochromat . . . . .	19
3.2.3 Signal Equation . . . . .	20
3.2.4 RF Pulse Design . . . . .	23
3.3 Methods . . . . .	26
3.4 Results . . . . .	27
3.4.1 Phantom Observations . . . . .	27
3.4.2 In-vivo Observations . . . . .	27
3.5 Discussion . . . . .	31
3.6 Conclusions . . . . .	33
<b>IV. Steady-state Functional MRI Using Spoiled Small-tip Fast Recovery Imaging</b>	<b>34</b>
4.1 Introduction . . . . .	34
4.2 Theory . . . . .	35
4.2.1 Small-tip Fast Recovery Imaging . . . . .	35
4.2.2 Possible Functional Contrast Mechanisms in STFR: Diffusion and “Static Dephasing” . . . . .	36
4.3 Methods . . . . .	38
4.3.1 Monte Carlo Bloch Simulations . . . . .	38
4.3.2 Functional Imaging . . . . .	40
4.3.3 fMRI Processing and Analysis . . . . .	42
4.4 Results . . . . .	42
4.4.1 Bloch Simulation Results . . . . .	42
4.4.2 Functional Imaging . . . . .	43
4.5 Discussion . . . . .	47
4.6 Conclusions . . . . .	48
<b>V. Small-Tip Fast Recovery Imaging Using Spectral Tailored Pre-winding Pulse</b>	<b>49</b>
5.1 Introduction . . . . .	49
5.2 Theory . . . . .	50
5.3 Methods . . . . .	51
5.3.1 Spectral RF pulse design . . . . .	51
5.3.2 Simulations . . . . .	52
5.3.3 Imaging experiments . . . . .	52
5.3.4 Results . . . . .	53
5.3.5 Discussion . . . . .	57
5.4 Conclusion . . . . .	61

<b>VI. Pulse Design using Minimax Algorithm</b>	62
6.1 Introduction	62
6.2 Theory	63
6.3 Solving the Unconstrained $L_\infty$ Minimization Problem	66
6.4 Simulation Results	68
6.5 B0 inhomogeneity and parallel excitation	70
6.5.1 Include B0 Map in the Model	70
6.5.2 Extend to Parallel Excitation	71
6.5.3 Simulation Results Considering B0 Map and Parallel Excitation	71
6.6 Minimax for general pulse design	73
6.6.1 Formulation	73
6.6.2 Modifications to our ADMM updates after including the regularizer	73
6.6.3 Simulation results	74
6.6.4 Magnitude minimax algorithm	75
6.7 Discussion	78
6.8 Conclusion	79
<b>VII. Joint Design of Excitation k-space Trajectory and RF pulse for Small-tip 3D Tailored Excitation in MRI</b>	80
7.1 Introduction	80
7.2 Theory	82
7.2.1 Problem Formulation	82
7.2.2 k-space parametrization	82
7.2.3 Efficient implementation of constraints	83
7.2.4 Gradient and Hessian	86
7.2.5 Optimization algorithms	87
7.2.6 Initialization	89
7.3 Methods	91
7.4 Results	93
7.5 Extension to parallel transmission	94
7.6 Experimental validation of the extended KT-points method	99
7.7 Discussion	99
7.8 Conclusions	102
<b>VIII. Rapid Inner-volume Imaging in the Steady-state with 3D Selective Excitation and Small-tip Fast Recovery (STFR) Imaging</b>	104
8.1 Introduction	104
8.2 Results	108
8.3 Discussion	109

8.4	Conclusion . . . . .	110
<b>IX.</b>	<b>Regularized Estimation of Bloch-Siegert <math> B_1^+ </math> Maps in MRI .</b>	<b>115</b>
9.1	Introduction . . . . .	115
9.2	Model . . . . .	116
9.2.1	Bloch Siegert B1 Mapping . . . . .	116
9.2.2	Penalized Likelihood Estimation . . . . .	116
9.3	Minimization Algorithms . . . . .	118
9.3.1	Maximum Curvature for the ML Term . . . . .	118
9.3.2	Minimization of the Surrogate Function . . . . .	120
9.3.3	Alternative Formulation . . . . .	120
9.4	Simulation and Experimental Results . . . . .	121
9.5	Discussion . . . . .	123
9.6	Conclusion . . . . .	123
<b>X.</b>	<b>Future Work . . . . .</b>	<b>124</b>
	<b>APPENDICES . . . . .</b>	<b>127</b>
	<b>BIBLIOGRAPHY . . . . .</b>	<b>138</b>

## LIST OF FIGURES

### Figure

2.1	Magnetization vector precesses around B0 field at Larmor frequency	6
2.2	RF field(B1) is rotating in xy-plane . . . . .	7
2.3	Comparing signal level between SPGR SSFP-ECHO and bSSFP . .	14
2.4	Demonstration of banding artifact in bSSFP . . . . .	15
3.1	Proposed “unspoiled STFR” pulse sequence. (a) Steady-state path for a spin isochromat. The spin is tipped back to the longitudinal axis by a tailored pulse with flip angle $-\beta(\mathbf{r})$ and phase $\phi(\mathbf{r})$ . $\phi(\mathbf{r})$ is designed to be equal to the accumulated free precession angle $\theta_f(\mathbf{r}) = \Delta\omega(\mathbf{r})T_{\text{free}}$ , where $T_{\text{free}}$ is the free precession time. (b) Example pulse sequence diagram, using tailored pulses for both tip-down (red) and tip-up (blue) excitations, and 3D Cartesian data readout. . . . .	19
3.2	Steady-state magnetization (Eq. (3.1)) for a spin isochromat as a function of $\phi + \theta_g$ , where $\phi$ is the phase of the tip-up pulse and $\theta_g$ is the precession induced by the applied unbalanced gradient. Narrow bands are spaced $2\pi$ apart, and neighboring bands are equal both in magnitude and phase. In the proposed unbalanced STFR sequence, the signal from a voxel can be calculated by integrating over one full cycle (shaded region). The result of this integration is given by Eq. (3.2). . . . .	21
3.3	Predicted tissue signal for unspoiled STFR (Eq. (2)), spoiled STFR [65] and bSSFP [58]. These calculations assumed $T1/T2 = 4000/2000\text{ms}$ , $1470/71\text{ms}$ , $1110/56\text{ms}$ for CSF, gray matter, and white matter, respectively [85]. The bSSFP curves were calculated using a flip angle of $2\alpha$ , which is expected to produce similar signal contrast as STFR using a flip angle of $\alpha$ . (a) STFR produces similar signal as bSSFP, as desired. (b) STFR and bSSFP are predicted to have similar gray/white matter contrast. . . . .	22

3.4	<p>(a) Steady-state signal for unspoiled STFR and spoiled STFR as a function of phase mismatch <math>\phi - \theta_f</math>, using the analytic result from Eq. (3.2) and [65] (<math>T_1/T_2 = 510/50</math> ms, <math>T_{\text{free}}/TR = 9/12</math> ms, <math>\alpha = \beta = 16^\circ</math>) and phantom observations. Note that the rate of signal drop due to phase mismatch is smaller for unspoiled STFR. We obtained the measured curves by applying a linear gradient shim in the x direction and imaging a gel phantom (shown in (b)) with <i>non-tailored</i> (sinc) pulses. We stress that the image in (b) was obtained for the sole purpose of obtaining the curve in (a), and is <i>not</i> representative of a typical STFR image acquisition. In particular, the goal in STFR is generally to design a tailored tip-up pulse that minimizes the phase mismatch and hence maximizes the signal within a target ROI. . . .</p>	23
3.5	<p>Steady-state signal for unspoiled STFR and spoiled STFR as a function of phase mismatch <math>\phi - \theta_f</math> for different tissues: gray matter (GM), white matter (WM), and cerebrospinal fluid (CSF). These calculations assumed <math>T_1/T_2 = 4000/2000</math> ms, 1470/71 ms, 1110/56ms for CSF, GM, and WM, respectively [85], and <math>T_{\text{free}}/TR = 7/10</math> ms, <math>\alpha = \beta = 20^\circ</math>. The spoiled STFR sequence is more sensitive to phase mismatch compared to unspoiled STFR for all three tissue types, and especially for CSF. . . . .</p>	24
3.6	<p>Steady-state imaging, phantom results. Images are shown on the same gray scale. For each image, the mean signal and standard deviation within the object are indicated. Unspoiled STFR with the proposed “Joint” RF pulse design (right) produces signal levels that are comparable to on-resonance bSSFP, and has improved uniformity compared to bSSFP and spoiled STFR. Unspoiled STFR with the simpler “Separate” RF pulse design approach (second from right) shows improved signal and uniformity compared to spoiled STFR, but slightly lower overall signal compared to the Joint design. Conventional SPGR and SSFP-FID images are included for reference. . . . .</p>	28
3.7	<p>(a) Comparison of bSSFP (left) with three different STFR acquisitions, in the same slice. (b) field map and phase mismatch maps using separate and joint design. Banding artifacts in the anterior part (arrow) of the bSSFP image are largely absent in the unspoiled STFR images. Spoiled STFR is less uniform than unspoiled STFR as predicted, and the signal drops more in the region with high phase mismatch. Note that the CSF in the oval region in the spoiled STFR image drops significantly more than the nearby tissue signal and the unspoiled STFR CSF signal, which agrees with the phase mismatch map and sensitivity to phase mismatch plot in Fig. 3.5. The Joint design has slightly smaller phase mismatch, which leads to improved signal uniformity and tissue contrast compared to the Separate design. Also note that the high through-plane vessel signal in the bSSFP image is suppressed in the STFR images (see, e.g., box). . . . .</p>	29

3.8	<p>(a) Proof-of-principle demonstration of 3D unspoiled STFR imaging, using Joint 3D tailored RF pulses. Images are shown for Joint unspoiled STFR, and bSSFP with different phase cycling schemes, in 5 adjacent axial slices spanning 4 cm: (Top) <math>0^\circ</math> phase cycled bSSFP; (Middle) <math>180^\circ</math> phase cycled bSSFP; (Bottom) Joint unspoiled STFR. Both bSSFP acquisitions suffer from banding artifacts, which are reduced with the 3D Joint unspoiled STFR sequence. (b) field map and phase mismatch maps. The STFR signal drops more in the region with high phase mismatch (See, e.g., arrows in (a)). . . . .</p>	30
4.1	<p>Proposed STFR functional imaging sequence. (a) Steady-state spin path for a single spin isochromat. The tip-up pulse (blue) is tailored to the local free precession angle. In general, there will be a mismatch <math>\theta_f - \phi</math> between the spin phase at the end of the free precession interval (<math>\theta_f</math>), and the phase (direction) of the tip-up pulse (<math>\phi</math>). In STFR imaging, the goal is to design a tip-up pulse that minimizes <math>\theta_f - \phi</math> within the ROI. (b) Steady-state STFR transverse magnetization for a single spin isochromat as a function of phase mismatch <math>\theta_f - \phi</math>, calculated from Eq. [4.2]. The observed voxel-averaged signal is obtained by weighted integrating the signal profile over the B0 distribution within a voxel (Eq. [4.3], illustrated with shaded gray column). (c) Pulse sequence diagram for the STFR sequence used in the <i>in vivo</i> functional experiments (spiral tip-up pulse). (d) fast-kz tailored tip-up pulse (only 5 subpulses are shown). . . . .</p>	37
4.2	<p>Monte Carlo Bloch simulation results. (a) Calculated microscopic B0 inhomogeneity (Hz) in the numerical voxel used in our Monte Carlo Bloch simulations. A 2D cut through the <math>1 \times 1 \times 1 \text{ mm}^3</math> voxel is shown. (b,c) Percent (b) and absolute (c) functional signal change for STFR and passband bSSFP over a range of TRs and flip angles. Note that bSSFP used twice the flip angle indicated. These simulations predict that STFR can produce a functional signal. The percent signal change increases with increasing flip angle across the whole range while the absolute signal change increases up to <math>20^\circ</math>. “Turning off” spin diffusion has a relatively small impact on the functional signal, which indicates that diffusion is unlikely be the main source of functional contrast in STFR. (d) The percent signal change when the mean phase mismatch in a voxel is not 0 (obtained by weighted integrating over a narrow spectrum off the center in Fig. 4.1-b). The functional signal change is maximized when mean phase mismatch for a voxel is 0. . . . .</p>	39

4.3	Repeated motor cortex imaging using STFR, BOLD and bSSFP in one subject (A, Session 1). (a) Activation maps with correlation threshold 0.3 and cluster size 10 [20]. All five scans demonstrate that STFR can produce similar activation maps as BOLD, which are well localized to the motor cortex area. (b) ROI used to calculate the mean time course for each sequence, obtained by selecting the pixels showing activations in at least 4 scans in both BOLD and STFR. (c) One cycle of the mean time course over the ROI (the rest state signal is normalized to be 1). STFR has slightly lower functional contrast than BOLD, but higher than bSSFP. The calculated percent functional signal change is reported in Table 4.2. . . . .	44
4.4	Summary of test-retest reliability results for 5 different subjects (Subjects A–E), calculated using the method in [22, 67] from motor cortex imaging data. The ROC curves for STFR are generally slightly lower than BOLD, but still demonstrate that it is a reliable sequence for detecting functional activity. One BOLD curve is much lower than other curves, which is probably due to the motion artifact we observed in that set of data. . . . .	45
4.5	Effect of flip angle on functional signal in STFR. (a) Correlation map obtained with STFR fMRI, using flip angles 16° and 8°. Threshold and cluster size are 0.22/12 for both flip angle acquisitions. (b) ROI used to calculate the mean time course for each flip angle, which includes pixels showing activation in both flip angle acquisitions. (c,d) One cycle of mean time course within ROI. 16° flip angle produces higher absolute and percent functional signal change compared to 8° flip angle, as predicted in simulation (Fig. 4.2(b,c)). . . . .	46
5.1	Proposed spectral-STFR pulse sequence. Spectral pre-winding pulses are used for both tip-down and tip-up excitations in this work. (a) Steady-state spin path. The tip-down pulse “prephases” the spins to have a phase equal to the negative of half the accumulated free precession phase $-\theta_f/2 = \omega T_{\text{free}}/2$ , where $T_{\text{free}}$ is the free precession time. After readout, the spin is tipped back to the z-axis by a pulse tailored to the phase $\theta_f/2$ . (b) Pulse sequence timing diagram. . .	50
5.2	Effect of regularization parameter $\mu$ on spectral pre-winding RF pulse waveforms. (a) Large $\mu$ (0.6) can suppress the b1 magnitude and keep the small tip angle approximation accurate (i.e., small difference between the small tip angle approximation and Bloch simulation). (b) With small $\mu$ (0.02), the excitation predicted by the small tip model matches the target, but the actual excitation pattern has large deviations from the target since the small tip approximation does not hold for the entire RF transmission window. (c) Actual flip angle of a spin during the RF pulse can be larger than the final target flip angle. Small regularization leads to higher intermediate flip angle and therefore less accurate excitation. We designed pulses with $\mu = 0.6$ in this study. . . . .	53

5.3	Simulated steady-state banding profile of (a) spectral-STFR and bSSFP for WM, GM, and CSF, using T1 and T2 values from [85], and (b) spectral-STFR for fat with T1 and T2 values from [28]. RF pulses were designed for 150 (+/-75) Hz target bandwidth, 4.9 ms T <sub>free</sub> , and $\beta = 0.6$ . In general, spectral-STFR and bSSFP have similar tissue contrast (e.g., high CSF signal). Spectral-STFR has wider passband than bSSFP. The banding shape for spectral-STFR is similar for different tissue types, indicating a relatively consistent tissue contrast across the frequency band. Fat can have high signal in spectral-STFR.	54
5.4	Comparison of SPGR, bSSFP, and spectral-STFR imaging in a phantom. (a) B <sub>0</sub> map. (b) Steady-state images, displayed on a common grayscale. Spectral-STFR (bottom row) reduces the banding artifact seen in bSSFP (middle row), and has a relatively uniform signal with varying off-resonance. Both bSSFP and STFR generally achieve higher signal than SPGR (top row).	55
5.5	Comparison between bSSFP and spectral-STFR imaging: representative human volunteer imaging results. (a) B <sub>0</sub> field map, and (b) bSSFP and (c) spectral-STFR images. Spectral-STFR has similar image contrast as bSSFP, but no hyperintense CSF signal near the edge of the bands. In addition, spectral-STFR successfully reduces the banding artifacts (e.g, red circle) within the target frequency range. Signal drop-out occurs when off-resonance goes beyond the target range (e.g., blue arrow). (d-g) Plots of signal level versus off-resonance frequency in CSF and WM/GM ROIs (segmented manually from slices 6-8). The center of target bandwidth is -35 Hz and 0 Hz for spectral-STFR and bSSFP, respectively. Balanced SSFP shows signal drop near -70 Hz, which is corrected at the corresponding frequency (-105 Hz) in spectral-STFR. The CSF signal variation of spectral-STFR is much smaller than bSSFP near the edge, agreeing with the simulation in Fig. 5.3. The fat signal near the skull shows high variability in the spectral-STFR images, as expected from the simulation results in Fig. 5.3(b).	56
5.6	Compare small-tip pulse design method with large-tip pulse design method for a wider target bandwidth. Using large-tip pulse design method, we can achieve target bandwidth larger than 1/(2TE) (TE = 2.5 ms, bandwidth = 240 Hz). The pulse duration is relatively long to keep the RF power within limit.	58
5.7	The phase of the pre-winding pulse is constant except a few $\pi$ changes.	60
6.1	Example pulse diagram of a fast-kz pulse. It consists of a train of short sinc subpulses, and gradient blips in the k <sub>x</sub> , k <sub>y</sub> directions are applied to achieve in-slice modulation.	63
6.2	test of unconstrained $l_\infty$ norm minimization	68
6.3	Comparing OMP and proposed algorithm	69

6.4	Simulation results with B0 map and parallel excitation. The proposed method leads to less maximum excitation error for all number of subpulses. The $l_2$ norm of excitation error is similar between the minimax method and modified OMP approach. Using 3 subpulses, the proposed method reduces the maximum excitation error by more than half. . . . .	72
6.5	Cost function value and maximum error over iterations using our ADMM-based minimax algorithm. The cost function is monotonic decreased, but the maximum error has small oscillations. The cost function converges faster than the maximum error. . . . .	75
6.6	Regularization parameter $\mu$ versus iterations in ADMM. It became constant after approximate 70 iterations. . . . .	76
6.7	Simulated excitation error in the pre-phasing problem using the conventional $l_2$ -norm based design and our minimax pulse design. The high error spot in the conventional design result is removed by our minimax optimization. The maximum excitation error using minimax pulse design is 0.33 of the error using the conventional design, at the expense of root mean square error (RMSE). The RMSEs for the conventional design and minimax design are 0.02 and 0.04, respectively. . . . .	77
7.1	2 <sup>nd</sup> -order B-spline function basis, and its 1 <sup>st</sup> , 2 <sup>nd</sup> -order derivative. The gradient and slew rate are linear combination of the 1 <sup>st</sup> , 2 <sup>nd</sup> -order derivative, respectively. Their extreme values can occur at only a limited number of points, greatly reducing the number of inequity constraints. . . . .	85
7.2	Different k-space trajectory initializations for the inner-volume excitation: stack-of-spirals (SoS); SPINS; KT-points; and “extended KT-points”. KT-points and extended KT-points selectively traverse the k-space based on the target excitation pattern. The extended KT-points method manages to traverse a larger k-space region than the simple KT-points because of the improved visiting order and the use of a time-optimal gradient waveform. . . . .	92
7.3	Convergence speed of different algorithms used to solve the parametrized constrained optimization problem (7.3): (Left) Cost function value versus time. (Right) NRMSE versus time. There are two data points at time 0: the lower one is using the initialized k-space trajectory and the higher one is using the k-space trajectory after B-spline fitting. The fitting at the beginning of optimization slightly increases the NRMSE and the cost function value. The interior point and projected LM algorithms converge much faster than the other two, with the interior point algorithm slightly faster. . . . .	94
7.4	Example k-space trajectory, gradient waveform, and slew rate. The extended KT-points k-space trajectory before (dashed line) and after 20 iterations of alternating optimization with interior point algorithm (solid line) have similar shape. Both gradient and slew rate are within our constraint, but the slew rates are closer to the limit. . . . .	95

7.5	Inner-volume excitation, simulation results. Target pattern (top left) and field map in Hz (top right) used in the simulation. Row 2 to 5: results for different pulse design methods: left column contains the results of initialization pulse, right column contains the results after optimization using interior point algorithm. Four initialization methods were investigated: from top to bottom: SoS, SPINS, KT-points, our extended KT-points. All pulses have 3.9 ms pulse length. Optimization always improve the excitation results, reducing the NRMSE by 10 to 30% depending on the initialization method. Using extended KT-points as the initialization gave the best results. . . . .	96
7.6	Prephasing excitation, simulation results. The B0 field map is acquired from a human brain scan, shown in Hz. The excitation error for different initializations are ordered in the same way as Figure 8.4, and the pulse lengths are 3.9 ms for all. We want small error (dark blue) in the whole image. Without optimization, SPINS performs the best in this case. Interior point optimization substantially reduces the excitation error for all initializations, and SPINS and extended KT-points produce final results with similar accuracy in this prephasing case. . . . .	97
7.7	A example pulse diagram from the extended KT-points. The measured trajectory matches well with the nominal trajectory, indicating the distortion caused by eddy current may not be a problem for our implementation. . . . .	100
7.8	Comparison between extended KT-points designs and design using predefined SPINS trajectory: simulation and experimental result of extended KT-points design with local optimization of phase encoding points (e, f); extended KT-points (c, d); SPINS trajectory (a, b). Both extended KT-points methods achieve higher excitation accuracy than SPINS (NRMSE: 0.15/0.17 vs 0.21) with a shorter pulse length, and adding local minimization to the phase encoding locations reduces the NRMSE by 10% compared with the design without local minimization. Notice the local optimization here is not the optimization to the 2nd-order B-spline as we proposed in this chapter, it is just performed on the discrete phase encoding locations [88]. . .	101
7.9	k-space trajectory, gradient waveform, and slew rate if we run more iterations of interior point algorithm. Compared to Figure 7.4, the slew rates are pushed much harder to their limits. . . . .	103
8.1	Proposed ‘IVex-STFR’ sequence with 3D selective tip-down pulse and spectral pre-winding tip-up pulse. (a-b) Spin paths for inner volume (IV) (a) and outer volume (OV) (b) regions. (c) Pulse sequence timing diagram. The IV region experiences both tip-down and tip-up pulses. The OV region mainly experiences the tip-up pulse. The use of RF spoiling will spoil and partially suppress the steady-state OV signal [66]. . . . .	111

8.2	<p>Inner volume, outer volume signal and their ratio for STFR, bSSFP and SPGR. The top row shows STFR results with different tip-down and tip-up angles. The bottom row shows SPGR, bSSFP results, and STFR result with tip-down angle equal to tip-up angle. We assume the one shot excitation in the outer volume is 15% of the inner volume, so a IV/OV steady state signal ratio larger than 1/0.15 means the sequence can suppress the relative outer volume signal, such as STFR with similar tip-down and tip-up angle. In contrast, bSSFP and SPGR can amplify the relative outer volume signal. With the flip angles used in our experiment, the IV/OV ratios are 10.5, 4.3, 2.2, for STFR, bSSFP, and SPGR, respectively. . . . .</p>	112
8.3	<p>Steady-state brain imaging without and with inner volume excitation. (a) IVex-SPGR, (b) IVex-bSSFP, (c) IVex-STFR, (d) Conventional bSSFP. Images are windowed to the maximum intensities of the corresponding acquisitions. As desired, bSSFP and STFR show similar tissue contrast for inner volume spins. STFR has good outer volume suppression. The IV/OV ratio are 12.5/4/2.4 for IVex-STFR, IVex-bSSFP, and IVex-SPGR, respectively, consistent with our simulation. The SNR of bSSFP and STFR are similar, about twice as SPGR according to our theory [93] . . . . .</p>	113
8.4	<p>Simulated rFOV acquisition with different reduction factors. Cropped full FOV images (top row) and difference images (bottom row) are also shown for comparison. The difference images are multiplied by 5 to better observing the artifacts. We can obtain good results when <math>FOV_{xy}/FOV_z = 10 \text{ cm}/7 \text{ cm}</math>. When the acquisition FOV approximately equal to the excitation region, we observe more aliasing artifacts, but the images may be still usable for some applications. . . .</p>	114
9.1	<p>Illustration of the potential function and its surrogate. . . . .</p>	117
9.2	<p>Results for the simulated data set. (a) simulated image data (magnitude). (b) Estimated <math> B_1^+ </math> maps. The RMSE in Gauss for all methods are shown in the parentheses. Both PL estimators generate more accurate <math> B_1^+ </math> maps than the MOM and MOM+smoothing approach. . . . .</p>	118
9.3	<p>Plots of RMSE in Gauss compared to the converged estimation with respect to iteration (a) and time (b). Plots of RMSE compared to the true <math> B_1^+ </math> with respect to iteration (c). Using true Hessian for the regularization term instead of SQS greatly improves the convergence rate. Using cost function (9.16) and its optimal curvature converges the fastest. . . . .</p>	118

9.4	Results for the <i>in vivo</i> data set: (a) acquired image with BS encoding from one of 8 channel transmit coil (red ellipse), (b) estimated $ B_1^+ $ map from the method of moments and the proposed penalized likelihood method (9.16). Artifact (arrow) due to T2* signal drop is greatly reduced in the proposed method. Also, our method removes the popcorn noise observed around the periphery of the head, and that noise can significantly affect subsequent RF pulse designs. . . .	121
-----	-------------------------------------------------------------------------------------------------------------------------------------------------------------------------------------------------------------------------------------------------------------------------------------------------------------------------------------------------------------------------------------------------------------------------------------------------------------------------------------------------	-----

## LIST OF TABLES

### Table

3.1	Summary of phantom and human imaging experiments. . . . .	26
3.2	Sequence timing. . . . .	26
4.1	Summary of fMRI experiments. . . . .	40
4.2	Simulated and measured percent functional signal change. . . . .	40
7.1	Pulse design methods . . . . .	92
8.1	Relative percent error with different readout FOV . . . . .	110

## LIST OF APPENDICES

### Appendix

A.	Derivation of the steady-state signal equation of unspoiled STFR . . .	128
B.	Derivation of Hessian matrix with respect to k-space trajectory . . . .	130
C.	Instructions for STFR experiments . . . . .	132
D.	Bloch simulations for steady-state sequences . . . . .	134
E.	Data and code for STFR-fMRI . . . . .	135
F.	Selected source code for Chapter VI to IX . . . . .	136

# ABSTRACT

Topics in steady-state MRI sequences and RF pulse optimization

by

Hao Sun

co-chair: Jon-Fredrik Nielsen

co-chair: Jeffrey A. Fessler

Small-tip fast recovery (STFR) is a recently proposed rapid steady-state magnetic resonance imaging (MRI) sequence that has the potential to be an alternative to the popular balanced steady-state free precession (bSSFP) imaging sequence, since they have similar signal level and tissue contrast, but STFR has reduced banding artifacts. In this dissertation, an analytic equation of the steady-state signal for the unspoiled version of STFR is first derived. It is shown that unspoiled-STFR is less sensitive to the inaccuracy in excitation than the previous proposed spoiled-STFR. By combining unspoiled-STFR with jointly designed tip-down and tip-up pulses, a 3D STFR acquisition over 3-4 cm thick 3D ROI with single coil and short RF pulses (1.7 ms) is demonstrated. Then, it is demonstrated that STFR can reliably detect functional MRI signal using human experiments and test-retest reliability analysis, and the contrast is driven mainly from intra-voxel dephasing, not diffusion, using Monte Carlo simulation. Following that another version of STFR that uses a spectral pre-winding pulse instead of the spatially tailored pulse is investigated, leading to less  $T_2^*$  weighting, easier implementation compared to the spatial implementation. Multidimensional selective RF pulse is a key part for STFR and many other MRI applications. Two novel RF pulse optimization methods are proposed. First, a minimax formulation that directly controls the maximum excitation error, and an effective optimization algorithm using variable splitting and alternating direction method of multipliers (ADMM). The proposed minimax method reduced the maximum excitation by more than half in all the testing cases. Second, a method that

jointly optimizes the excitation k-space trajectory and RF pulse is presented. In this method, the k-space trajectory is parametrized using 2nd-order B-splines, and an interior point algorithm is used to explicitly solve the constrained optimization. The proposed method improves excitation accuracy for all the initializations being tested. An effective initialization method is also suggested. The joint design reduced the NRMSE by more than 30 percent compared to existing pulse designs in inner volume excitation and pre-phasing problem, and the computation is fast enough for online pulse design. Using the proposed joint design, rapid inner volume STFR imaging with a 4 ms excitation pulse with single transmit coil on a clinical scanner is demonstrated. Finally, a regularized Bloch-Siegert B1 map reconstruction method is presented that can significantly reduce the noise in estimated B1 maps.

# CHAPTER I

## Introduction

Magnetic resonance imaging (MRI) is a popular medical imaging modality for its good soft tissue contrast, no ionizing radiation, and ability to detect functional signal. MRI relies on a properly designed sequence of time varying RF and gradient field (pulses) to excite the spins inside the object. Then the signal from the spins is spatially encoded using gradient field waveforms for image reconstruction later. To fully encode the excited spins in an object without aliasing artifacts, a relatively long readout gradient waveform has to be transmitted. However, a long readout waveform can lead to signal drop, geometric distortion, or blurring in the final image, due to T2 decay and B0 field inhomogeneity. Also, the object may be moving during the long readout gradient in some applications (e.g., cardiac MRI). Therefore, it is desirable to divide the readout gradient waveform into segments and only acquire one or several segments after each excitation, so each readout time can be short. As the number of segments increases, it is better to have shorter repetition time (TR) so the total scan time can be relatively short. Therefore, sequences with TR even shorter than T2 has been widely used in MRI. Spins can not fully recover to their equilibrium with such a short TR, so there is signal oscillation in the beginning of the sequence. After a several seconds, spins achieve steady state, and steady-state imaging is to only acquire signal after spins enter steady state.

Balanced steady-state free precession (bSSFP) is one of the short TR steady-state sequences that has been widely used in many applications, due to its high signal to noise ratio, and useful tissue contrast. However, it suffers from off-resonance banding artifacts [79]. Numerous methods have been proposed in the past decade for correcting these artifacts, however, all of these methods sacrifice signal strength and/or imaging time, and are not universally applicable to all bSSFP applications. My co-advisor Jon Nielsen recently proposed a new steady-state imaging sequence named “small-tip

fast recovery” (STFR) sequence, that can acquire bSSFP-like images in a single scan, but with removed/reduced banding artifact.

However, it is challenging to implement STFR in practice, due to the need for accurate tailored RF pulses, especially in 3D imaging since the required 3D tailored pulse can be prohibitively long. In chapter III, I derive the steady-state signal equation of the unspoiled version of STFR and demonstrate that it is less sensitive to excitation error than the previously proposed spoiled-STFR. I also propose to jointly design the tip-down and tip-up pulse. With those two strategies, we demonstrate 3D ROI imaging over a 3-4 cm thick volume using a standard quadratic transmit/receive coil and short tailored 3D RF pulse of 1.7 ms duration [91, 87, 93].

The STFR sequence using a spatially tailored pulse has very similar image contrast to bSSFP, but with a key difference: it has some T2\*-like contrast induced by intra-voxel dephasing. Therefore, it is possible to be used in functional MRI (fMRI) to detect the blood oxygenation level dependent (BOLD) signal. In Chapter IV, I confirm this hypothesis using Monte Carlo Bloch simulation and in vivo experiment. Our simulations suggest that the functional contrast is driven primarily by static dephasing, not diffusion. Our in vivo experiments and test-retest reliability analysis suggest that STFR can be used as a reliable fMRI sequence [97, 64, 90].

On the other hand, one may want to reduce the T2\*-like weighting of STFR images in some applications. In Chapter V, we propose another version of the STFR sequence named spectral-STFR that has less T2\* influence. In spectral-STFR, we use a spectral pre-winding pulse instead of a spatially tailored pulse. The spectral-STFR has the additional advantages that it can be pre-computed since no field map must be acquired, and is easier to implement in practice [92, 89].

The key to successful STFR imaging is to design a short multidimensional selective excitation pulse that pre-phases spins in the object. In conventional selective excitation pulse design, the k-space (gradient) trajectory is pre-defined, allowing the RF waveform to be obtained using linear least-squares optimization, but leading to suboptimal excitation accuracy. Designing the k-space trajectory jointly with RF waveform poses a non-linear, nonconvex, constrained optimization problem with relatively large problem size that is difficult to solve directly. Existing joint pulse design approaches are therefore typically restricted to predefined trajectory types that intrinsically satisfy the gradient maximum and slew rate constraints. In Chapter VII, I propose to use a 2nd-order B-spline basis that can be fitted to an arbitrary k-space trajectory, and allows the gradient constraints to be considered explicitly and efficiently. I investigate several constrained optimization algorithms and find the in-

terior point algorithm to be the best choice in our setting. I also extend the existing KT-points method to form a continuous RF pulse and demonstrate that it is a good initialization to our algorithm. With our proposed joint design method, we are able to achieve substantial improvement in excitation accuracy for a given pulse duration compared to existing methods in both of our testing cases: inner volume excitation and pre-phasing problem. The computation time is fast enough for online applications [88].

In addition to pre-phasing in the STFR sequence, the multidimensional selective pulse can also be used in inner volume imaging (IVI). Existing 3D IVI method using conventional RF pulse design needs a more than 12 ms RF pulse, even with 8 channel parallel transmit coil. This pulse length can be too long for many rapid steady-state imaging sequences, and also the parallel transmit hardware is not accessible to every MRI scanner. In Chapter VIII, we propose to combine our joint pulse design method with the STFR sequences for rapid steady-state IVI, that enables us to achieve successful inner volume imaging with bSSFP-like image contrast, using a 4 ms RF pulse and single transmit coil [94].

Existing pulse design methods typically regulate the  $l_2$  norm of the excitation error instead of the maximum error, which may lead to dark or light spots in the final image. In Chapter VI, we propose a pulse design formulation that directly minimizes the maximum error. We also propose an optimization algorithm using variable splitting and ADMM, that can efficiently solve this minimax problem. Our proposed minimax pulse design reduces the maximum error by more than half, in all our testing cases [96].

Transmit coil sensitivity mapping (B1 mapping) is an important step for pulse design, especially in parallel transmission. The popular Bloch-Siegert B1 map reconstruction method can have large noise in the low image magnitude region, significantly affecting subsequent RF pulse designs. In Chapter IX, we propose a regularized estimation method for the Bloch-Siegert B1 map that significantly reduce the noise in final estimate. We propose a majorize-minimization method that essentially converged in just 3 iterations within 0.1 sec [95].

The chapters after this introduction are organized as follows. Chapter II briefly introduces the background about MRI physics, RF pulse design, steady-state imaging, and functional MRI. Chapters III to Chapter V cover three projects related to STFR: strategies for improving 3D STFR (Chapter III); functional MRI using the STFR sequence (Chapter IV); and STFR using spectral pre-winding pulse (Chapter V). Chapter VI describes the minimax pulse design method. In Chapter VII, I

present our joint design of excitation k-space and RF pulse. Chapter VIII demonstrates using joint RF pulse design and STFR for rapid steady-state IVI imaging. Chapter IX presents the regularized Bloch-Siegert B1 map reconstruction method. Finally, Chapter X summarizes future work.

## CHAPTER II

# Background

### 2.1 MRI Physics

#### 2.1.1 Spin and bulk Magnetization

To understand the MRI physics, we begin with the object to be imaged. A physical object can be broken down into its constituent molecules, then to atoms, and then to nuclei and their orbiting electrons. A fundamental property of nuclei is that those with odd atomic weights or odd atomic numbers possess an angular momentum  $\vec{J}$ ; such a nucleus is referred to as spin. Although the behaviour of spin is characterized by quantum mechanics, it can also be viewed as a physical rotation similar to the rotation of a top around its axis in a classical vector model. Similar to other rotating charged bodies, spins can possess a magnetic moment, which is represented as a vector quantity  $\vec{\mu}$ . To describe the collective behaviour of a spin system, a macroscopic magnetization vector  $\vec{M}$  is introduced as  $\vec{M} = \sum_{n=1}^{N_s} \vec{\mu}_n$ , where  $\vec{\mu}_n$  represents magnetic moment of the  $n$ th nuclear spin and  $N_s$  is the number of spins within a certain volume.  $\vec{M}$  is a three dimensional vector  $[M_x, M_y, M_z]$  and the detected signal strength is proportional to the transverse part  $|M_x + \iota M_y|$ . Among all the spins, Hydrogen( $^1H$ ) is the most abundant in the body and produces the largest signal, therefore, it is imaged in most of our studies in human MRI. It is worth noting that in MRI field, people often use “spin” to refer the magnetization vector  $\vec{M}$ , and I will follow this convention in the proposal report.

#### 2.1.2 Three Magnetic Fields

Three magnetic field are used in magnetic resonance imaging: the main field ( $\vec{B}_0$ ), the radio-frequency (RF) field ( $\vec{B}_1$ ), and a field gradient ( $\vec{G}$ ). Without an external magnetic field, the spins in the body are randomly oriented resulting in a net magnetic

moment of zero. However, in the presence of an external magnetic field,  $\vec{B}_0$ , the spins align either parallel (spin up) or anti-parallel (spin down) to  $\vec{B}_0$ . By quantum physics, the spin up state is in lower energy state and thus there are more spins in this state. Also, although there is a microscopic transverse component for each magnetic moment vector  $\vec{\mu}$ , the transverse component of the macroscopic magnetization vector  $\vec{M}$  is zero in equilibrium because the precessing magnetic moments have random phases. Therefore the macroscopic effect of an external field  $\vec{B}_0$  on an ensemble of nuclei with non-zero spins is the generation of an observable bulk magnetization vector  $M$  along  $\vec{B}_0$  direction. By convention, the direction of  $\vec{B}_0$  is referred to as longitudinal or z direction.

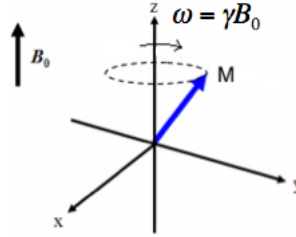


Figure 2.1: Magnetization vector precesses around B0 field at Larmor frequency

If  $\vec{M}$  is tipped away from z-direction, it will precess around the z-direction at the *Larmor frequency*,  $\omega$ :

$$\omega = \gamma B$$

where  $\gamma$  is the *gyromagnetic ratio* and  $B$  is the magnetic field strength. For Hydrogen,  $\gamma/2\pi = 42.58$  MHz/T, which yield a Larmor frequency of 127.7 MHz for a field strength of 3T. Ideally, we want  $\vec{B}_0$  to be uniform magnitude, but there is always some field inhomogeneity ( $\Delta\vec{B}_0(r)$ ) in practice, depending on the strength of main field, the shimming, and the subject inside of the scanner. The resulting frequency inhomogeneity in a 3T scanner is typically within -200 Hz to 200 Hz over a human brain.

Establishment of a phase coherence among these randomly precessing spins in a magnetized spin system is called resonance. By quantum model, we can achieve resonance condition by applying another external magnetic field in xy-plane rotating with frequency  $\omega_{rf} = \omega$ . This magnetic field is often referred to as radio-frequency (RF) field or  $\vec{B}_1$  field. The magnitude of  $\vec{B}_1$  is much weaker, which is in the order of tens of  $\mu T$ , while  $\vec{B}_0$  ranges from hundred of  $mT$  to tens of  $T$ . A typical  $\vec{B}_1$  field

takes the following form:

$$\vec{B}_1(t, r) = S(r)B_1^e(t)(\cos(\omega_{rf}t + \phi)\vec{x} - \sin(\omega_{rf}t + \phi)\vec{y})$$

where,  $S(r)$  is the spatially varying transmit sensitivity,  $B_1^e(t)$  is the complex number pulse envelope,  $\omega_{rf}$  is the excitation carrier frequency, and  $\phi$  is the initial phase angle.  $S(r)$  is typically assumed to be uniform in the low field single coil excitation, but it can spatially vary a lot in high field MRI and parallel excitation. The process of measuring the actual transmit sensitivity is called *B1 mapping*[75].

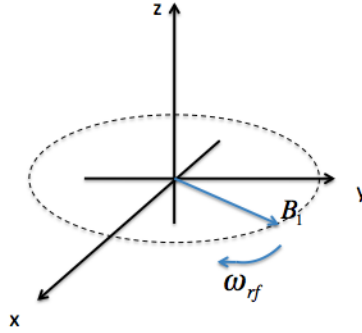


Figure 2.2: RF field( $B_1$ ) is rotating in xy-plane

In the presence of only  $\vec{B}_0$ , all the spins precess at the same frequency ( $\omega_0 = \gamma\vec{B}_0$ ). Thus there is no way to excite or detect a specific region of interest. To achieve spatial localization, a spatially varying magnetization field with linear gradient is applied in the same direction with  $\vec{B}_0$ , called gradient magnetic field. Thus, the total magnitude field pointing to the longitudinal direction becomes:  $B_0 + G_x(t)x + G_y(t)y + G_z(t)z$ , where  $G_x(t), G_y(t), G_z(t)$  are the time varying spatial gradient in the x, y, and z direction, respectively. The gradients are typically within the range ( $\pm 50$  mT/m), and the time varying slew rate of the gradients are typically limited between -200 mT/m/s and +200 mT/m/s.

### 2.1.3 The Bloch Equation

The behaviour of the magnetization vector  $\vec{M}(\vec{r}, t)$  under a magnetic field  $\vec{B}(\vec{r}, t)$  is characterized by the Bloch equation:

$$\begin{aligned} \frac{d\vec{M}(\vec{r}, t)}{dt} &= \gamma \vec{M}(\vec{r}, t) \times \vec{B}(\vec{r}, t) - \frac{M_x(\vec{r}, t)\mathbf{x} + M_y(\vec{r}, t)\mathbf{y}}{T_2} - \frac{(M_z(\vec{r}, t) - M_z^0)\mathbf{z}}{T_1} \\ &= \gamma \vec{M}(\vec{r}, t) \times [\vec{B}_0 + \Delta\vec{B}_0(\vec{r}) + \vec{B}_1(\vec{r}, t) + \mathbf{z}(\vec{G}(\vec{r}, t) \cdot \vec{r})] - \frac{M_x(\vec{r}, t)\mathbf{x} + M_y(\vec{r}, t)\mathbf{y}}{T_2} \\ &\quad - \frac{(M_z(\vec{r}, t) - M_z^0)\mathbf{z}}{T_1} \end{aligned} \quad (2.1)$$

where  $\Delta\vec{B}_0$  represents the field inhomogeneity of  $\vec{B}_0$ . T1 and T2 are the spin-lattice and spin-spin relaxation parameters that described the recovery of  $M_z$  and the decay of  $M_{xy}$  over time, respectively.

In MRI, it is more convenient to work with rotating frame of reference. A rotating frame of reference is a coordinate system that rotates along z-axis clockwise with angular frequency  $\omega = \gamma B_0$ . Then, the precession due to  $\vec{B}_0$  is not seen and the general Bloch equation 2.1 becomes the following (for simplicity, we ignore the dependence on  $\vec{r}$  and  $t$  in the following equations):

$$\frac{d\vec{M}}{dt} = \gamma \vec{M} \times [\delta\vec{B}_0 + \vec{B}_1 + \mathbf{z}(\vec{G} \cdot \vec{r})] - \frac{M_x\mathbf{x} + M_y\mathbf{y}}{T_2} - \frac{(M_z - M_z^0)\mathbf{z}}{T_1} \quad (2.2)$$

We can rewrite the above equation in matrix vector form as follow:

$$\frac{d}{dt} \begin{pmatrix} \vec{M}_x \\ \vec{M}_y \\ \vec{M}_z \end{pmatrix} = \gamma \begin{pmatrix} -1/T_2 & \vec{G} \cdot \vec{r} + \Delta\vec{B}_0 & -B_{1y} \\ \vec{G} \cdot \vec{r} + \Delta\vec{B}_0 & -1/T_2 & B_{1x} \\ B_{1y} & -B_{1x} & -1/T_1 \end{pmatrix} \begin{pmatrix} \vec{M}_x \\ \vec{M}_y \\ \vec{M}_z \end{pmatrix} + \begin{pmatrix} 0 \\ 0 \\ M_0/T_1 \end{pmatrix} \quad (2.3)$$

## 2.2 RF Pulse Design

### 2.2.1 Excitation Pulse Design Problem

We can tip spin away from the longitudinal axis by applying a proper  $\vec{B}_1$  magnetic field, and this process is called *excitation*. The pulse design problem is how to determine both the RF pulse and linear gradient waveforms to achieve the desired excitation pattern. This can be formulated as an optimization problem as follows.

- **Unknown input**

- RF pulse waveform: Complex valued  $B_1(t)$ .

- Linear gradient waveform: Real valued  $G_x(t)$ ,  $G_y(t)$ ,  $G_z(t)$ .
- **Target output** Magnetization pattern at the end of RF pulse:  $\vec{M}(\vec{r}, T)$ .  $T$  is the length of the RF pulse, and a shorter  $T$  is preferred.
- **Input-output relationship**  
Bloch equation [2.3]. Initial condition of magnetization vector:  $\vec{M}(\vec{r}, 0)$
- **Constraints**  
RF pulse: maximum magnitude is limited, and lower integrated power is preferred.  
Linear gradients: maximum magnitude and slew rate are limited.
- **Cost function**  
Difference between the actual excitation pattern  $\vec{M}(\vec{r}, T)$  and the desired excitation pattern  $d(\vec{r})$ .

The above formulations target to a single frequency. In some cases, the desired and actual excitation patterns are a function of off-resonance frequency and/or space.

Unfortunately, it is generally hard to solve this optimization problem for arbitrary desired excitation and an arbitrary initial state, because either there may be no analytical solution to the Bloch equation or it is too computationally intensive to numerically solve the optimization problem. However, in some cases, the pulse design problem becomes more tractable, and the small-tip-angle pulse design is one of them.

### 2.2.2 Small-tip-angle Approximation

When the initial magnetization vector is at equilibrium and the desired flip angle is small ( $< 30^\circ$ ), we can linearize the Bloch equation using small-tip-angle (STA) approximation [72]. The STA approximation assumes the longitude magnetization is approximately equal to  $M_0$  during the whole excitation period ( $M_z(t) \approx M_0$ ). Ignoring T1/T2 terms in the Bloch equation, and define  $M_{xy} = M_x + \imath M_y$ ,  $B_1 = B_{1,x} + \imath B_{1,y}$ , leads to the following equation:

$$\dot{M}_{xy}(\vec{r}, t) = -\imath\gamma\vec{G}(t) \cdot \vec{r} + \imath\gamma B_1(t)M_0 \quad (2.4)$$

Then using the initial condition  $\vec{M}(\vec{r}, 0) = (0, 0, M_0)^T$ , we can solve this equation and get the final magnetization at time  $T$ ,

$$M_{xy}(\vec{r}, T) = \iota M_0 \int_0^T \gamma \vec{B}_1(t) e^{-\iota \int_t^T \gamma \vec{G}(s) \vec{r} ds} dt$$

This equation describes the relation between the excitation pattern and the applied RF and gradient field. We can further change the form of this equation to get a  $k$ -space interpretation. Defining:

$$\vec{k}(t) = -\gamma \int_t^T \vec{G}(s) ds, \quad (2.5)$$

we can rewrite equation 2.4 as:

$$M_{xy}(\vec{r}, T) = \iota \gamma M_0 \int_0^T \vec{B}_1(t) e^{i\vec{r} \cdot \vec{k}(t)} dt. \quad (2.6)$$

Then if we define

$$p(\vec{k}) = \int_0^T \vec{B}_1(t) \delta(\vec{k}(t) - \vec{k}) dt$$

we can further express the above equation as [72]

$$M_{xy}(\vec{r}, T) = \iota \gamma M_0 \int p(\vec{k}) e^{i\vec{r} \cdot \vec{k}(t)} d\vec{k}. \quad (2.7)$$

Now we can clearly see under small tip angle approximation, the transverse magnetization after excitation is just the Fourier transform of  $k$ -space weighting  $p(\vec{k})$ . This is a very important property in RF pulse design. It allows us to design any target excitation pattern  $M_{xy}(\vec{r})$  by depositing energy in  $k$ -space according to the Fourier transform of the excitation pattern. One example is called slice selective excitation, in which we deposit energy in  $k_z$  direction using a truncated sinc function or a Gaussian function weighing. This allows us to excite only a slice in the  $z$  direction. The other example is the tailored pulse design, in which we design a specific excitation pattern in the  $xy$  plane using this relation. Although this relation is derived for flip angle smaller than 30 degree, it has been shown in simulation that it holds well until 90 degree [72]. Most STA pulse design methods are based on this assumption.

### 2.2.3 Iterative Small-tip-angle RF Pulse Design

An iterative small-tip-angle RF pulse design method is proposed by Yip et al. [103]. In that method, equation [2.6] is discretized and rewritten as follows:

$$\mathbf{m} = \mathbf{A}\mathbf{b} \quad (2.8)$$

where  $\mathbf{m}$  is a complex vector containing the transverse magnetization for  $N_s$  spatial positions,  $\mathbf{b}$  is a  $N_t$  long complex number vector containing the time samples of the RF pulse, and  $\mathbf{A}$  is the  $N_s \times N_t$  *system matrix* with elements:

$$a_{ij} = \nu\gamma M_0 e^{i\vec{k}(t_j)\cdot\vec{r}_i + i\Delta\omega(\vec{r}_i)(t_j-T)} \quad (2.9)$$

Now we can set up the RF pulse design problems as follows:

$$\hat{\mathbf{b}} = \underset{\mathbf{b} \in \mathbb{C}^{N_s}}{\operatorname{argmin}} \|\mathbf{A}\mathbf{b} - \mathbf{d}\|_{\mathbf{W}}^2 + \beta \mathbf{b}'\mathbf{b}$$

where  $\mathbf{W}$  is diagonal matrix containing the user-selected error weighting, and  $\beta$  is the regularization parameter. This problem can then be solved efficiently using conjugate gradient algorithm.  $\mathbf{A}\mathbf{b}$  can be efficiently computed using FFT or nonuniform FFT (NUFFT) [18]

In the iterative pulse design framework, it is much easier to employ non-Cartesian k-space trajectory than the previous density compensation methods [72]. Also, we can easily incorporate a “don’t care region” in the weighting matrix  $\mathbf{W}$ , which effectively reduces the number of rows in  $\mathbf{A}$ , and thus reduces the excitation error in this typically overdetermined problem ( $N_t < N_s$ ). Furthermore, we can set the regularization of RF power here to reduce the specific absorption rate (SAR). Finally, it is much easier than the Fourier based methods to consider the field inhomogeneity of  $B_0$  and  $B_1$ , and generalize the pulse design problem to parallel excitation [23].

The method described above is the conventional approach for small-tip-angle RF pulse design nowadays. In this method, one designs the RF waveforms with a predefined k-space trajectory, which leads to suboptimal pulses in terms of excitation accuracy for a given pulse duration. A joint optimization of RF pulse and the k-space trajectory should be able to generate better result. Some works have been done to jointly design the k-space trajectory and RF pulse, but most of them are limited to discrete k-space trajectories like fast-kz/spoke pulse (discrete in x-y plane) [111, 53, 109, 10, 24],

or KT-points method [11]. There are relative few works on the joint design of RF pulse and continuous 3D k-space trajectory. I will briefly describe them in Ch.7, and then propose my approach for the joint design.

## 2.3 Steady-state Imaging

Steady-state magnetic resonance imaging (MRI) is a fast MRI technique based on the steady state of magnetization achieved by a series of RF pulses with relative short interval (TR). In conventional MRI sequence, TR is the order of  $T_1$  (ranges from hundred of milliseconds to a few second) to allow the full recovery of longitudinal magnetization, while in steady-state imaging, the TR is usually less than  $T_2$ . A direct result of this short TR is that the Ernst formula used to describe the signal level after excitation in conventional MRI sequence can no longer be used in steady state imaging (except SPGR) since the transverse magnetization is non zero before the RF pulse and can be refocussed and contributes to the following echos by the subsequent RF pulse.

The sufficient and necessary condition to produce stationary states are given by [78],

- The de-phasing of states between RF pulses must be constant.
- The time TR between RF pulses must be constant.
- The flip angle  $\alpha$  of RF pulses must be constant.
- The phase of the RF pulses must satisfy the equation:  $\Phi_n = a + bn + cn^2$ .

Strictly speaking, a sequence is not a true steady state, but a *pseudo - steady state* if the last condition has  $c \neq 0$ . It means each magnetization vector  $\vec{M}$  is not in steady state, but the integrated signal in a voxel achieves steady state. These conditions are given for a typical MRI sequence with one RF pulse per TR. For a sequence with multiple RF pulses per TR, we may need to group RF pulses and then apply those conditions. To get an intuitive understanding of the behaviour of steady-state imaging, we may think of the power iteration as an analogy: the behaviour of spins during excitation, precession can be fully characterized by a rotation matrix operations. By applying the same matrix operation again and again,  $\vec{M}$  will finally converge to the eigenvector of a certain matrix [31]. It usually takes about  $4T_1$  time ( $4T_1/\text{TR}$  cycles) to achieve steady state.

### 2.3.1 Phase Graph

The behaviour of a magnetization vector under RF and gradient waveform can be described by the classical Bloch equation. The RF and gradient field simply rotate the magnetization vector around different axis. We can calculate the steady state signal by first calculating the steady state of each magnetization vector and then integrating them across the voxel. This method is widely used to characterize the signal property of steady-state imaging, and will be used to describe our proposed steady-state imaging sequence in Ch. III. However, it was demonstrated that the description of steady state imaging sequence using this method is not adequate for a pictorial understanding of the simulated echo, and by no means able to illustrate the appearance of all higher-order echoes [78]. To better understand the echo formation in the steady state imaging, we can use the *phase graph* proposed by Hennig [33]. In phase graph, we use the *dephased states* with zero net magnetization as a fundamental building block instead of isolated magnetization vectors. A good summary of steady-state imaging using phase graph interpretation is presented in Scheffler [78] (the first MRI paper I have ever read).

### 2.3.2 RF Spoiling

*RF spoiling* is an important concept in steady state imaging. The goal of the RF spoiling is to achieve a zero net transverse magnetization within a voxel before each RF pulse. The RF spoiling technique contains two key parts: (1) a gradient crusher is applied before each RF pulse; (2) the phase of the RF pulses varies quadratically in each TR, or in other words, the phase increment between TR follows

$$\phi(n + 1) - \phi(n) = cn. \quad (2.10)$$

where  $n$  is the number of RF pulses, and  $c$  is a constant. It has been shown that, under the above conditions, the integrated signal from a voxel forms a steady state [120]. However, there is no analytic relation between the steady state signal and the constant  $c$ . In [120], Zur suggested that choosing  $c = 117^\circ$  can effectively remove the net transverse magnetization  $M_t$  before the RF pulse according to the simulation. When we set  $c$  to be a different constant, we often refer the sequence as *partial RF spoiling*.

Besides the RF spoiled GRE sequence (*aka* SPGR, FLASH, and  $T_1$ -FFE), there are two other basic types of steady state sequence: steady state free precession (SSFP), and balanced steady state free precession (bSSFP, *aka* TureFISP, FIESTA, b-FFE). The bSSFP sequence is similar to SSFP but with zero net gradient. The

SSFP sequence has two basic variations: SSFP-FID (*aka* FISP, GRASS, FFE) if the net gradient area is zero before read out, SSFP-ECHO (*aka* PSIF, SSFP,  $T_2$ -FFE) if the net gradient area is zero after the read out.

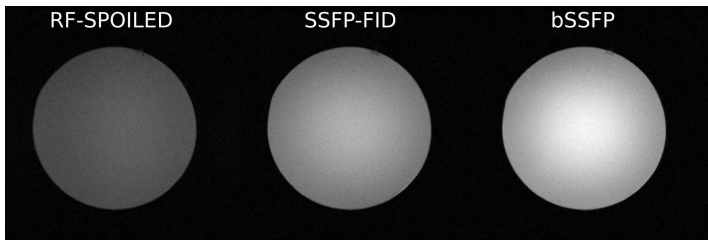


Figure 2.3: Comparing signal level between SPGR SSFP-ECHO and bSSFP

### 2.3.3 Balanced Steady-state Sequence (bSSFP)

bSSFP sequence is a popular steady-state sequence for clinical and research application. It offers higher signal to noise ratio than SPGR and SSFP-FID/ECHO (Figure [2.3]), and it has useful T2/T1-weighted image contrast. However, bSSFP suffers from two main drawbacks. The first one is its transient signal fluctuations during the initial approach toward steady-state. Without any catalyzing sequence before the bSSFP sequence, it needs  $3T_1$  to  $4T_1$  time to achieve steady state [78], and this time may be too long for some applications. However, this time can be effectively reduced by using a catalyzing sequence before bSSFP [31]. The second drawback of bSSFP sequence is the well known banding artifact, which means the signal level can be quite low for some off-resonance, and therefore causes a dark band in the image (illustrated in Figure 2.4).

One strategy to avoid/reduce banding artifact is to put the off-resonance frequency of the target region to the pass band of the bSSFP frequency response by better shimming [48]. However, even with better shimming, the pass band bandwidth can still be too narrow to achieve a banding free image. Numerous other methods have been proposed in the past decade for correcting these artifacts, including multi-TR sequences that seek to widen the separation between bands [69, 13, 62, 49], multiple phase-cycled acquisitions that are combined to produce uniform signal independent of off-resonance. However, all of these methods sacrifice signal strength and/or imaging time, and are not universally applicable to all bSSFP applications. Another drawback of bSSFP is it is not compatible with many magnetization preparation sequence like fat saturation.

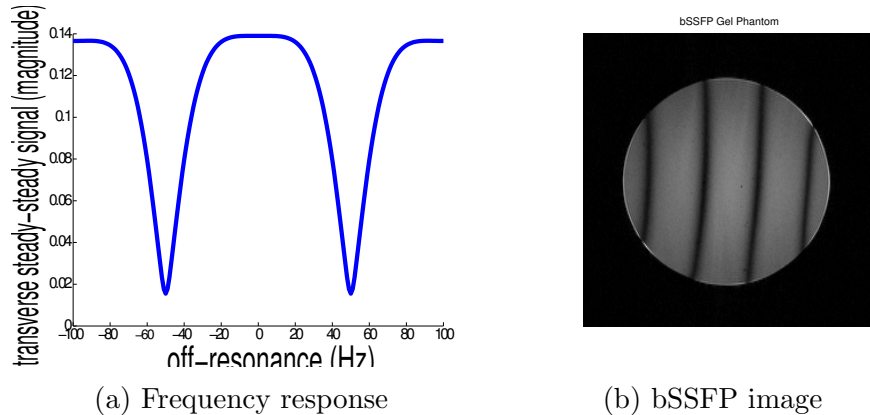


Figure 2.4: Demonstration of banding artifact in bSSFP

## 2.4 Functional MRI

### 2.4.1 Blood-oxygen-level-dependent (BOLD)

Functional MRI (fMRI) is a neural imaging technique that measures the brain activity map by detecting the change of blood flow. Most of the current fMRI relies on the “blood-oxygen-level-dependent(BOLD)” effect, discovered by Ogawa [68]. Through hemodynamic response, more blood flow into the active region of brain, causes an increasing oxygenation blood level near active neurons. Since oxygen is paramagnetic, the increasing oxygenation level will decrease the intra-voxel B0 field inhomogeneity and therefore reduce the  $T_2^*$ , leading to a higher signal in  $T_2^*$ -weighted MR images.

In most of the conventional fMRI sequences, a long echo time (TE) is required to build up sufficient BOLD functional contrast, which makes the sequence susceptible to background B0 inhomogeneity unrelated to oxygenation, leading to signal dropout near air/tissue boundaries and geometric distortions or blurring. Several tailored RF pulse design methods have been proposed to reduce the signal drop [104, 106] by pre-phasing the spins such that they can be refocused at the echo time. However, without parallel excitation, those pulses may be too long in practice. Our group has been working on the implementation of signal recovery pulse using parallel excitation hardware [34].

### 2.4.2 bSSFP fMRI

bSSFP fMRI based using segmented readouts can produce high resolution functional maps with reduced geometric distortions. bSSFP fMRI falls in to two categories: transition-band fMRI [80, 57] and pass-band fMRI [8, 118, 59, 47, 58, 61, 45].

In transition-band fMRI, people shim the off-resonance frequency of the target region to the transition-band of bSSFP profile, and the neuron activity can cause a spreading and a shift of the local off-resonance frequency, which causes 10% signal change [80]. While this technique can achieve relative high percent signal change, it suffers from two main drawbacks: first, the signal level at the transition band is typically low, which leads to a low signal to noise ratio (SNR); second, it is generally hard to shim all the target region to the transition band since the transition band is typically very narrow.

In pass-band fMRI, the diffusion effect can cause effective change of  $T_2$ , and this change is different during active and resting states, which leads to detectable signal. While the pass-band fMRI is much easier to implement than its transition-band sibling and generally have high SNR, it is susceptible to dark “banding” artifacts in regions of high  $B_0$  inhomogeneity and generally has lower functional contrast than BOLD [118]. bSSFP with multiple phase-cycles may be used to reduce the banding artifact. We note, however, that multiple acquisitions may not be preferred in fMRI, repeating runs of a paradigm produces confounding effects from cognitive habituation to stimuli and is not ideal [47, 57]. Alternating bSSFP that interleaves two phase-cycled bSSFP imaging can potentially solve this problem [70], but it needs catalyzation pulses every time the phase-cycling is changed, which reduces its SNR efficiency.

We proposed a new steady-state functional imaging method using the STFR sequence [97] and I will describe it in Ch. IV.

## CHAPTER III

# Strategies for Improved 3D Small-tip Fast Recovery Imaging

### 3.1 Introduction

<sup>1</sup>Balanced steady-state free precession (bSSFP) is a rapid imaging sequence that has high signal-to-noise ratio (SNR) and useful tissue contrast, but suffers from off-resonance banding artifacts and transient fluctuations [79]. Numerous methods have been proposed in the past decade for correcting these artifacts, including multi-TR sequences that seek to widen the separation between bands [69, 12, 62, 49], and multiple phase-cycled acquisitions that are combined to produce uniform signal independent of off-resonance. However, all of these methods sacrifice signal strength and/or imaging time, and are not universally applicable to all bSSFP applications.

Recently, our group proposed a new steady state imaging sequence called small-tip fast recovery (STFR) [65], which is a potential alternative to bSSFP. There are two key ideas in STFR: First, after excitation and readout, a tip-up radio-frequency (RF) pulse tailored to the accumulated phase during free precession is transmitted to bring spins back to the longitudinal-axis, which “fast recovers” the transverse magnetization and preserves it as longitudinal magnetization for the next TR [32, 65]. Second, after the tip-up pulse, it is necessary to play an unbalanced gradient to dephase residual transverse spins. With accurate tailored pulses, STFR imaging may have many of the benefits of bSSFP such as high SNR efficiency, good flow properties, and combined T2/T1 weighting [79], but does not suffer from banding artifacts. STFR therefore has the potential to provide an alternative to bSSFP for some applications, and may obviate the need for special artifact-reduction techniques such as phase-cycled imaging [4] or multiple-TR sequences [69, 12, 62, 49].

---

<sup>1</sup>This chapter is based on the publications [91, 87, 93]

However, STFR is challenging to implement in practice, due to the need for accurate tailored tip-up pulses. This is particularly true in 3D imaging, since the required 3D tailored pulses can be prohibitively long. Here we propose new strategies for improved 3D STFR imaging, based on (i) unspoiled imaging, and (ii) joint design of non-slice-selective tip-down/tip-up 3D tailored RF pulses.

We begin this chapter by deriving an analytic signal equation for the proposed unspoiled STFR sequence, which is then used to compare the properties of unspoiled and spoiled STFR. We then describe the proposed joint RF pulse design algorithm that treats the tip-down and tip-up pulses as one combined RF pulse, which is in turn designed using magnitude least-squares optimization. Next we describe our experimental methods and results (phantom and in-vivo), demonstrating that the proposed unspoiled STFR sequence is less sensitive to tip-up excitation error compared to the spoiled sequence in [65] and hence is a promising candidate for 3D imaging. We conclude with a discussion of limitations and future extensions of this work.

## 3.2 Theory

### 3.2.1 Unspoiled STFR

The proposed unspoiled STFR sequence and associated spin path are illustrated in Fig. 3.1(a). The spin is first tipped down by a small tip angle pulse with flip angle  $\alpha(\mathbf{r})$ . This tip-down pulse can be spatially tailored, i.e., the flip angle (magnitude and phase) may vary with the spatial coordinate  $\mathbf{r}$ . During the signal readout interval  $T_{\text{free}}$ , the spin precesses by an angle  $\theta_f(\mathbf{r}) = \Delta\omega(\mathbf{r})T_{\text{free}}$ , where  $\Delta\omega(\mathbf{r})$  is the off-resonance frequency (B0 inhomogeneity) at position  $\mathbf{r}$ . A “tip-up”, or “fast recovery”, RF pulse with flip angle  $\beta(\mathbf{r})$  tailored to the accumulated phase  $\theta_f(\mathbf{r})$  is then transmitted to bring the magnetization vector back toward the longitudinal axis. The purpose of the tip-up pulse is to preserve as much longitudinal magnetization as possible prior to the next sequence repetition interval (TR) and hence to maximize SNR efficiency, and to introduce T2 weighting. Immediately after the tip-up pulse, an unbalanced gradient  $g$  is played out, designed to dephase the residual transverse magnetization left over after the tip-up pulse. This gradient causes a rotation  $\theta_g$  of each spin isochromat, with  $\theta_g$  varying along the direction of  $g$ . We will see below that this unbalanced gradient is necessary for banding-free imaging. Note that the RF phase offset from TR-to-TR is held constant, i.e., we do not use RF-spoiling (quadratic phase cycling, as was done in [65]) in the sequence proposed here.

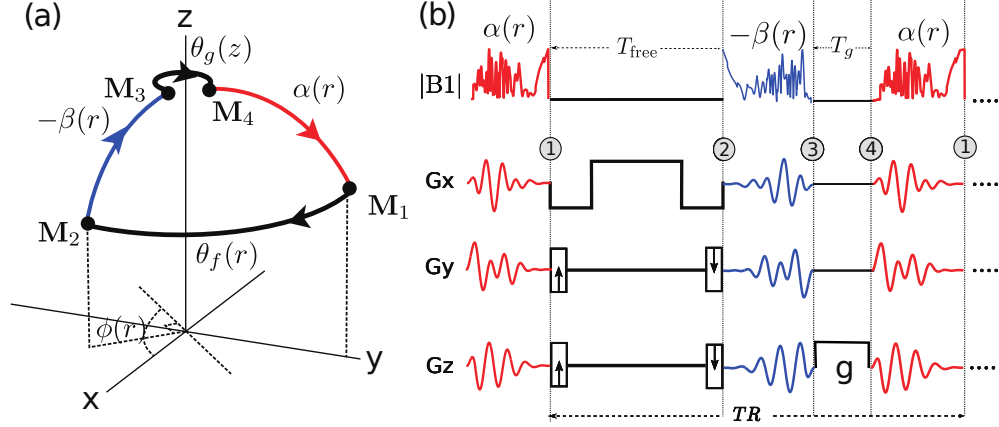


Figure 3.1: Proposed “unspoiled STFR” pulse sequence. (a) Steady-state path for a spin isochromat. The spin is tipped back to the longitudinal axis by a tailored pulse with flip angle  $-\beta(\mathbf{r})$  and phase  $\phi(\mathbf{r})$ .  $\phi(\mathbf{r})$  is designed to be equal to the accumulated free precession angle  $\theta_f(\mathbf{r}) = \Delta\omega(\mathbf{r})T_{\text{free}}$ , where  $T_{\text{free}}$  is the free precession time. (b) Example pulse sequence diagram, using tailored pulses for both tip-down (red) and tip-up (blue) excitations, and 3D Cartesian data readout.

### 3.2.2 Steady-state Magnetization for a Spin Isochromat

To obtain a signal equation for unspoiled STFR, we first develop an expression for the steady state magnetization  $\vec{M}_1(\theta_g)$  for a spin isochromat immediately after the tip-down pulse (see Fig. 3.1(a)), and then integrate the resulting expression over all isochromats within a voxel, i.e., we integrate over  $\theta_g = [0, 2\pi]$ . For clarity, we drop the explicit dependence on spatial position  $\mathbf{r}$  in the following.

Without loss of generality, our derivation assumes the tip-down pulse to be aligned with the x-axis (zero phase). We ignore the RF pulse duration (which can vary depending on, e.g., excitation k-space trajectory), which is a common assumption when deriving analytic models for steady state sequences, especially for RF pulses that are short compared to TR [6]. We obtain the steady-state magnetization by modeling each step of the spin path using the Bloch equation in matrix form. Details of the derivation are provided in the Appendix. We obtain the following expression for the steady-state transverse magnetization of a spin isochromat:

$$M_{1,t} = M_0 \frac{a \cos(\theta_g + \phi) + b \sin(\theta_g + \phi) + c}{d \cos(\theta_g + \phi) + e \sin(\theta_g + \phi) + f} \quad (3.1)$$

where  $M_{1,t}$  is the transverse component of  $\vec{M}_1$ ,  $M_0$  is the equilibrium magnetization

and the factors  $a$  through  $f$  are defined as:

$$\begin{aligned}
a &= -iE_{g2}(E_{f2}(-1 + E_{g1} + (-1 + E_{f1})E_{g1} \cos \beta) \cos(\theta_f - \phi) \sin \alpha + (E_{f1}(-1 + E_{g1}) \\
&\quad + (-1 + E_{f1}) \cos \alpha) \sin \beta + iE_{f2}(-1 + E_{g1} + (-1 + E_{f1})E_{g1} \cos \beta) \sin \alpha \sin(\theta_f - \phi)) \\
b &= E_{g2}(E_{f2}((-1 + E_{f1})E_{g1} + (-1 + E_{g1}) \cos \beta) \cos(\theta_f - \phi) \sin \alpha - (-1 + E_{f1} \\
&\quad + E_{f1}(-1 + E_{g1}) \cos \alpha) \sin \beta + iE_{f2}((-1 + E_{f1})E_{g1} + (-1 + E_{g1}) \cos \beta) \sin \alpha \sin(\theta_f - \phi)) \\
c &= i((-1 + E_{g1} + (-1 + E_{f1})E_{g1} \cos \beta) \sin \alpha + E_{f2}E_{g2}^2(E_{f1}(-1 + E_{g1}) \\
&\quad + (-1 + E_{f1}) \cos \alpha) \sin \beta (\cos(\theta_f - \phi) + i \sin(\theta_f - \phi))) \\
d &= E_{g2}(-E_{f2}(-1 + E_{f1}E_{g1})(1 + \cos \alpha \cos \beta) \cos(\theta_f - \phi) + (E_{f1} - E_{f2}^2E_{g1}) \sin \alpha \sin \beta) \\
e &= E_{f2}(-1 + E_{f1}E_{g1})E_{g2}(\cos \alpha + \cos \beta) \sin(\theta_f - \phi) \\
f &= -1 + E_{f1}E_{f2}^2E_{g1}E_{g2}^2 + (E_{f1}E_{g1} - E_{f2}^2E_{g2}^2) \cos \alpha \cos \beta \\
&\quad + E_{f2}(E_{g1} - E_{f1}E_{g2}^2) \cos(\theta_f - \phi) \sin \alpha \sin \beta
\end{aligned}$$

In the above expression, the T1 and T2 relaxation exponentials during the free precession and gradient dephasing intervals are denoted as  $E_{f1} = e^{-T_{\text{free}}/T_1}$ ,  $E_{f2} = e^{-T_{\text{free}}/T_2}$ ,  $E_{g1} = e^{-T_g/T_1}$  and  $E_{g2} = e^{-T_g/T_2}$ .

Although Eq. (3.1) is only an intermediate expression needed to obtain the total voxel signal, it is instructive to examine its dependence on  $\theta_g$  when the tip-up pulse is perfectly matched to the spin precession angle, i.e.,  $\phi = \theta_f$  and  $\beta = \alpha$ . Then the  $\theta_f$  terms in the coefficients  $a$  through  $f$  are canceled by  $\phi$ , and these coefficients therefore become independent of the local off-resonance.  $M_{1,t}$  then depends on off-resonance only through  $\cos(\phi + \theta_g)$  and  $\sin(\phi + \theta_g)$ . Figure 3.2 plots Eq. (3.1) under these conditions, for T1/T2 = 510/50 ms and  $\alpha = \beta = 16^\circ$ . The most striking feature of Fig. 3.2 is the presence of narrow minima spaced  $2\pi$  apart, which explains why fully balanced ( $g = 0$  and thus  $\theta_g = 0$ ) STFR imaging would be problematic, since narrow bands would be present in regions of the image where  $\phi$  (and  $\theta_f$ ) equals an integer multiple of  $2\pi$ . The minima in Fig. 3.2 are reminiscent of dark signal bands in bSSFP, except for one crucial difference: the neighboring ‘‘bands’’ in Fig. 3.2 are in-phase. We therefore expect the total voxel signal for unbalanced STFR, obtained by integrating over one full cycle (shaded region) in Fig. 3.2, to be high and contain no such banding artifacts.

### 3.2.3 Signal Equation

To obtain the steady-state signal  $M_t$  from a voxel, we integrate  $M_{1,t}(\theta_g)$  over the full distribution of spins:

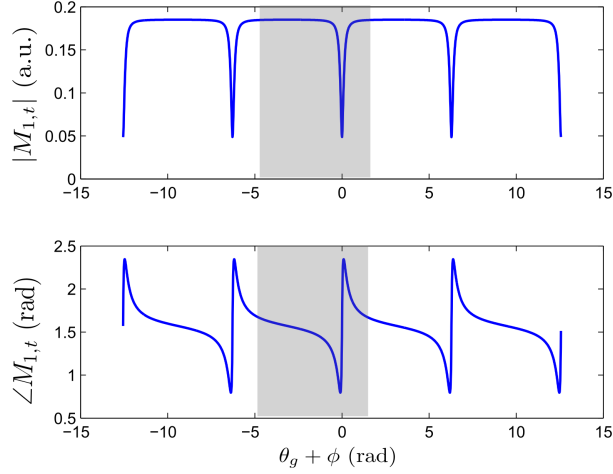


Figure 3.2: Steady-state magnetization (Eq. (3.1)) for a spin isochromat as a function of  $\phi + \theta_g$ , where  $\phi$  is the phase of the tip-up pulse and  $\theta_g$  is the precession induced by the applied unbalanced gradient. Narrow bands are spaced  $2\pi$  apart, and neighboring bands are equal both in magnitude and phase. In the proposed unbalanced STFR sequence, the signal from a voxel can be calculated by integrating over one full cycle (shaded region). The result of this integration is given by Eq. (3.2).

$$\begin{aligned}
M_t(\phi, \theta_f, \alpha, \beta, T_1, T_2, T_{\text{free}}, T_g) &= \frac{1}{2\pi} \int_0^{2\pi} M_{1,t}(\phi + \theta_g) d\theta_g \\
&= M_0 \frac{1}{2\pi} \int_0^{2\pi} \frac{a \cos(\theta_g + \phi) + b \sin(\theta_g + \phi) + c}{d \cos(\theta_g + \phi) + e \sin(\theta_g + \phi) + f} d\theta_g \\
&= M_0 \left( \frac{c}{\sqrt{f^2 - d^2 - e^2}} - \frac{ad + be}{d^2 + e^2} \frac{f - \sqrt{f^2 - d^2 - e^2}}{\sqrt{f^2 - d^2 - e^2}} \right) \quad (3.2)
\end{aligned}$$

Here we denote the dependence on the various tissue and sequence parameters on the left-hand side only. Equation (3.2) describes the signal from a voxel immediately after the tip-down pulse, and must be multiplied by  $e^{-TE/T_2 - jTE\Delta\omega}$  to obtain the signal at the echo time (TE). Equation (3.2) is valuable in several respects: First, it provides a fast way to analyze the sequence properties and optimize the imaging parameters. Second, it shows that the STFR signal is independent of off-resonance if we have a perfectly tailored pulse (off-resonance induced phase  $\theta_f$  is canceled out by  $\phi$  in coefficients  $a$  through  $f$ ). Also, this expression can be used to describe the extended Chimera sequence [7] that is similar to our unspoiled STFR except conventional RF

pulses are used instead of tailored pulses. Finally, we propose to use this Equation 3.2 for simultaneous water-fat separation and band reduction using STFR [115].

Figure 3.3(a) plots Eq. (3.2) over a range of flip angles, for three different tissue types. Here we assume that the tip-up pulse is ideal, i.e.,  $\phi = \theta_f$  and  $\beta = \alpha$ . For comparison, the calculated signals for bSSFP and spoiled STFR are also shown, using analytic results from [58] and [65], respectively. Notice we use twice the flip angle of STFR sequences in the calculation of bSSFP signals. Figure 3.3(b) plots the corresponding white/gray matter contrast. We see that unspoiled STFR produces similar tissue signal and contrast as bSSFP, as desired.

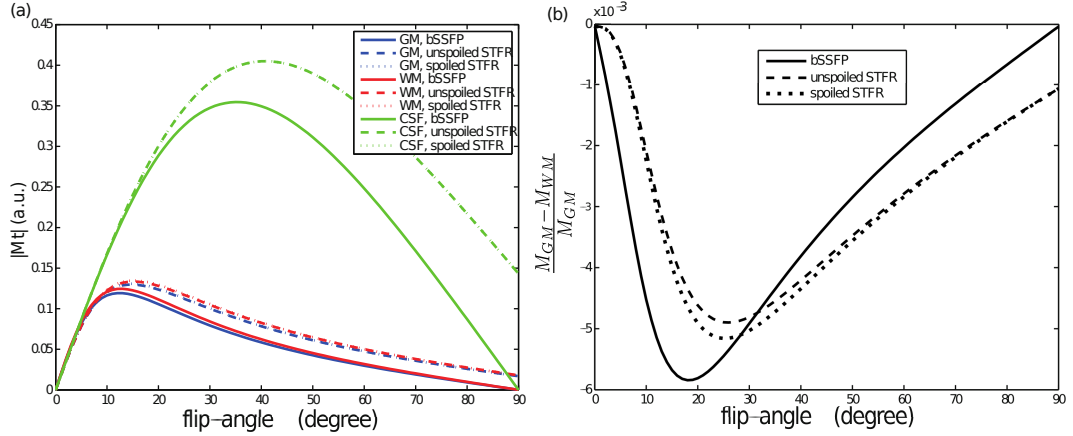


Figure 3.3: Predicted tissue signal for unspoiled STFR (Eq. (2)), spoiled STFR [65] and bSSFP [58]. These calculations assumed  $T1/T2 = 4000/2000\text{ms}$ ,  $1470/71\text{ms}$ ,  $1110/56\text{ms}$  for CSF, gray matter, and white matter, respectively [85]. The bSSFP curves were calculated using a flip angle of  $2\alpha$ , which is expected to produce similar signal contrast as STFR using a flip angle of  $\alpha$ . (a) STFR produces similar signal as bSSFP, as desired. (b) STFR and bSSFP are predicted to have similar gray/white matter contrast.

Figure 3.4(a) plots Eq. (3.2) as a function of the phase mismatch  $\phi - \theta_f$  between the tip-up phase  $\phi$  and the spin phase  $\theta_f$ . Such a phase mismatch is unavoidable in practice, since the tip-up pulse will never be perfectly accurate everywhere within the imaging region of interest (ROI). For comparison, the corresponding plot for spoiled STFR is also shown. In addition, experimentally observed signal curves are plotted, obtained by applying a linear gradient shim and imaging with sinc (i.e., untailored) tip-down and tip-up pulses (see Fig. 3.4(b)). The analytic curve was calculated based on the actual T1, T2 values of the phantom ( $T1/T2 = 510/50\text{ms}$ ), which were measured using inversion recovery and spin echo sequences, respectively. The signal for both unspoiled and spoiled STFR depends on  $\phi - \theta_f$ , but unspoiled STFR decays

less rapidly with increasing phase error. In other words, unspoiled STFR is less sensitive to tip-up phase error compared to spoiled STFR. The difference in the rate of signal drop versus phase mismatch varies with tissue relaxation parameters, as shown in Fig. 3.5. Note that the CSF signal of spoiled STFR drops significantly faster than for other tissues, and faster than the unspoiled STFR CSF signal.

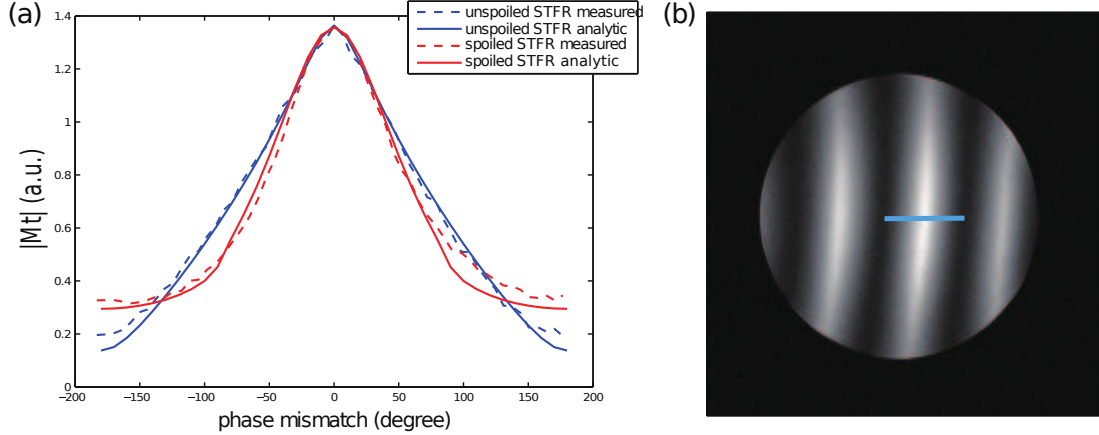


Figure 3.4: (a) Steady-state signal for unspoiled STFR and spoiled STFR as a function of phase mismatch  $\phi - \theta_f$ , using the analytic result from Eq. (3.2) and [65] ( $T_1/T_2 = 510/50$  ms,  $T_{\text{free}}/\text{TR} = 9/12$  ms,  $\alpha = \beta = 16^\circ$ ) and phantom observations. Note that the rate of signal drop due to phase mismatch is smaller for unspoiled STFR. We obtained the measured curves by applying a linear gradient shim in the x direction and imaging a gel phantom (shown in (b)) with *non-tailored* (sinc) pulses. We stress that the image in (b) was obtained for the sole purpose of obtaining the curve in (a), and is *not* representative of a typical STFR image acquisition. In particular, the goal in STFR is generally to design a tailored tip-up pulse that minimizes the phase mismatch and hence maximizes the signal within a target ROI.

### 3.2.4 RF Pulse Design

The key to successful STFR imaging is to design accurate tailored tip-up pulses that bring the magnetization close to the longitudinal axis. Here we consider 3D imaging using unspoiled STFR, and we restrict our designs to non-slice-selective 3D tailored pulses. (Although we could in principle use slice- or slab-selective 3D pulses, such pulses would most likely be prohibitively long.) We propose two different approaches to RF pulse design in STFR: “Separate” and “Joint”.

In our first approach, we design the tip-down and tip-up pulses independently, as follows: First, we tailor the tip-down pulse  $\alpha(\mathbf{r})$  to a uniform magnitude excitation pattern with phase  $-\theta_f(\mathbf{r})/2$ , i.e., half the expected free precession angle. We then

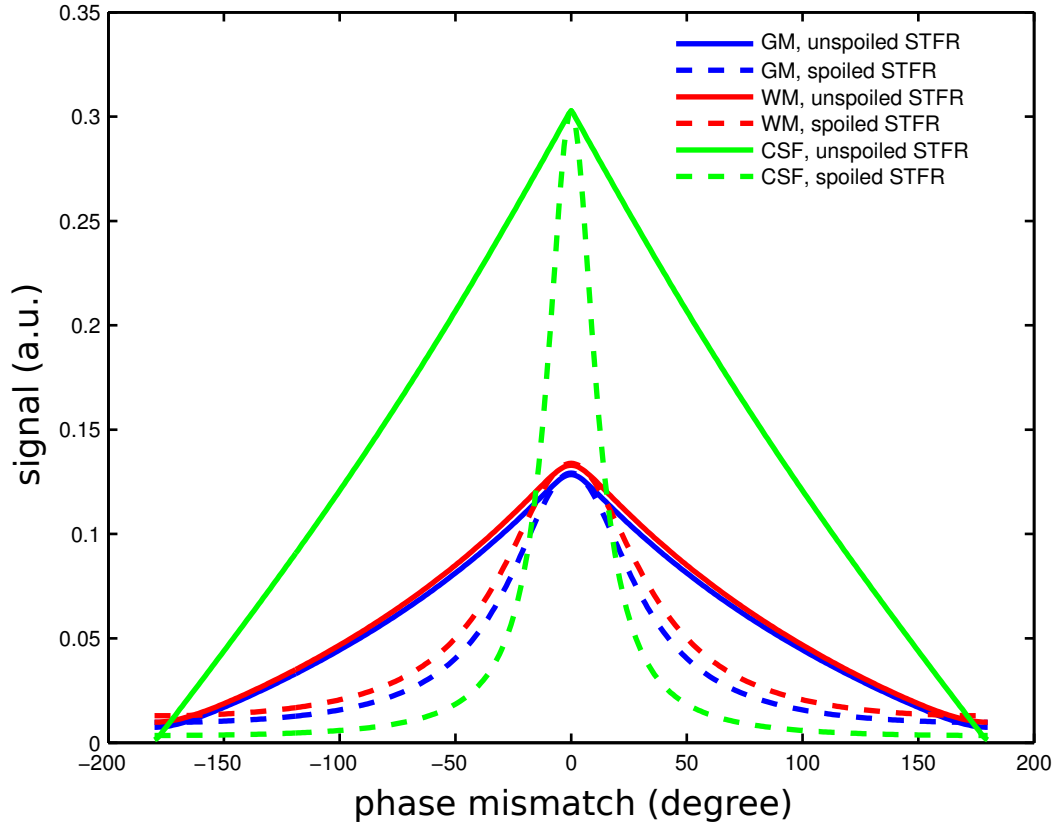


Figure 3.5: Steady-state signal for unspoiled STFR and spoiled STFR as a function of phase mismatch  $\phi - \theta_f$  for different tissues: gray matter (GM), white matter (WM), and cerebrospinal fluid (CSF). These calculations assumed  $T_1/T_2 = 4000/2000$  ms,  $1470/71$  ms,  $1110/56$ ms for CSF, GM, and WM, respectively [85], and  $T_{\text{free}}/TR = 7/10$  ms,  $\alpha = \beta = 20^\circ$ . The spoiled STFR sequence is more sensitive to phase mismatch compared to unspoiled STFR for all three tissue types, and especially for CSF.

design an “intermediate” tip-down pulse  $\beta_{\text{int}}(\mathbf{r})$  tailored to the expected spin phase at the end of  $T_{\text{free}}$ , i.e.,  $\angle\alpha(\mathbf{r}) + \theta_f(\mathbf{r})$ . Finally, we obtain the tip-up pulse  $\beta(\mathbf{r})$  by “rewinding” the intermediate pulse  $\beta_{\text{int}}(\mathbf{r})$  as in [65], i.e., by time-reversing and negating  $\beta_{\text{int}}(\mathbf{r})$ . The advantage of this approach is that it is relatively easy to implement, e.g., using existing methods for small-tip RF pulse design.

The second approach to RF pulse design in STFR is based on the observation that the phase of tip-down pulse  $\angle\alpha(\mathbf{r})$  does not in general need to be constrained to a particular pattern, as long as it varies reasonably smoothly across the ROI. In fact, the only requirement that should be imposed on the tip-down pulse is that the magnitude  $|\alpha(\mathbf{r})|$  should be as uniform as possible to avoid image shading. Using the small-tip (Fourier) approximation in which the transverse component of the excitation pattern is expressed as a linear transformation of the time-varying RF waveform [72], this requirement can be stated as

$$\sin \boldsymbol{\alpha} = |A_1 \mathbf{b}_1| \quad (3.3)$$

where  $\mathbf{b}_1$  is a discretization of the time-varying tip-down RF waveform  $b_1(t)$ , and  $\boldsymbol{\alpha}$  is the desired (uniform) flip angle.  $A_1$  is a system matrix with elements  $a_{ij} = \gamma M_0 e^{-ik(t_j)r_i - i\Delta\omega(r_i)(t_j - T)}$ , where  $k(t)$  is the excitation k-space trajectory determined by the gradient waveforms for tip-down part and  $T$  is the duration of tip-down pulse. Similarly, we require that the magnitude of the magnetization after the tip-up pulse be as small as possible:

$$|A_2 \mathbf{b}_1 + A_3 \mathbf{b}_2| = 0 \quad (3.4)$$

where  $A_2$  and  $A_3$  are blocks of  $\tilde{A} = [A_2 \ A_3]$  with elements  $\tilde{a}_{ij} = \gamma M_0 e^{-i\tilde{k}(t_j)r_i - i\Delta\omega(r_i)(t_j - \tilde{T})}$ , where  $\tilde{T}$  and  $\tilde{k}(t)$  are the duration and excitation k-space trajectory determined by the gradient waveforms for the whole combined pulse, i.e., including tip-down excitation, free precession, and tip-up recovery.

We propose to solve Eqs. (3.3)-(3.4) jointly using the following magnitude least-squares formulation:

$$\begin{bmatrix} \hat{\mathbf{b}}_1 \\ \hat{\mathbf{b}}_2 \end{bmatrix} = \underset{\mathbf{b}_1, \mathbf{b}_2}{\operatorname{argmin}} \left\{ \left\| \begin{bmatrix} \sin(\boldsymbol{\alpha}) \\ \mathbf{0} \end{bmatrix} - \begin{bmatrix} A_1 & 0 \\ A_2 & A_3 \end{bmatrix} \begin{bmatrix} \mathbf{b}_1 \\ \mathbf{b}_2 \end{bmatrix} \right\|_2^2 + \mu \|\mathbf{b}_1\|_2^2 + \mu \|\mathbf{b}_2\|_2^2 \right\}, \quad (3.5)$$

where  $\mu$  is a Tikhonov regularization parameter that constrains the total RF energy [103]. Although the joint formulation in Eq. (3.5) is more computationally intensive than the Separate design, it may allow for improved tip-up accuracy for a given RF pulse duration since we are removing the constraints on spin phase.

### 3.3 Methods

Table 3.1: Summary of phantom and human imaging experiments.

Object	Sequence	RF pulse	Flip angle	TR
Phantom	spoiled gradient echo (SPGR, FLASH)	sinc	20	10ms
Phantom	SSFP-FID (GRASS, FISP)	sinc	20	10ms
Phantom	bSSFP (FIESTA, TrueFISP)	sinc	40	7.6ms
Phantom	spoiled STFR	tailored (Separate)	20	10ms
Phantom	unspoiled STFR	tailored (Separate)	20	10ms
Phantom	unspoiled STFR	tailored (Joint)	20	10ms
Brain	bSSFP (FIESTA, TrueFISP)	sinc	40	7.6ms
Brain	spoiled STFR	tailored (Separate)	20	10ms
Brain	unspoiled STFR	tailored (Separate)	20	10ms
Brain	unspoiled STFR	tailored (Joint)	20	10ms

Table 3.2: Sequence timing.

Sequence	Tip-down	Readout	Tip-up	Gradient crusher
STFR	1.7ms	4.9ms	1.7ms	1.2ms
bSSFP	1.2ms	4.9ms	n/a	n/a

We performed imaging experiments on a GE 3T scanner equipped with a quadrature transmit/receive head coil. Table 3.1 lists the various image acquisitions. The phantom was a GE resolution phantom, and the human subject was a healthy volunteer.

Table 3.2 lists the sequence timing for STFR and bSSFP. All image acquisitions used 256x256x65 matrix size, 24x24x24 cm field of view (FOV), and 62.5 KHz receive bandwidth. We used a FOV along  $z$  that was large enough to eliminate aliasing from untargeted slices, which in practice could be avoided by, e.g., aligning the frequency encoding direction with the  $z$  direction [55]. The bSSFP acquisitions used twice the flip angle as the STFR acquisitions, since our equation and simulations predict that bSSFP will give the same (on-resonance) signal level with twice the flip angle of the STFR sequence.

For the STFR acquisitions, we tailored the RF pulses to a 3D ROI consisting of a 3 cm axial slab. For this purpose we obtained a B0 map of the ROI using SPGR with echo times 3 ms and 5 ms. For the tailored pulses (both tip-down and tip-up), we used the spiral nonselective excitation k-space trajectory (SPINS) proposed in [55]. For the Separate design, we calculated the B1 waveforms using the small-tip iterative RF pulse design method in [103]. For the Joint design, we obtained the B1 waveforms by performing the magnitude least-square minimization in Eq. (3.5) using the method in [82]. Both designs were implemented with the MATLAB image reconstruction toolbox (IRT) from University of Michigan (<http://www.eecs.umich.edu/~fessler>). An example of the resulting B1 waveforms and SPINS gradients are shown in Fig. 3.1(b).

## 3.4 Results

### 3.4.1 Phantom Observations

Figure 3.6 shows steady-state images of one of the target slices in the resolution phantom acquired with several different sequences, displayed using the same gray scale. For each image, the mean signal and standard deviation within the object are indicated. We observe a characteristic banding artifact in the bSSFP image, which is largely removed in the Joint unspoiled STFR acquisition. However, some non-uniformity remains in the Joint unspoiled STFR image, due to the limited ability to correct for B0 inhomogeneity over the ROI with the short (1.7 ms) RF pulses used here. Furthermore, STFR and (on-resonance) bSSFP have similar signal levels, about twice as high as SSFP-FID and significantly higher than SPGR, in agreement with theory. We also observe that unspoiled STFR produces more uniform images than spoiled STFR, as predicted. Finally, we note that Joint design produces a modest improvement in mean signal level (1.41) compared to Separate design (1.36). Based on this comparison experiment, we think the Joint unspoiled version is more suitable than other STFR sequences for 3D imaging.

### 3.4.2 In-vivo Observations

Figure 3.7(a) shows steady-state images from the same slice obtained with bSSFP (180° RF phase cycling) and STFR. Similar to Fig. 3.6, we observe a banding artifact in the bSSFP image (arrow) that is not present in the unspoiled STFR image. Apart from the banding region, unspoiled STFR and bSSFP have similar signal levels and

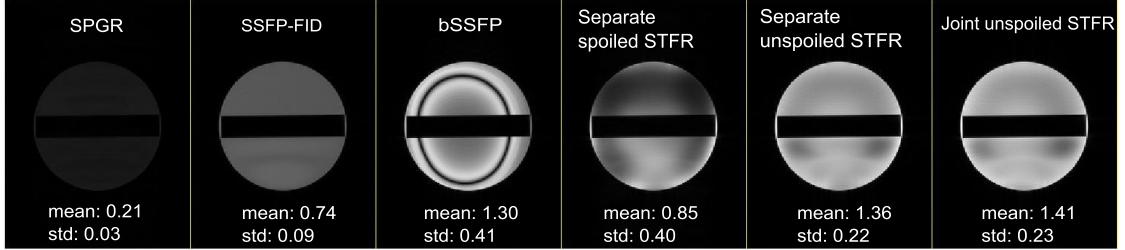


Figure 3.6: Steady-state imaging, phantom results. Images are shown on the same gray scale. For each image, the mean signal and standard deviation within the object are indicated. Unspoiled STFR with the proposed “Joint” RF pulse design (right) produces signal levels that are comparable to on-resonance bSSFP, and has improved uniformity compared to bSSFP and spoiled STFR. Unspoiled STFR with the simpler “Separate” RF pulse design approach (second from right) shows improved signal and uniformity compared to spoiled STFR, but slightly lower overall signal compared to the Joint design. Conventional SPGR and SSFP-FID images are included for reference.

exhibit similar tissue contrast (e.g., bright cerebrospinal fluid (CSF)), as desired. The unspoiled STFR images still have signal loss in some regions due to phase mismatch (see Fig. 3.7(b)), but it is much more uniform than spoiled STFR, as predicted. We observe significant CSF signal loss in the spoiled STFR image in some regions (see, e.g., oval), which can be explained by comparing the phase mismatch in that region and the phase mismatch sensitivity plot (Fig. 3.5). The Joint design slightly improves image quality compared to the Separate design, i.e., Joint unspoiled STFR produces a more uniform image with better contrast, and we think this improvement is due to the decrease of phase mismatch using the Joint design. Finally, the high through-plane vessel signal in bSSFP is suppressed in the STFR images (see, e.g., box), which is generally desirable.

Figure 3.8(a) compares Joint unspoiled STFR and bSSFP in 5 adjacent slices spanning a 4 cm FOV along  $z$  (S/I), and highlights the ability of the proposed sequence to image a 3D ROI. The top two rows show bSSFP images obtained with  $0^\circ$  and  $180^\circ$  RF phase cycling, while the bottom row shows the Joint unspoiled STFR images. Both bSSFP acquisitions suffer from banding artifacts. The Joint unspoiled STFR sequence achieves similar signal level and tissue contrast as bSSFP over most of the FOV, although we observe some non-uniformity (image shading) due to large phase mismatch in some region, (see Fig. 3.8(b)). Note that the observation FOV (4 cm) along  $z$  is larger than the target FOV (3 cm) of the tailored pulse; however we can still get reasonably good images in the whole observation FOV because the excitation pattern and free precession accumulated phase pattern are all relatively smooth here.

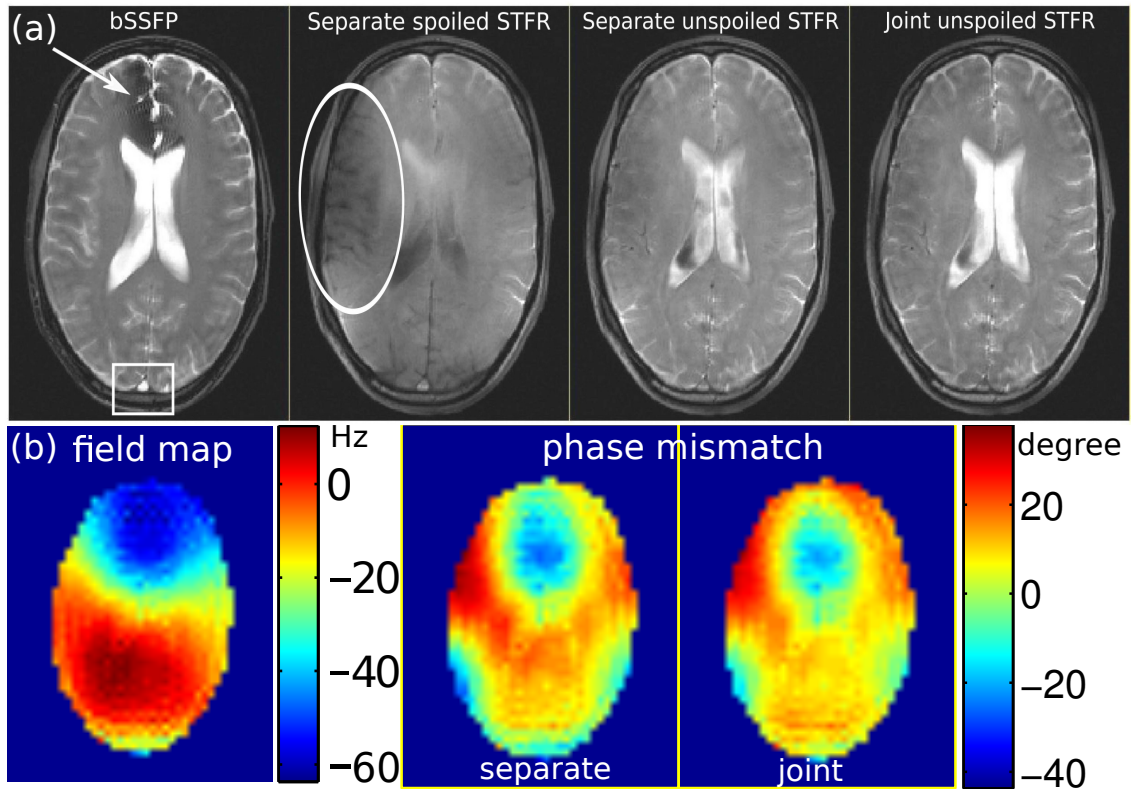


Figure 3.7: (a) Comparison of bSSFP (left) with three different STFR acquisitions, in the same slice. (b) field map and phase mismatch maps using separate and joint design. Banding artifacts in the anterior part (arrow) of the bSSFP image are largely absent in the unspoiled STFR images. Spoiled STFR is less uniform than unspoiled STFR as predicted, and the signal drops more in the region with high phase mismatch. Note that the CSF in the oval region in the spoiled STFR image drops significantly more than the nearby tissue signal and the unspoiled STFR CSF signal, which agrees with the phase mismatch map and sensitivity to phase mismatch plot in Fig. 3.5. The Joint design has slightly smaller phase mismatch, which leads to improved signal uniformity and tissue contrast compared to the Separate design. Also note that the high through-plane vessel signal in the bSSFP image is suppressed in the STFR images (see, e.g., box).

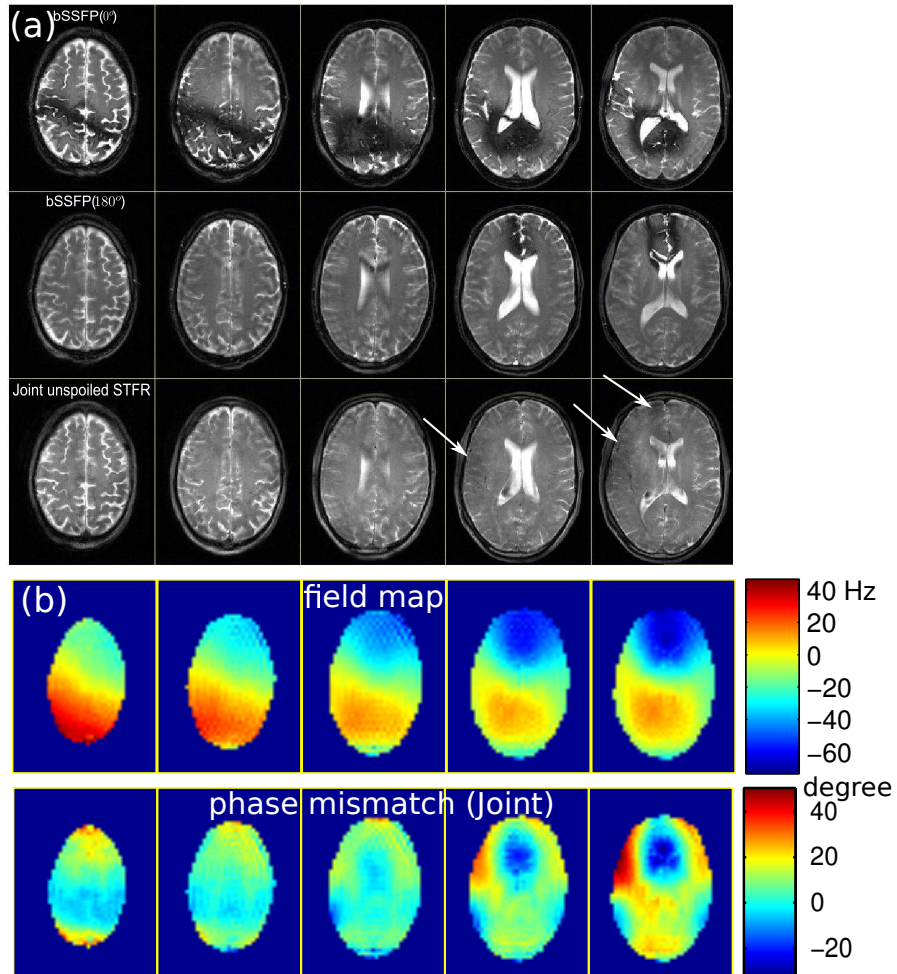


Figure 3.8: (a) Proof-of-principle demonstration of 3D unspoiled STFR imaging, using Joint 3D tailored RF pulses. Images are shown for Joint unspoiled STFR, and bSSFP with different phase cycling schemes, in 5 adjacent axial slices spanning 4 cm: (Top)  $0^\circ$  phase cycled bSSFP; (Middle)  $180^\circ$  phase cycled bSSFP; (Bottom) Joint unspoiled STFR. Both bSSFP acquisitions suffer from banding artifacts, which are reduced with the 3D Joint unspoiled STFR sequence. (b) field map and phase mismatch maps. The STFR signal drops more in the region with high phase mismatch (See, e.g., arrows in (a)).

### 3.5 Discussion

Our theory predicts that STFR has similar SNR as bSSFP (see Fig. 3.3), which agrees with our measured results (44.2/45.3 dB and 31.6/32.4 dB for bSSFP/STFR in phantom and gray matter ROIs, respectively). Therefore, the SNR efficiency (defined as  $\text{SNR}/\sqrt{\text{total scan time}}$ ) of STFR will be lower than on-resonance bSSFP, since its TR is necessarily longer than the corresponding bSSFP sequence. Compared to multiple phase-cycled bSSFP acquisitions, whether STFR is more SNR efficient or not depends on the actual timing of the specific sequences and the method used to combine the phase-cycled images. In our experiments, we use TR = 7.6 ms and 10 ms for bSSFP and STFR respectively. The TR of bSSFP is not optimized in our experiment and can be as low as 6.8 ms given our scanner control code and the same readout time (4.9 ms) as STFR. Assuming TR = 6.8 ms for bSSFP and TR = 10 ms for STFR, the total scan time of STFR is 1/1.36 of two phase-cycled bSSFP and 1/2.04 of three phase-cycled bSSFP. On the other hand, the SNR increases by combining the phase-cycled bSSFP images, and the amount of increase depends on the tissue parameters, noise level and the combination method [4]. For simplicity, if we assume maximum intensity combination, STFR as implemented in our experiments would have similar SNR efficiency as two phase-cycled bSSFP, and better SNR efficiency than three phase-cycled bSSFP. It is therefore possible that in applications where image SNR is critical, bSSFP with two phase-cycles may be preferred over STFR. We note, however, that multiple acquisitions may not be preferred in some applications. For example, in bSSFP fMRI, repeating runs of a paradigm produces confounding effects from cognitive habituation to stimuli and is not ideal [47, 57]. Alternating bSSFP that interleaves two phase-cycled bSSFP imaging can potentially solve this problem [70], but it needs catalyzation pulses every time the phase-cycling is changed, which reduces its SNR efficiency.

Here we have shown that STFR and bSSFP image contrast is similar with respect to T1 and T2 sensitivity, however we have performed preliminary work that indicates that these sequences have different sensitivity to diffusion and intra-voxel B0 homogeneity [64]. In bSSFP, because of the relative flat magnitude and phase frequency response curve in the passband, all the spins within a voxel typically have similar magnitude and phase, therefore, there is no  $T_2^*$  contrast. In STFR, because of the low spatial resolution of the tailored pulse, the spins within one voxel may experience different phase mismatch due to intra-voxel B0 field variation leading to a  $T_2^*$ -like contrast. This property of STFR can be used to detect blood-oxygen-level-dependent

(BOLD) signal in functional imaging, which is reported in [64], and which will be discussed in the next chapter.

We have proposed a joint RF pulse design method for STFR, which produced a modest improvement over the Separate design. We expect that our Joint algorithm can be improved in at least two ways. First, since the Joint approach formulates a nonconvex magnitude least squares problem, it is possible that our solver gets “stuck” in a local minimum. Specifically, at each iteration our algorithm solves a least squares problem  $\underset{\mathbf{b}}{\operatorname{argmin}}\|\mathbf{A}\mathbf{b} - \mathbf{d}\|$  whereby the phase of the target excitation pattern  $\mathbf{d}$  is updated. We attempted several different initializations to the phase pattern of  $\mathbf{d}$  including all zero and random phase, and achieved similar results, suggesting we may not get “stuck” in a bad local minimum in our experiments. However, it is possible that alternative solvers may improve the RF design. Second, in our Joint design formulation, we used the small tip angle approximation but we enforced the spins to be tipped down in the middle of the combined pulse. Although we are working in the small tip regime ( $\leq 20^\circ$ ), this forced tip-down in the middle may still make the small tip angle approximation method less accurate. It is possible that our Joint design can be improved by borrowing ideas from large-tip-angle pulse design, e.g., the additive angle method [26] or designs based on perturbation analysis of the Bloch equation [117].

In addition to improving the RF pulse design algorithm, other complementary methods can be used to improve STFR imaging performance. One straightforward approach is to reduce data acquisition time and hence  $T_{\text{free}}$ , which reduces the spatial inhomogeneity of the target phase pattern  $\theta_f(\mathbf{r})$ . This can be done by, e.g., employing fast non-Cartesian readout trajectories. This approach may reduce the SNR but the SNR efficiency may not decrease much because the tailored pulse length may be shorter. In addition, high-order gradient shim systems can be employed to reduce B0 inhomogeneity, which also makes  $\theta_f(\mathbf{r})$  vary more smoothly across the ROI. This approach would benefit bSSFP as well, but shimming itself may not be sufficient to remove all the banding in bSSFP [48]. Alternatively, parallel RF transmission should allow for improved RF pulse accuracy for a given pulse duration. Parallel excitation has been an active research area in recent years, including by our group [34], and commercial support for such systems is emerging.

A drawback of the proposed non-slice-selective imaging approach is that signal from outside the ROI may alias into the FOV. Although slab selective 3D tailored pulses could in principle be used, such pulses may be prohibitively long [104]. One potential solution to this problem is to use Cartesian readout with frequency encoding

in the S/I direction, i.e., using the data acquisition filter to remove signal from outside the FOV, but this approach may require longer scan time since the A/P and R/L directions must be fully phase encoded, and these directions typically have larger matrix size. Another potential solution is to use surface coils near the region of interest such that signal contribution from outside the ROI is minimized. Also, with parallel excitation, it is possible that the fast-kz(spoke) slice selective 3D tailored pulse [108] can be short enough to be used in STFR.

### 3.6 Conclusions

We have developed a new steady-state sequence, unspoiled STFR, and demonstrated using analytic modeling and experiments that this sequence produces bSSFP-like signal and tissue contrast but with reduced banding artifacts. Our analysis shows that the proposed sequence is less sensitive to RF pulse inaccuracies than its spoiled counterpart. We have also proposed a novel joint RF pulse design approach that formulates the RF design problem in STFR as a magnitude least-squares minimization problem, modestly improving image quality. With this approach, we have demonstrated that brain imaging over a 3-4 cm thick 3D ROI is possible using a standard quadrature transmit/receive head coil and short tailored 3D RF pulses of 1.7 ms duration. We expect that future improvements in high-order shimming or parallel transmit systems will allow expanded 3D ROIs to be imaged with the proposed approach.

## CHAPTER IV

# Steady-state Functional MRI Using Spoiled Small-tip Fast Recovery Imaging

### 4.1 Introduction

<sup>1</sup>The majority of functional magnetic resonance imaging (fMRI) studies in the brain use T2\*-weighted gradient-echo sequences with single-shot readout (blood oxygen level dependent (BOLD) fMRI) [68]. The long echo time (TE) required to build up sufficient functional contrast makes BOLD fMRI susceptible to background B0 inhomogeneity unrelated to oxygenation, leading to signal dropout near air/tissue boundaries and geometric distortions or blurring. Steady-state fMRI based on passband balanced steady-state free precession (passband bSSFP) uses segmented readouts and can produce high resolution functional maps with reduced geometric distortions [8, 118, 59, 47, 58, 61, 45], but is susceptible to dark “banding” artifacts in regions of high B0 inhomogeneity and generally has lower functional signal than BOLD [118].

Small-tip fast recovery (STFR) imaging is a recently-proposed steady-state imaging sequence [66, 93]. STFR relies on a tailored “tip-up”, or “fast recovery”, RF pulse to align the spins with the longitudinal axis after each data readout segment, such that the magnetization is preserved for the next TR and a T2 dependence is introduced. The design of the tip-up pulse is based on the acquisition of a separate B0 map. STFR can provide bSSFP-like image contrast, but with reduced signal variations due to B0 inhomogeneity. However, it is not yet known whether STFR is suitable for fMRI, and whether the functional contrast mechanism is the same as in passband bSSFP.

---

<sup>1</sup>This chapter is based on the publications [97, 90]

Here we investigate the possibility of using STFR for steady-state fMRI, using Monte Carlo Bloch simulations and proof-of-concept *in vivo* functional imaging experiments. We first review the STFR imaging concept, and discuss potential functional contrast mechanisms. We then describe our steady-state Monte Carlo Bloch simulations, which account for spin diffusion in a realistic microvascular environment. We continue by describing our STFR functional experiments, including the design of the tailored tip-up RF pulse. Our results indicate that STFR can produce reliable functional contrast, and that diffusion plays only a minor role.

## 4.2 Theory

### 4.2.1 Small-tip Fast Recovery Imaging

The STFR imaging principle is illustrated in Fig. 4.1. As in most conventional imaging sequences, a tip-down pulse  $\alpha$  is first played out, and the signal is acquired during a free precession interval of duration  $T_{\text{free}}$ . During this interval, the spin precesses in the transverse plane by an angle

$$\theta(\vec{r}) = \omega(\vec{r}) T_{\text{free}}, \quad (4.1)$$

where  $\omega(\vec{r})$  is the spatially varying local B0 off-resonance frequency. After data read-out, spins within the desired imaging region are tipped back toward the longitudinal axis ( $m_z$ ) by a spatially-tailored tip-up pulse  $\beta(\vec{r})$  that depends on  $\theta(\vec{r})$ . The residual transverse magnetization remaining after the tip-up pulse can be spoiled using RF-spoiling, i.e., by inserting an unbalanced gradient area and cycling the RF phase quadratically [120]. RF-spoiling has the additional benefit that it suppresses signal from outside the field-of-view (FOV) in the slice-select direction, and hence allows a thin slab (or slice) to be imaged by using a slab-selective tip-down pulse and a non-slice-selective tip-up pulse [65]. The transverse magnetization for an isochromat is [65]

$$M_T = M_0 \sin \alpha \frac{e^{-T_g/T_1}(1 - e^{-T_{\text{free}}/T_1}) \cos \beta + (1 - e^{-T_g/T_1})}{1 - e^{-T_g/T_1} e^{-T_{\text{free}}/T_2} \sin \alpha \sin \beta \cos(\theta_f - \phi) - e^{-T_g/T_1} e^{-T_{\text{free}}/T_1} \cos \alpha \cos \beta} \quad (4.2)$$

where  $T_{\text{free}}$  is the free precession time,  $T_g$  is the duration of the gradient crusher,  $\phi$  is the phase of the tip-up pulse,  $\alpha$  and  $\beta$  are the flip angle of tip-down pulse and tip-up pulse, respectively. Based on this equation, when there is no phase mismatch ( $\phi = \theta_f$ ), the transverse magnetization would be close to passband bSSFP (see plot in [65]). Note that even though STFR is a spoiled sequence, it still has T2 dependence

since the transverse magnetization recovered by the tip-up pulse is a function of T2, and this magnetization will contribute to the final steady-state signal.

#### 4.2.2 Possible Functional Contrast Mechanisms in STFR: Diffusion and “Static Dephasing”

Increased brain activation is generally assumed to be accompanied by reduced B0 inhomogeneity within a voxel, due to increased oxy-hemoglobin concentration resulting from overcompensatory arterial blood flow increases in response to increased oxygen demand [68]. In conventional BOLD fMRI, these intra-voxel inhomogeneity changes are detected as changes in T2\* using single-shot imaging with long TE. In passband bSSFP, on the other hand, functional contrast is believed to be driven at least in part by the interaction between spin diffusion and intra-voxel B0 inhomogeneity: during activation, diffusion-related deviations in spin free precession angle between RF excitations are reduced, leading to a signal change that can be modeled as a change in “apparent” T2 [58, 45]. The functional contrast mechanism is therefore (at least in part) decoupled from the choice of TE, which enables segmented readouts and hence reduced geometric distortions. Given the similarity between STFR and passband bSSFP [65], one might expect STFR to exhibit a similar diffusion-driven functional contrast.

In addition to spin diffusion, STFR has a second possible source of functional contrast, which arises from the dependence of the steady-state transverse magnetization on the mismatch between the spin phase after data readout ( $\theta_f$ ) and the phase ( $\phi$ ) of the tailored tip-up pulse (Fig. 4.1(a)). Fig. 4.1(b) plots the transverse magnetization for a spin isochromat as a function of the phase mismatch  $\theta_f - \phi$ , using Eq. [4.2]. The tip-up pulse is tailored to the mean phase of spins within a voxel, therefore, different spins in a voxel experience different phase mismatch and the total voxel signal must be obtained by weighted integration of the isochromat signal profile over the B0 distribution within a voxel (illustrated in Fig. 4.1(b)):

$$S(\vec{r}) = \int M_T(\theta_f - \phi(\vec{r})) f_{\vec{r}}(\theta_f) d\theta_f$$

where  $\vec{r}$  is the voxel position,  $f_{\vec{r}}(\theta_f)$  is the intra-voxel phase distribution for a voxel at  $\vec{r}$ , which is often modeled as a Lorentzian distribution. It is therefore possible that an activation-induced change in the distribution of intra-voxel phase can lead to a measurable signal change in spoiled STFR imaging. We will refer to this signal dependence as “static dephasing”.

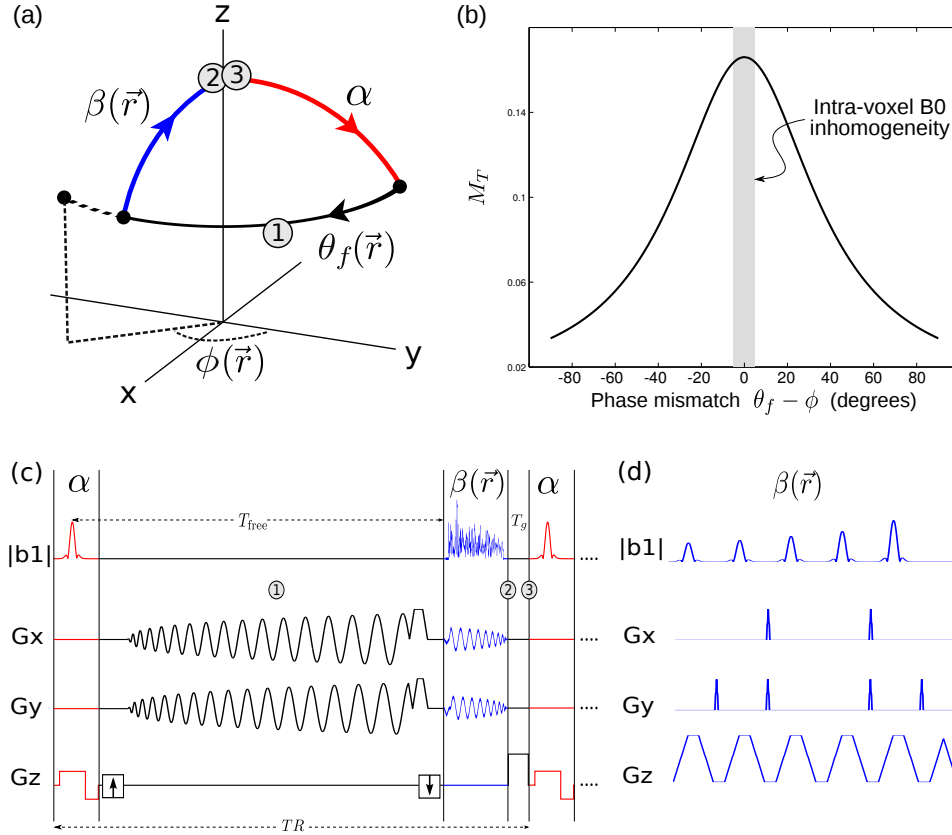


Figure 4.1: Proposed STFR functional imaging sequence. (a) Steady-state spin path for a single spin isochromat. The tip-up pulse (blue) is tailored to the local free precession angle. In general, there will be a mismatch  $\theta_f - \phi$  between the spin phase at the end of the free precession interval ( $\theta_f$ ), and the phase (direction) of the tip-up pulse ( $\phi$ ). In STFR imaging, the goal is to design a tip-up pulse that minimizes  $\theta_f - \phi$  within the ROI. (b) Steady-state STFR transverse magnetization for a single spin isochromat as a function of phase mismatch  $\theta_f - \phi$ , calculated from Eq. [4.2]. The observed voxel-averaged signal is obtained by weighted integrating the signal profile over the B0 distribution within a voxel (Eq. [4.3], illustrated with shaded gray column). (c) Pulse sequence diagram for the STFR sequence used in the *in vivo* functional experiments (spiral tip-up pulse). (d) fast-kz tailored tip-up pulse (only 5 subpulses are shown).

It is not immediately clear (i) which of these mechanisms dominate, and (ii) whether they are sufficient to produce detectable functional signal. In this chapter we use numerical Bloch simulations and *in vivo* functional experiments to address these questions.

## 4.3 Methods

### 4.3.1 Monte Carlo Bloch Simulations

To investigate the functional contrast behavior of STFR, we performed time-resolved Bloch simulations similar to those in [58, 45]. We constructed a  $1\text{mm}^3$  numerical 3D voxel model containing cylindrical vessels with random orientations. The simulated vessel diameters were in the range  $5.6\text{--}60\ \mu\text{m}$  [84]. We assumed a constant blood fraction  $f_b = 7.3\%$  [58], and venous oxygenation of 67% and 81% during rest and activation, respectively [27]. We calculated the intra- and extravascular field according to Eqs. [4-6] in [58]. To keep memory requirements manageable, only a 2D plane through the 3D numerical voxel was simulated, as in [58]. Figure 4.2(a) shows the resulting 2D intra-voxel  $B_0$  field map.

We simulated the steady-state signals for STFR, both with and without diffusion. In each simulation, 2500 spins were randomly placed into the 2D numerical voxel. Spins were assigned a 2D random walk using diffusion coefficient of  $0.001\ \text{mm}^2/\text{s}$  with  $50\ \mu\text{s}$  simulation step size [58]. We assumed circular voxel edge conditions (i.e., spins leaving the voxel at one edge were allowed to enter the voxel through the opposite edge). We used  $T_1/T_2=1470/71\ \text{ms}$  in simulation [85]. In the non-diffusion case, we fixed all spin locations and repeated the simulations. We simulated a range of TRs (8–24 ms) and flip angles ( $16^\circ\text{--}90^\circ$  for bSSFP,  $8^\circ\text{--}45^\circ$  for STFR). We assumed non-selective 1.5 ms hard pulses,  $\text{TE}=1.8\ \text{ms}$  for both bSSFP and STFR, and 1.2 ms gradient crusher for STFR. We ran the simulations for a duration of  $5.5\times T_1$  prior to “recording” the signal to establish a steady state.

For reference, we also simulated the bSSFP sequence with the same settings with double flip angle, and spoiled gradient echo (GRE) BOLD with  $16^\circ$  flip angle, 44 ms TR, and 32 ms TE, which is matched to our experiments. For computational efficiency, we assumed ideal RF spoiling for STFR and BOLD in the simulation, in other words, the transverse magnetization is set to 0 prior to each tip-down pulse. We implemented the Bloch simulator in Matlab using C-mex files, available online (<http://www.eecs.umich.edu/~sunhao>).

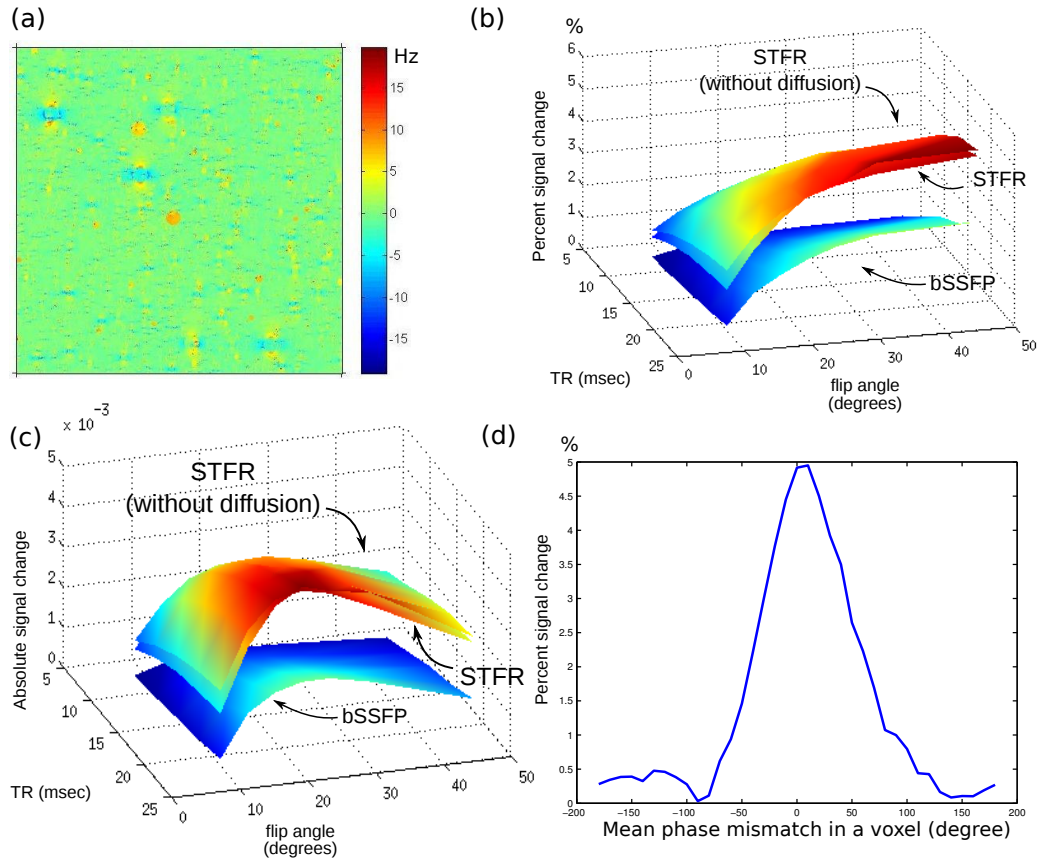


Figure 4.2: Monte Carlo Bloch simulation results. (a) Calculated microscopic B0 inhomogeneity (Hz) in the numerical voxel used in our Monte Carlo Bloch simulations. A 2D cut through the 1x1x1 mm<sup>3</sup> voxel is shown. (b,c) Percent (b) and absolute (c) functional signal change for STFR and passband bSSFP over a range of TRs and flip angles. Note that bSSFP used twice the flip angle indicated. These simulations predict that STFR can produce a functional signal. The percent signal change increases with increasing flip angle across the whole range while the absolute signal change increases up to 20°. “Turning off” spin diffusion has a relatively small impact on the functional signal, which indicates that diffusion is unlikely to be the main source of functional contrast in STFR. (d) The percent signal change when the mean phase mismatch in a voxel is not 0 (obtained by weighted integrating over a narrow spectrum off the center in Fig. 4.1-b). The functional signal change is maximized when mean phase mismatch for a voxel is 0.

### 4.3.2 Functional Imaging

Table 4.1: Summary of fMRI experiments.

Subject	A, Session 1	A, Session 2	B to E
Region	Motor	Motor	Motor
Sequence(s)	STFR/BOLD/bSSFP	STFR	STFR/BOLD
No. Repetitions	5	1	3 to 5
Tip-up pulse	fast-kz (7 ms)	spiral (4.5 ms)	fast-kz (7 ms)
TR (ms)	20.2/43.4/11.2	18	24/44
Frame rate (s)	1.62/3.47/0.90	1.44	1.92/3.52
TE (ms)	1.8/32/1.8	1.8	1.8/32
Flip-angle ( $^{\circ}$ )	16/16/32	16 and 8	16/16
Results	Fig. 3, Fig. 4	Fig. 5	Fig. 4

Table 4.2: Simulated and measured percent functional signal change.

	BOLD	STFR	bSSFP
Simulation	5.2 %	3.6 %	0.8 %
Measurement	4.1 %	3.1 %	0.7 %

To establish whether STFR can produce useful functional contrast, we performed fMRI experiments in 5 healthy volunteers. Table 4.1 summarizes these experiments. We performed all imaging experiments on two different GE 3T scanners equipped with quadrature transmit/receive head coils. The subjects underwent visual checkerboard stimulation and performed bilateral finger-tapping, using 5 cycles of a 20 second on, 20 second off, block paradigm.

We repeated the fMRI run 3-5 times for each subject, to quantitatively compare STFR and BOLD in terms of test-retest reliability [22, 67]. The number of repeated scans varied across subjects (from 3 to 5) depending on how long the volunteer could comfortably stay in the scanner. One subject was scanned in a second session to demonstrate: (1) the effect of varying flip angle, and (2) the use of an alternative tip-up pulse design (spiral).

In one subject (Subject A) we additionally acquired bSSFP functional activation maps (5 repetitions). This was done to compare the functional contrast between STFR, BOLD, and bSSFP. We used twice the flip angle ( $32^{\circ}$ ) for the bSSFP experiments, which is expected to produce similar image contrast as STFR using half the flip angle [65]. Note that we used identical readout for STFR and bSSFP, which leads

to a longer TR for STFR because of its tip-up pulse and gradient crusher. The other subjects (B-E) were not scanned using bSSFP due to the long scan times needed for the BOLD/STFR test-retest acquisitions.

We acquired time-series image volumes using the sequence shown in Fig. 4.1(c,d), which consists of a 3 cm axial slab-selective Shinnar-Le Roux tip-down pulse [71], a balanced 3D stack-of-spirals readout, and a tailored tip-up pulse. Other sequence parameters were: 5 cm FOV with 10 partitions in z; 8 spiral kx-ky segments supporting 128x128 matrix size; in-plane FOV 24 cm. To suppress out-of-slab steady-state signal formation (primarily a concern when using non-slice-selective tip-up pulses such as spiral), we used RF-spoiling with 117° linear phase increment, as described in [65].

To minimize the possible influence of eddy-currents on the steady-state, we minimized the frequency of large jumps in k-space (caused, e.g., by rotating the spiral leafs) by acquiring all z partitions in linear fashion before moving to the next spiral leaf, and by alternating the direction of kz-space traversal when jumping to the next spiral leaf [5, 63].

We designed the tailored tip-up pulses using two different RF designs: fast-kz [77] and spiral. The fast-kz (spoke) pulse is longer and can only be tailored to a relatively smooth in-plane phase pattern, but it has the advantage that there is no out-of-slice signal. The fast-kz tailored tip-up pulse duration was 7 ms, and consisted of 10 slice-selective subpulses at different kx-ky locations. We designed the kx-ky locations and RF waveform jointly using a greedy approach as in [109]. The spiral non-slice-selective tailored tip-up RF waveform was 4.5 ms, designed as in [65]. We used the small-tip (Fourier) approximation [72] and the discretized design method in [107], implemented with the IRT Matlab toolbox (<http://www.eecs.umich.edu/~fessler>).

In each scan session, we tailored the tip-up pulse to a 2D region-of-interest (ROI) containing most of the central slice, but excluding regions with severe B0 inhomogeneity if present (such as the frontal sinus). To design the pulse, we acquired an axial 2D B0 map  $\omega(x, y)$  located at the center of the 3D fMRI image volume ( $z=0$ ). We calculated the 2D B0 map from two spoiled gradient-echo (SPGR) images with echo time difference of 2.3 ms to minimize the contribution of fat to the measured image phase difference (flip angle 16°; 64x64 matrix size).

We designed a 2D, rather than 3D, tip-up pulse to ensure accurate tip-up pulses in the center slice with acceptable pulse duration. Hence, these functional experiments were designed as proof-of-concept experiments, i.e., to investigate whether STFR can in fact produce functional contrast; A true 3D functional experiment would require a tip-up pulse tailored to a 3D ROI, which would extend the RF pulse duration

significantly. We also note that we could in principle have performed single-slice functional experiments for our purposes here; however this could have introduced slice-profile errors and blood in-flow effects that could confound the results.

### 4.3.3 fMRI Processing and Analysis

We reconstructed 3D image volumes using iterative nonuniform fast Fourier transform (NUFFT) [18, 17] in the axial plane, and FFT in the through-slab ( $z$ ) direction. We performed 2D image co-registration along the temporal dimension for each slice. We then applied linear time drift removal for each pixel. We correlated the resulting filtered time-series with the block stimulus to obtain a correlation value for each voxel.

We estimated test-retest reliability following [22, 67], and the method is described here: this analysis is based on calculating activation maps using multiple activation thresholds, and obtaining a maximum likelihood estimate (MLE) of sensitivity and false positive rate at each threshold. These rates are then plotted to form a receiver operating characteristic (ROC) curve for each subject, which gives a quantitative reliability measure for each acquisition method (STFR and BOLD).

## 4.4 Results

### 4.4.1 Bloch Simulation Results

Figure 4.2 shows the simulated functional signal change for STFR (both with and without diffusion) and passband bSSFP over a range of TRs (8 ms – 24 ms) and flip angles ( $8^\circ$  –  $45^\circ$  for STFR and  $16^\circ$  –  $90^\circ$  for bSSFP). Figure 4.2 (b) and (c) show the percent signal change, i.e., as a fraction of the rest state signal, and absolute signal change, i.e., as a fraction of  $M_0$ , respectively, which predicts that STFR can in fact produce a functional signal. The percent signal increases with increasing flip angle across the whole simulated range, while the absolute signal change keeps increasing until  $20^\circ$ . Both increase with increasing TR. “Turning off” spin diffusion has a relatively small impact on the functional signal, indicating that functional contrast in STFR is primarily driven by static dephasing (as illustrated schematically in Fig. 4.1(b)). These simulations also predict that under ideal imaging conditions (i.e., tip-up pulse is perfectly tailored to the mean phase for each voxel), STFR can produce significant functional signal increase compared to passband bSSFP. As a reference, the simulated percent and absolute functional signal change of the spoiled GRE BOLD sequence (TR = 44 ms, TE = 32 ms, flip angle =  $16^\circ$ ) is 5.24 % and

0.0037 respectively. Note that the percent signal change of conventional BOLD is 40% higher than STFR with  $TR = 20$  ms, flip angle =  $16^\circ$ , but the absolute signal change is 20% lower.

The simulation was performed assuming the tip-up pulse perfectly matches the mean accumulated phase of each voxel, which corresponds to a weighted integration over a narrow spectrum located in the center of Fig. 4.1(b). We also simulated the percent signal change when the mean phase mismatch is not 0 (that would correspond to a weighted integration over a narrow spectrum off the center), and the result is shown in Fig. 4.2(d), which predicts that the functional signal change is maximized when mean phase mismatch is  $0^\circ$ .

#### 4.4.2 Functional Imaging

Figure 4.3(a) shows the thresholded correlation maps of STFR, BOLD, and bSSFP imaging for 5 scans in one subject (A, Session 1). Both STFR and BOLD show high correlation in the motor cortex areas. Balanced SSFP imaging shows some activation in the motor cortex area, but also displays correlations in other regions. To quantitatively evaluate the functional signal, we first selected a region of interest (ROI) by choosing all the pixels that show activations in at least 4 scans in both STFR and BOLD (see Fig. 4.3(b)), and then obtained the mean signal time course for voxels within that ROI (Fig. 4.3(c)). STFR shows slightly smaller signal change than BOLD, but higher than bSSFP. The measured percent signal change is reported in Table 4.2, and is in good agreement with simulation results, scaled by an arbitrary factor (1.2 times). The absolute signal change is not reported because the receive gain of the scanner changed between scans, which leads to different baseline image intensity.

Figure 4.4 shows ROC curves for STFR and BOLD in 5 subjects (A-E). STFR functional imaging shows good reliability in general, but slightly lower than conventional BOLD. One BOLD curve had very low reliability, which may be due to motion artifact (observed in the functional maps corresponding to that subject).

Finally, Fig. 4.5 shows STFR functional imaging results of one subject for two different flip angles ( $8^\circ$  and  $16^\circ$ ). Imaging with  $16^\circ$  flip angle results in more active voxels in the expected region compared to  $8^\circ$ . To quantitatively compare the results for different flip angles, we plotted the mean time course over an ROI in Figs. 4.5(c) and 4.5(d). The ROI is chosen by selecting the voxels that are classified as active in both flip angle acquisitions. Higher flip angle has more absolute and percent signal change, which agrees with the simulation.

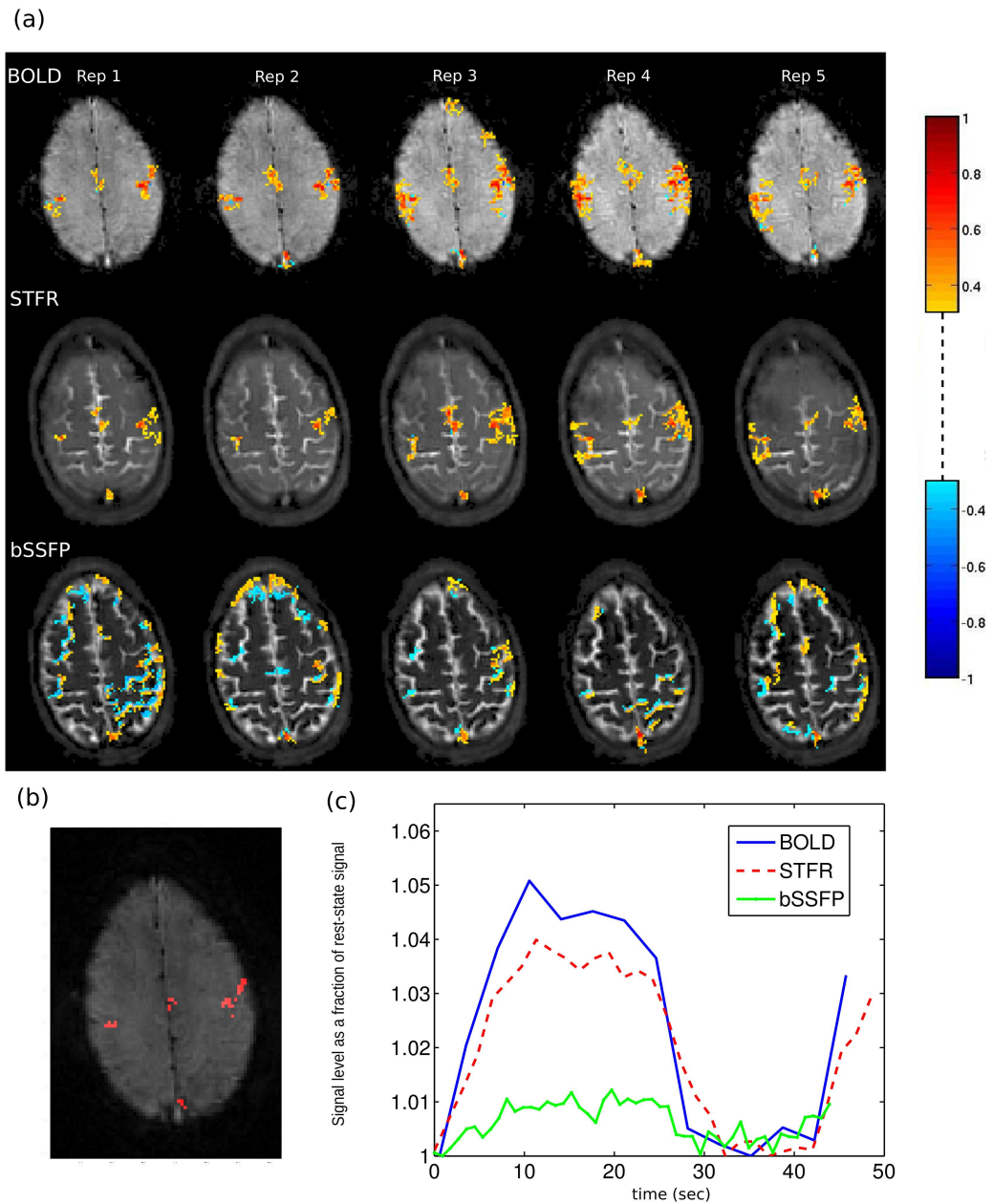


Figure 4.3: Repeated motor cortex imaging using STFR, BOLD and bSSFP in one subject (A, Session 1). (a) Activation maps with correlation threshold 0.3 and cluster size 10 [20]. All five scans demonstrate that STFR can produce similar activation maps as BOLD, which are well localized to the motor cortex area. (b) ROI used to calculate the mean time course for each sequence, obtained by selecting the pixels showing activations in at least 4 scans in both BOLD and STFR. (c) One cycle of the mean time course over the ROI (the rest state signal is normalized to be 1). STFR has slightly lower functional contrast than BOLD, but higher than bSSFP. The calculated percent functional signal change is reported in Table 4.2.

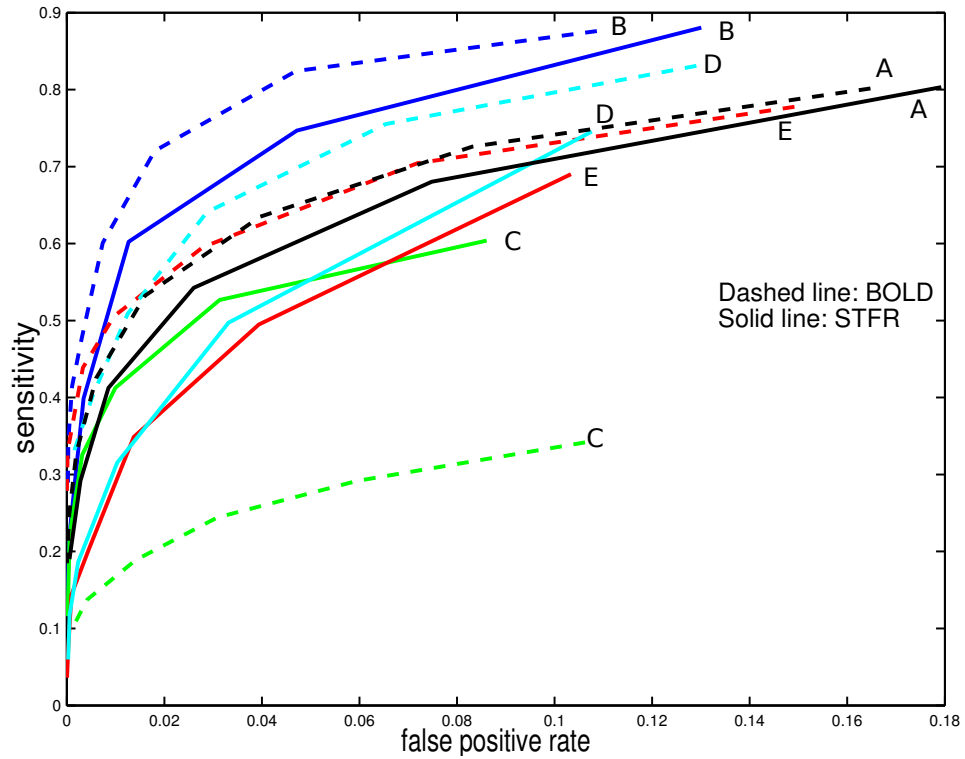


Figure 4.4: Summary of test-retest reliability results for 5 different subjects (Subjects A–E), calculated using the method in [22, 67] from motor cortex imaging data. The ROC curves for STFR are generally slightly lower than BOLD, but still demonstrate that it is a reliable sequence for detecting functional activity. One BOLD curve is much lower than other curves, which is probably due to the motion artifact we observed in that set of data.

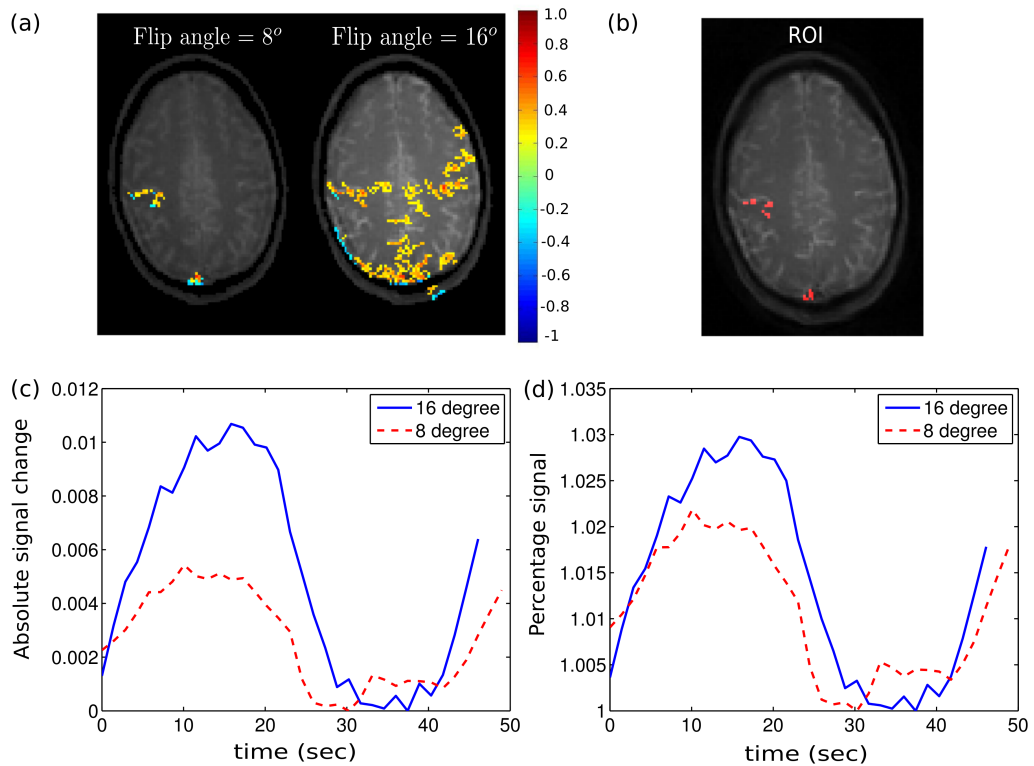


Figure 4.5: Effect of flip angle on functional signal in STFR. (a) Correlation map obtained with STFR fMRI, using flip angles  $16^\circ$  and  $8^\circ$ . Threshold and cluster size are 0.22/12 for both flip angle acquisitions. (b) ROI used to calculate the mean time course for each flip angle, which includes pixels showing activation in both flip angle acquisitions. (c,d) One cycle of mean time course within ROI.  $16^\circ$  flip angle produces higher absolute and percent functional signal change compared to  $8^\circ$  flip angle, as predicted in simulation (Fig. 4.2(b,c)).

## 4.5 Discussion

The Bloch simulation results suggest that the STFR functional signal arises primarily from interactions between the intra-voxel dephasing and the tip-up pulse. If we ignore the relatively small diffusion effect, we can obtain the STFR functional signal by numerical weighted integration of the steady-state signal over the intra-voxel frequency distribution as in Eq. [4.3], instead of performing a full Monte Carlo Bloch simulation. Using this method, we predict a 3.3% signal change, which is close to the Monte Carlo simulation result of 3.6%.

The dephasing effect in STFR is similar, but not exactly the same as the  $T2^*$  effect in the conventional BOLD sequence. We can not simply replace  $T2$  in Eq. [4.2] with a conventionally defined  $T2^*$ , i.e.,  $1/T2^* = 1/T2 + 2\pi\gamma$ , where  $\gamma$  is the half-width at half-maximum (HWHM) of the intra-voxel Lorentzian distribution, to obtain the voxel signal. Fitting a Lorentzian line shape to the simulated frequency distribution with  $T2 = 71$  ms [85] yields  $T2^*$  values of 62 ms and 68 ms in rest and active conditions, respectively (we have not found literature supporting those  $T2^*$  values but we believe  $T2^*$  change of this size is reasonable, as it would produce a  $\sim 4\%$  BOLD functional change assuming  $TE=30$  ms, which is within the commonly observed range). By replacing  $T2$  with  $T2^*$  in Eq. [4.2] we obtain a percentage signal change of 7.0%, which is almost twice the contrast obtained from Monte Carlo simulation or numerical integration, supporting the idea that the functional contrast mechanism is not quite the same as  $T2^*$  decay. In addition, from Eq. [4.2], we note that  $T2$  is paired with  $T_{\text{free}}$ , not  $TE$ , which decouples the main source of functional signal from  $TE$ .

In our Monte Carlo Bloch simulations, we observed that the effect of diffusion is to increase the image signal and decrease the functional contrast compared to the result without diffusion (see Fig. 4.2). We think the reason for this change is that with diffusion, spins effectively experience different frequencies during the free precession interval, and that the accumulated phase therefore tends to be closer to the mean phase of that voxel. This effectively narrows the line spread of the intra-voxel distribution, which increases the image signal but decreases the functional contrast.

Flip angle and  $TE$  are two other variables that affect the signal contrast. We used 16 degrees in most of our experiments, which is approximately the Ernst angle for the BOLD acquisitions (assuming a  $T1$  of about 1.1 sec). According to the simulation in Fig. 4.2(b), a flip angle around 20 degrees generates the maximum absolute signal change. We used the minimum available  $TE$  for STFR in our experiments, but we found later in simulation that the functional signal increases with increasing  $TE$  (not

shown here), probably due to the normal  $T2^*$  effect. This suggests that a spiral-in readout rather than a spiral-out readout could be used to increase the effective TE and therefore the functional signal.

Physiological fluctuations in  $B0$  (e.g., due to respiration) would shift the voxel signal as a whole along the curve in Fig. 4.2(d), which would reduce the functional contrast. We expect the  $B0$  shift due to respiration to be of order 1-2 Hz at 3T (fluctuations of 1.45-4 Hz have been reported at 7T [60]), which would not shift the voxel signal significantly (e.g., 5-11 degrees assuming  $T_{\text{free}} = 15$  ms) along the curve in Fig. 2(d). In the experiments presented here we have not observed significant physiological noise increases in STFR compared to BOLD.

A potential advantage of STFR compared to BOLD is that it can achieve high resolution segmented 3D imaging with reduced signal loss and image distortion. However, to achieve this across the whole brain, a 3D tailored tip-up pulse would be necessary, which may be prohibitively long. We have suggested methods for improving 3D tailored pulse design [93], but it is still challenging to tailor to the whole brain including regions with high field inhomogeneity (e.g., near frontal sinus). A potential solution is to use parallel transmission to reduce the pulse duration, and we plan to explore the feasibility of 3D STFR functional protocol using an 8-channel parallel transmit head array [34].

## 4.6 Conclusions

Taken together, the work presented here indicates that STFR has the potential to become a sensitive functional imaging modality. The functional contrast mechanism is decoupled from the echo time, enabling segmented readouts and high image quality. Our Monte Carlo Bloch simulations indicate that STFR fMRI can produce observable functional contrast, and proof-of-concept *in vivo* STFR fMRI observations using a 2D tailored tip-up pulse support this prediction. Our simulations also indicate that the functional contrast in STFR is driven primarily by “static dephasing”, and that diffusion plays a relatively minor role. In the future, we plan to evaluate the feasibility of whole-brain STFR fMRI, using 3D tailored tip-up pulses. We expect the design of such 3D pulses to benefit greatly from parallel transmission systems, high-order gradient shimming, and novel RF pulse design approaches.

## CHAPTER V

# Small-Tip Fast Recovery Imaging Using Spectral Tailored Pre-winding Pulse

### 5.1 Introduction

<sup>1</sup>In chapter III and chapter IV, we proposed a new steady-state imaging sequence named Small-tip fast recovery (STFR), which relies on a tailored tip-up RF pulse (Fig. 5.1) and a gradient crusher to achieve comparable signal level as bSSFP, but with potential for reduced banding artifacts and transient oscillations. In addition, unlike bSSFP, STFR is compatible with magnetization preparation pulses, such as fat saturation or magnetization transfer pulses [114].

However, previous STFR implementations used spatially tailored pulses that introduce some T2\* weighting [97], unlike bSSFP that refocuses microscopic B0 inhomogeneities and therefore produces more pure T2 (and T1) tissue contrast. Here we propose to modify the STFR sequence using a spectral tip-up pulse, specifically the “pre-winding” RF pulse proposed recently by Asslander et al. [2]. This modification removes the intra-voxel dephasing-induced T2\* weighting in spatial-STFR, making the contrast more similar to bSSFP, and has the additional advantage that tip-up pulses can be precomputed to a target frequency range and do not rely on detailed patient-specific fieldmap (B0) information. This chapter compares this new “spectral-STFR” sequence with bSSFP in terms of (1) signal level, (2) brain tissue contrast, and (3) off-resonance signal (banding) profile, using Bloch simulations and phantom and *in vivo* imaging experiments.

---

<sup>1</sup>This chapter is based on the publications [89, 92]

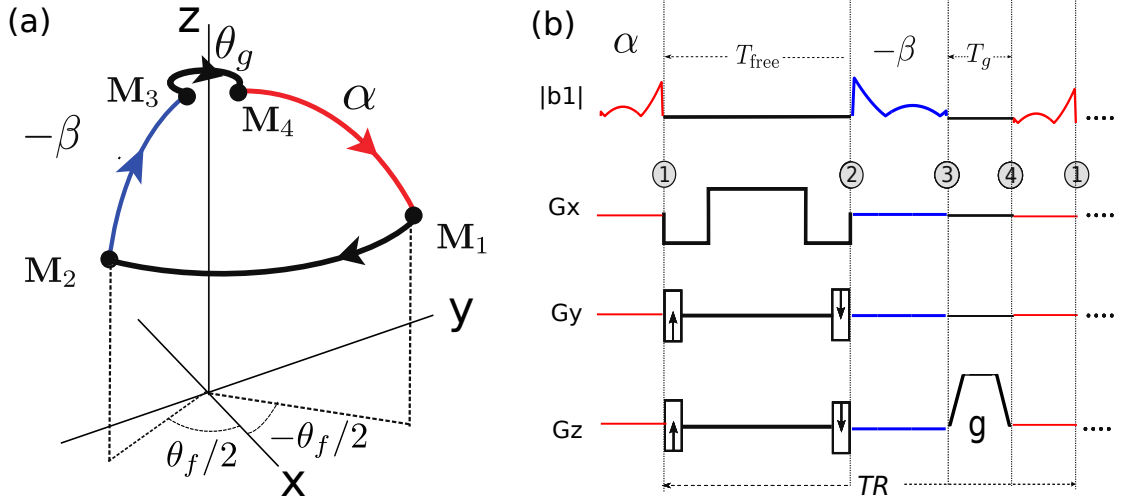


Figure 5.1: Proposed spectral-STFR pulse sequence. Spectral pre-winding pulses are used for both tip-down and tip-up excitations in this work. (a) Steady-state spin path. The tip-down pulse “prephases” the spins to have a phase equal to the negative of half the accumulated free precession phase  $-\theta_f/2 = \omega T_{\text{free}}/2$ , where  $T_{\text{free}}$  is the free precession time. After readout, the spin is tipped back to the z-axis by a pulse tailored to the phase  $\theta_f/2$ . (b) Pulse sequence timing diagram.

## 5.2 Theory

In [66, 93], we described the theory and implementation of STFR in detail. There are two key ideas in STFR: First, after readout, a tip-up radio-frequency (RF) pulse tailored to the accumulated phase during free precession is transmitted to bring spins back to the longitudinal-axis, which “fast recovers” the transverse magnetization and preserves it as longitudinal magnetization for the next TR. Second, after the tip-up pulse, an unbalanced gradient is played out to dephase residual transverse spins [93]. Figure 5.1 shows the spin path and an example sequence diagram of the proposed spectral-STFR sequence, where  $\alpha$  (red waveform) and  $-\beta$  (blue waveform) correspond to the tip-down and tip-up parts, respectively. The pulse diagram is similar to its spatial sibling, but with the gradient waveforms during the RF pulse duration set to zero. We use an unspoiled sequence (constant RF phase over time) here since it is less sensitive to phase mismatch between pre-winding pulse and actual accumulated phase than RF-spoiled STFR [93].

Unlike bSSFP, which typically has short slice-selective RF pulses that can be approximated by instantaneous rotations, the relatively long RF pulses in spectral-STFR can incur significant signal decay (“finite RF pulse effects” [6]). This T2 decay mechanism is exacerbated by the fact that the instantaneous flip angle during RF

excitation can go well beyond the final target angle. Since the detailed shape of the spectral RF pulse will vary depending on, e.g., target bandwidth and details of the pulse design implementation (as described below), we did not derive an analytic signal model for spectral-STFR but instead rely on Bloch simulations for steady-state signal calculations.

Beside the steady state signal level, it is important to note that spectral-STFR may not have the T2\*-like contrast in spatial-STFR. In spatial-STFR, intravoxel spins may experience different spin/tip-up phase mismatch because the phase of the spatially tailored pulse is relatively smooth (we can assume it is a linear for a voxel). The mismatch between the phase of the tip-up pulse and the intravoxel field inhomogeneity leads to T2\*-like contrast, which can be used to detect blood oxygenation level dependent (BOLD) functional signal [97]. Spectral-STFR, on the other hand, does not have this property since ideally the phase of all spins match their off-resonance frequency regardless of spatial position.

## 5.3 Methods

### 5.3.1 Spectral RF pulse design

We use spectral pre-winding pulses for both tip-down and tip-up excitations in our current implementation. The tip-down pulse is tailored to the following spectrum:  $\mathbf{d}(\Delta\omega) = \sin \alpha e^{(i\Delta\omega T_{\text{free}}/2)}$  where  $\alpha$  is the flip angle (uniform for all spins),  $\Delta\omega$  is a vector containing the range of target off-resonance frequencies <sup>2</sup>, and  $T_{\text{free}}$  is the free precession time between tip-down and tip-up excitations. After readout, the spins will have phase  $-\Delta\omega T_{\text{free}}/2$ , and a tip-up pulse is tailored to this to bring all spins back to the longitudinal axis. The tip-up pulse is designed by first designing an intermediate tip-down pulse with negative B0 field map, and then negating and time-reversing this intermediate pulse [66]. The target excitation pattern for this intermediate pulse is determined by Bloch simulation of the tip-down and free precession. The effective flip angle of the tip-up pulse is usually smaller than the tip-down pulse in STFR due to T2 decay during the free precession, leading to a lower RF power for the tip-up pulse. Note that in previous spatial designs,  $\mathbf{d}$  is a function of position, but here  $\mathbf{d}$  is a function only of off-resonance frequency.

We compute the RF waveform under the small tip angle approximation [72, 103]; specifically, we solve  $\hat{\mathbf{b}} = \underset{\mathbf{b} \in \mathbb{C}^{N_s}}{\text{argmin}} \|\mathbf{A}\mathbf{b} - \mathbf{d}(\omega)\|_2^2 + \mu \mathbf{b}'\mathbf{b}$ , where  $\mu$  is the Tikhonov

---

<sup>2</sup>We use the convention  $\omega = \gamma B$  in our work. Since the free precession is rotate clockwise with a positive B field, the accumulated phase is in the negative direction:  $\theta_f = -\omega T_{\text{free}}$

Regularization parameter controlling the tradeoff between RF power and excitation accuracy.  $\mathbf{A}$  is the small tip system matrix with  $a_{ij} = \nu\gamma M_0 e^{i\Delta\omega_i(t_j-T)}$ . Unlike the conventional small tip angle system matrix [103], there is no phase encoding term  $i\mathbf{k}_j \cdot \mathbf{r}_j$  in  $\mathbf{A}$  here since all gradients are set to zero for spectral selectivity.

### 5.3.2 Simulations

We designed spectral pre-winding RF pulses with  $10^\circ$  flip angle and  $\pm 75$  Hz target bandwidth. We evaluated the RF pulse design for different Tikhonov regularization parameters. We also simulated the steady-state signals for spectral-STFR and bSSFP using T1/T2 values for gray matter (GM), white matter (WM), and cerebrospinal fluid (CSF) [85], over a 300 Hz bandwidth with 4.9 ms readout time to compare the banding profile and tissue contrast.

### 5.3.3 Imaging experiments

To evaluate the steady state signal level and demonstrate the banding reduction of STFR, we acquired RF-spoiled gradient echo (SPGR), bSSFP and spectral-STFR images of a GE resolution phantom using a GE 3.0 T scanner and a birdcage T/R headcoil. We designed a spectral-STFR pulse covering the B0 bandwidth (BW) in the target slices (-75 Hz to 75 Hz). Spectral-STFR used a  $10^\circ$  flip angle, which is expected to produce similar signal as bSSFP with  $20^\circ$  flip angle [93]. The pulse lengths were 2 ms for each RF pulse, and a 3D readout was used with 256x256x65 sampling, 24x24x32 cm field of view (FOV), and 62.5 KHz receive bandwidth, resulting in a 4.9 ms readout time, including dephasing, rephasing, and phase encoding gradients, and 10 ms TR, which also includes a crusher after the tip-up pulse. We used a large readout FOV in z to eliminate aliasing from untargeted slices since the spectral pre-winding pulse is not spatially selective. For comparison, SPGR/bSSFP images were acquired with the same resolution,  $10^\circ/20^\circ$  flip angle, and 10 ms/7 ms TR.

A healthy volunteer was imaged with the same hardware setup as the phantom experiments. We acquired a low resolution 3D B0 map solely to estimate and specify the target off-resonance range. We designed a spectral-STFR sequence ( $10^\circ$  flip angle) targeted to -120 to +50 Hz. The pulse lengths were 2 ms for each RF pulse. We determined that the specific absorption rate (SAR) of our sequence was moderate; specifically the integrated total RF power of our spectrally tailored pulse was approximately equal to a  $35^\circ$  sinc pulse of time-bandwidth 6 and duration 1.2 ms. The 3D readout was the same as in the phantom experiment. For comparison, bSSFP images

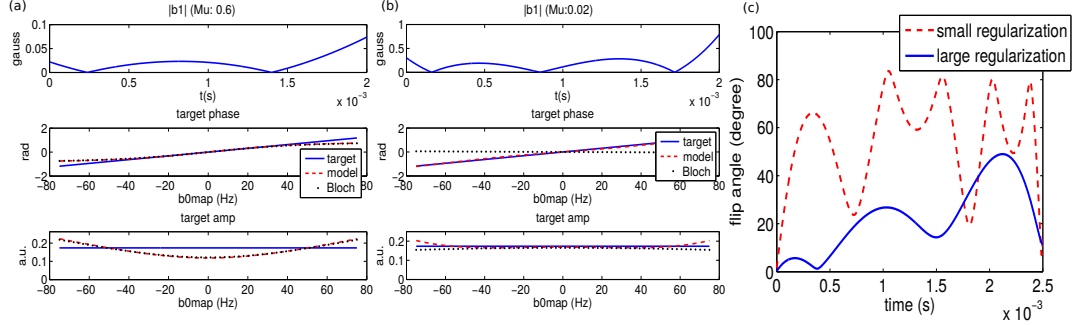


Figure 5.2: Effect of regularization parameter  $\mu$  on spectral pre-winding RF pulse waveforms. (a) Large  $\mu$  (0.6) can suppress the b1 magnitude and keep the small tip angle approximation accurate (i.e., small difference between the small tip angle approximation and Bloch simulation). (b) With small  $\mu$  (0.02), the excitation predicted by the small tip model matches the target, but the actual excitation pattern has large deviations from the target since the small tip approximation does not hold for the entire RF transmission window. (c) Actual flip angle of a spin during the RF pulse can be larger than the final target flip angle. Small regularization leads to higher intermediate flip angle and therefore less accurate excitation. We designed pulses with  $\mu = 0.6$  in this study.

were acquired with the same resolution,  $20^\circ$  flip angle, and 7 ms TR.

### 5.3.4 Results

Figure 5.2 demonstrates the impact of regularization parameter choice on the spectral pulse. Although the final excitation flip angle is small in our implementation (e.g.,  $10^\circ$  in this simulation), the instantaneous flip angle during RF transmission can be large (Fig. 5.2 (c)). Therefore, the small tip approximation can be inaccurate for this pulse design. To keep the small tip approximation accurate, we used a large regularization parameter that keeps the flip angle relatively small during the whole excitation process. With relatively large regularization (a), the small tip approximation matches the Bloch simulation very well, but both deviate somewhat from the target. With small regularization (b), the small tip prediction matches the target, but the actual excitation does not match the target. All experiments in this study used  $\mu = 0.6$ .

Figure 5.3(a) shows the simulated steady-state signal for spectral-STFR and bSSFP for gray matter (GM), white matter (WM), and CSF over a 300 Hz bandwidth with 4.9 ms readout time. In this figure, the sequence was designed for 150 Hz target bandwidth, with  $\mu = 0.6$ . The flip angles are  $10^\circ$  and  $20^\circ$  for spectral-STFR and bSSFP, respectively. Both sequences have high CSF signal, as expected. Spectral-STFR has

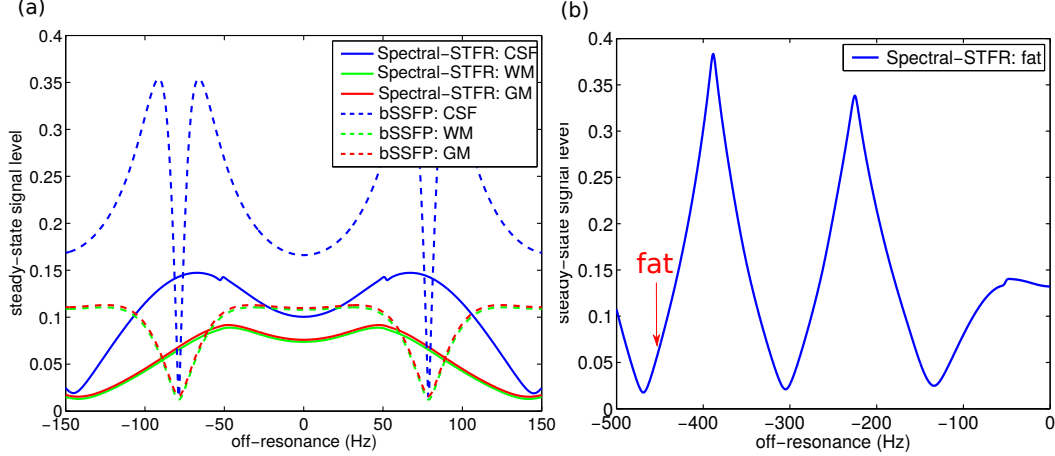


Figure 5.3: Simulated steady-state banding profile of (a) spectral-STFR and bSSFP for WM, GM, and CSF, using T1 and T2 values from [85], and (b) spectral-STFR for fat with T1 and T2 values from [28]. RF pulses were designed for 150 (+/-75) Hz target bandwidth, 4.9 ms T<sub>free</sub>, and  $\beta = 0.6$ . In general, spectral-STFR and bSSFP have similar tissue contrast (e.g., high CSF signal). Spectral-STFR has wider passband than bSSFP. The banding shape for spectral-STFR is similar for different tissue types, indicating a relatively consistent tissue contrast across the frequency band. Fat can have high signal in spectral-STFR.

wider passband ( $\approx 50\%$  increase in FWHM). The banding shape of spectral-STFR is more consistent across different tissues, e.g., the CSF signal near the band edge is less hyperintense relative to the corresponding bSSFP curve. Figure 5.3(b) shows the simulated banding profile for fat. Fat can have high signal depending on its off-resonance, which is a potential drawback of spectral-STFR. Potential ways to suppress the fat signal are discussed further below.

Figure 5.4 shows the field map, SPGR, bSSFP, and the spectral-STFR image for 4 slices spanning 4 cm in the phantom. As predicted from simulation, the banding artifacts observed in bSSFP are successfully reduced in the STFR images, and the STFR signal is relatively uniform across the passband.

Finally, Fig. 5.5 shows the field map, bSSFP image, and spectral-STFR image for 10 slices spanning 7 cm in a volunteer. The banding artifacts observed in bSSFP that are within our target frequency range have been successfully removed in the STFR images. As off-resonance goes beyond the target range, signal drop occurs (e.g., blue arrow), but the rate of this drop across the object is smaller than the bSSFP signal drop, agreeing with our simulations (Fig. 3). The fat signal in spectral-STFR varies more across the object compared to bSSFP, also in agreement with simulations.

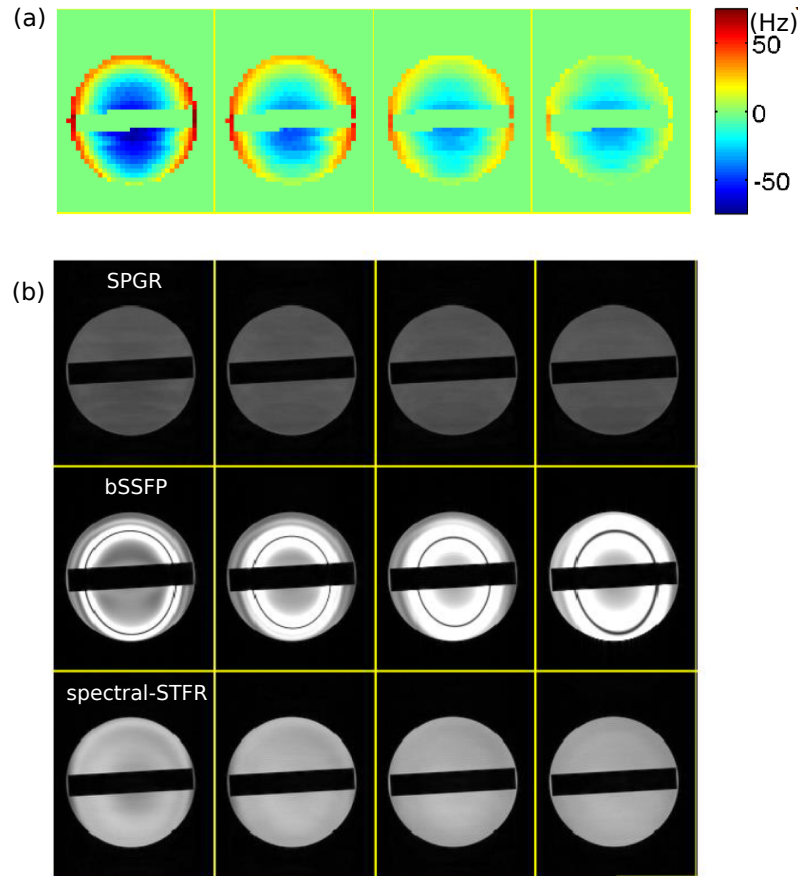


Figure 5.4: Comparison of SPGR, bSSFP, and spectral-STFR imaging in a phantom. (a) B0 map. (b) Steady-state images, displayed on a common grayscale. Spectral-STFR (bottom row) reduces the banding artifact seen in bSSFP (middle row), and has a relatively uniform signal with varying off-resonance. Both bSSFP and STFR generally achieve higher signal than SPGR (top row).

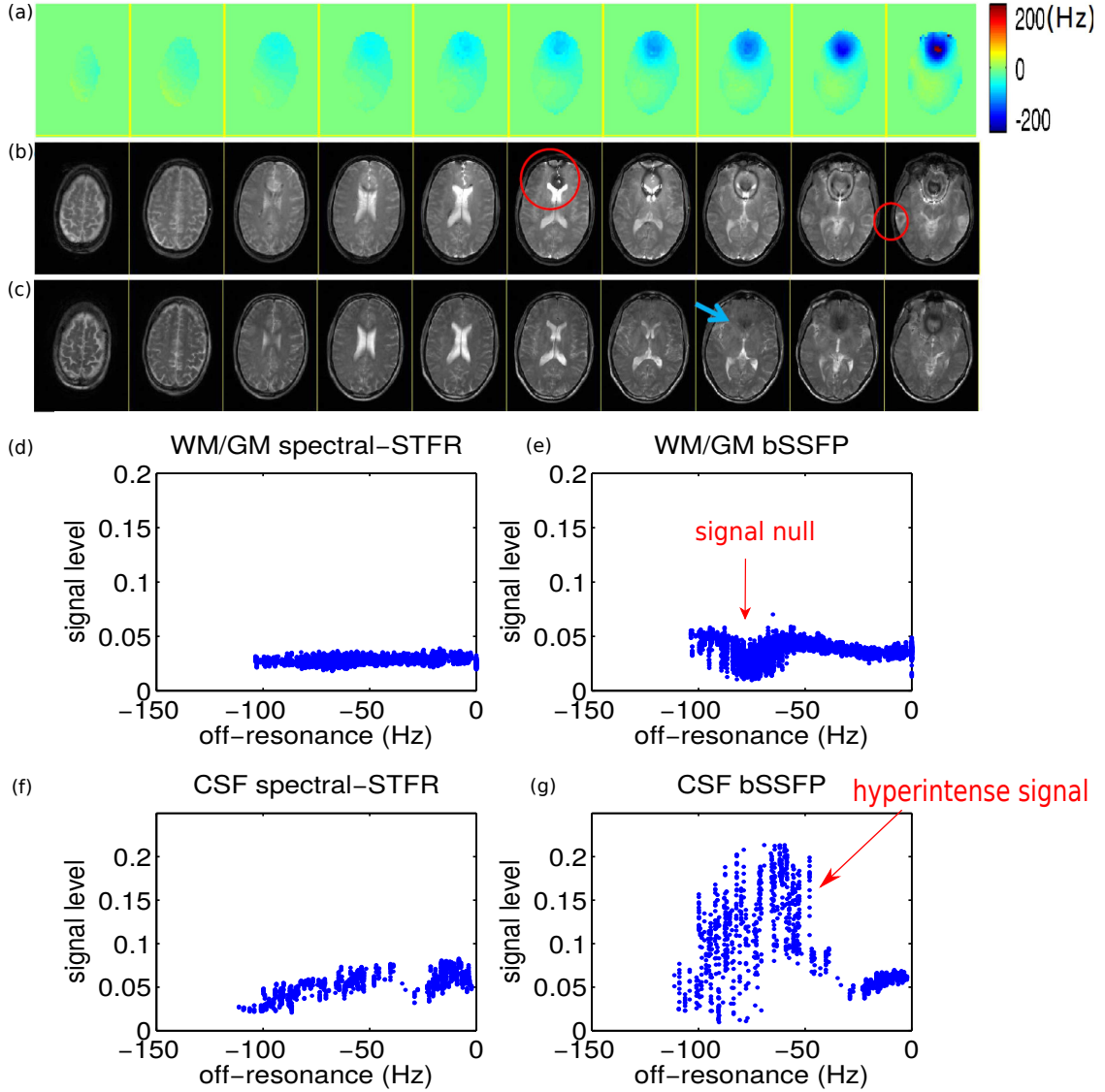


Figure 5.5: Comparison between bSSFP and spectral-STFR imaging: representative human volunteer imaging results. (a) B0 field map, and (b) bSSFP and (c) spectral-STFR images. Spectral-STFR has similar image contrast as bSSFP, but no hyperintense CSF signal near the edge of the bands. In addition, spectral-STFR successfully reduces the banding artifacts (e.g, red circle) within the target frequency range. Signal drop-out occurs when off-resonance goes beyond the target range (e.g., blue arrow). (d-g) Plots of signal level versus off-resonance frequency in CSF and WM/GM ROIs (segmented manually from slices 6-8). The center of target bandwidth is -35 Hz and 0 Hz for spectral-STFR and bSSFP, respectively. Balanced SSFP shows signal drop near -70 Hz, which is corrected at the corresponding frequency (-105 Hz) in spectral-STFR. The CSF signal variation of spectral-STFR is much smaller than bSSFP near the edge, agreeing with the simulation in Fig. 5.3. The fat signal near the skull shows high variability in the spectral-STFR images, as expected from the simulation results in Fig. 5.3(b).

### 5.3.5 Discussion

The key to the proposed spectral-STFR sequence is to design a spectral pre-winding pulse that can successfully prephase the spins over a wide bandwidth. Based on our simulations using the small-tip pulse design method, we find it is hard to achieve bandwidth wider than  $1/(2T_{\text{free}})$ . Therefore, with the same pulse design method, the only way to increase the target bandwidth is to reduce the readout time, leading to lower resolution, lower SNR, or increased number of TRs. There are several potential improvements of the pulse design method. As shown above, the actual flip angle during RF transmission can be large enough to significantly violate the small tip angle approximation, so a large tip design may therefore generate better results. We have evaluated the large tip design method proposed by Grissom [25] that combines optimal control with a linearization of the Bloch equation. Using this method, we can design pulses that have bandwidths wider than  $1/(2T_{\text{free}})$  (Figure 5.6); However we found that the final pulse is sensitive to how the algorithm is initialized (initial pulse). In [25], a scaled small tip design pulse was used as the initial pulse. We have found that if we use a large regularization parameter in designing the initial pulse, the resulting large tip design does not improve the result significantly compared to the initial pulse. If we use a small regularization parameter, the large tip design step can significantly improve the result and perfectly match the target phase pattern, but leads to high RF power and low steady-state signal (not shown). The fact that a high power pulse leads to a lower steady-state signal for short T2 species may be useful to enhance image contrast (e.g., increase the contrast between CSF and WM/GM, or between CSF and cranial nerves). However, the general problem of enforcing the RF power constraint while designing a pulse that matches the target phase remains an open problem.

In this work we used non-spatially-selective RF pulses for both tip-down and tip-up excitations, however it is possible to limit the FOV by using a spatially selective tip-down excitation (e.g., a conventional slice-selective RF pulse) followed by a spectral tip-up pulse. In this case it is necessary to use RF-spoiling to suppress unwanted SSFP-echo signal created by the non-spatially-selective tip-up pulse [66]. Another way to limit the FOV may be to use a slab saturation pulse between time-points (3) and (4) in Fig. 1(b). Thirdly, in Cartesian imaging sequences (e.g., spin-warp or EPI) the FOV in the frequency encoding direction is limited by the readout bandwidth.

This work considered the excitation accuracy following a single shot only, however it may be possible to design the RF pulses for optimal *steady-state* signal across the target off-resonance bandwidth. For example, in [66, 93] we showed that the steady-

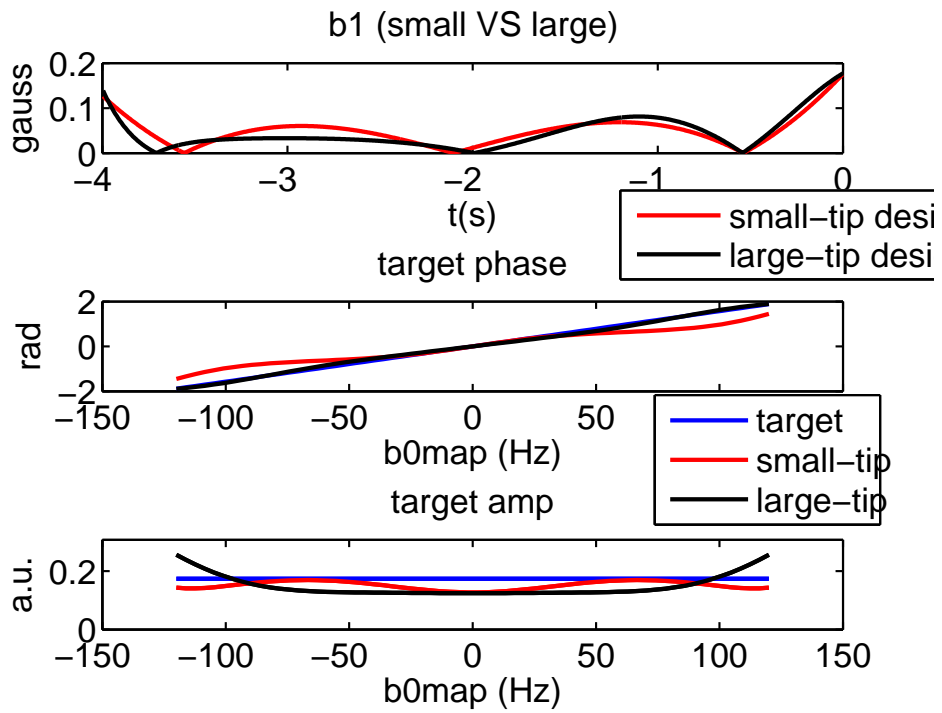


Figure 5.6: Compare small-tip pulse design method with large-tip pulse design method for a wider target bandwidth. Using large-tip pulse design method, we can achieve target bandwidth larger than  $1/(2TE)$  ( $TE = 2.5$  ms, bandwidth = 240 Hz). The pulse duration is relatively long to keep the RF power within limit.

state signal is relatively insensitive to flip angle over a certain range (e.g.,  $10^\circ$  to  $25^\circ$  for gray matter and white matter). We can therefore partially relax the magnitude (flip angle) constraint or limit the maximum deviation [96] in the pulse design, which may improve steady-state accuracy. Also, a joint pulse design that considers both tip-down and tip-up pulses in one RF pulse design step may be helpful [93].

We observed in our simulations (Fig. 5.3(b)) and our *in vivo* experiments (Fig. 5.5) that fat signal varies significantly with off-resonance, which is a potential disadvantage of our sequence. However, since a key advantage of STFR is the ability to incorporate magnetization-preparation pulses (between time-points (3) and (4) in Fig. 1(b)), as demonstrated in [114], we can incorporate fat-suppression pulses to suppress the fat signal. In our *in vivo* experiment, the peak of the measured 10 second SAR average is 0.8 W/Kg on our GE scanner, which is well below the 6.4 W/Kg limit. The integrated RF power of a 6 ms SLR fat saturation pulse is only half the integrated power of our spectral-rewinding pulses. So adding this fat saturation pulse to our sequence will not violate the SAR limit. However, adding magnetization preparation pulses can increase the length of the sequence and therefore reduce the SNR efficiency. Alternatively, we may change the readout time to shift fat to the null of its banding profile, but it may be difficult to place fat in a signal null over the whole brain imaging due to B0 inhomogeneity.

Some differences between spectral-STFR and bSSFP should be noted. First, for a given readout duration and acquisition matrix, the total acquisition time for spectral-STFR will be longer, due to the tip-up RF pulses. Second, we observe in our *in vivo* results that blood signal in large vessels is suppressed in spectral-STFR relative to bSSFP. One possible cause for this is that the phase of flowing blood spins at the beginning and end of the free precession interval may not be consistent, i.e., the phase at end of  $T_{\text{free}}$  may deviate from the predicted phase based on the local off-resonance frequency at the position of the spin at the beginning of the readout interval. Another possibility is that the imaging gradients induce flow-related spin phase due to non-zero gradient first moments, also causing the spin phase at end of  $T_{\text{free}}$  to deviate from the tip-up target excitation phase. This may be problematic for applications that rely on bright blood signal, such as cardiac functional imaging or phase-contrast velocity mapping.

Although the spectral pre-winding pulse does not need spatial off-resonance information, a B0 field map may still need to be acquired in practice to estimate the center of target off-resonance frequency. However, this field map can be in very low resolution. Also, if the scanner can auto-shim the center off-resonance close to 0 in

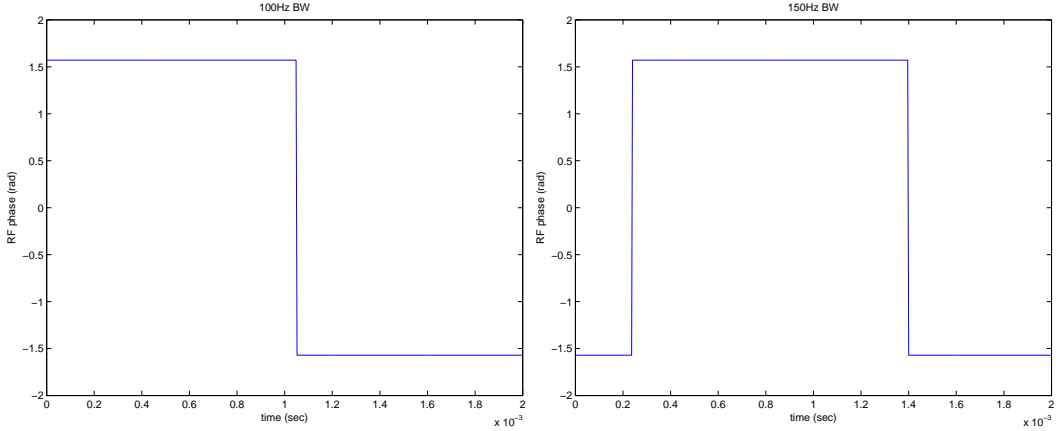


Figure 5.7: The phase of the pre-winding pulse is constant except a few  $\pi$  changes.

the target region, the B0 field map acquisition step can be avoided.

We note that the GRASS sequence can also be an alternative to bSSFP in some applications, and produces bright CSF like bSSFP. However, since GRASS relies on multiple-TR echo pathways to form its T2 and T1-weighted steady-state signal, we expect that GRASS is generally less compatible with magnetization preparation compared to STFR. In addition, GRASS is relatively sensitive to flow and motion, which limits its applications. Also, we observed in simulation that for the sequence used in this work, spectral-STFR has 30% higher signal than GRASS.

The behavior of spins under the spectral pre-winding pulse is investigated in [3]. The spins are first tipped down to one direction with a relative large flip angle. After some phase accumulation, the spins are tipped back to the other side of the z-axis. The Euclidean distances between spins are kept constant when tipped back, but the phase differences are amplified if the final flip angle is smaller than the flip angle in the initial direction. Their explanation agrees with our observation that there is a  $\pi$  phase change in the spectral pre-winding pulse (Figure 5.7 (left)). Moreover, we find that the number of direction changes of the pulse can be more than once when the target bandwidth is large (Figure 5.7 (right)).

Finally, we can try spectral-spatial (SPSP) pulse design instead of pure spectral pre-winding pulse. In SPSP pulse, the target excitation pattern spans a small BW for each pixel, and the BW is centered at the local off-resonance of that pixel. The pure 3D spatial pulse design can be viewed as a SPSP pulse with target frequency only at zero, which is typically a over-determinant problem. So adding more frequency constraints leads to a more over-determinant problem. Therefore, the excitation error at the local off-resonance frequency of each pixel will increase compared to pure spatial

design. So we have to reduce the design resolution in spatial domain compared to the pure spatial pulse to obtain better excitation accuracy.

## **5.4 Conclusion**

We have proposed a new steady-state MRI imaging sequence that combines STFR and a spectrally tailored pulse, and that may offer an alternative to bSSFP in some applications. We have demonstrated that the resulting spectral-STFR sequence has similar tissue contrast as bSSFP but has increased passband width, and more consistent CSF/brain tissue contrast across the passband.

## CHAPTER VI

# Pulse Design using Minimax Algorithm

### 6.1 Introduction

<sup>1</sup> All previous RF pulse design methods attempt to minimize the  $l_2$ -norm of excitation error, which does not strictly enforce a maximum deviation ( $l_\infty$ -norm) between the desired and actual excitation patterns. This can result in undesired image artifacts such as bright or dark spots that may decrease the diagnostic utility of the image. Therefore, in this chapter, we propose to minimize the  $l_\infty$ -norm instead of  $l_2$ -norm to potentially reduce these artifacts. This chapter starts from a special type of k-space trajectory: fast-kz trajectory (also know as spoke or echo volumnar). Then, we extend our method to pulse design with arbitrary k-space trajectories in section 6.6.

The fast-kz trajectory is an important pulse type because it can achieve both slice selection and in-slice modulation, which is widely used in B1 shimming [24]. Figure 6.1 shows an example pulse diagram of a fast-kz RF pulse, which consists of a train of short ( $<1$  msec) sinc subpulses. A through-plane gradient is transmitted simultaneously with the RF subpulses to achieve slice selection, and gradient blips in the  $k_x$  and  $k_y$  directions are interleaved between subpulses to achieve within-slice modulation. The gradient blips determine the in-plane k-space locations of those subpulses, which is referred to as phase encoding location.

In practice, only a small number of subpulses can be transmitted due to time constraints on the whole RF pulse. Therefore, it is desirable to select only a few in-plane phase encoding locations. These locations are not selected a priori but are chosen as part of the fast-kz pulse design. In other words, the k-space trajectory and RF pulse weights should be designed jointly. This problem can be solved by exhaustively searching all the possible phase encoding locations and selecting the

---

<sup>1</sup>This chapter is extended from the conference paper [96]

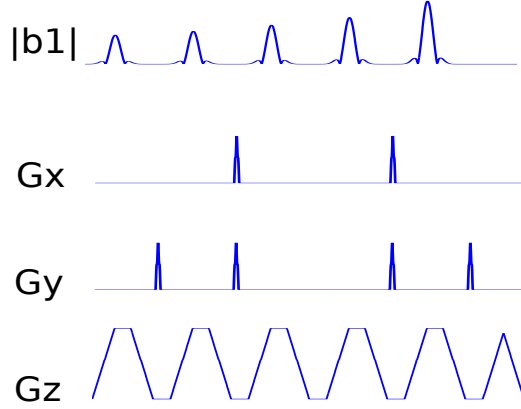


Figure 6.1: Example pulse diagram of a fast-kz pulse. It consists of a train of short sinc subpulses, and gradient blips in the  $k_x$ ,  $k_y$  directions are applied to achieve in-slice modulation.

best, but this will lead to a combinatorial problem, which is hard to solve online while the subject is in the scanner. Recently, several approaches using orthogonal matching pursuit (OMP) [99] or modified OMP have been proposed, which achieve good approximations with much less computation time[53, 109, 10, 111, 24]. However, as I mentioned, all of these approaches attempt to minimize the  $l_2$ -norm of excitation error instead of directly controls the maximum error, which may result in undesired image artifacts such as bright or dark spots in the image. Therefore, in the first half of this chapter, we modelled the fast-kz pulse design problem as a sparse approximation problem with minimization of the  $l_\infty$ -norm to potentially reduce these artifacts. We also proposed a greedy-like algorithm to solve it.

## 6.2 Theory

A typical spoke RF pulse design problem is solved as follows:

$$\min_{\mathbf{x} \in \mathbb{C}^N} \|\mathbf{d} - \mathbf{F}\mathbf{x}\|_2, \text{ such that } \|\mathbf{x}\|_0 = k, \quad (6.1)$$

where  $\mathbf{d} \in \mathbb{C}^N$  is the desired excitation pattern,  $\mathbf{F} \in \mathbb{C}^{N \times N}$  is the system matrix under the small tip angle approximation[72].  $N$  is number of pixels in desired excitation pattern. To begin with, we ignore B0 inhomogeneity, which is a reasonable approximation to short RF pulse. Under this assumption,  $\mathbf{F}$  is a (inverse) discrete Fourier transform matrix multiplied by the coil sensitivity, and  $\mathbf{x}$  is a vector of the RF pulse weights to solve for. The  $l_0$ -(semi)norm in (6.1) ensures  $k$ -sparsity of  $\mathbf{x}$ , i.e., the number of “phase encoding” locations (subpulses) is  $k$ . This problem can be

solved using OMP.

The above modelling does not regulate spikes that can occur in  $\mathbf{d} - \mathbf{F}\mathbf{x}$ , which may lead to dark or light spot artifacts in the result image, and we therefore propose the following slightly different problem:

$$\min_{\mathbf{x} \in \mathbb{C}^N} \|\mathbf{d} - \mathbf{F}\mathbf{x}\|_\infty, \text{ such that } \|\mathbf{x}\|_0 = k. \quad (6.2)$$

This problem explicitly minimizes the maximum absolute value of the entries in  $\mathbf{d} - \mathbf{F}\mathbf{x}$ , so that the previously mentioned artifacts are reduced. Sparsity is again enforced using the  $l_0$ -(semi)norm of  $\mathbf{x}$ .

To solve the problem in (6.2), we propose the following greedy selection algorithm, Algorithm 1, shown below.

---

**Algorithm 1** Greedy Algorithm.

---

- 1: Input:  $\mathbf{F}$ ,  $\mathbf{d}$ , and  $k$ .
  - 2: Output:  $\mathbf{x}$
  - 3: Initialize:  $\Lambda = \emptyset$
  - 4: **for**  $j = 1$  to  $k$  **do**
  - 5:    $\lambda_j = \arg \min_{l \notin \Lambda} \min_{\tilde{\mathbf{x}}} \|\mathbf{d} - \mathbf{F}(:, l \cup \Lambda)\tilde{\mathbf{x}}\|_\infty$
  - 6:    $\Lambda = \Lambda \cup \{\lambda_j\}$
  - 7: **end for**
  - 8:  $\mathbf{x} = \arg \min_{\mathbf{x}} \|\mathbf{d} - \mathbf{F}(:, \Lambda)\mathbf{x}\|_\infty$  {Calc coeffs.}
- 

The inputs to Algorithm 1 are the coil-sensitivity modulated inverse DFT matrix  $\mathbf{F}$ , the desired excitation pattern  $\mathbf{d}$ , and the desired sparsity level  $k$ . The output is a vector of pulse weights  $\mathbf{x}$ . The set  $\Lambda$  is a set of indices of the atoms in  $\mathbf{F}$  that we use to approximate  $\mathbf{d}$ . In each iteration, the algorithm finds the index  $l$  of an atom of  $\mathbf{F}$  that results in the minimum possible  $l_\infty$ -norm approximation (in Line 5). The index is then added to the set  $\Lambda$ , and the pulse weights  $\mathbf{x}$  are calculated by minimizing the  $l_\infty$ -norm in line 8 using the atoms specified by  $\Lambda$ .

Lines 5 and 8 in Algorithm 1 both involve solving the following unconstrained  $l_\infty$ -norms minimization problem, where  $\mathbf{A}$  are the columns of  $\mathbf{F}$  in line 5 of Algorithm 1.

$$\min_{\mathbf{x} \in \mathbb{C}^k} \|\mathbf{d} - \mathbf{A}\mathbf{x}\|_\infty \quad (6.3)$$

We propose an efficient algorithm to solve this unconstrained  $l_\infty$  norm minimiza-

tion problem, which is described in detail in section 6.3. However, algorithm 1 can still be slow in practice because of line 5. Almost *every* single column in  $\mathbf{F}$  has to be used for solving an unconstrained  $l_\infty$  norm minimization problem. A typical target excitation pattern is 64x64 pixels (e.g., slice selective excitation), which results in  $\mathbf{F}$  having 4096 columns, and it would be very time consuming to run our unconstrained  $l_\infty$  norm minimization 4096 times at each iteration of algorithm 2. It is therefore desirable to use fewer candidate atoms in this step. One way to do this is to try only the  $q$  atoms (e.g.  $q = 10$ ) that have the  $q$  largest dot products with the residual. This algorithm is shown below as Algorithm 2, and is called “greedy-like” because it is not strictly guaranteed to pick the best  $l_\infty$ -norm minimization vector at each iteration.

---

**Algorithm 2** Greedy-like Algorithm.

---

- 1: Input:  $\mathbf{F}$ ,  $\mathbf{d}$ ,  $k$ , and  $q$ .
  - 2: Output:  $\mathbf{x}$
  - 3: Initialize:  $a = 0$ ,  $\Lambda = \emptyset$
  - 4: **for**  $j = 1$  to  $k$  **do**
  - 5:    $\mathbf{r} = \mathbf{d} - \mathbf{a}$  {Update residual.}
  - 6:    $\mathbf{p} = \mathbf{F}'\mathbf{r}$  {Dot products.}
  - 7:    $S = \{ \text{set of (indices } \notin \Lambda) \text{ of max } q \text{ elements of } \mathbf{p} \}$
  - 8:    $\lambda_j = \arg \min_{l \in S} \min_{\tilde{\mathbf{x}}} \|\mathbf{d} - \mathbf{F}(:, l \cup \Lambda)\tilde{\mathbf{x}}\|_\infty$
  - 9:    $\Lambda = \Lambda \cup \{ \lambda_j \}$
  - 10:    $\mathbf{x} = \arg \min_{\mathbf{x}} \|\mathbf{d} - \mathbf{F}(:, \Lambda)\mathbf{x}\|_\infty$  {Calc coeffs.}
  - 11:    $\mathbf{a} = \mathbf{F}(:, \Lambda)\mathbf{x}$  {Update approximation.}
  - 12: **end for**
- 

In line 6 of Algorithm 2, the dot product of the residual with each atom in  $\mathbf{F}$  is computed. In line 7, indices of the  $q$  candidate atoms not in  $\Lambda$  that have the  $q$  biggest dot products are saved in the set  $S$ . Finally, in line 8, the algorithm picks the atom in  $S$  that when added to the set  $\Lambda$ , results in the minimum  $l_\infty$ -norm approximation to  $\mathbf{d}$ . The  $l_\infty$ -norms in lines 8 and 10 are again solved using the proposed unconstrained  $l_\infty$  norm minimization algorithm, to be described below.

Algorithm 2 uses the dot products,  $\mathbf{F}'\mathbf{r}$ , to eliminate the need for trying every atom with the relatively slow procedure of unconstrained  $l_\infty$  norm minimization algorithm. This shortcut does not guarantee that the  $q$  candidate atoms with largest dot product will generate the lowest  $l_\infty$ -norm out of all possible atoms. Thus, the choice of  $q$  presents a tradeoff between algorithm speed and “greediness.”

### 6.3 Solving the Unconstrained $L_\infty$ Minimization Problem

This section describes our algorithm to solve (6.3). We propose to use variable-splitting to transform this unconstrained problem into the following equivalent constrained problem:

$$\min_{\mathbf{x}, \mathbf{v}} \|\mathbf{v}\|_\infty, \text{ such that } \mathbf{v} = \mathbf{A}\mathbf{x} - \mathbf{d}. \quad (6.4)$$

Then we form the augmented Lagrangian function:

$$L(\mathbf{x}, \mathbf{v}, \mathbf{y}) = \|\mathbf{v}\|_\infty + \frac{\mu}{2} \|\mathbf{A}\mathbf{x} - \mathbf{v} - \mathbf{d} + \mathbf{y}\|_2^2 \quad (6.5)$$

where  $\mathbf{y}$  is the scaled dual variable and  $\mu$  is a penalty parameter. We then solve the  $\min_{\mathbf{x}, \mathbf{v}, \mathbf{y}} L(\mathbf{x}, \mathbf{v}, \mathbf{y})$  problem using the following alternating direction method of multipliers (ADMM) update [9]

$$\mathbf{x}^{k+1} = \underset{\mathbf{x}}{\operatorname{argmin}} L(\mathbf{x}, \mathbf{v}^k, \mathbf{y}^k) \quad (6.6)$$

$$\mathbf{v}^{k+1} = \underset{\mathbf{v}}{\operatorname{argmin}} L(\mathbf{x}^{k+1}, \mathbf{v}, \mathbf{y}^k) \quad (6.7)$$

$$\mathbf{y}^{k+1} = \mathbf{y}^k + (\mathbf{A}\mathbf{x}^{k+1} - \mathbf{v}^{k+1} - \mathbf{d}) \quad (6.8)$$

The update of  $\mathbf{x}$  is easy, which is  $\mathbf{x}^{k+1} = \mathbf{A}^+(\mathbf{v}^k + \mathbf{d} + \mathbf{y}^k)$ , where  $\mathbf{A}^+$  is the pseudo-inverse of  $\mathbf{A}$ . The update of  $\mathbf{y}$  is trivial, which consists of adding the primal error to the current  $\mathbf{y}$ . To solve (6.7) and update  $\mathbf{v}$ , we propose the following method. The derivation is similar to the approach for deriving the soft-thresholding method.

Let  $\mathbf{c} = \mathbf{A}\mathbf{x}^k - \mathbf{d} - \mathbf{y}^k$ , and equation (6.7) now becomes:

$$\min_{\mathbf{v}} (\|\mathbf{v}\|_\infty + \frac{\mu}{2} \|\mathbf{v} - \mathbf{c}\|_2^2) \quad (6.9)$$

To solve the problem of this form, we divide it to two steps: first consider minimizing the function  $h(\mathbf{v}) = u + \frac{\mu}{2} \|\mathbf{v} - \mathbf{c}\|_2^2$  over complex  $\mathbf{v}$  that satisfies  $\|\mathbf{v}\|_\infty \leq u$  for fixed  $u$ ; then minimize this minimum value, which is a function of  $u$ , over  $u$ . In the first step, the objective  $h(\mathbf{v})$  is obviously separable in  $\mathbf{v} = [v_1, \dots, v_M]^T$ , so each  $v_i$  can be chosen independently. Consider the corresponding element of  $\mathbf{c} = [c_1, \dots, c_M]^T$ : if  $|c_i| \leq u$ , then setting  $v_i = c_i$  obviously minimizes  $|v_i - c_i|^2$  while satisfying  $|v_i| \leq u$ . Otherwise, the closest  $v_i$  to  $c_i$  lies on the boundary  $|v_i| = u$ , and at the phase closest

to  $c_i$ :  $v_i = c_i \frac{u}{|c_i|}$ . Putting these together yields the thresholding-like solution

$$\hat{v}_i(u) = c_i \frac{\min\{u, |c_i|\}}{|c_i|}. \quad (6.10)$$

Then, if we plug our optimal  $v_i$ 's into  $h(\mathbf{v})$ , we get

$$h(\hat{\mathbf{v}}(u)) = u + \frac{\mu}{2} \sum_{i=1}^M \max\{|c_i| - u, 0\}^2 \quad (6.11)$$

Let  $\phi_i(u) = \frac{1}{2} \max\{|c_i| - u, 0\}^2$ ; this function is convex over all  $u$  and strictly convex when  $u < |c_i|$ . Then, re-parameterizing  $h(\cdot)$  in terms of distance  $u$  yields

$$h(u) = u + \mu \sum_{i=1}^M \phi_i(u). \quad (6.12)$$

Since the sum of convex functions is strictly convex as long as one is strictly convex, we see that  $h(u)$  is strictly convex for  $u < \|\mathbf{c}\|_\infty$ , which is the maximum distance we would consider (since its boundary contains  $\mathbf{v} = \mathbf{c}$ ). The derivative of  $\phi_i(u)$  is  $\min\{u - |c_i|, 0\}$ , so the derivative

$$\dot{h}(u) = 1 + \mu \sum_{i=1}^M \min\{u - |c_i|, 0\}. \quad (6.13)$$

The extremum  $u^* \in (0, \|\mathbf{c}\|_\infty)$  must satisfy

$$\frac{1}{\mu} = \sum_{i=1}^M \max\{|c_i| - u^*, 0\} = \sum_{i:|c_i|>u^*} (|c_i| - u^*). \quad (6.14)$$

Finding this extremum is easy: denote  $\tilde{\mathbf{c}} = [\tilde{c}_1, \dots, \tilde{c}_M]^T$  the vector  $\mathbf{c}$  sorted by magnitude largest to smallest, and find the largest value of  $I$  such that  $\sum_{i=1}^I (|\tilde{c}_i| - |\tilde{c}_I|) \leq 1/\mu$ . Then,  $u^*$  lies between  $|\tilde{c}_I|$  and  $|\tilde{c}_{I+1}|$  (or between  $|c_M|$  and zero, for  $I = M$ ); in particular,  $u^* = |\tilde{c}_I| - (1/\mu - \sum_{i=1}^I (|\tilde{c}_i| - |\tilde{c}_I|))/I$ . It is possible if  $I = M$  that  $u^*$  becomes less than zero for  $\mu$  is small enough, in which case the optimal  $u^* = 0$ . Plugging in  $u^*$  into Eq. (6.10) yields the non-iterative solution  $\mathbf{v}$  for the sub-problem (6.9) which is used in the update in (6.7).

## 6.4 Simulation Results

The simulation contains two parts. First, we demonstrate that our algorithm can solve the unconstrained  $l_\infty$  norm minimization problem shown in equation (6.3). Second, we simulate our algorithms for the overall  $l_\infty$  norm sparse approximation problem defined in equation (6.2). In the first simulation, we first create a 2D DFT matrix with size  $n$  by  $n$  and modulate it by the sensitivity map. Then we randomly pick  $m$  ( $=n/2$ ) columns from this matrix to form matrix  $\mathbf{A}$  in (6.3). We randomly create a vector  $b$  with length  $n$ , and feed them into our code and plot  $\|Ax - b\|_\infty$  versus number of iterations, The simulation result is shown in Fig. 6.2. The coefficient  $x$  is initialized by obtaining the least square solution to (6.3), and  $\mu$  is set to 2 in (6.5) for ADMM. As we can see, the cost converges after about 40 iterations. The decrease of the cost function is not monotonic, which is reasonable since the ADMM method does not guarantee monotonic convergence. To test whether it converges to the optimal solution, we used the output of our algorithm as an input to the MATLAB `fminsearch` function and observed no improvement in the cost function. This suggests that our algorithm finds a local minimum, which should be the global minimum since the cost function is convex.

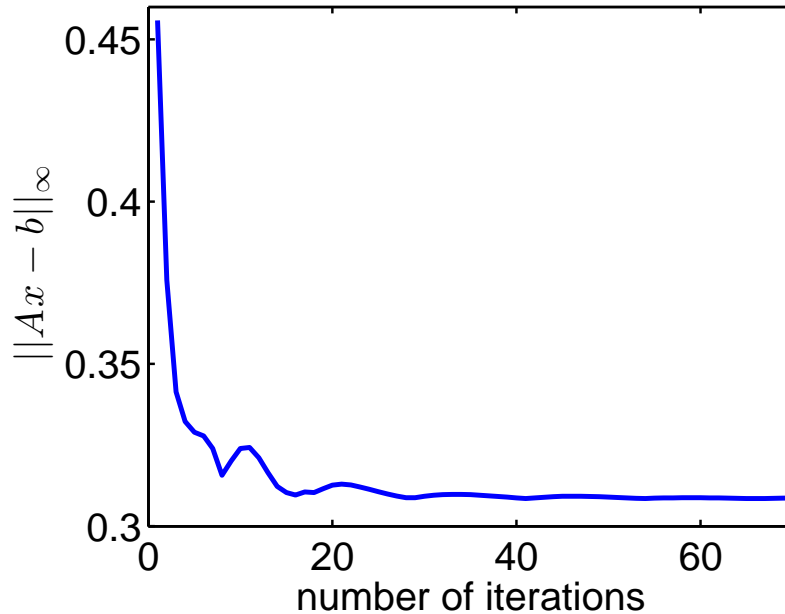
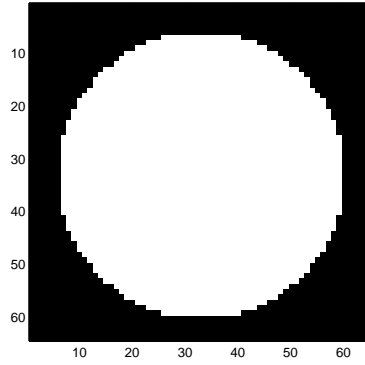
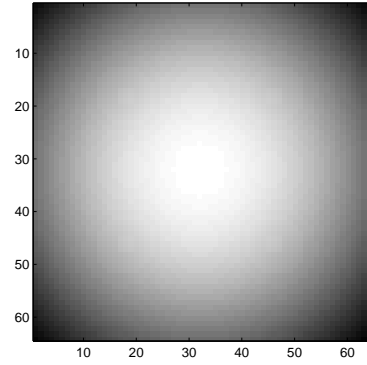


Figure 6.2: test of unconstrained  $l_\infty$  norm minimization

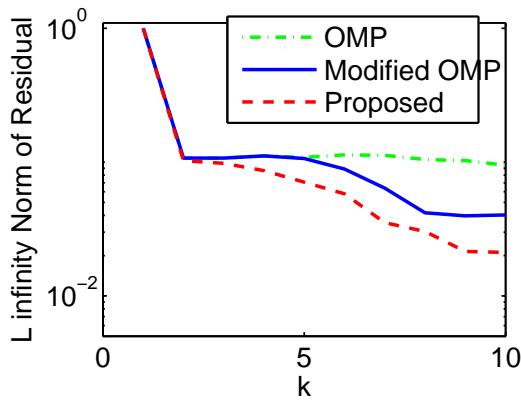
In the second simulation, we investigated our proposed method in the context of RF shimming. RF shimming is an important application of spoke RF pulse design, especially in high field or parallel excitation, with the goal of uniformly exciting a region with non-uniform transmit sensitivities. This problem is typically modelled as a



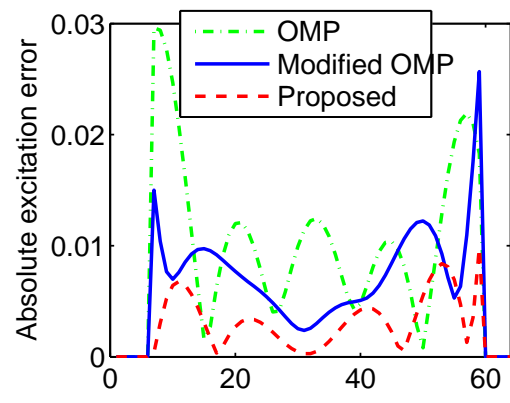
(a) Desired pattern



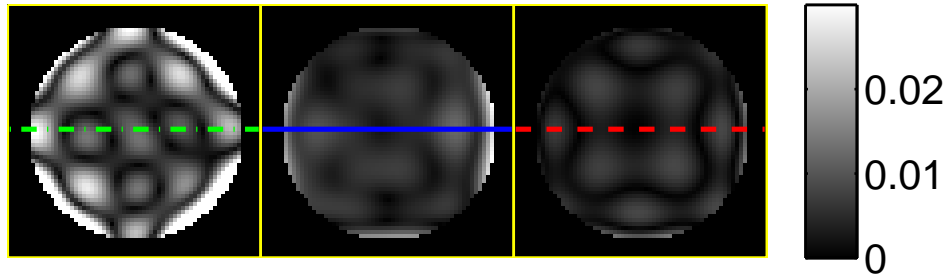
(b) Sensitivity map



(c)  $l_\infty$  norm of residual



(d) cross line in image



(e) Difference between excitation patterns and desired pattern (left: OMP; middle: modified OMP; right: proposed)

Figure 6.3: Comparing OMP and proposed algorithm

sparse approximation problem as shown in (6.1). OMP is one conventional algorithm to solve problem (6.1) and there are many modifications to OMP to improve its performance fast-kz pulse design [53, 109, 10, 111, 24]. In our simulation, we compared our algorithm to a modified OMP with exactly the same structure as our proposed Algorithm 2 except that the  $l_\infty$  norm minimization of lines 8 and 10 are replaced with  $l_2$  norm minimization. We choose this algorithm for comparison for two reasons: first, keeping the structure the same provides a common ground for the choice of the norm between  $l_\infty$  and  $l_2$  norm; second, there are many variations of OMP, and it is not practical to compare all of them. As a reference, we also include the classical OMP in our simulation. In the simulation, the desired excitation pattern is a uniform circle shown in Fig.6.3-a, which is then reshaped to a column vector  $\mathbf{d}$  (4096 by 1). The region outside the circle is not in our region-of-interest. We create the system matrix  $\mathbf{F}$  by multiplying a 2D DFT matrix (4096 by 4096) with the nonuniform coil sensitivity map shown in Fig.6.3-b. The comparison of  $l_\infty$  norm versus number of phase encoding locations ( $k$ ) is shown in Fig. 6.3-c for OMP, modified OMP and the proposed Algorithm 2. We set our simulation range of  $k$  to be 1 to 10 since we usually want a small number of spokes in practice to reduce overall pulse length. We can see in Fig.6.3-c that OMP fails to significantly decrease the  $l_\infty$  norm of the residual after  $k = 2$ , while modified OMP can decrease  $l_\infty$  norm further, but still has higher (about twice)  $l_\infty$  norm compared to our proposed algorithm. The difference between desired and true excitation patterns is shown in Fig.6.3-e. It demonstrates that the excitation pattern of our proposed algorithm is much closer to the desired pattern than the OMP algorithm and modified OMP algorithm. We also plot the cross section line of excitation error for all three methods in Fig. 6.3-d, and the proposed method has the smallest ripples.

## 6.5 B0 inhomogeneity and parallel excitation

### 6.5.1 Include B0 Map in the Model

Like most of current greedy fast-kz pulse design algorithm, the proposed method above doesn't consider B0 map in the design. The main obstacle to consider the B0 map in the greedy algorithm is we don't know the corresponding time for each columns in the dictionary matrix since we don't know whether those phase encoding locations will be visited or not, and when they will be visited. To solve this problem, Yoon [109] proposed an algorithm that visits the selected phase encoding locations in a reverse order, and updates the target excitation patten after each selection. In other words,

we first select the last phase encoding location (in time) using the target excitation pattern for the whole RF pulse, and then back calculate the excitation pattern before the last subpulse based on the final pattern, the duration of this subpulse and the B0 map, and then use this excitation pattern to get the second-to-last subpulse. I adapt the same idea into our above algorithm.

### 6.5.2 Extend to Parallel Excitation

In parallel excitation, the system matrix  $\mathbf{A}$  need to be modified to include all the coils as following:

$$\mathbf{A} = [\mathbf{S}_1\mathbf{F}, \mathbf{S}_2\mathbf{F}, \dots, \mathbf{S}_L\mathbf{F}] \quad (6.15)$$

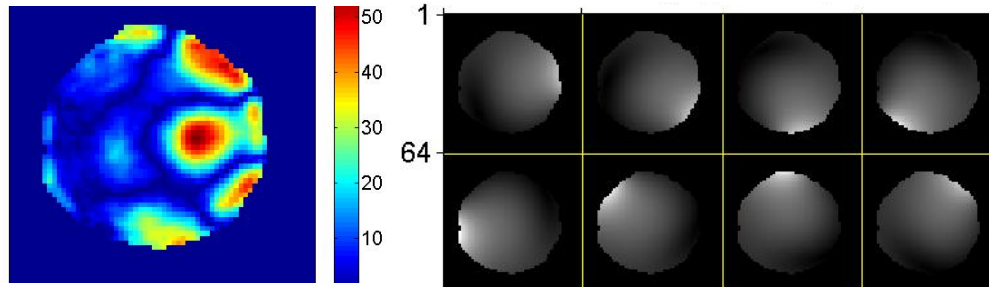
where  $L$  is the total number of coils and  $\mathbf{S}_l$  is sensitivity of the  $l^{th}$  coil. Each time we select the phase encoding location, we have to consider the cumulative inner product defined as the following to preselect candidates  $l$  before calculate  $\|\mathbf{d} - \mathbf{A}(:, l \cup \Lambda)\mathbf{x}\|_\infty$ . When calculating  $\|\mathbf{d} - \mathbf{A}_\Lambda\mathbf{x}\|_\infty$ , we have to redefine  $\mathbf{A}_\Lambda$  as the following:

$$\mathbf{A}_\Lambda = [\mathbf{S}_1\mathbf{F}(:, \Lambda), \mathbf{S}_2\mathbf{F}(:, \Lambda), \dots, \mathbf{S}_L\mathbf{F}(:, \Lambda)].$$

Then the  $\mathbf{x}$  that minimized  $\|\mathbf{d} - \mathbf{A}_\Lambda\mathbf{x}\|_\infty$  will be the coefficients of  $L$  coils corresponding to the phase encoding locations in  $\Lambda$ . We run our greedy algorithm for  $k$  iterations and we will obtain  $k$  phase encoding locations with  $kL$  non-zero coefficients in  $\mathbf{x}$ .

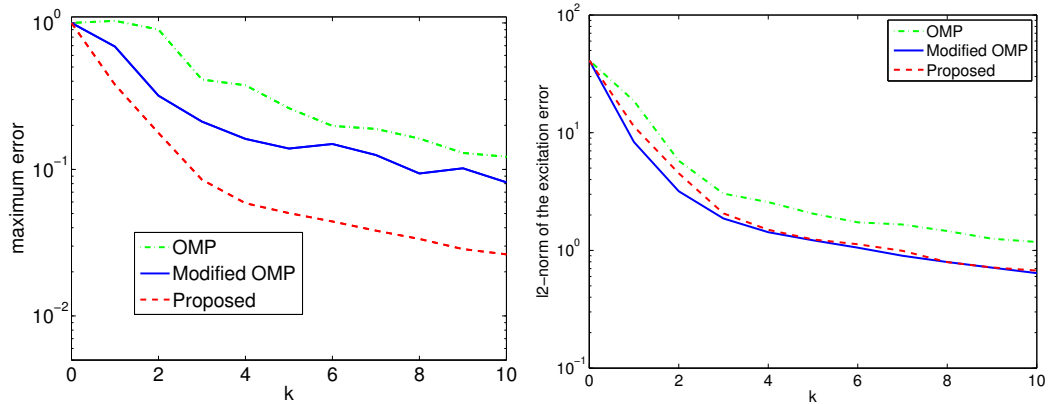
### 6.5.3 Simulation Results Considering B0 Map and Parallel Excitation

Figure 6.4 shows the simulation results for OMP, modified OMP and the proposed method with measured B0 map (a) and simulated transmit coil sensitivity map (b). In all three methods, we treat the B0 map and parallel excitation as suggested above. The proposed method leads to less maximum excitation error for all number of subpulses. Although we do not directly target the l2 norm of the excitation error in the minimax formulation, we find that it actually achieve similar error in l2 norm compared with the modified OMP approach. This is probably because the sparse approximation is a non-convex problem and both methods are greedy algorithms, so the l2 norm based OMP is not guaranteed to have less l2 norm than the minimax method. Using 3 subpulses, the proposed method reduces the maximum excitation error by more than half.

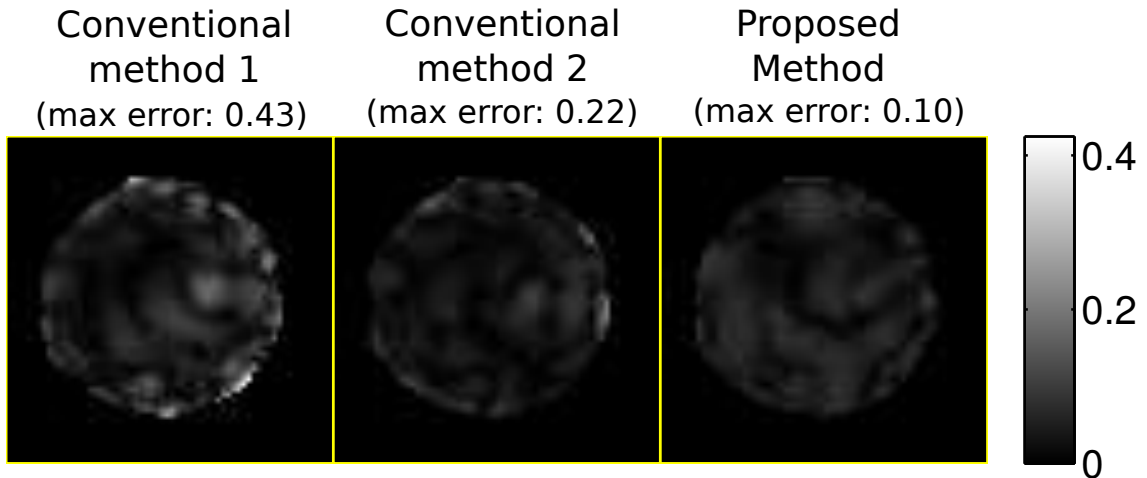


(a) B0 map

(b) Coil sensitivity map



(c)  $l_\infty$  norm of residual VS number of sub-pulses. (d)  $l_2$  norm of residual VS number of sub-pulses.



(e) Residual after 3 subpulses ( left: OMP; middle: modified OMP; right: proposed )

Figure 6.4: Simulation results with B0 map and parallel excitation. The proposed method leads to less maximum excitation error for all number of subpulses. The  $l_2$  norm of excitation error is similar between the minimax method and modified OMP approach. Using 3 subpulses, the proposed method reduces the maximum excitation error by more than half.

## 6.6 Minimax for general pulse design

In previous sections, we proposed a greedy minimax algorithm for fast-kz (spoke) pulse design. In this section, we investigate the minimax algorithm for the design of general RF pulse.

### 6.6.1 Formulation

The conventional small-tip RF pulse design is to solve the following problem [103].

$$\min_{\mathbf{b} \in \mathbb{C}^{N_t}} \|\mathbf{d} - \mathbf{A}\mathbf{b}\|_2 + R(\mathbf{b}) \quad (6.16)$$

where  $\mathbf{A}$  is the small-tip system matrix,  $\mathbf{b}$  is the discretized RF pulse.  $R(\mathbf{b})$  is a regularization term to limit the RF power. As mentioned in previous chapters, we may want to limit the maximize error instead of the L2 norm in some applications, by solving the following problem:

$$\min_{\mathbf{b} \in \mathbb{C}^{N_t}} \|\mathbf{d} - \mathbf{A}\mathbf{b}\|_\infty + R(\mathbf{b}) \quad (6.17)$$

This is similar to Equation 6.3, but directly solving the actual RF pulse instead of the weightings of subpulses in the fast-kz pulse. Therefore, the problem size of this optimization is larger than the optimization in 6.3, and it is unclear whether our proposed ADMM-based minimax algorithm would still be fast enough for online pulse design.

Another difference between Equation 6.17 and Equation 6.3 is the additional regularization term in 6.17. In the conventional pulse design, we typical choose simple  $\beta\|\mathbf{b}\|_2^2$  as the regularizer. Here for minimax pulse design, we use the same regularizer. We will demonstrate the modifications to our ADMM updates 6.66.76.8 and the simulation result using this regularizer.

### 6.6.2 Modifications to our ADMM updates after including the regularizer

If we choose  $\beta\|\mathbf{b}\|_2^2$  as the regularizer, then the problem becomes:

$$\min_{\mathbf{b} \in \mathbb{C}^{N_t}} \|\mathbf{d} - \mathbf{A}\mathbf{b}\|_\infty + \beta\|\mathbf{b}\|_2^2 \quad (6.18)$$

Similar to before, we use variable-splitting to transform this unconstrained prob-

lem into the following equivalent constrained problem:

$$\min_{\mathbf{b}, \mathbf{v}} \|\mathbf{v}\|_{\infty} + \beta \|\mathbf{b}\|_2^2, \text{ such that } \mathbf{v} = \mathbf{A}\mathbf{b} - \mathbf{d}. \quad (6.19)$$

We form the augmented Lagrangian function:

$$L_R(\mathbf{b}, \mathbf{v}, \mathbf{y}) = \|\mathbf{v}\|_{\infty} + \beta \|\mathbf{b}\|_2^2 + \frac{\mu}{2} \|\mathbf{A}\mathbf{b} - \mathbf{v} - \mathbf{d} + \mathbf{y}\|_2^2. \quad (6.20)$$

Then we alternative update  $\mathbf{b}$ ,  $\mathbf{v}$ , and  $\mathbf{y}$ . The updates of  $\mathbf{v}$  and  $\mathbf{y}$  are the same as before. To update  $\mathbf{b}$ , we have the following close form solution:

$$\mathbf{b} = (\mathbf{A}'\mathbf{A} + \frac{2\beta}{\mu}\mathbf{I}_d)^{-1}\mathbf{A}'(\mathbf{v} + \mathbf{d} - \mathbf{y}) \quad (6.21)$$

With varying regularization parameter  $\mu$  as we used in previous sections, the least square problem to update  $\mathbf{b}$  would also change over iterations. Therefore, we can not pre-compute  $(\mathbf{A}'\mathbf{A} + \frac{2\beta}{\mu}\mathbf{I}_d)^{-1}\mathbf{A}'$ , and just multiply it to  $\mathbf{v} + \mathbf{d} - \mathbf{y}$  to get the result. Directly solving Equation 6.21 or using MATLAB backslash in each iteration can be relatively slow. To solve it efficiently, we pre-compute the SVD of  $\mathbf{A} = \mathbf{U}\mathbf{\Sigma}\mathbf{V}$ , and update  $\mathbf{b}$  in each iteration by back calculating the following formula:

$$\mathbf{b} = \mathbf{V}(\mathbf{\Sigma}^2 + \frac{2\beta}{\mu}\mathbf{I}_d)^{-1}\mathbf{\Sigma}\mathbf{U}'(\mathbf{v} + \mathbf{d} - \mathbf{y}) \quad (6.22)$$

### 6.6.3 Simulation results

We simulated a pre-phasing problem, where we want to achieve the following excitation pattern:  $\mathbf{d}(\Delta\omega(\mathbf{r})) = e^{i\Delta\omega(\mathbf{r})T_{\text{free}}} \sin \alpha$ , where  $\alpha$  is the flip angle (uniform for all spins),  $\Delta\omega(\mathbf{r})$  is the B0 field map, and  $T_{\text{free}}$  is the free precession time. The goal is to achieve refocusing  $T_{\text{free}}$  after the excitation. Prephasing pulses may be used to compensate for susceptibility (T2\*) signal loss, and are needed in the “small-tip fast recovery” steady-state imaging sequence being developed by our group [104, 65, 93]. We designed a prephasing pulse with 10 degree flip angle, 2.5 ms  $T_{\text{free}}$ , and measured B0 field map from a human brain. We used a 4.7 ms SPINS [55] k-space trajectory in the pulse design. We simulated with 64x64x8 matrix size and 24x24x4 cm<sup>3</sup> FOV.

We started from a  $\mu = 0.5$  in our ADMM algorithm, and updated it over iterations following the rule in [9]. The plot of  $\mu$  over iterations is shown in 6.6, where  $\mu$  kept unchanged after approximately 70 iterations.

The convergence plot of our ADMM-based minimax algorithm is shown in Fig-

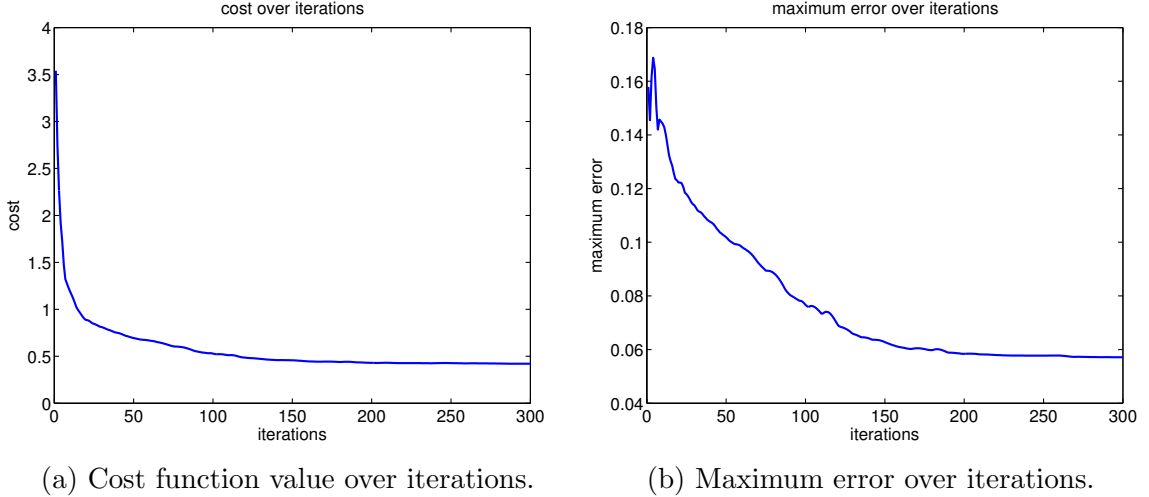


Figure 6.5: Cost function value and maximum error over iterations using our ADMM-based minimax algorithm. The cost function is monotonic decreased, but the maximum error has small oscillations. The cost function converges faster than the maximum error.

ure 6.5. The cost function almost converged after 100 iterations. The maximum error converged slower, reached to its minimum after 150 iterations. The total computation time (300 iterations) was 33 sec in our setting.

Figure 6.7 shows the simulated excitation error using the conventional  $l_2$ -norm based design and the proposed minimax algorithm (after 150 iterations). Using our minimax design, the excitation error does not have a high error spot as shown in the conventional design result. The maximum excitation error using the minimax design is 0.34 of the maximum error in the conventional design. We used  $\beta = 0.01$  and  $\beta = 8$  for the minimax design (Equation 6.18) and conventional design (Equation 6.17) respectively, resulting in approximately the same RF power (the RF power ( $\|\mathbf{b}\|_2^2$ ) using the minimax design is 0.92 of the conventional design).

#### 6.6.4 Magnitude minimax algorithm

The phase of the target excitation pattern is not important in many MRI applications, and therefore pulse design methods based on the following magnitude least square [82, 35] problem were proposed:

$$\min_{\mathbf{b} \in \mathbb{C}^{N_t}} \left| \|\mathbf{d}\| - \|\mathbf{A}\mathbf{b}\| \right|_2 + R(\mathbf{b}) \quad (6.23)$$

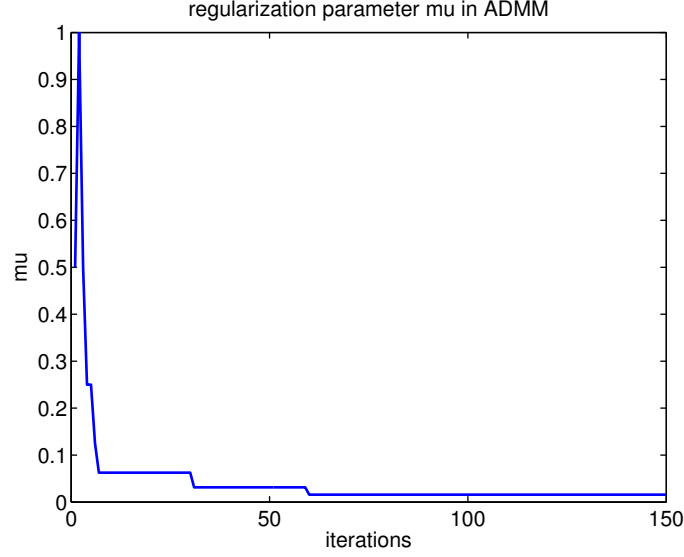


Figure 6.6: Regularization parameter  $\mu$  versus iterations in ADMM. It became constant after approximate 70 iterations.

The variable exchange method (also called Gerchberg-Saxton) [41] is used widely in solving the above problem, and its convergence can be shown using the optimization transfer principle (majorize-minimization).

Here we proposed to solve the following magnitude minimax problem for pulse design:

$$\min_{\mathbf{b} \in \mathbb{C}^{N_t}} \|\mathbf{d} - |\mathbf{A}\mathbf{b}|\|_{\infty} + R(\mathbf{b}). \quad (6.24)$$

We derived an algorithm for solving problem 6.24 using the majorize-minimization method as follows.

$$\begin{aligned} & \min_{\mathbf{b}} \|\mathbf{A}\mathbf{b} - \mathbf{d}\|_{\infty} \\ \Leftrightarrow & \min_{\mathbf{b} \in \mathbb{C}^{N_t}} \max_i |\mathbf{A}_i \mathbf{b} - d_i| \\ \Leftrightarrow & \min_{\mathbf{b} \in \mathbb{C}^{N_t}} \max_i \min_{z_i \in \mathbb{C}, |z_i|=1} |\mathbf{A}_i \mathbf{b} - d_i z_i| \end{aligned}$$

,where  $\mathbf{A}_i$  is the  $i^{\text{th}}$  row vector of  $\mathbf{A}$ . Define  $\tilde{z}_i^{(n)} = \operatorname{argmin}_{z_i \in \mathbb{C}, |z_i|=1} |\mathbf{A}_i \mathbf{b}^{(n)} - d_i z_i|$ , then since

$$\max_i \min_{z_i \in \mathbb{C}, |z_i|=1} |\mathbf{A}_i \mathbf{b}^{(n)} - d_i z_i| = \max_i |\mathbf{A}_i \mathbf{b}^{(n)} - d_i \tilde{z}_i^{(n)}|$$

and

$$\max_i \min_{z_i \in \mathbb{C}, |z_i|=1} |\mathbf{A}_i \mathbf{b} - d_i z_i| \leq \max_i |\mathbf{A}_i \mathbf{b} - d_i \tilde{z}_i^{(n)}| \quad \forall \mathbf{b},$$

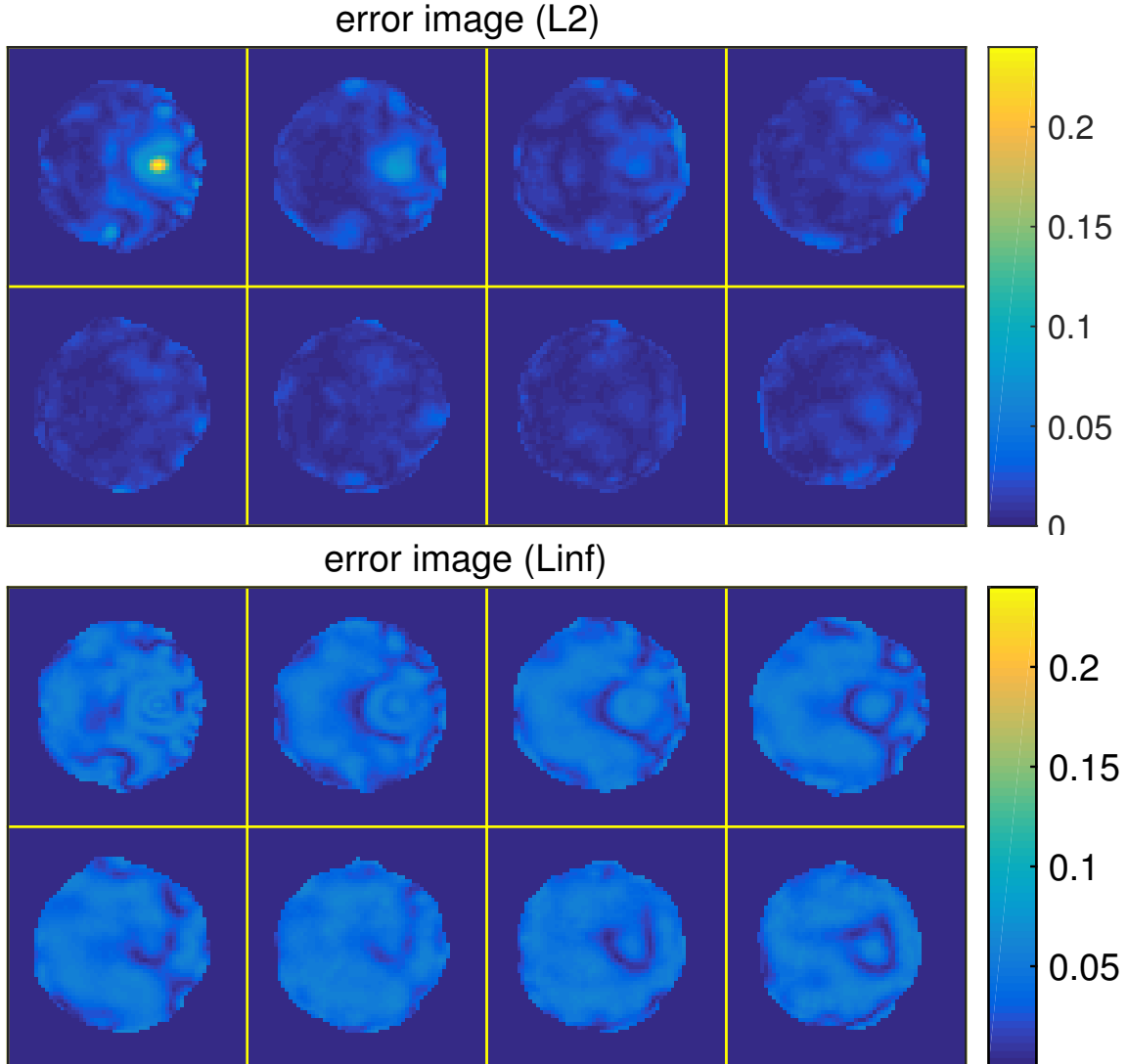


Figure 6.7: Simulated excitation error in the pre-phasing problem using the conventional  $l_2$ -norm based design and our minimax pulse design. The high error spot in the conventional design result is removed by our minimax optimization. The maximum excitation error using minimax pulse design is 0.33 of the error using the conventional design, at the expense of root mean square error (RMSE). The RMSEs for the conventional design and minimax design are 0.02 and 0.04, respectively.

$\max_i |\mathbf{A}_i \mathbf{b} - d_i \tilde{z}_i^{(n)}|$  is a surrogate function of  $\max_i \min_{z_i \in \mathbb{C}, |z_i|=1} |\mathbf{A}_i \mathbf{b} - d_i z_i|$ . Therefore  $\max_i |\mathbf{A}_i \mathbf{b} - d_i \tilde{z}_i^{(n)}| + R(\mathbf{b})$  is also a surrogate function of  $\max_i \min_{z_i \in \mathbb{C}, |z_i|=1} |\mathbf{A}_i \mathbf{b} - d_i z_i| + R(\mathbf{b})$ . Then the following alternating update is a majorize-minimization algorithm and guaranteed to converge.

$$\begin{aligned} \tilde{z}_i^{(n)} &= \operatorname{argmin}_{z_i \in \mathbb{C}, |z_i|=1} |\mathbf{A}_i \mathbf{b}^{(n)} - d_i z_i| = e^{i \angle \mathbf{A}_i \mathbf{b}^{(n)}} \\ \mathbf{b}^{(n+1)} &= \operatorname{argmin}_{\mathbf{b} \in \mathbb{C}^{N_t}} \max_i |\mathbf{A}_i \mathbf{b} - d_i \tilde{z}_i^{(n)}| + R(\mathbf{b}) = \operatorname{argmin}_{\mathbf{b} \in \mathbb{C}^{N_t}} \|\mathbf{A} \mathbf{b} - \mathbf{d}^{(n)}\|_\infty + R(\mathbf{b}) \end{aligned}$$

To solve the first update, we just assign the phase of  $\mathbf{A}_i \mathbf{b}$  to the phase of  $z_i$ . To update  $\mathbf{b}^{(n+1)}$ , we use the algorithm we proposed in previous sections for solving problem 6.17.

## 6.7 Discussion

The joint design of phase encoding locations and RF weighing in the fast-kz trajectory is a non-convex problem and our greedy approaches are not guaranteed to find the global minimum. Therefore, it is possible to obtain lower or similar  $l_2$ -norm excitation error using the minimax formulation compared to the  $l_2$ -norm formulation, as we demonstrated in Figure 6.4. On the other hand, it is also possible to obtain lower maximum error using the  $l_2$  based approach in the fast-kz pulse design. However, if we use the same method in finding the phase encoding locations, but obtain the RF weights using minimax formulation, then the minimax method should be able to always achieve lower or equal maximum error.

The lower maximum error of the proposed method comes at a possible expense of the average error, as we observed in Figure 6.7. In practice, we may want to use some adaptive scanning strategies. For example, we may want to use the minimax designed pulse to do the first scan and select some ROI, and then use a weighted minimax or weighted conventional design with larger weight in the ROI to reduce the error in that region, so we can have a better image for the ROI.

In the minimax pulse design, a weighting matrix or a mask can be incorporated to our formulation and algorithm easily by pre-multiplying a weighting matrix to the system matrix and the target excitation pattern.

## 6.8 Conclusion

In this chapter, we proposed a novel method to model the spoke RF pulse design problem in MRI: instead of modelling it as a sparse approximation problem with a  $l_2$  norm cost function, we use  $l_\infty$  in the cost function to limit the maximum error. To solve this new problem, we proposed a greedy algorithm. The core part of that greedy algorithm is an unconstrained  $l_\infty$  norm minimization in the complex domain (6.3), and that is solved using variable-splitting and ADMM. A non-iterative solution is derived to solve the most difficult part in the ADMM update (6.9) efficiently. To our knowledge, this is also novel. Our simulation results show that our proposed model and algorithm yields a much smaller maximum error than the classical OMP and the modified OMP (i.e., the  $l_2$  norm counterpart of proposed algorithm) for the spoke RF pulse design problem. We extended our proposed method by including the B0 inhomogeneity effect and considering parallel excitation. We also extended our minimax algorithm to more general pulse design with arbitrary k-space trajectory and a Tikhonov RF power regularization term. For applications where only the magnitude of excitation pattern is of interest, we formulated a “magnitude minimax” problem and derived an algorithm based on the majorize-minimization principle.

## CHAPTER VII

# Joint Design of Excitation k-space Trajectory and RF pulse for Small-tip 3D Tailored Excitation in MRI

### 7.1 Introduction

<sup>1</sup>Spatially tailored RF excitation has a range of applications in MRI, including B1 shimming [15, 76, 77, 111, 11, 55], reduced FOV excitation [74, 116, 14, 81, 54, 52], susceptibility artifact correction [104, 65, 93, 97], and fat suppression [113, 114]. The task of designing time-varying RF and gradient waveforms for a desired target excitation pattern poses a non-linear, non-convex, constrained optimization problem with relatively large problem size that is difficult to solve directly. In conventional tailored excitation pulse design, the k-space (gradient) trajectory is pre-defined, allowing the RF waveform to be obtained using linear least-squares optimization [103]. However, for a given pulse duration, using a pre-determined k-space trajectory leads to suboptimal excitation accuracy.

Several methods have been proposed for jointly designing the k-space trajectory and RF pulse, achieving improved tailored excitation accuracy compared to pre-defined gradient approaches. These methods can be classified into two categories: sparse approximation and parametrization approaches. In the sparse approximation approach, a complete dictionary  $\mathbf{A}$  based on the small-tip-angle approximation [72] is defined, and the joint pulse design task is reduced to selecting a few k-space phase encoding locations (i.e., columns in  $\mathbf{A}$ , typically less than 20) by either thresholded Fourier transform or greedy algorithms. The output of those methods are discrete k-space trajectories like fast-kz/spoke pulses (discrete in kx-ky plane) [111, 53, 109,

---

<sup>1</sup>This chapter is based on the publications [88]

10, 96], or kT-points (discrete in 3D) [11]. Grissom [24] recently combined sparse approximation with local optimization in fast-kz pulse design to improve the result and incorporate B0 inhomogeneity information. However, complex target excitation patterns require more than a few phase encoding locations, so sparse approximation approaches are typically used only for B1 shimming, and they would be difficult to use for other applications needing non-smooth target excitation patterns (especially in 3D).

In parametrization approaches to RF pulse design, the k-space trajectory is approximated by a linear combination of basis functions, and the joint pulse design task is then to optimize the basis function coefficients as well as the RF waveform. Hardy expressed the k-space trajectory and RF pulse as Fourier series and then optimized the coefficients using simulated annealing [29] for 2D tailored excitation, but it is computationally too expensive for real-time tailored RF pulse design. Levin approximated the spiral trajectory by concentric rings and then optimized the radius of those rings [50]. Yip proposed a general approach for selecting basis coefficients, and applied it to the optimization of an EPI trajectory [105]. Shao optimized the extent of the stack-of-spiral trajectory and the fast-kz trajectory [83]. Davids optimized the extent of a 3D cross trajectory in  $\mathbf{k}_x$ ,  $\mathbf{k}_y$ ,  $\mathbf{k}_z$  for its different shells/segments [14]. By parametrization, those methods reduced the problem dimension, and the computation complexity. However, these methods (except [29, 14]) did not explicitly consider the maximum gradient and slew rate constraint in the optimization, instead avoiding this constrained minimization problem by limiting solutions to a certain type of trajectory (e.g., EPI, spiral, stack-of-spiral). Hardy and Davids [29, 14] considered the constraint, but their methods require large computation time, making it impractical for online pulse design problems. Also, all the parametrization methods do not choose the trajectory type based on the information of the excitation pattern.

In this work, we present a general approach for jointly optimizing the k-space trajectory and RF waveforms in 3D tailored excitation. Our method starts with some initial k-space trajectory (e.g., such as those obtained with any of the approaches described above), parametrizes the trajectory using 2<sup>nd</sup>-order B-spline functions, and optimizes the basis coefficients and RF waveform using constrained optimization. The peak gradient and slew rate are directly included in the optimization, and the trajectory is not limited to a pre-defined type such as concentric rings or EPI. We demonstrate our approach using four different k-space initializations: stack-of-spirals(SoS), spiral nonselective (SPINS) [55], kT-points, and a new proposed initialization which we refer to as “extended kT-points”. We demonstrate our method in two differ-

ent applications: 3D reduced FOV excitation, and spin pre-phasing. In all cases, our optimized k-space trajectories achieve improved excitation accuracy compared to the initial trajectory, and our proposed extended KT-points method provides good initialization.

## 7.2 Theory

### 7.2.1 Problem Formulation

In joint design of k-space trajectory and RF pulse, we want to solve the following optimization problem [105]:

$$\begin{aligned}
& \min_{\mathbf{b} \in \mathbb{C}^{N_t}, \mathbf{k}_x, \mathbf{k}_y, \mathbf{k}_z \in \mathbb{R}^{N_t}} \|\mathbf{S}\mathbf{A}(\mathbf{k}_x, \mathbf{k}_y, \mathbf{k}_z)\mathbf{b} - \mathbf{d}\|_2^2 + R(\mathbf{b}) \\
s.t. \quad & \|\mathbf{D}_1\mathbf{k}_x\|_\infty \leq \gamma \Delta t g_{max}, \quad \|\mathbf{D}_2\mathbf{k}_x\|_\infty \leq \gamma \Delta t^2 s_{max}, \\
& \|\mathbf{D}_1\mathbf{k}_y\|_\infty \leq \gamma \Delta t g_{max}, \quad \|\mathbf{D}_2\mathbf{k}_y\|_\infty \leq \gamma \Delta t^2 s_{max}, \\
& \|\mathbf{D}_1\mathbf{k}_z\|_\infty \leq \gamma \Delta t g_{max}, \quad \|\mathbf{D}_2\mathbf{k}_z\|_\infty \leq \gamma \Delta t^2 s_{max}, \\
& \mathbf{k}_x(N_t) = 0, \mathbf{k}_y(N_t) = 0, \mathbf{k}_z(N_t) = 0,
\end{aligned} \tag{7.1}$$

where  $\mathbf{k}_x, \mathbf{k}_y, \mathbf{k}_z$  are  $N_t$ -length vectors containing 3D k-space trajectory locations, and  $\mathbf{b}$  is an  $N_t$ -length vector containing the complex RF pulse values.  $R(\mathbf{b})$  is a regularizer to limit the RF power, and we use  $\gamma\|\mathbf{b}\|_2^2$  with  $\gamma = 8$  in our study.  $\mathbf{D}_1$  and  $\mathbf{D}_2$  are the first and second order difference matrices,  $\mathbf{A}$  is the small-tip-angle approximation system matrix with  $a_{ij} = i\gamma\vec{M}_0 e^{i(k_{xj}x_i + k_{yj}y_i + k_{zj}z_i + \Delta\omega(t_j - T))}$ , where  $i$  is the spatial index from 1 to  $N_s$  and  $j$  is the time index from 1 to  $N_t$ .  $\mathbf{A}$  is similar to an inverse DFT matrix, but with an additional term due to B0 inhomogeneity  $\Delta\omega$ . The problem size varies in practice depending on the pulse length and the resolution of the target excitation pattern, but  $\mathbf{A}$  is typically a tall matrix ( $N_s$  typically ranges from 3000 to 36000, and  $N_t$  ranges from 250 to 1500).  $\mathbf{S}$  is the transmit coil sensitivity matrix; often it is simply chosen to be the identity matrix. The first and second order derivative constraints correspond to the maximum gradient ( $g_{max}$ ) and gradient slew rate ( $s_{max}$ ) limits of the MR scanner. The equality constraints mean the k trajectory must end at zero, by definition.

### 7.2.2 k-space parametrization

Problem (7.1) is a nonlinear, nonconvex, and constrained problem that is difficult to solve. Following [105], we simplify this problem by parametrizing the k-space

trajectory using basis functions:

$$\begin{aligned}
\mathbf{k}_x(\mathbf{c}_x) &= \mathbf{H}_x \mathbf{c}_x, \\
\mathbf{k}_y(\mathbf{c}_y) &= \mathbf{H}_y \mathbf{c}_y, \\
\mathbf{k}_z(\mathbf{c}_z) &= \mathbf{H}_z \mathbf{c}_z.
\end{aligned} \tag{7.2}$$

where  $\mathbf{H}_x, \mathbf{H}_y, \mathbf{H}_z$  are  $N_t \times L$  matrices containing  $L$  basis vectors as columns, and  $\mathbf{c}_x, \mathbf{c}_y, \mathbf{c}_z$  are the basis coefficients. Now the joint trajectory/RF design problem (7.1) becomes

$$\begin{aligned}
& \min_{\mathbf{b} \in \mathbb{C}^{N_t}, \mathbf{c}_x, \mathbf{c}_y, \mathbf{c}_z \in \mathbb{R}^L} && \|\mathbf{SA}(\mathbf{c}_x, \mathbf{c}_y, \mathbf{c}_z)\mathbf{b} - \mathbf{d}\|_2^2 + R(\mathbf{b}) \\
& \text{s.t.} && \|\mathbf{D}_1 \mathbf{H}_x \mathbf{c}_x\|_\infty \leq \gamma \Delta t g_{max}, \\
& && \|\mathbf{D}_2 \mathbf{H}_x \mathbf{c}_x\|_\infty \leq \gamma \Delta t^2 s_{max}, \\
& && \|\mathbf{D}_1 \mathbf{H}_y \mathbf{c}_y\|_\infty \leq \gamma \Delta t g_{max}, \\
& && \|\mathbf{D}_2 \mathbf{H}_y \mathbf{c}_y\|_\infty \leq \gamma \Delta t^2 s_{max}, \\
& && \|\mathbf{D}_1 \mathbf{H}_z \mathbf{c}_z\|_\infty \leq \gamma \Delta t g_{max}, \\
& && \|\mathbf{D}_2 \mathbf{H}_z \mathbf{c}_z\|_\infty \leq \gamma \Delta t^2 s_{max}, \\
& && \mathbf{k}_x(N_t; \mathbf{c}_x) = 0, \mathbf{k}_y(N_t; \mathbf{c}_y) = 0, \\
& && \mathbf{k}_z(N_t; \mathbf{c}_z) = 0.
\end{aligned} \tag{7.3}$$

Unlike previous joint pulse design approaches that are based on predefined trajectory types (e.g., EPI or spiral) that intrinsically satisfy the gradient constraints, here we aim to solve the constrained optimization problem (7.3) directly. In our approach, we do not predefine the trajectory type to form the basis, but instead use a 2nd-order B-spline basis that can closely approximate an arbitrary trajectory. In particular, for a given k-space trajectory initialization, we first approximate the trajectory using a B-spline basis, and then optimize the corresponding coefficients. A second reason for choosing a 2nd-order B-spline basis is that the gradient constraints can be implemented efficiently, as shown next.

### 7.2.3 Efficient implementation of constraints

To satisfy the maximum gradient and slew rate constraints, we would in general need to consider  $N_t$  time points. However, by using 2nd-order B-splines, the extreme points of the gradient and slew rate can occur only at a limited number of time points,

greatly reducing the number of constraints.

Define  $\beta^{(m)}(t)$  as the B-spline basis function of order  $m$ . The  $x$  component of the k-space trajectory parametrized by  $L$  such basis functions is:

$$k_x(t) = \sum_{l=1}^L c_{xl} \beta^{(m)}(t - \tau_l). \quad (7.4)$$

The gradient and slew rate are:

$$\begin{aligned} g_x(t) &= \frac{\partial k_x(t)}{\partial t} \\ &= \sum_{l=1}^L c_{xl} (\beta^{(m-1)}(t - \tau_l + 1/2) \\ &\quad - \beta^{(m-1)}(t - \tau_l - 1/2)) \\ s_x(t) &= \frac{\partial g_x(t)}{\partial t} \\ &= \sum_{l=1}^L c_{xl} (\beta^{(m-2)}(t - \tau_l + 1) \\ &\quad - 2\beta^{(m-2)}(t - \tau_l) + \beta^{(m-2)}(t - \tau_l - 1)). \end{aligned} \quad (7.5)$$

$$(7.6)$$

The extreme points of  $g_x(t)$  occur only at the zero-crossing point of  $s_x(t)$ , as illustrated in Figure 7.1. The slew rate  $s_x(t)$  is linear combination of rect functions, and its extreme points also occur at a limited number of points. Higher order B-splines do not have this property. Define  $\mathbf{P}_1$  and  $\mathbf{P}_2$  as the matrices that pick the rows corresponding to the candidate extreme points of gradient and slew rate, respectively. Then we can rewrite the inequality constraints for the x gradient in the following form (only one term is shown for simplicity):

$$\|\mathbf{P}_1 \mathbf{D} \mathbf{H}_x \mathbf{c}_x\|_{\infty} \leq \gamma \Delta t g_{max}. \quad (7.7)$$

Therefore, the total number of inequality constraints is reduced from  $12N_t$  to  $12L$  ( $L \ll N_t$ ). To provide a compact notation, we combine all inequality constraints as follows:

$$\mathbf{U} \mathbf{c} - \mathbf{v} \preceq \mathbf{0} \quad (7.8)$$

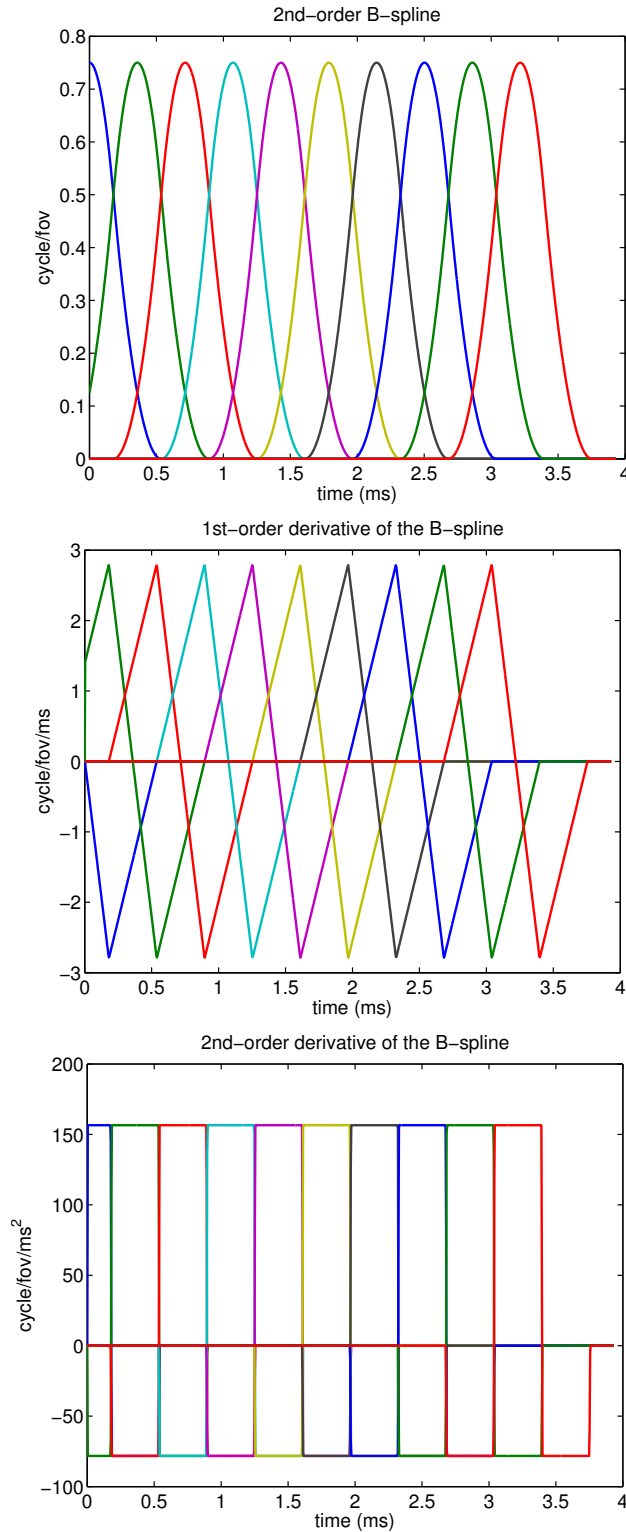


Figure 7.1: 2<sup>nd</sup>-order B-spline function basis, and its 1<sup>st</sup>, 2<sup>nd</sup>-order derivative. The gradient and slew rate are linear combination of the 1<sup>st</sup>, 2<sup>nd</sup>-order derivative, respectively. Their extreme values can occur at only a limited number of points, greatly reducing the number of inequity constraints.

where

$$U = \begin{bmatrix} P_1 D_1 H_x & 0 & 0 \\ -P_1 D_1 H_x & 0 & 0 \\ 0 & P_1 D_1 H_y & 0 \\ 0 & -P_1 D_1 H_y & 0 \\ 0 & 0 & P_1 D_1 H_z \\ 0 & 0 & -P_1 D_1 H_z \\ P_2 D_2 H_x & 0 & 0 \\ -P_2 D_2 H_x & 0 & 0 \\ 0 & P_2 D_2 H_y & 0 \\ 0 & -P_2 D_2 H_y & 0 \\ 0 & 0 & P_2 D_2 H_z \\ 0 & 0 & -P_2 D_2 H_z \end{bmatrix}, \quad (7.9)$$

$$\mathbf{c} = \begin{bmatrix} c_x \\ c_y \\ c_z \end{bmatrix}, \quad (7.10)$$

$$\mathbf{v} = \begin{bmatrix} \gamma \Delta t \mathbf{g}_{\max} \\ \dots \\ \gamma \Delta t \mathbf{g}_{\max} \\ \gamma \Delta t^2 \mathbf{s}_{\max} \\ \dots \\ \gamma \Delta t^2 \mathbf{s}_{\max} \end{bmatrix}. \quad (7.11)$$

The B-spline basis are properly shifted to end with 0, so the k-space trajectory always ends with 0, and the equality constraint can be ignored.

#### 7.2.4 Gradient and Hessian

The optimization algorithms we investigated (see Section E) involve calculating the gradient and Hessian of the cost function (7.3) with respect to the coefficients ( $\mathbf{c}_x$ ). Denoting the cost function as  $f$ , it can be shown that the gradient is [105]:

$$\nabla_{\mathbf{c}_x} f = 4\pi \text{Re}\{\iota \mathbf{H}' \mathbf{B}' \mathbf{A}' \mathbf{X} \mathbf{S}' \mathbf{W} \mathbf{e}\} \quad (7.12)$$

where  $\mathbf{H}$  is the basis function,  $\mathbf{B}$  is a diagonal matrix with the RF pulse  $\mathbf{b}$  on the diagonal,  $\mathbf{A}$  is the small-tip-angle system matrix,  $\mathbf{X}$  is a diagonal matrix containing the x spatial coordinates,  $\mathbf{S}$  is the diagonal coil sensitivity matrix,  $\mathbf{W}$  is a diagonal

weighting matrix, and  $\mathbf{e}$  is the excitation error. Denote the Jacobian matrix as:

$$\mathbf{J}_x = \frac{d\mathbf{e}}{d\mathbf{c}_x} = \mathbf{S}\mathbf{X}\mathbf{A}\mathbf{B}\mathbf{H}. \quad (7.13)$$

The gradient can then be written as:

$$\nabla_{\mathbf{c}_x} f = \text{Re}\{\mathbf{J}'\mathbf{W}\mathbf{e}\}. \quad (7.14)$$

$\nabla_{\mathbf{c}_y} f$  and  $\nabla_{\mathbf{c}_z} f$  have the same form except  $\mathbf{X}$  is replaced with  $\mathbf{Y}$  and  $\mathbf{Z}$ , respectively.

The Hessian with respect to  $\mathbf{k}$  is calculated to be (see Appendix B):

$$\begin{aligned} \frac{\partial^2}{\partial k_{xi} \partial k_{xj}} f &= 8\pi^2 \text{Re}\{b_j^* \mathbf{a}'_j \mathbf{X} \mathbf{S}' \mathbf{W} \mathbf{S} \mathbf{X} \mathbf{a}_i b_i\}, \quad i \neq j \\ \frac{\partial^2}{\partial k_{xi} \partial k_{xj}} f &= 8\pi^2 \text{Re}\{b_j^* \mathbf{a}'_j \mathbf{X} \mathbf{S}' \mathbf{W} \mathbf{S} \mathbf{X} \mathbf{a}_i b_i\} \\ &\quad - 2\text{Re}\{\mathbf{e}' \mathbf{W} \mathbf{S} \mathbf{X} \mathbf{X} \mathbf{a}_i b_i\}, \quad i = j \end{aligned} \quad (7.15)$$

The second term in (7.15) is usually much smaller than the first term since  $\mathbf{e}$  is close to zero. We therefore ignore the second term and use the following approximation (with respect to  $\mathbf{c}_x$ ):

$$\nabla_{\mathbf{c}_x}^2 f = 2\text{Re}\{\mathbf{J}'_x \mathbf{W} \mathbf{J}_x\} \quad (7.16)$$

The overall  $3L \times 3L$  Hessian matrix for the x, y, z coordinates is:

$$\nabla_{\mathbf{c}}^2 f = 2\text{Re}\{\mathbf{J}'\mathbf{W}\mathbf{J}\}, \quad (7.17)$$

where  $\mathbf{J} = [\mathbf{J}_x, \mathbf{J}_y, \mathbf{J}_z]$  is typically a tall matrix since the number of spatial locations  $N_s$  is much larger than the number of basis function  $3L$ , so the Hessian matrix  $\mathbf{J}'\mathbf{W}\mathbf{J}$  can be easily stored ( $3L \times 3L$ ), and efficiently calculated ( $\mathcal{O}(N_s L^2)$ ).

### 7.2.5 Optimization algorithms

To minimize the cost function (7.3), we alternate between optimizing the RF waveform  $\mathbf{b}$  and k-space trajectory coefficients  $\mathbf{c}$ , as shown in Algorithm 3. We use conjugate gradient (CG) for the update of  $\mathbf{b}$ , implemented using [19]. For the update of  $\mathbf{c}$ , we want the optimization algorithm to be monotonically decreasing and feasible in each iteration. This ensures that the optimization can be terminated at any point, which is useful in practical “online” settings where patient-tailored pulses must be designed quickly. We investigated four different algorithms that are both monotone

and feasible: (1) projected gradient descent algorithm with backtracking line search, (2) projected Levenberg-Marquardt (LM) algorithm [40], (3) interior point algorithm with backtracking line search, and (4) MATLAB ‘fmincon’ function using an active-set solver. We implemented the algorithms and compared their speed in MATLAB on an Intel Xeon 3.3.GHz desktop.

---

**Algorithm 3** Alternative minimization

---

- 1: Initialize: Calculate  $\mathbf{c}^{(0)}$  by B-spline curve fitting to some initial  $\mathbf{k}$ . Obtain  $\mathbf{b}$  using CG. Set  $N_{iter} = 20$ .
  - 2: **for**  $i = 1$  to  $N_{iter}$  **do**
  - 3:   Approximately optimize  $\mathbf{c}$ .
  - 4:   Run 20 iterations CG to optimize  $\mathbf{b}$ .
  - 5: **end for**
- 

In the projected LM algorithm, the projection is a quadratic programming problem that we solved using MATLAB function “quadprog”. Instead of finding the exact minimizer over  $\mathbf{c}$ , we ran the algorithms for only 3 iterations before updating  $\mathbf{b}$  again.

The projected LM algorithm is shown in Algorithm 4. It is similar to the normal LM algorithm but with two differences: (1) the update are projected to the feasible set in each iteration, (2) if the cost function does not decrease in the current iteration, we run one iteration of the gradient descent algorithm. The projection is a quadratic programming problem, can be efficiently computed using MATLAB function ‘quadprog’. We do not solve for exact solution of  $\mathbf{c}$ , but only run the algorithm for 3 iterations before update  $\mathbf{b}$  again.

---

**Algorithm 4** Projected LM[40]

---

- 1: Initialize:  $\mathbf{c}^{(0)}$  from the last outer iteration,  $\mu = 0.05$ ,  $N_{iter} = 3$
  - 2: **for**  $i = 1$  to  $N_{iter}$  **do**
  - 3:   Set  $\lambda = \mu f(\mathbf{c}^{(i)})$
  - 4:   Compute  $\boldsymbol{\delta}$  from  $(\mathbf{J}'(\mathbf{c}^{(i)})\mathbf{J}(\mathbf{c}^{(i)}) + \lambda\mathbf{I})\boldsymbol{\delta} = \nabla f(\mathbf{c}^{(i)})$
  - 5:   **if**  $f(P_C(\mathbf{c}^{(i)} + \boldsymbol{\delta})) < f(\mathbf{c}^{(i)})$  **then**
  - 6:     Set  $\mathbf{c}^{(i+1)} = \mathbf{c}^{(i)} + \boldsymbol{\delta}$
  - 7:   **else**
  - 8:     Run one iteration of projected gradient descent with backtrack line search.
  - 9:   **end if**
  - 10: **end for**
- 

The interior point algorithm used in our work is shown in Algorithm 5. In each

iteration, we minimize the following cost function  $\Phi$  that combines a scaled original cost function and a log barrier function, using Newton’s method

$$\Phi = tf + \Psi \quad (7.18)$$

where  $\Psi = -\sum_{i=1}^{12L} \log(\mathbf{u}_i^T \mathbf{c} - v_i)$ . The gradient and Hessian of  $\Psi$  are:

$$\nabla \Psi(\mathbf{c}) = \sum_{i=1}^{12L} \frac{\mathbf{u}_i}{v_i - \mathbf{u}_i^T \mathbf{c}} = \mathbf{U}^T \mathbf{w}, \quad (7.19)$$

$$\nabla^2 \Psi(\mathbf{c}) = \sum_{i=1}^{12L} \frac{\mathbf{u}_i \mathbf{u}_i^T}{(v_i - \mathbf{u}_i^T \mathbf{c})^2} = \mathbf{U}^T \text{diag}(\mathbf{w}^2) \mathbf{U}^T, \quad (7.20)$$

where  $w_i = 1/(v_i - \mathbf{u}_i^T \mathbf{c})$ . We use approximated Hessian instead of true Hessian in our implementation (line 4).  $\alpha$  is a parameter ensuring enough decrease of the cost function, and we set it to 0.01 in our implementation (line 5). Strictly feasible condition is enforced in our implementation (line 5).

---

**Algorithm 5** Interior point

---

- 1: Initialize:  $\mathbf{c}^{(0)}$  from the last outer iteration,  $t = 20$ ,  $N_{iter} = 2$
  - 2: **for**  $i = 1$  to  $N_{iter}$  **do**
  - 3:   **for**  $j = 1$  to  $N_{Newton}$  **do**
  - 4:     Compute  $\boldsymbol{\delta}$  from  $(\mathbf{J}'(\mathbf{c}^{(i)})\mathbf{J}(\mathbf{c}^{(i)}))\boldsymbol{\delta} = \nabla \Phi(\mathbf{c}^{(i)})$
  - 5:     **if**  $\Phi(\mathbf{c}^{(i)} + s\boldsymbol{\delta}) < \Phi(\mathbf{c}^{(i)}) - \alpha\boldsymbol{\delta}'\nabla\Phi$  **AND**  $\mathbf{c}^{(i)} + s\boldsymbol{\delta}$  is feasible **then**
  - 6:       Set  $\mathbf{c}^{(i+1)} = \mathbf{c}^{(i)} + s\boldsymbol{\delta}$
  - 7:     **else**
  - 8:        $s = 0.5s$
  - 9:     **end if**
  - 10:   **end for**
  - 11:    $t = 2t$
  - 12: **end for**
- 

### 7.2.6 Initialization

The above algorithms are local optimization algorithms that require good initialization. To demonstrate that our method can be applied to any initial k-space trajectory, we evaluated four different initial 3D trajectories: (1) stack-of-spirals (SoS) [83], (2) spiral nonselective (SPINS) [55], (3) KT-points [11], and (4) a novel trajectory design initialization approach which we will refer to as “extended KT-points” [88].

The KT-points method models the joint design problem as the following sparse approximation problem:

$$\min_{\mathbf{x} \in \mathbb{C}^{N_t}} \|\mathbf{S}\mathbf{F}\mathbf{x} - \mathbf{d}\|_2, \text{ such that } \|\mathbf{x}\|_0 = N_k. \quad (7.21)$$

$\mathbf{F}$  is a complete DFT matrix and  $\mathbf{x}$  is the RF weighting vector. This minimization problem tries to select  $N_k$  phase encoding locations from a total  $N_s$  possible locations that best approximate  $\mathbf{d}$ , and the non-zero term in  $\mathbf{x}$  corresponds to the RF pulse weighting at those phase encoding locations. The B0 field inhomogeneity term in  $\mathbf{A}$  in (7.1) is ignored. The reason is that the actual visiting time for each phase encoding location is undetermined when constructing the dictionary. The sparse approximation problem can be solved by either thresholding the inverse discrete Fourier transform or using greedy algorithms. We choose a modified OMP [109] method since it can easily model the region of interest and transmit sensitivities in the system matrix. KT-points method produces initial 3D k-space phase encoding locations and RF weights at those locations. Those phase encoding locations are traversed using gradient blips.

This conventional KT-point method is inefficient in 3D excitation since moving between phase encoding locations takes a large portion of the pulse duration but no RF is transmitted during this time. A natural extension is to use the k-space trajectory from KT-points but transmit continuous RF during the whole pulse duration. This is our third initialization method.

However, this simple extension may also be inefficient since the visiting order and the gradient waveform is not optimized. We therefore propose to order those phase encoding points before generating the gradient waveform. We treat this as a traveling salesman problem, and use a genetic algorithm to solve it [46]. We then generate the fastest gradient waveform to transverse those optimally ordered points using the method in [51, 100]. This “extended KT-points” initialization is summarized in Algorithm 7. Our extension is similar to [10], but [10] does not optimize the visiting order of phase encoding locations, and was demonstrated only for 2D tailored excitation.

---

**Algorithm 6** Extended KT-points

---

- 1: Find phase encoding locations using method [109].
  - 2: Find the optimal visiting order using traveling salesman algorithm [46].
  - 3: Generate the fastest gradient waveform using [51].
-

### 7.3 Methods

We applied our method to two pulse design problems: 3D inner-volume excitation and spin prephasing. For inner-volume excitation, we excited a  $6 \times 6 \times 6 \text{ cm}^3$  cube with 10 degree flip angle using an RF pulse of approximate duration 4 ms transmitted on a single transmit coil. We simulated the excitation results for a  $64 \times 64 \times 8$  matrix over a  $24 \times 24 \times 16 \text{ cm}^3$  FOV. To reduce computation time, we down sampled the matrix to  $32 \times 32 \times 8$  for optimization. We used a measured B0 field map from an Agar ball phantom in the simulation. We measured the B0 field map by acquiring spoiled gradient-echo (SPGR) images with two different echo times (3 ms and 5.3 ms), and taking the phase difference on a voxel-by-voxel basis. We assume uniform coil transmit sensitivity.

For spin prephasing [104], we want to achieve the following excitation pattern:  $\mathbf{d}(\Delta\omega(\mathbf{r})) = e^{i\Delta\omega(\mathbf{r})T_{\text{free}}} \sin \alpha$ , where  $\alpha$  is the flip angle (uniform for all spins),  $\Delta\omega(\mathbf{r})$  is the B0 field map, and  $T_{\text{free}}$  is the free precession time. The goal is to achieve refocusing  $T_{\text{free}}$  after the excitation<sup>2</sup>. Prephasing pulses may be used to compensate for susceptibility (T2\*) signal loss, and are needed in the “small-tip fast recovery” steady-state imaging sequence being developed by our group [104, 65, 93]. We designed a prephasing pulse with 10 degree flip angle, 2.5 ms  $T_{\text{free}}$ , and measured B0 field map from a human brain. We simulate with  $64 \times 64 \times 8$  matrix size and  $24 \times 24 \times 4 \text{ cm}^3$  FOV.

We evaluated four different algorithms for parametric optimization, and four initializations, but we did not compare all 16 combinations. Instead, we first compare the speed of optimization algorithms for inner-volume excitation using the extended KT-point initialization. After finding the fastest algorithm, we compared the excitation accuracy using different initializations. The 8 methods that are compared are summarized in Table 1.

Figure 7.2 shows the four different k-space trajectory initializations used in the inner-volume excitation. The prephasing problem uses the same SoS and SPINS initialization, but different KT-points and extended KT-points initialization since they are excitation pattern dependent. The parameters for SoS and SPINS trajectories were manually tuned to achieve good initial excitation results. For SoS, we used 5 spiral stacks with 17 cm excitation FOV in z direction, and each spiral has 6 cycles with 24 cm excitation FOV in the x-y plane. For SPINS, we set the maximum extent of k-space to 0.48 cycles/cm, polar angular velocity to  $3\pi/\text{ms}$ , azimuthal angular ve-

---

<sup>2</sup>I use the convention  $\omega = \gamma B$  in my thesis. Since the free precession is rotated clockwise with a positive B field, the accumulated phase is in the negative direction:  $\theta_f = -\omega T_{\text{free}}$

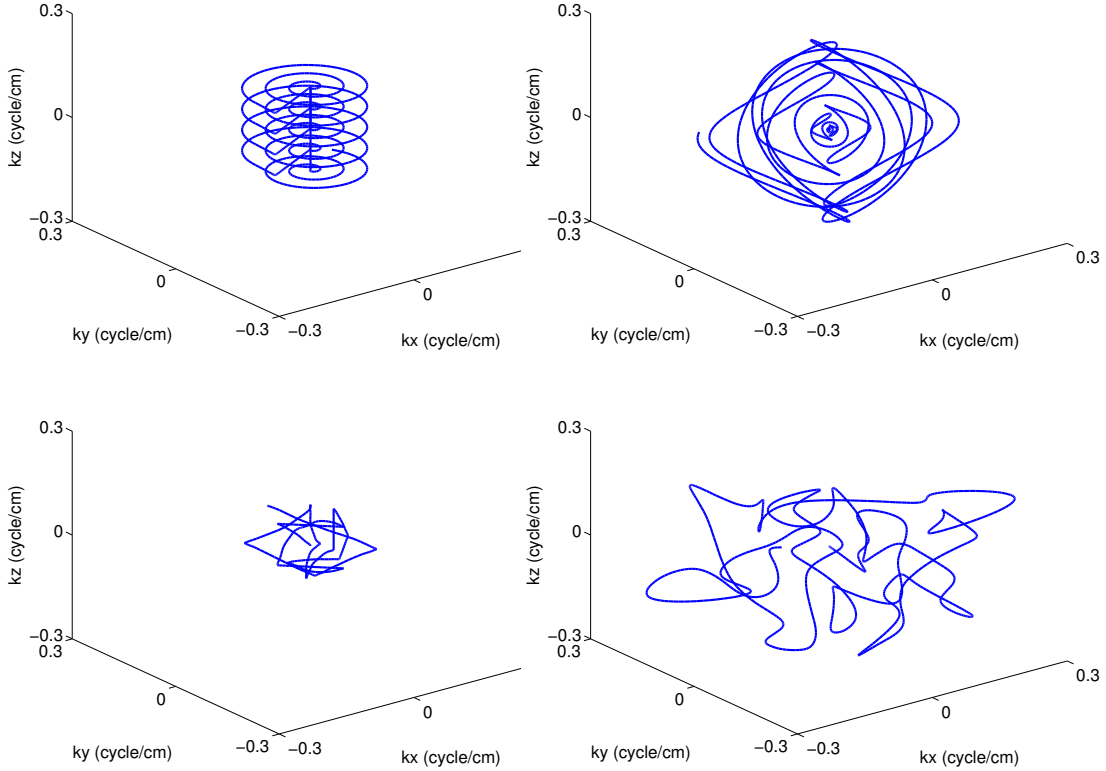


Figure 7.2: Different k-space trajectory initializations for the inner-volume excitation: stack-of-spirals (SoS); SPINS; KT-points; and “extended KT-points”. KT-points and extended KT-points selectively traverse the k-space based on the target excitation pattern. The extended KT-points method manages to traverse a larger k-space region than the simple KT-points because of the improved visiting order and the use of a time-optimal gradient waveform.

locity to  $2\pi/\text{ms}$ , and speed and position of transition between slow and radial phase to 10 and 0.5 [55]. The resulting SPINS trajectory is accelerated using the fastest gradient waveform [100]. There are small variations in the pulse length since it can not be directly constrained when generating different initializations. For fair comparison, we tuned the parameters to generate initial trajectories around 4 ms, and then cut all of them to the same length as the shortest one, resulting 3.9 ms for all initial trajectories (Figure 7.2).

Table 7.1: Pulse design methods

SoS	SPINS	KT-points	extended KT-points
SoS+IP	SPINS+IP	KT-points+IP	extended KT-points+IP

## 7.4 Results

Figure 7.3 shows the cost function value and normalized root mean square error (NRMSE) of the excitation versus computation time for different algorithms in solving the parametrized constrained optimization (7.3) in the inner-volume excitation case using extended KT-points as the initialization. NRMSE is defined as  $\frac{\|\mathbf{S}\mathbf{A}\mathbf{b}-\mathbf{d}\|_2}{\sqrt{N_s} \sin \alpha}$ , where  $\alpha$  is the target excitation angle, and the transmit sensitivity matrix  $\mathbf{S}$  is set to identity matrix. The interior point and projected LM algorithms are much faster than the simple projected GD and MATLAB ‘fmincon’. Compared to projected LM, the interior point algorithm is slightly faster and its final k-space trajectory has lower slew rate (not shown). We use the ‘active-set’ solver for the MATLAB ‘fmincon’ function. There is an ‘interior-point’ solver for the MATLAB ‘fmincon’ function, but it is not strictly feasible in each iteration and its speed is slower than our projected LM and interior point implementations. The shapes are similar between the NRMSE plot and the cost function value plot. There is a small increase in the first iteration for projected GD. This is because the first point in the plot corresponds to the initial k-space trajectory, not the initial approximation using B-spline basis, and applying the approximation can lead to a potentially higher cost and/or NRMSE in the first iteration. Based on these results we chose the interior point algorithm for all subsequent simulations.

Figure 7.4 shows the k-space trajectory before (dashed line) and after (solid line) the interior point optimization using an extended KT-point initialization for reduced FOV excitation. There is noticeable deviation between the final k-space trajectory and the initialization, but they have similar shape. The peak gradient is well below the 4 G/cm limit we set, while the slew rate is close to the imposed limit of 15 G/cm/ms.

Figure 8.4 shows inner-volume excitation results. Four different methods are used as initialization to the parametrized optimization (7.3). Bloch simulation results before and after initialization are shown in the left and right column, respectively. Without parametrized optimization, our extended KT-points method generates the least excitation error with the shortest pulse. With parametrized optimization, all methods are improved by 20~40%. Using SPINS or extended KT-points as initialization generate the best final results. The peak RF is 0.012 gauss, well below the limit of our GE scanner. The measured 10 sec average SAR (or the integrated RF power) is below 0.3 W/Kg, much lower than the 6.4 W/Kg limit for human brain.

Figure 7.6 shows the excitation error of the prephasing problem using the same 8 methods. Similar to the reduced FOV excitation case, optimization greatly reduced

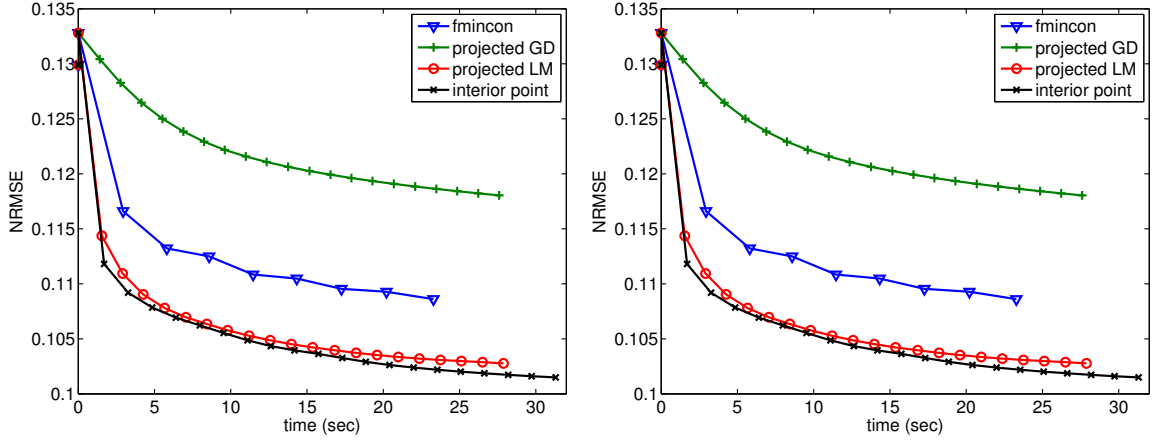


Figure 7.3: Convergence speed of different algorithms used to solve the parametrized constrained optimization problem (7.3): (Left) Cost function value versus time. (Right) NRMSE versus time. There are two data points at time 0: the lower one is using the initialized k-space trajectory and the higher one is using the k-space trajectory after B-spline fitting. The fitting at the beginning of optimization slightly increases the NRMSE and the cost function value. The interior point and projected LM algorithms converge much faster than the other two, with the interior point algorithm slightly faster.

the excitation error for all initializations. Without interior point optimization, the SPINS generates the best result. The extended KT-points generates good result, but not as good as in the reduced FOV case, probably because the energy in k-space is more uniformly distributed in this case than the reduced FOV excitation case.

## 7.5 Extension to parallel transmission

Parallel transmission (Ptx) has been developing for several years as a means of improving the tailored excitation accuracy using multiple coils. We demonstrated our proposed method only for single coil excitation in previous section, but it should be easily extend to parallel excitation using the spatial domain pulse design method [23], as we will briefly illustrated in this section. First of all, in PTX, the pulse design

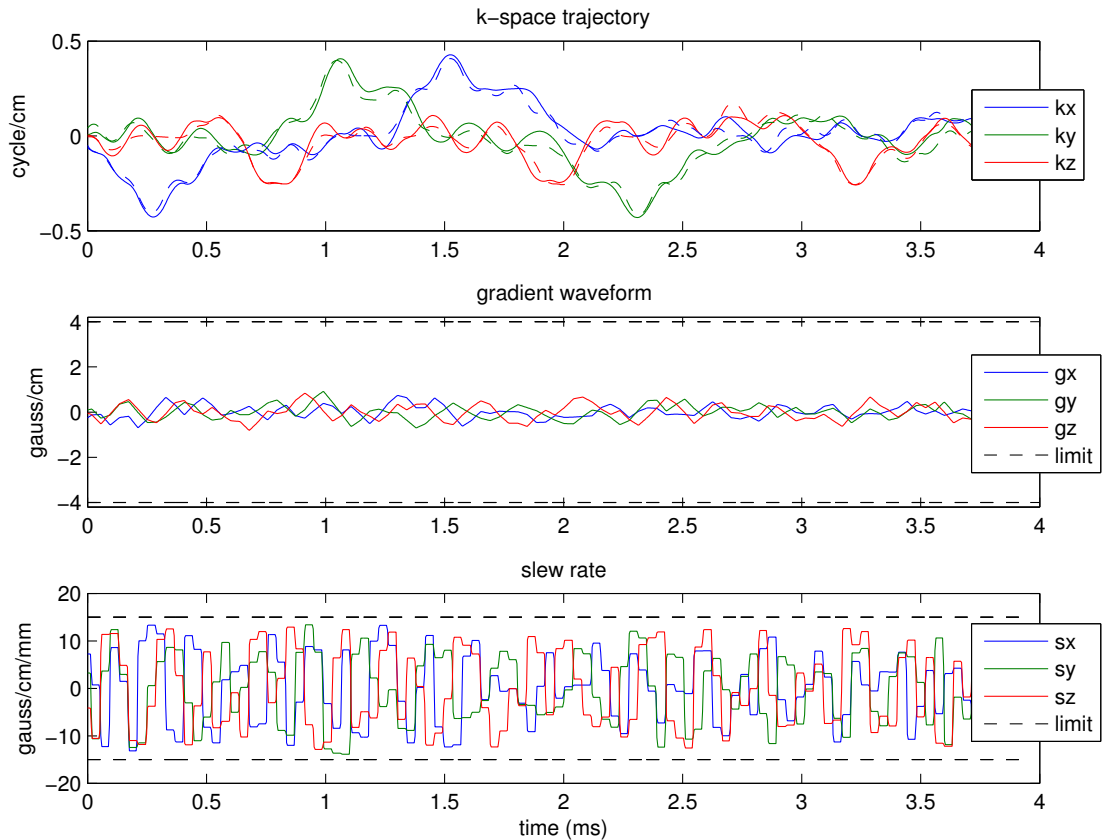


Figure 7.4: Example k-space trajectory, gradient waveform, and slew rate. The extended KT-points k-space trajectory before (dashed line) and after 20 iterations of alternating optimization with interior point algorithm (solid line) have similar shape. Both gradient and slew rate are within our constraint, but the slew rates are closer to the limit.

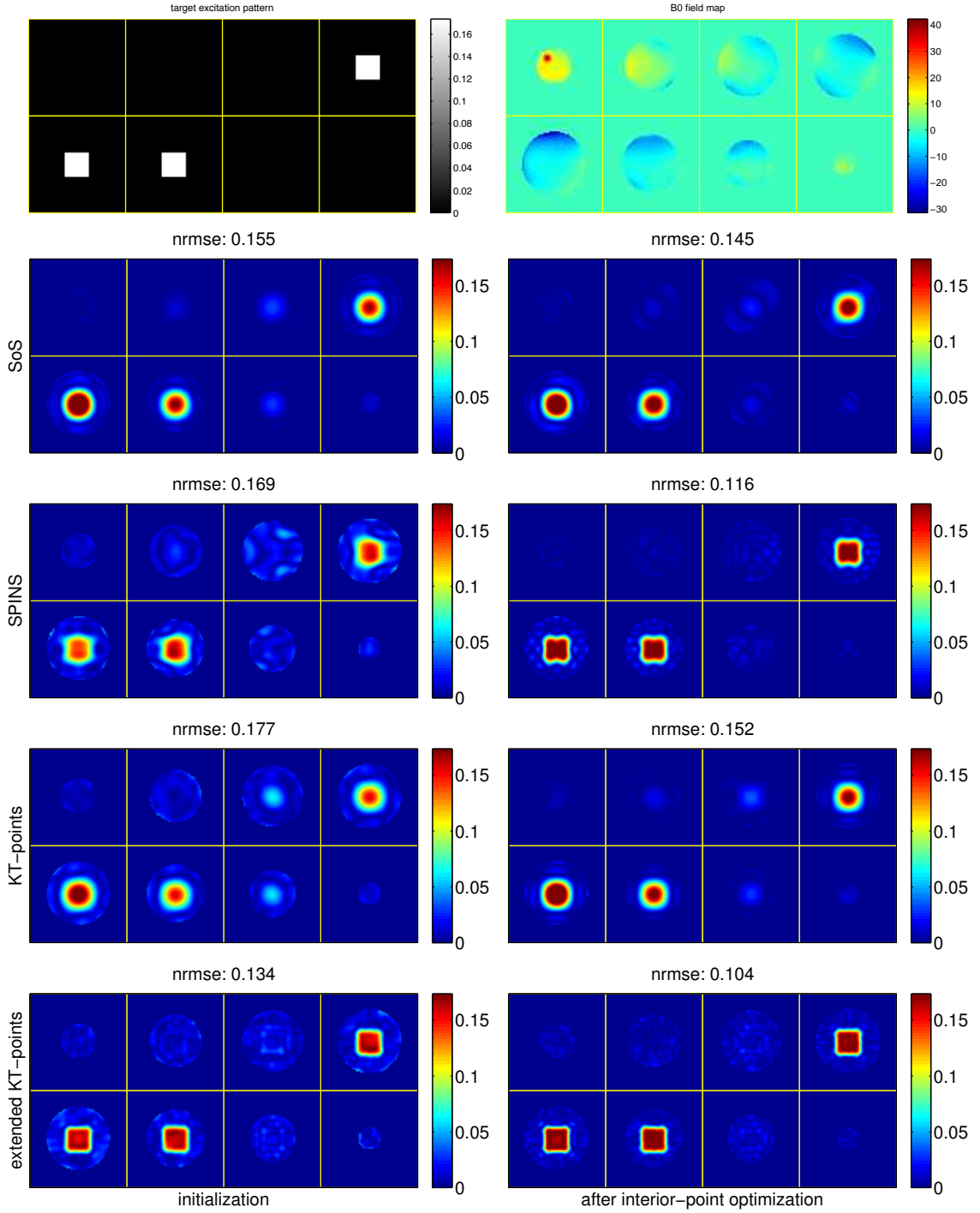


Figure 7.5: Inner-volume excitation, simulation results. Target pattern (top left) and field map in Hz (top right) used in the simulation. Row 2 to 5: results for different pulse design methods: left column contains the results of initialization pulse, right column contains the results after optimization using interior point algorithm. Four initialization methods were investigated: from top to bottom: SoS, SPINS, KT-points, our extended KT-points. All pulses have 3.9 ms pulse length. Optimization always improve the excitation results, reducing the NRMSE by 10 to 30% depending on the initialization method. Using extended KT-points as the initialization gave the best results.

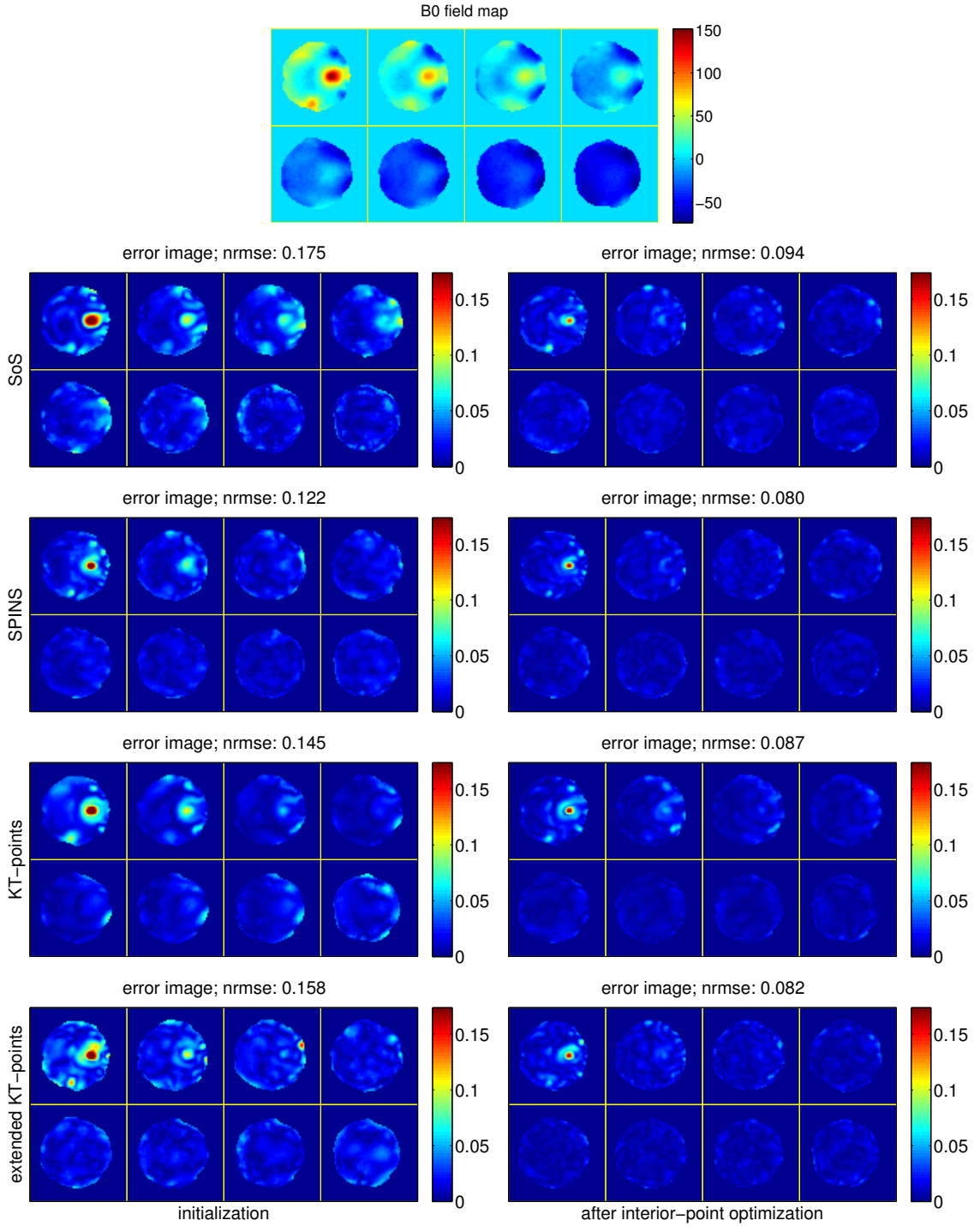


Figure 7.6: Prephasing excitation, simulation results. The B0 field map is acquired from a human brain scan, shown in Hz. The excitation error for different initializations are ordered in the same way as Figure 8.4, and the pulse lengths are 3.9 ms for all. We want small error (dark blue) in the whole image. Without optimization, SPINS performs the best in this case. Interior point optimization substantially reduces the excitation error for all initializations, and SPINS and extended KT-points produce final results with similar accuracy in this prephasing case.

optimization problem in (7.3) becomes:

$$\begin{aligned}
\min_{\mathbf{b} \in \mathbb{C}^{N_t}, \mathbf{c}_x, \mathbf{c}_y, \mathbf{c}_z \in \mathbb{R}^L} \quad & \left\| \sum_{n=1}^{N_c} \mathbf{S}_n \mathbf{A}(\mathbf{c}_x, \mathbf{c}_y, \mathbf{c}_z) \mathbf{b} - \mathbf{d} \right\|_2^2 + R(\mathbf{b}) \\
s.t. \quad & \|\mathbf{D}_1 \mathbf{H}_x \mathbf{c}_x\|_\infty \leq \gamma \Delta t g_{max}, \\
& \|\mathbf{D}_2 \mathbf{H}_x \mathbf{c}_x\|_\infty \leq \gamma \Delta t^2 s_{max}, \\
& \|\mathbf{D}_1 \mathbf{H}_y \mathbf{c}_y\|_\infty \leq \gamma \Delta t g_{max}, \\
& \|\mathbf{D}_2 \mathbf{H}_y \mathbf{c}_y\|_\infty \leq \gamma \Delta t^2 s_{max}, \\
& \|\mathbf{D}_1 \mathbf{H}_z \mathbf{c}_z\|_\infty \leq \gamma \Delta t g_{max}, \\
& \|\mathbf{D}_2 \mathbf{H}_z \mathbf{c}_z\|_\infty \leq \gamma \Delta t^2 s_{max}, \\
& \mathbf{k}_x(N_t; \mathbf{c}_x) = 0, \mathbf{k}_y(N_t; \mathbf{c}_y) = 0, \\
& \mathbf{k}_z(N_t; \mathbf{c}_z) = 0.
\end{aligned} \tag{7.22}$$

We can still use the same interior point algorithm with 2nd-order B-spline parametrization we did in the single case, but we need to update the formulas for gradient, Hessian matrix, and Jacobian matrix. The Jacobian matrix in PTx is:

$$\mathbf{J}_x = \frac{d\mathbf{e}}{d\mathbf{c}_x} = \sum_{n=1}^{N_c} \mathbf{S}_n \mathbf{X} \mathbf{A} \mathbf{B} \mathbf{H}. \tag{7.23}$$

Then, the gradient has the following form:

$$\nabla_{\mathbf{c}_x} f = \text{Re}\{\mathbf{J}' \mathbf{W} \mathbf{e}\}. \tag{7.24}$$

The Hessian in PTx case is calculated to be (see Appendix B):

$$\begin{aligned}
\frac{\partial^2}{\partial k_{xi} \partial k_{xj}} f &= 8\pi^2 \text{Re}\left\{ \sum_{m=1}^{N_c} \sum_{n=1}^{N_c} b_{mj}^* \mathbf{a}'_j \mathbf{X} \mathbf{S}'_m \mathbf{W} \mathbf{S}_n \mathbf{X} \mathbf{a}_i b_{ni} \right\}, \quad i \neq j; \\
\frac{\partial^2}{\partial k_{xi} \partial k_{xj}} f &= 8\pi^2 \text{Re}\left\{ \sum_{m=1}^{N_c} \sum_{n=1}^{N_c} b_{mj}^* \mathbf{a}'_j \mathbf{X} \mathbf{S}'_m \mathbf{W} \mathbf{S}_n \mathbf{X} \mathbf{a}_i b_{ni} \right\} \\
&\quad - 2(2\pi)^2 \text{Re}\left\{ \sum_{n=1}^{N_c} \mathbf{e}' \mathbf{W} \mathbf{S}_n \mathbf{X} \mathbf{X} \mathbf{a}_i b_{ni} \right\}, \quad i = j.
\end{aligned}$$

## 7.6 Experimental validation of the extended KT-points method

We did not acquire experimental data after we fully developed our 2nd-order B-spline based optimization algorithm. We have experimental validation that using SPINS and extended KT-points without further optimization [88]. Those experimental results agree well with our simulation, suggesting our proposed method can be successfully used in MRI scanner.

Figure 7.7 compares the measured trajectory and nominal trajectory for an extended KT-points design output. Both trajectories match very well, indicating that eddy currents distortion may not be a problem for our implementation (in our MR scanner).

Figure 7.8 shows Bloch simulation and experimental results in 6 slices spanning  $24 \times 24 \times 20$  cm<sup>3</sup> FOV for three different methods: extended KT-points joint design, extended KT-points with local optimization over the KT-points, and predefined SPINS trajectory. The extended KT-points with local optimization has a step that locally optimizes the phase encoding locations before connecting them and forming the continuous trajectory [88]. It can reduce the NRMSE by 10 % compared with the simple extended KT-points method, both have less excitation error than the SPINS trajectory. We did not use this extended KT-points with local optimization as initialization in our proposed method, since it may not be worth the extra time of running local optimization if it is just for initialization. The experimental results agree well with simulation.

## 7.7 Discussion

For the examples shown here, the computation time for the parametric optimization step is typically less than 1 minute. Using KT-points or extended KT-points requires additional optimization to form the initial pulse, which takes less than 1 minute. The overall computation time for all methods tested in this study is less than 2.5 minutes, fast enough for normal online pulse design, particularly with a faster computer.

We conclude that both SPINS and extended KT-points provide good initializations. SPINS initialization has shorter computation time (no sparse approximation step). However, it has the disadvantage that more parameters (e.g., k-space extent, rotation speeds) need to be manually tuned in the design, while the extended KT-points method generates a trajectory automatically without manual parameter

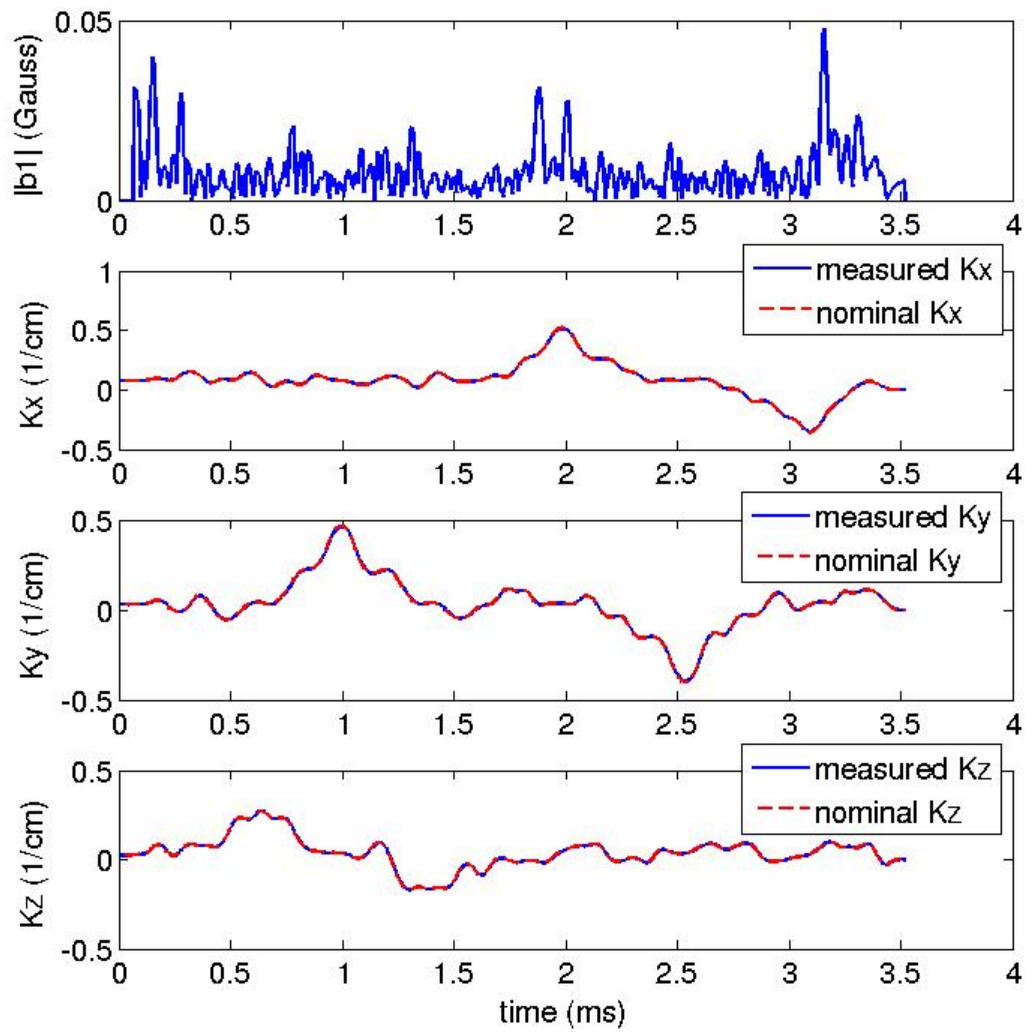


Figure 7.7: A example pulse diagram from the extended KT-points. The measured trajectory matches well with the nominal trajectory, indicating the distortion caused by eddy current may not be a problem for our implementation.

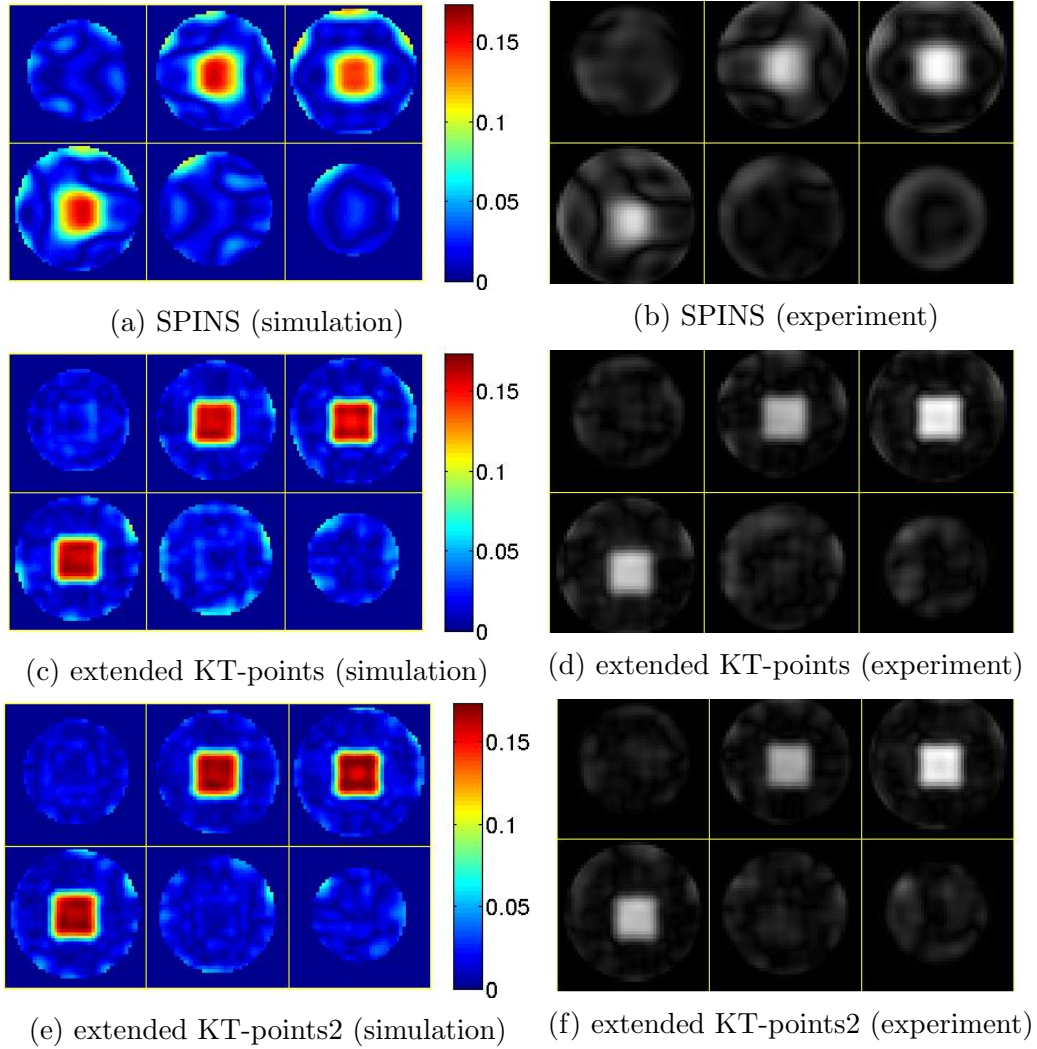


Figure 7.8: Comparison between extended KT-points designs and design using predefined SPINS trajectory: simulation and experimental result of extended KT-points design with local optimization of phase encoding points (e, f); extended KT-points (c, d); SPINS trajectory (a, b). Both extended KT-points methods achieve higher excitation accuracy than SPINS (NRMSE: 0.15/0.17 vs 0.21) with a shorter pulse length, and adding local minimization to the phase encoding locations reduces the NRMSE by 10% compared with the design without local minimization. Notice the local optimization here is not the optimization to the 2nd-order B-spline as we proposed in this chapter, it is just performed on the discrete phase encoding locations [88].

tuning.

We use 2nd-order B-spline functions to represent the k-space trajectory since it is widely used in parametrization of curves and it can significantly reduce the number of inequality constraints. We used 100 basis functions to represent a trajectory around 3.9 ms (corresponding to 981 time points), and we found that the resulting fits are quite good for all four k-space initializations. We also simulated using different number of basis functions ( $L = 20$  to 200), and observed that the final NRMSEs are quite similar for  $L = 50$  to 200 (not shown). The computational time increased from 20 sec ( $L = 20$ ) to 50 sec ( $L = 200$ ). We obtained good results using this basis, but we do not claim this is the optimal choice.

In Figure 7.4, we note that neither the gradient nor the slew rate reached their limits, indicating a suboptimal pulse since it means the pulse can be faster or we can cover more k-space with the same pulse length. We think the reason for this relatively low gradient/slew rate is because we only run a limited number of interior point iterations for updating k-space trajectory, before switched to updating RF, so the k-space trajectory was not fully optimized. We tried to increase the number of interior point iterations for the inner-volume excitation, which did push the slew rates to their limits Figure 7.9. However, the final NRMSE was only reduced slightly from 0.103 to 0.102. We think this small improvement did not qualify the extra computation time (changed from 30 sec to 400 sec).

We observed that the optimized gradient waveform is usually well below the maximum gradient limit. So we tried to relax the gradient constraints and only kept the slew rate constraints. The computation time was slightly reduced, but the excitation accuracy was not improved.

## 7.8 Conclusions

We have proposed a new joint design method for 3D tailored excitation, that can improve excitation results for arbitrary k-space trajectory initializations. We also proposed a new k-space initialization method, extended KT-points, that appears to be better or at least as good as several existing 3D trajectory choices, even for slightly shorter RF pulse length.

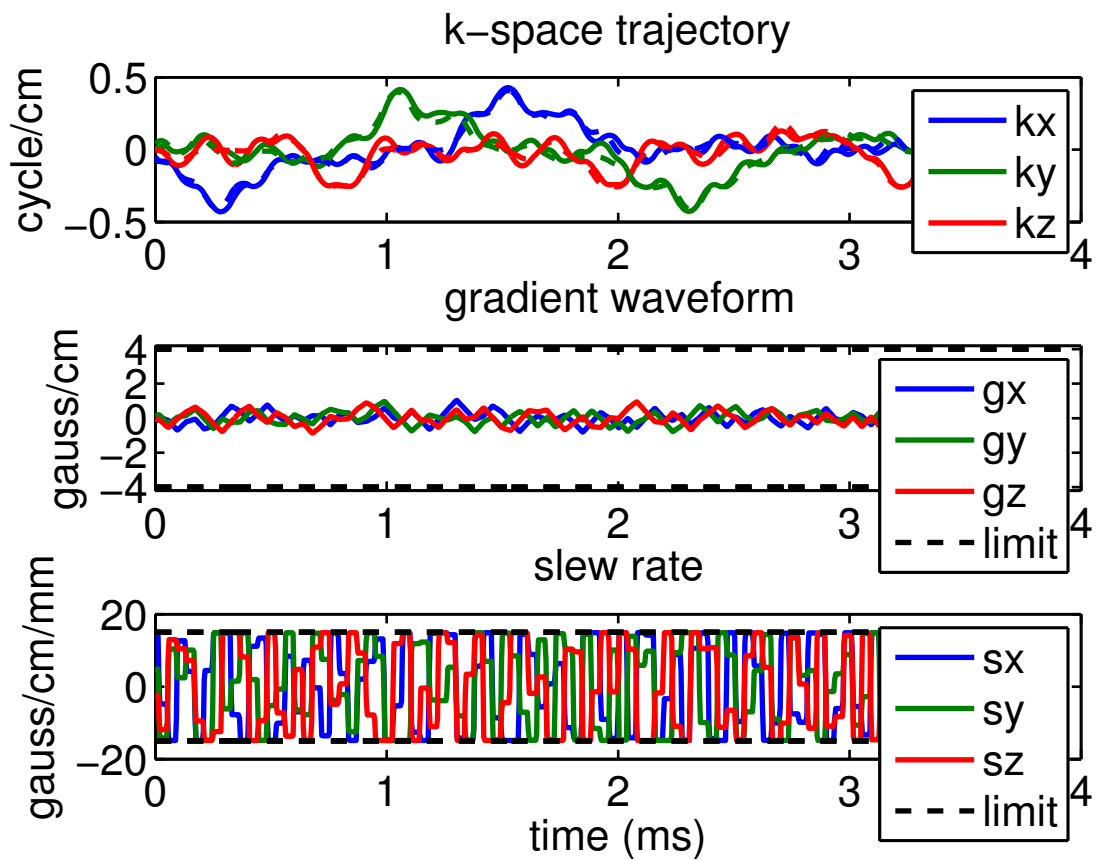


Figure 7.9: k-space trajectory, gradient waveform, and slew rate if we run more iterations of interior point algorithm. Compared to Figure 7.4, the slew rates are pushed much harder to their limits.

## CHAPTER VIII

# Rapid Inner-volume Imaging in the Steady-state with 3D Selective Excitation and Small-tip Fast Recovery (STFR) Imaging

### 8.1 Introduction

1

In inner-volume imaging (IVI), a 2D or 3D sub-volume is excited within the object such that only a reduced field-of-view (rFOV) needs to be encoded. Ideally, one wants to directly excite the desired 3D rFOV using a single radiofrequency (RF) pulse of short duration, and choose a “tight” readout trajectory that matches the rFOV. However, a 3D selective excitation pulse with non-smooth target pattern (e.g., a cube) can be prohibitively long. Therefore, most existing IVI methods are only 2D selective, using either spin echo or 2D excitation pulses. A typical spin echo IVI method is proposed in [16], where a 90 degree slice-selective pulse is followed by a 180 degree slice-selective pulse in the perpendicular direction. Only spins inside the “pencil beam” region that is excited by both RF pulses are refocused and generate detectable signal. In this case the field of view in the unrestricted dimension can be limited by using a cartesian readout with frequency encoding along the pencil beam direction in combination with a low pass filter. In some other methods, a 2D selective pulse is transmitted to directly excite a column, with the FOV in the third dimension restricted with frequency encoding or other special readout encoding techniques [30, 116, 86, 110, 56].

Parallel transmit methods have been proposed recently for IVI with 3D selective excitation [81, 54, 52]. In [81], a 3.2 ms pulse for IVI was demonstrated with an

---

<sup>1</sup>This chapter is based on the publications [94]

8-channel parallel excitation system, but it used a preclinical scanner with gradient specs (660 mT/m maximum amplitude; 5600 T/m/s maximum slew rate) that far exceed the capability of clinical systems. Parallel excitation experiments on human scanners have reported IVI RF pulses of duration 12–14.89 ms [54, 52] that are undesirably long for some applications such as rapid steady-state imaging. Moreover, parallel excitation requires specialized hardware that is not widely available.

Here we propose a novel implementation of IVI imaging, based on (1) 3D selective excitation using a recently proposed joint RF/gradient pulse design approach [88], and (2) the small-tip fast recovery (STFR) steady-state imaging sequence [66, 93, 97]. With this approach we demonstrate that steady-state imaging with 3D IV excitation using a short (4 ms) RF pulse is possible on a standard clinical scanner equipped with single-channel excitation. We show that STFR achieves a higher inner- to outer-volume signal ratio compared to spoiled gradient-echo imaging (FLASH/T1-FFE/SPGR) or balanced steady-state free precession (bSSFP). The proposed method may allow for rapid IV imaging in the steady-state with 3D IV excitation and non-cartesian readouts optimized for the rFOV.

## Theory

### RF pulse design

The parallel excitation IVI experiments reported in [81, 54, 52] employed 3D selective RF pulses with a pre-defined gradient trajectory such as concentric shells and stack of spiral. Ideally, however, one would want to optimize both the gradients and the RF pulse for a given target excitation pattern. Unfortunately, this joint RF/gradient design task poses a difficult non-convex and non-linear optimization problem, and the gradient waveforms are therefore typically chosen a priori, independently of the target pattern.

In [88], we proposed a method for the *joint* design of RF waveform and excitation k-space trajectory that achieved improved accuracy compared to several existing 3D selective excitation designs [11, 55]. In particular, we were able to accurately excite a cube using a 4 ms RF pulse and single-coil transmission. Our joint design is an extension of the KT-points method [11], and is summarized in Algorithm 7. Briefly, we first obtain a KT-points trajectory (discrete “phase-encoding” locations in  $k_x$ - $k_y$ - $k_z$ ) using a modified orthogonal matching pursuit (OMP) approach [109]. We then locally optimize the encoding locations using gradient-based algorithms. We then determine the optimal visiting order for those phase encoding locations using a trav-

eling salesman algorithm [46]. Finally, we generate a continuous gradient waveform that traverses those points using the method in [51], and design the RF pulse on this optimized k-space trajectory using iterative small-tip selective pulse design [103].

---

**Algorithm 7** Extended KT-points

---

- 1: Find phase encoding locations using method [109].
  - 2: Locally optimize those phase encoding locations using Levenberg-Marquardt algorithm [73].
  - 3: Find the optimal visiting order using traveling salesman algorithm [46].
  - 4: Generate the fastest gradient waveform using [51].
- 

**STFR**

The second component of our IVI method is small-tip fast recovery (STFR) imaging, a recently proposed steady-state sequence that can achieve similar signal level and tissue contrast as bSSFP, but with reduced banding artifacts. STFR relies on a “tip-up” (or fast recovery) RF pulse to preserve the magnetization in the longitudinal direction after the readout, and a gradient crusher after the tip-up pulse to remove the banding artifact. The tip-up pulse requires either a spatially tailored RF pulse [66, 93] or a spectrally pre-winding RF pulse [92, 101].

The main challenge in STFR is to design an accurate 3D tailored tip-up pulse that recovers all spins within the imaging volume. In particular, whole-brain STFR imaging in a single scan is currently not practical on clinical scanners. Fortunately, the tip-up pulse design task generally becomes easier as the inner-volume decreases in size, since a local shimming can be more effective than a shimming of the whole object, and therefore our tip-up pulse need to target only a narrow off-resonance bandwidth. This property, together with the fact that the tip-up pulse in STFR acts to suppress the steady-state outer-volume signal relative to SPGR or bSSFP IV acquisitions as shown here, makes STFR a very attractive candidate for rapid IV imaging.

Figures 8.1(a) and (b) show the inner- and outer-volume spin paths, respectively, for a idealized STFR sequence, i.e., assuming tip-down and tip-up pulses of negligible duration that are perfectly matched to the local off-resonance. Consider first the inner-volume spins. First the IV excitation pulse tips the spins down toward the transverse plane, after which the spin precesses with off-resonance frequency  $\omega$ . After data readout, a non spatially selective tip-up pulse is played out, whose phase is nominally equal to the spin phase  $\theta = \omega T$  such that the spin is tipped back up toward the longitudinal axis. The resulting steady-state signal is bSSFP-like, as described in

detail in [66, 93].

Consider next the outer-volume spins; these mainly experience the non spatially selective tip-up pulse (2→3). Since RF-spoiling is used, the non-selective tip-up pulse does not directly contribute to the signal at the time of data acquisition (TE) [66]. However, since the IV excitation pulse can never be perfect, some direct outer-volume excitation from the tip-down pulse (4→1) is inevitable. This small unwanted excitation leads to a detectable outer-volume signal at the echo, which of course is undesirable. However, the central point here is that the tip-up pulse helps to partially saturate outer-volume spins, such that the steady-state outer-volume signal resulting from non-ideal IV excitation is relatively small in STFR compared to the corresponding SPGR or bSSFP sequence (using the same IV excitation pulse).

## Methods

To evaluate the ability of STFR to improve the inner- to outer-volume signal ratio relative to SPGR and bSSFP, we first performed simulations using a range of tip-down and tip-up angle combinations (1–60 degrees). TR is set to 10 ms, and T1/T2 values are set according to the values of white matter (1.1/0.06 sec [85]). Based on simulations of our 3D IV pulses (not shown), we assumed that the 3D IV excitation pulse produced a maximum residual (unwanted) transverse magnetization in the outer-volume that equaled 15% of the inner-volume transverse magnetization.

We then evaluated the inner- to outer-volume signal ratio *in vivo*, by acquiring steady-state brain data in a volunteer with 3D inner-volume excitation (IVex) using STFR, SPGR, and bSSFP (Table 1). Imaging experiments were done on a GE 3T scanner equipped with a quadrature transmit/receive head coil and standard gradients (50 mT/m amplitude and 150 mT/m/ms slew rate limits). We also acquired a conventional bSSFP data set for reference. Except for the conventional bSSFP sequence, all sequences used a 4 ms 3D RF pulse designed to excite a 6x6x3 cm<sup>3</sup> inner-volume. All sequences used the same 3D spin warp readout (192x192x42 matrix; 24x24x21 cm<sup>3</sup> FOV). The IVex-STFR sequence, shown in Figure 8.1(c), used a spectral pre-winding “tip-up” pulse targeted to -30 to 30 Hz [2, 89]. We did not measure the field map to determine the off-resonance of inner volume but used auto-prescan to properly shim the inner volume to be near center frequency. The shimming here is easier than a global whole field shimming.

Finally, to investigate the effect of aliasing of OV signals into the images, we simulated a series of reduced FOV acquisitions with stack-of-spirals readout trajectories

by retrospectively sub-sampling the fully sampled Cartesian *in vivo* data. We first reconstructed the image from the fully sampled Cartesian k-space data, and then simulated the k-space data on stack-of-spiral trajectories using NUFFT [18], and finally we reconstructed the image using iterative reconstruction [98]. We simulated different undersampling factors (FOV) and tabulated the error for each reconstructed image, relative to the fully sampled Cartesian ground truth images. The relative error is defined as:  $\|\mathbf{r} - \mathbf{c}\|_2 / \|\mathbf{c}\|_2$ , where  $\mathbf{r}$  and  $\mathbf{c}$  are vectors contain the pixel values in the 6x6x3 cm<sup>3</sup> ROI of the rFOV image and cropped full FOV image, respectively. The simulated FOV were 24, 12, 10, and 8 cm in-plane; and 21, 10.5, 7, and 3.5 cm through-plane (the full FOV is 24x24x21 cm<sup>3</sup>). The number of spiral leafs and time length of each leaf are 72/36/30/24, and 2.9/2.6/2.6/2.6 ms for 21/10.5/7/3.5 cm FOV<sub>xy</sub>, respectively.

## 8.2 Results

Figure 8.2 shows the inner/outer volume signal and their ratio for SPGR, bSSFP and STFR. We assume the outer volume excitation is 15% of the inner volume excitation, so an IV/OV steady-state signal ratio larger than 6.7 (1/0.15) means the sequence can suppress the relative outer volume excitation in steady-state, while a ratio smaller than 6.7 means an amplification. STFR can achieve effective outer volume suppression when the tip-down and tip-up angles are similar, with a peak IV/OV ratio of 15.5 at tip-down/tip-up flip angle 15°/17°. The IV/OV ratio is 10.5 for the tip-down/tip-up angle used in our experiment (10°/10°). In contrast, both bSSFP and SPGR has lower IV/OV ratio, showing amplification of the relative outer volume signal. With the flip angles used in our experiment, the IV/OV ratios are 4.3 and 2.2 for bSSFP and SPGR, respectively.

Figure 8.3 shows the *in vivo* experimental results for IVex-SPGR, IVex-bSSFP, IVex-STFR, and non-selective bSSFP. Eight representative slices spanning the 21 cm FOV in *z* are shown. The gray scale is normalized by the maximum image value of each acquisition. The inner volume in bSSFP and STFR shows similar tissue contrast, consistent with previous reports [66, 93]. However the IVex-bSSFP images have undesired outer volume signal, especially near banding regions. This may be due to the fact that bSSFP can have hyperintense signal near the banding edge even for low flip angles. The outer volume in IVex-STFR is effectively suppressed. We think there are two reasons for this: first, the outer volume spins are partially suppressed by the tip-up pulse and RF spoiling, as demonstrated in the simulation

(Figure 8.2); second, STFR does not have the hyperintense signal behavior near band edges [89]. The IVex-SPGR images show very strong relative outer volume signal. The mean relative outer volume signal is 0.42/0.25/0.08 for IVex-SPGR, IVex-bSSFP, and IVex-STFR, respectively, consistent with our simulation (Figure 8.2).

Figure 8.4 shows the simulated rFOV acquisition results for two reduction factors: one with 10x10 cm<sup>2</sup> FOV in plane and 7 cm FOV in z; the other one with 8x8 cm<sup>2</sup> FOV in plane and 3.5 cm FOV in z. We also show the cropped full FOV Cartesian acquisition images and the differences images (multiply by 5) for comparison. With 10x10 cm<sup>2</sup> FOV<sub>xy</sub> and 7 cm FOV<sub>z</sub>, the rFOV acquired results are quite close to the true images. We see more artifacts with 8x8 cm<sup>2</sup> FOV<sub>xy</sub> and 3.5 cm FOV<sub>z</sub> acquisition.

Table 8.1 shows the relative errors for different reduction factors. The relative error increases as the acquisition FOV decreases.

### 8.3 Discussion

There may be several ways to reduce the direct outer-volume excitation without compromising IV excitation accuracy significantly. First, since the steady-state signal is relatively insensitive to flip angle in our operating region (e.g., 10–15°) compared to the low flip angle region, we can partially relax the excitation requirement for the IV by using a smaller weighting for the IV and a larger weighting for the OV in the pulse design cost function. Another possibility is to limit the maximum excitation error instead of the L2 norm of the error in the OV, by generating an RF pulse using the method in [96]. Second, most of the excitation error occurs at the boundary between IV and OV, where target excitation changes sharply, so the optimization algorithm may put more effort to minimize error in this region. However, the error near the boundary is actually not important since we can slightly increase our imaging FOV to cover this region. Therefore, we can exclude the boundary region from the pulse design cost function [103], so the optimization can focus more on the interior of IV and OV. Alternatively, one could smooth the target excitation pattern so the cost function is less dominated by the error in the boundary region. Furthermore, one could use parallel excitation to further improve the excitation accuracy. Finally, in our work, we use 10° flip angle, to match the 10° Ernst angle of SPGR acquisition. However, as our simulation suggested, a higher flip angle around 15° may lead to better relative OV signal suppression.

In addition to improving the 3D selective pulse itself to reduce OV signal, we can

also incorporate a slab-selective OV suppression pulse between the tip-up pulse and the gradient crusher to further suppress the OV signal.

## 8.4 Conclusion

By combing the recently proposed joint pulse design method and the STFR sequence, we were able to achieve successful inner volume imaging with bSSFP-like image contrast, using a 4 ms RF pulse and single transmit coil.

Table 8.1: Relative percent error with different readout FOV

	24 cm FOV <sub>xy</sub>	12 cm FOV <sub>xy</sub>	10 cm FOV <sub>xy</sub>	8 cm FOV <sub>xy</sub>
21 cm FOV <sub>z</sub>	1 %	6 %	8 %	12 %
10.5 cm FOV <sub>z</sub>	3 %	7 %	9 %	13 %
7 cm FOV <sub>z</sub>	4 %	8 %	10 %	14 %
3.5 cm FOV <sub>z</sub>	6 %	10 %	13 %	18 %

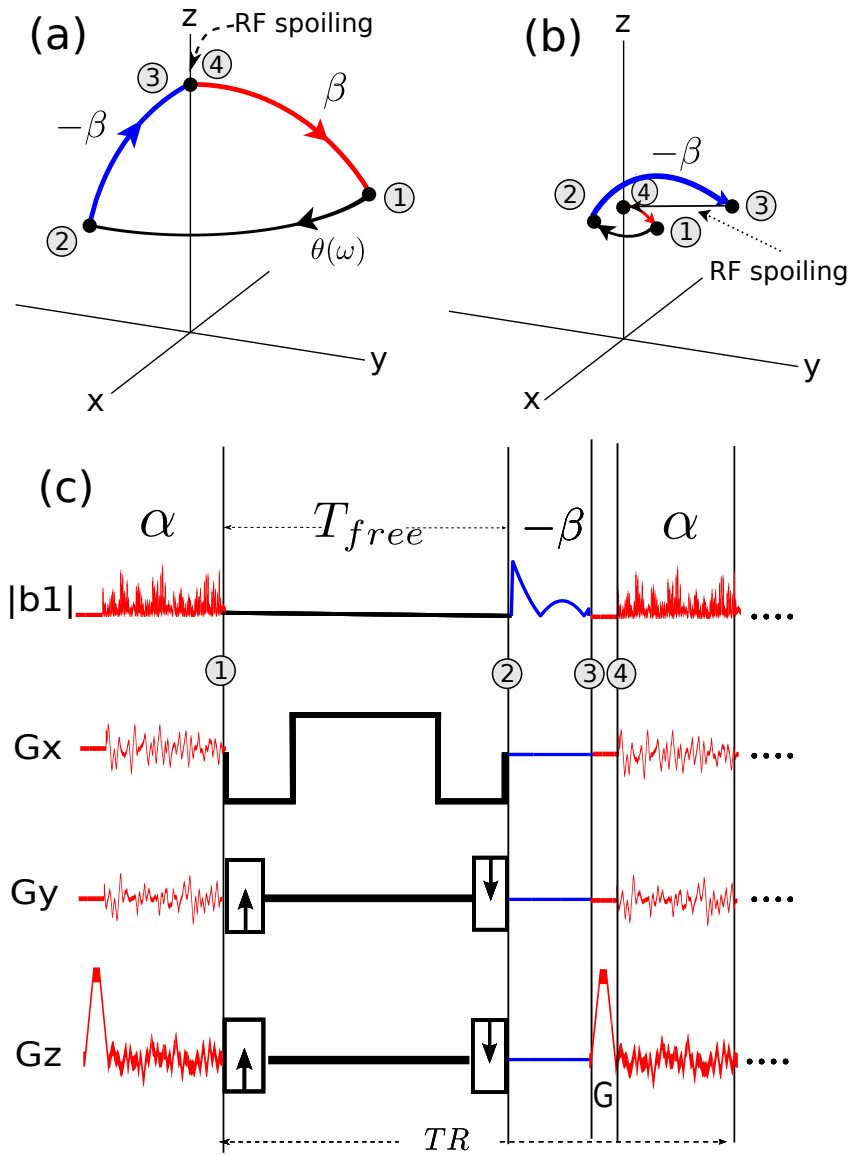


Figure 8.1: Proposed 'IVex-STFR' sequence with 3D selective tip-down pulse and spectral pre-winding tip-up pulse. (a-b) Spin paths for inner volume (IV) (a) and outer volume (OV) (b) regions. (c) Pulse sequence timing diagram. The IV region experiences both tip-down and tip-up pulses. The OV region mainly experiences the tip-up pulse. The use of RF spoiling will spoil and partially suppress the steady-state OV signal [66].

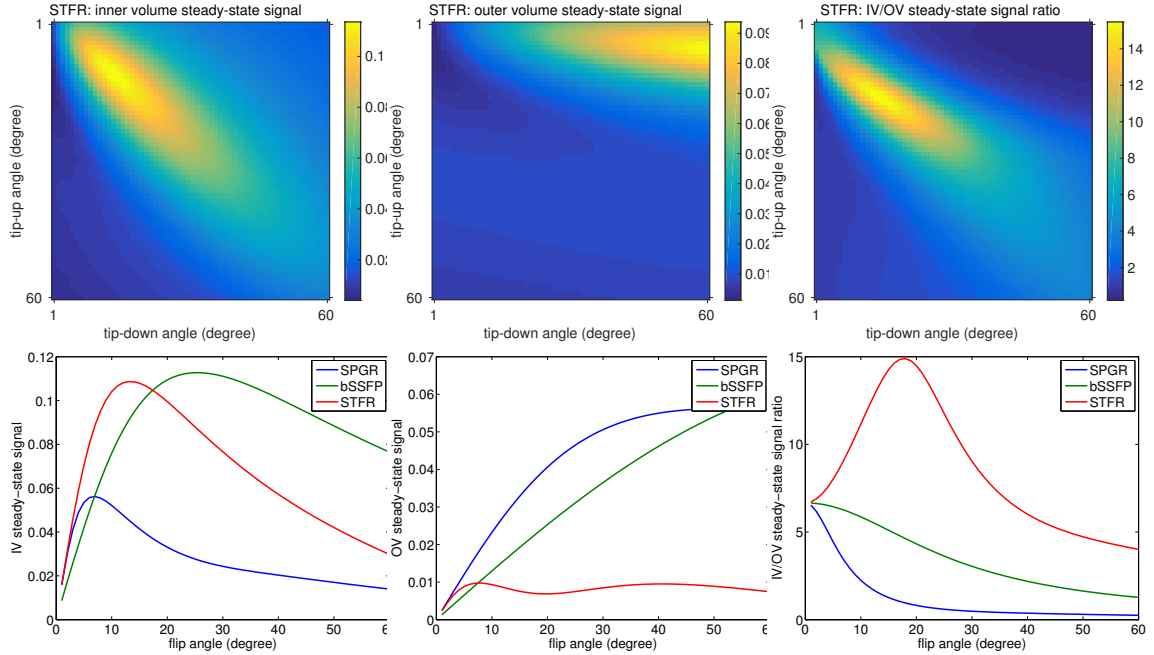


Figure 8.2: Inner volume, outer volume signal and their ratio for STFR, bSSFP and SPGR. The top row shows STFR results with different tip-down and tip-up angles. The bottom row shows SPGR, bSSFP results, and STFR result with tip-down angle equal to tip-up angle. We assume the one shot excitation in the outer volume is 15% of the inner volume, so a IV/OV steady state signal ratio larger than  $1/0.15$  means the sequence can suppress the relative outer volume signal, such as STFR with similar tip-down and tip-up angle. In contrast, bSSFP and SPGR can amplify the relative outer volume signal. With the flip angles used in our experiment, the IV/OV ratios are 10.5, 4.3, 2.2, for STFR, bSSFP, and SPGR, respectively.

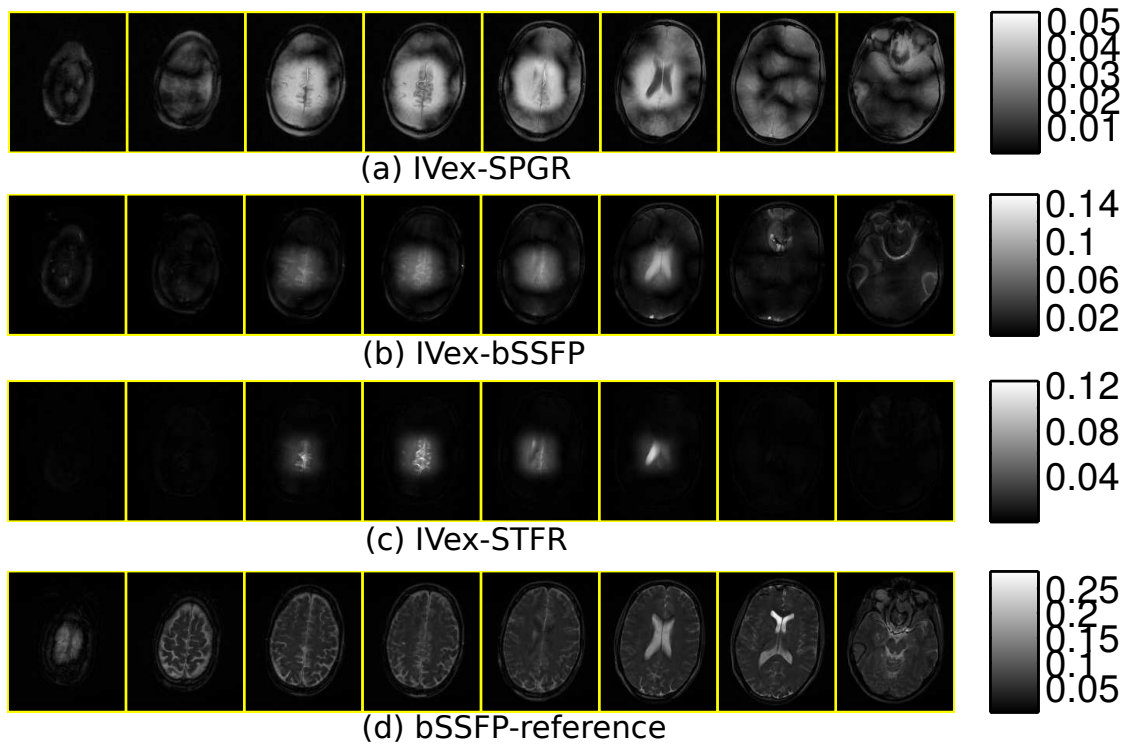


Figure 8.3: Steady-state brain imaging without and with inner volume excitation. (a) IVex-SPGR, (b) IVex-bSSFP, (c) IVex-STFR, (d) Conventional bSSFP. Images are windowed to the maximum intensities of the corresponding acquisitions. As desired, bSSFP and STFR show similar tissue contrast for inner volume spins. STFR has good outer volume suppression. The IV/OV ratios are 12.5/4/2.4 for IVex-STFR, IVex-bSSFP, and IVex-SPGR, respectively, consistent with our simulation. The SNR of bSSFP and STFR are similar, about twice as SPGR according to our theory [93]

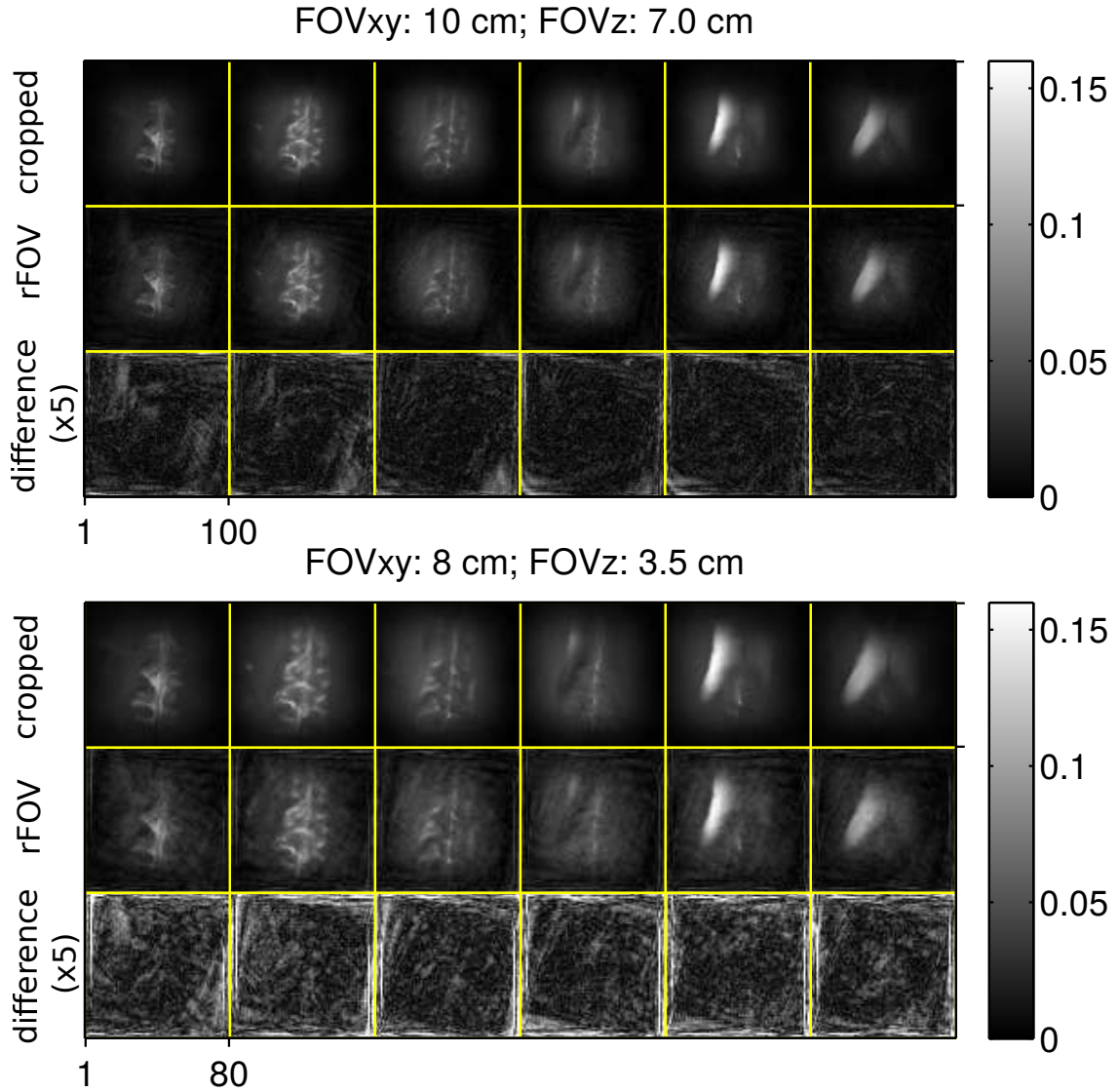


Figure 8.4: Simulated rFOV acquisition with different reduction factors. Cropped full FOV images (top row) and difference images (bottom row) are also shown for comparison. The difference images are multiplied by 5 to better observing the artifacts. We can obtain good results when  $\text{FOV}_{xy}/\text{FOV}_z = 10 \text{ cm}/7 \text{ cm}$ . When the acquisition FOV approximately equal to the excitation region, we observe more aliasing artifacts, but the images may be still usable for some applications.

## CHAPTER IX

# Regularized Estimation of Bloch-Siegert $|B_1^+|$ Maps in MRI

### 9.1 Introduction

<sup>1</sup>Mapping the magnitude of the RF transmit magnetic field ( $|B_1^+|$ ) is important for a variety of applications in MRI, such as parallel transmission [42, 119, 23], electrical property tomography [43]. Various methods have been proposed for  $|B_1^+|$  mapping, like double-angle method [37], actual flip-angle imaging (AFI) [102]. Recently Sacolick et al. [75] proposed using the Bloch-Siegert (BS) shift for  $|B_1^+|$  mapping. The method has the advantages of speed, relatively large dynamic range, and robustness to relaxation and off-resonance. However, the conventional method of moments (MOM) estimator proposed in [75] can be inaccurate in regions with low image magnitude, because the BS method relies on the phase difference between two acquisitions, and the phase difference calculation can be quite noisy in those regions. Also, because the image magnitude is proportional to the tissue properties and the flip angle of the excitation pulse in the BS mapping sequence, and is not influenced by the BS encoding pulse itself, it is possible that those low magnitude regions will coincide with high  $|B_1^+|$  values, resulting in noisy  $|B_1^+|$  estimates where it is important for subsequent pulse design. This chapter proposes a penalized likelihood estimator that is less sensitive to this type of problem, and develops and compares several optimization algorithms. We compare our methods to the conventional  $|B_1^+|$  estimator using both simulation and experimental data sets.

---

<sup>1</sup>This chapter is based on the publications [95]

## 9.2 Model

### 9.2.1 Bloch Siegert B1 Mapping

A Bloch-Siegert  $|B_1^+|$  mapping sequence acquires two images; each one is a gradient echo image with an excitation pulse followed by an off-resonance pulse (Fermi pulse is often used [75]). The off-resonance frequency of the Fermi pulses in those two acquisitions are often set to be opposite in practice to eliminate the first-order Bloch-Siegert phase shift dependence on the B0 effect [75]. Define  $\mathbf{b} = [|B_{1,1}^+|, \dots, |B_{1,N}^+|]^T$  to be the vector of unknown  $|B_1^+|$  map values, and  $\mathbf{f} = [f_1, \dots, f_N]^T$  to be the unknown complex-valued image in the absence of a Fermi pulse, where  $N$  is the number of pixels. The mathematical model for the complex signal at spatial location  $j$  in these two images is:

$$\begin{aligned} y_j^1 &= f_j e^{ikb_j^2} + \epsilon_j^1 \\ y_j^2 &= f_j e^{-ikb_j^2} + \epsilon_j^2 \end{aligned} \quad (9.1)$$

where  $k$  is a known constant determined by the pulse shape and off-resonance frequency of the pulse, and  $\epsilon_j$  is the complex Gaussian noise. The method of moments estimator in current use is given by:

$$|\hat{B}_{1,j}^+| = \sqrt{\frac{\angle(y_j^1 y_j^{2*})}{2k}} \quad (9.2)$$

The phase calculation can be dominated by noise when  $f_j$  is small, leading to inaccurate estimation.

### 9.2.2 Penalized Likelihood Estimation

To improve the  $|B_1^+|$  mapping, we propose a penalized-likelihood estimator. The joint maximum likelihood estimate of  $\mathbf{b}$  and  $\mathbf{f}$  is the minimizer of the following cost function subject to  $\mathbf{b} \geq 0$ :

$$\begin{aligned} \Psi_{\text{ML}}(\mathbf{b}, \mathbf{f}) &= \frac{1}{2} \sum_{i=1}^N |y_j^1 - f_j e^{ikb_j^2}|^2 \\ &\quad + \frac{1}{2} \sum_{i=1}^N |y_j^2 - f_j e^{-ikb_j^2}|^2 \end{aligned} \quad (9.3)$$

This function is quadratic and separable in  $f_j$  and the ML estimate for  $f_j$  (given  $\mathbf{b}$ )

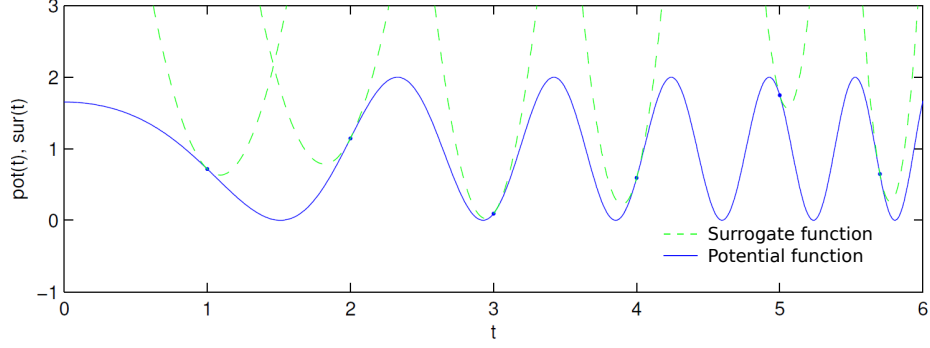


Figure 9.1: Illustration of the potential function and its surrogate.

is:

$$\hat{f}_j = \frac{1}{2}(y_j^1 e^{-ikb_j^2} + y_j^2 e^{ikb_j^2}) \quad (9.4)$$

Substituting this into the cost function (9.3) yields

$$\Psi_{\text{ML}}(\mathbf{b}) = \sum_{j=1}^N |y_j^1 y_j^2| [1 - \cos(2kb_j^2 - \angle y_j^1 + \angle y_j^2)]. \quad (9.5)$$

The ML estimator of  $\mathbf{b}$  ignores the prior knowledge that the  $|B_1^+|$  map tends to be spatially smooth due to the physical nature of the transmit field. A natural approach to incorporating this characteristic is to add a roughness penalty to form the following penalized-likelihood cost function:

$$\Psi(\mathbf{b}) = \sum_{j=1}^N |y_j^1 y_j^2| [1 - \cos(2kb_j^2 - \angle y_j^1 + \angle y_j^2)] + R(\mathbf{b}) \quad (9.6)$$

We estimate the  $|B_1^+|$  map  $\mathbf{b}$  by solving the following minimization problem:

$$\hat{\mathbf{b}} = \arg \min_{\mathbf{b} \in \mathbb{R}^N; \mathbf{b} \geq 0} \Psi(\mathbf{b}) \quad (9.7)$$

The non-negativity constraint can be relaxed in practice since a pixel with negative estimated value typically has very low  $B_1^+$  magnitude and can be set to 0 after solving the unconstrained problem.

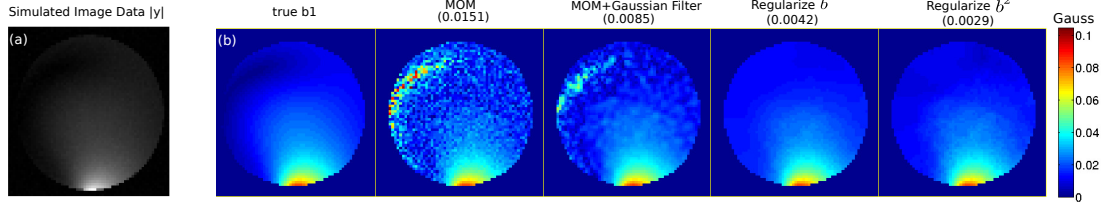


Figure 9.2: Results for the simulated data set. (a) simulated image data (magnitude). (b) Estimated  $|B_1^+|$  maps. The RMSE in Gauss for all methods are shown in the parentheses. Both PL estimators generate more accurate  $|B_1^+|$  maps than the MOM and MOM+smoothing approach.

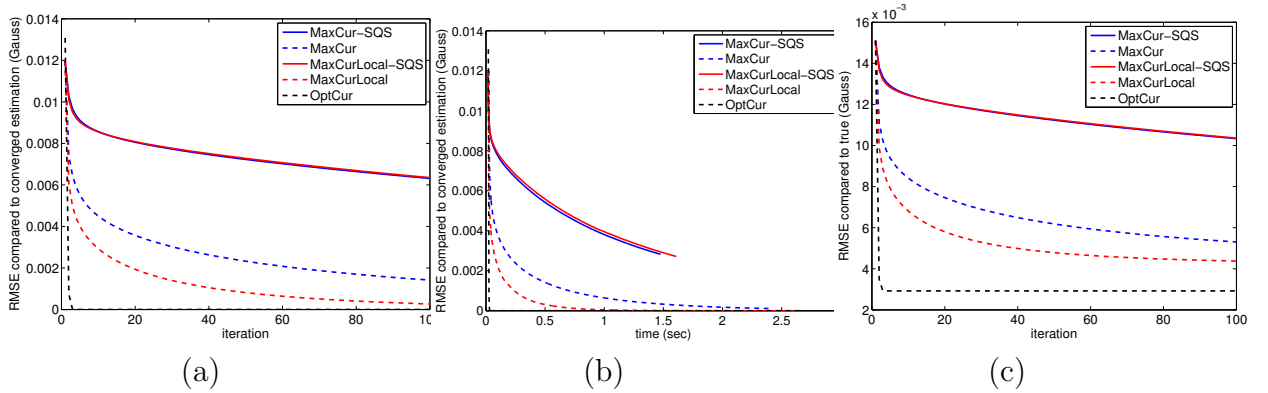


Figure 9.3: Plots of RMSE in Gauss compared to the converged estimation with respect to iteration (a) and time (b). Plots of RMSE compared to the true  $|B_1^+|$  with respect to iteration (c). Using true Hessian for the regularization term instead of SQS greatly improves the convergence rate. Using cost function (9.16) and its optimal curvature converges the fastest.

### 9.3 Minimization Algorithms

This section proposes to solve the optimization problem (9.7) using optimization transfer methods [38]. We consider several possible surrogate function designs.

#### 9.3.1 Maximum Curvature for the ML Term

Let  $t_j^2 = 2kb_j^2$  and  $\gamma_j = -\angle y_j^1 + \angle y_j^2$ , then the maximum likelihood data fitting term can be expressed as

$$\Psi_{\text{ML}}(\mathbf{t}) = \sum_{j=1}^N |y_j^1 y_j^2| \psi(t_j). \quad (9.8)$$

where  $\psi(t) = 1 - \cos(t^2 + \gamma)$ . The first order derivative of  $\psi(t)$  is

$$\dot{\psi}(t) = 2t \sin(t^2 + \gamma), \quad (9.9)$$

which does not satisfy the Huber's conditions [36, P.184] because  $\dot{\psi}(t)/t$  is not non-increasing for  $t > 0$ . Furthermore, the second order derivative is

$$\begin{aligned} \ddot{\psi}(t) &= 4t^2 \cos(t^2 + \gamma) + 2 \sin(t^2 + \gamma) \\ &= 2\sqrt{4t^4 + 1} \cos(t^2 + \gamma - \arctan(\frac{1}{2t^2})). \end{aligned}$$

which is unbounded as  $t$  goes to  $\infty$ , so a ‘‘maximum curvature’’ approach is also infeasible in theory. However, the  $|B_1^+|$  field is typically bounded in practice; therefore,  $t$  is also bounded and we can design a ‘‘maximum curvature’’ by assuming an upper bound of  $t$ . Assuming  $t \in [0, t_{\max}]$ , then  $\ddot{\psi}(t) \leq 2\sqrt{4t^4 + 1} \leq 2\sqrt{4t_{\max}^4 + 1}$ , so we can use a quadratic surrogate function with the following curvature:

$$\check{c} = 2\sqrt{4t_{\max}^4 + 1} \quad (9.10)$$

In this approach, we must consider the box constraint  $[0, t_{\max}]$ ; we can either project the solution to the feasible set in each iteration if using a separate quadratic surrogate, or set a relatively large  $t_{\max}$  such that the estimated value in each iteration is always smaller than  $t_{\max}$  in practice.

However, this maximum curvature approach may lead to slow convergence. Fig. 1 shows that the potential function  $\psi$  is an oscillating function with the same upper and lower bound in each cycle; a quadratic surrogate in one cycle is guaranteed to be a surrogate over the entire feasible domain, leading to the following quadratic surrogate design.

The function  $\psi(t)$  has a local maximum at every  $t_n^{\max} = \sqrt{2\pi n + \pi - \gamma}$  if  $\gamma < \pi$ ,  $t_{-1}^{\max} = 0$  if  $\gamma > \pi$ . For any  $s \geq t_1^{\max}$ , let  $n(s) = \lfloor \frac{s^2 + \gamma - \pi}{2\pi} \rfloor$ , then  $s$  is in the interval  $[t_{n(s)}^{\max}, t_{n(s)+1}^{\max}]$ , and therefore an upper bound on the curvature over this cycle containing  $s$  is

$$\check{c}(s) = 2\sqrt{4(t_{n(s)+1}^{\max})^4 + 1}. \quad (9.11)$$

Thus we create a separable quadratic surrogate for the negative log-likelihood based on this upper bound.

### 9.3.2 Minimization of the Surrogate Function

Because  $|B_1^+|$  maps are smooth, we use the following quadratic roughness penalty:

$$R(\mathbf{b}) = \frac{1}{2}\beta\|\mathbf{C}\mathbf{b}\|^2 \quad (9.12)$$

where  $\beta$  is the regularization parameter, and  $\mathbf{C}$  is the first-order 2D finite difference matrix. Combining with the surrogate function for the ML term, we get the following surrogate function for the cost function:

$$\begin{aligned} \Phi(\mathbf{b}; \mathbf{b}^{(n)}) &= \Psi(\mathbf{b}^{(n)}) + \nabla\Psi(\mathbf{b}^{(n)})(\mathbf{b} - \mathbf{b}^{(n)}) \\ &+ \frac{1}{2}(\mathbf{b} - \mathbf{b}^{(n)})'\mathbf{D}(\mathbf{b} - \mathbf{b}^{(n)}) + \frac{1}{2}\beta\mathbf{b}'\mathbf{C}'\mathbf{C}\mathbf{b} \end{aligned} \quad (9.13)$$

where  $\mathbf{D}$  is the diagonal matrix with elements  $d_j^{(n)} = 2k|y_j^1 y_j^2| \check{c}(\sqrt{2kb_j^{(n)}})$ , where  $\check{c}(\cdot)$  is defined in (9.10).

The Hessian matrix of the surrogate is  $\mathbf{H}^{(n)} = \mathbf{D}^{(n)} + \beta\mathbf{C}'\mathbf{C}$ . We investigate two ways to deal with this Hessian. First, we can design a diagonal majorizer for  $\mathbf{C}'\mathbf{C}$ , namely  $\mathbf{C}'\mathbf{C} \leq 4\mathbf{I}$ , leading to the following algorithm:

$$\mathbf{b}^{(n+1)} = \mathbf{b}^{(n)} - \text{diag}\left\{\frac{1}{d_j^{(n)} + 4\beta}\right\}\nabla\Psi(\mathbf{b}^{(n)}) \quad (9.14)$$

Alternatively, since  $\mathbf{C}'\mathbf{C}$  has a sparse banded structure, we can calculate  $\mathbf{H}^{-1}\nabla\Psi(\mathbf{b}^{(n)})$  efficiently by sparse Cholesky factorization techniques [1], leading to the following Huber's algorithm:

$$\mathbf{b}^{(n+1)} = \mathbf{b}^{(n)} - \mathbf{H}^{(n)-1}\nabla\Psi(\mathbf{b}^{(n)}) \quad (9.15)$$

### 9.3.3 Alternative Formulation

In the above approach, the curvature for the data fitting term is suboptimal, and it is not straight forward to find the optimal curvature. Alternatively, we can change the regularization term in (9.7) to a roughness penalty on  $\mathbf{b}^2$  instead of  $\mathbf{b}$ . Letting  $\mathbf{x} = \mathbf{b}^2$ , the problem to solve becomes:

$$\begin{aligned} \hat{\mathbf{x}} &= \arg \min_{\mathbf{x} \in \mathbb{R}^N; \mathbf{x} \geq 0} \sum_{j=1}^N |y_j^1 y_j^2| \\ &[1 - \cos(2kx_j - \angle y_j^1 + \angle y_j^2)] + R(\mathbf{x}) \end{aligned} \quad (9.16)$$

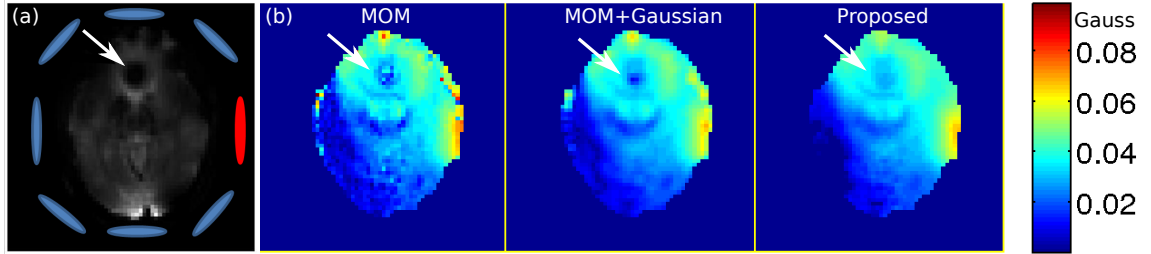


Figure 9.4: Results for the *in vivo* data set: (a) acquired image with BS encoding from one of 8 channel transmit coil (red ellipse), (b) estimated  $|B_1^+|$  map from the method of moments and the proposed penalized likelihood method (9.16). Artifact (arrow) due to  $T_2^*$  signal drop is greatly reduced in the proposed method. Also, our method removes the popcorn noise observed around the periphery of the head, and that noise can significantly affect subsequent RF pulse designs.

where  $R(\cdot)$  is the same quadratic roughness penalty defined in Eq. (9.12). The data fitting term in this formulation satisfies Huber's condition [21], and we can therefore design a SQS with optimal curvature as in [21]:

$$\check{c}(x_j) = 4k^2 |y_j^1 y_j^2| \frac{\sin(s_j^{(n)})}{s_j^{(n)}} \quad (9.17)$$

where  $s_j^{(n)} = (2kx_j - \angle y_j^1 + \angle y_j^2) \bmod \pi \in [-\pi, \pi]$ . Then we get the following Huber's algorithm:

$$\mathbf{x}^{(n+1)} = \mathbf{x}^{(n)} - \mathbf{H}^{(n)-1} \nabla \Psi(\mathbf{x}^{(n)}) \quad (9.18)$$

where  $\mathbf{H}^{(n)} = \mathbf{D}^{(n)} + \beta \mathbf{C}' \mathbf{C}$ , and where  $\mathbf{D}^{(n)}$  is a diagonal matrix with element  $\mathbf{D}_{jj}^{(n)} = \check{c}(x_j^{(n)})$ .

This formulation differs from Eq. (9.7) in the sense that we are regularizing the spatial variation of  $\mathbf{b}^2$  instead of  $\mathbf{b}$ , so now  $R(\mathbf{b}^2) = \beta \sum_{j=1}^N (b_j^2 - b_{j-1}^2)^2 = \beta \sum_{j=1}^N (b_j + b_{j-1})^2 (b_j - b_{j-1})^2$ . Compared to  $R(\mathbf{b})$ , we are putting more regularization in the region with high transmit field strength, which may be undesired. One could compensate for this effect by adding a weighting matrix in the regularization if needed.

## 9.4 Simulation and Experimental Results

We compared the penalized likelihood methods with the method of moments with both simulated and measured data. The simulated data were synthesized for one

channel of a 8-channel transmit array in the image domain by applying the  $\sin |B_1^+(\vec{r})|$  magnitude weighting and BS phase shift to an uniform ball phantom image and then adding Gaussian white noise with 60 dB SNR. Figure 2(b) shows the simulated true  $|B_1^+|$  map and reconstruction maps using different methods. The MOM estimate suffers from large noise, especially in the region with low transmit magnitude. Applying Gaussian low pass filter to the MOM estimate is a conventional way to improve the result in practice, but still shows mismatch in the region with low transmit magnitude. Both PL estimates using formulation (9.7) and (9.16) generate more accurate maps. Figure 3 shows convergence plot using different minimization methods with respect to iteration (a) and time (b). In the maximum curvature approach (9.10), we assume maximum  $|B_1^+| = 0.2$  Gauss, which is larger than the maximum  $|B_1^+|$  in this simulated data and a reasonable upper limit in practice. Using the local maximum curvature (9.11) has faster convergence rate than using the global maximum curvature (9.10). The Cholesky approach is implemented in MATLAB using “\”, which converges faster than the SQS approach, with respect to iteration and time. The fastest algorithm is using formulation (9.16) with the optimal curvature and the Cholesky factorization, which converges in just 3 iteration. Figure 2 (c) shows the error plot compared to the true  $|B_1^+|$  map for each method.

The proposed methods were also validated with real experiment data. Data were acquired with a 8 channel transmit/receive array in a GE 3.0 T scanner. A 12 ms,  $\pm$  4KHz Bloch-Siegert encoding pulse was transmitted in one of the 8 coil (see, red ellipse in Fig. 4(a)). We used 64x64 spin warp readout, 24 cm FOV, TE = 15 ms. The acquired image is shown in Fig. 3(a), which shows a dark hole due to large T2\* signal drop. Figure 4(b) shows the  $|B_1^+|$  estimates using the MOM, MOM with Gaussian low pass filter, and the proposed method (9.16). We observe a steep  $|B_1^+|$  drop in the frontal sinus region from the MOM based estimation (see the arrow), which is unexpected because the  $|B_1^+|$  should change relatively smoothly in brain in 3T. The proposed approach greatly reduced this artifact. Also, our method removes the popcorn noise observed around the periphery of the head, and that noise can significantly affect subsequent RF pulse designs. We tried adding weighting matrix to the regularization in (9.16) to compensate the difference between  $R(\mathbf{b}^2)$  and  $R(\mathbf{b})$ , but it made little difference in both simulation and experimental data sets (not shown).

## 9.5 Discussion

During the writing of this chapter, we noticed [112] also proposed a regularized Bloch-Siegert  $|B_1^+|$  mapping method that uses similar formulation as our proposed method. However, in [112], a simple gradient descent (GD) method is used, which is much slower than our proposed optimization method.

In the future, we plan to combine the proposed estimation method with lower energy Fermi pulses to reduce the specific absorption rate (SAR) without sacrificing the B1 mapping accuracy. Also, we will try to extend our method to the optimized Bloch-Siegert encoding pulses [44, 39].

## 9.6 Conclusion

We proposed a penalized likelihood estimator for Bloch-Siegert  $|B_1^+|$  mapping in the image domain, and compared several optimization algorithms to solve this problem. By penalizing  $|B_1^+|^2$  instead of  $|B_1^+|$ , we can find an optimal curvature quadratic surrogate and solve the problem efficiently using Huber’s algorithm with Cholesky factorization technique. The proposed method is validated in both simulated data set and *in vivo* data, showing reduced noise and artifact compared to the conventional MOM based methods.

## CHAPTER X

### Future Work

Whole brain STFR is still a challenging problem. There are some possible ways to improve it. First, the proposed joint design of k-space trajectory and RF pulse method should lead to improved result. Second, parallel excitation may improve the excitation accuracy dramatically. In practice, a difficulty in whole brain STFR is that it is harder to design a prephasing pulse with slice/slab selectivity compared with a non-slice/slab selective tailored pulse. Without the slice/slab selectivity, full brain encoding is typically necessary to avoid the aliasing artifacts in the z-direction, leading to long total acquisition time. One way to avoid the full FOV acquisition in z is to use frequency encoding in the z-direction, but it may also lead to long acquisition time since the total number of TR can be large due to phase encoding in both x and y directions. Parallel imaging may be necessary here to limit the total acquisition time. Another possible way to limit the FOV in z is to apply a slab saturation pulse before the gradient crusher. We may also want to try STFR with different phase cycling and then combine the images to remove the signal drop.

Inner-volume STFR is a very promising research direction, since STFR suppresses the outer volume excitation in our 3D excitation, and the 3D inner-volume excitation pulse reduces the target bandwidth of STFR. There are several ways to improve the inner-volume STFR. First, the STFR steady-state signal is relatively insensitive to flip angle in our operating regime compared to the low flip angle regime. A simple way to utilize this property is to partially relax the excitation requirement for the IV by using a smaller weighting for the IV and a larger weighting for the OV in the pulse design cost function. A more sophisticated way is to directly put the steady-state signal into the cost function, instead of the one shot excitation. Since the steady-state signal equation is not a linear function of the RF pulse, we may have to use some non-linear optimization methods to solve this problem. This “steady-state pulse design” idea may be applied to other steady-state sequences as well, since most

steady-state sequences have a operating regime that is relatively insensitive to flip angle. Second, if we know the readout gradient in advance, we can directly consider the image from reduced FOV acquisition instead of the full excitation pattern. In this way, we can relax the excitation requirement since outer volume excitation is allowed as long as it is not aliased into our ROI. Finally, some target patterns other than the sharp-edge cube used in our current work may be easier to achieve for the RF pulse. We may also want to evaluate inner volume STFR in more applications, like high speed functional MRI, or MR microscopy in body.

For the spectral-STFR work in Chapter V, there are many possibilities in the pulse design side and the application side. Large-tip-angle pulse design method is capable of targeting a larger bandwidth, but leads to lower steady-state signal and higher SAR. It is worth a real scan to see if it satisfies the SAR limit and if there is unknown image contrast due to finite RF effect. We may need to develop a SAR constrained approach. Using spectral-spatial pulse instead of pure spectral pre-winding pulse can potentially be beneficial, as demonstrated in [101]. To further improve the spectral-spatial pulse, k-space trajectory should also be optimized, where the joint design method from Chapter VII may be applied. Also, we could also try to exploit the property that the final steady-state signal is insensitive to the flip angle over a certain range (e.g.,  $16^\circ$  to  $25^\circ$ ). We can also incorporate fat-suppression pulses into the sequence and test it for cranial nerve imaging. The flow effect in STFR has not been well investigated yet and is worth studying.

For the joint design of RF pulse and k-space trajectory in Chapter VII, we can explore other possible basis functions and optimization methods, like higher-order B-spline and ADMM algorithm. It is possible that a non-monotone decreasing algorithm can lead to lower cost function than our current algorithm with the same amount of time. Also, the algorithms evaluated are all local optimization algorithms, and we can try random perturbations to the initialization to find a better local minimum, or try some global optimization algorithms like simulated annealing. Another possible future work is to extend our algorithm to parallel excitation. The modifications to equations are easy, as I presented in Chapter VII. However, I have not finished modifying the code for simulation, and there may be some computational issues as the size of the system matrix increases due to the increasing number of coils. In our method, we do not directly control the pulse length when generating the extended KT-points initialization, since the pulse length varies case by case even with the same number of KT-points. It may be desirable to have some initialization methods where the pulse length is directly constrained, or formulate the pulse design problem by

putting the excitation error into constraints and minimizing the total pulse length in the cost function.

For the minimax pulse design work in Chapter VI, we may want to evaluate its performance in applications other than the B1 shimming, like STFR or reduced FOV imaging. We may find that a combination of  $l_\infty$  norm and  $l_2$  norm, or some higher-order  $l_p$  norm is more beneficial in practice. I proposed an algorithm for magnitude minimax pulse design, but have not implemented and tested it yet. Also, the RF power is regularized using its  $l_2$  norm, and an explicit RF/SAR constraint may be desirable.

Our regularized B1 mapping method in Chapter IX can be combined with a fast readout trajectory (e.g., spiral) for reduced acquisition time and SAR. Also, extension to B1 encoding pulses other than Fermi pulse [44, 39] is worth investigating.

## APPENDICES

## APPENDIX A

### Derivation of the steady-state signal equation of unspoiled STFR

Referring to Fig. 3.1, we model each spin path segment as follows:

1.  $\mathbf{M}_1$  to  $\mathbf{M}_2$  : Free precession and T1, T2 relaxation.

Define  $\Delta\omega$  as the local off-resonance frequency, and  $T_{\text{free}}$  as the free precession time. The free precession phase is then  $\theta_f = \Delta\omega T_{\text{free}}$ . The Bloch equation in matrix form for this rotation is:

$$\mathbf{M}_2 = \mathbf{P}\mathbf{C}_f\mathbf{M}_1 + \mathbf{D}_f$$

where  $\mathbf{C}_f = \begin{bmatrix} e^{-\frac{T_{\text{free}}}{T_2}} & 0 & 0 \\ 0 & e^{-\frac{T_{\text{free}}}{T_2}} & 0 \\ 0 & 0 & e^{-\frac{T_{\text{free}}}{T_1}} \end{bmatrix}$ ,  $\mathbf{D}_f = (\mathbf{I} - \mathbf{C}_f) \begin{bmatrix} 0 \\ 0 \\ M_0 \end{bmatrix}$ ,

$$\mathbf{P} = \begin{bmatrix} \cos\theta_f & \sin\theta_f & 0 \\ -\sin\theta_f & \cos\theta_f & 0 \\ 0 & 0 & 1 \end{bmatrix}.$$

2.  $\mathbf{M}_2$  to  $\mathbf{M}_3$  : “Tip-up” RF pulse with phase  $\phi$  and flip angle  $\beta$ .

$$\mathbf{M}_3 = \mathbf{R}_u\mathbf{M}_2$$

where  $\mathbf{R}_u = \begin{bmatrix} \cos\phi & \sin\phi & 0 \\ -\sin\phi & \cos\phi & 0 \\ 0 & 0 & 1 \end{bmatrix} \begin{bmatrix} 1 & 0 & 0 \\ 0 & \cos\beta & -\sin\beta \\ 0 & \sin\beta & \cos\beta \end{bmatrix} \begin{bmatrix} \cos\phi & -\sin\phi & 0 \\ \sin\phi & \cos\phi & 0 \\ 0 & 0 & 1 \end{bmatrix}$ .

3.  $\mathbf{M}_3$  to  $\mathbf{M}_4$  : Unbalanced gradient  $g$  rotates  $\mathbf{M}$  about z axis by  $\theta_g$ . Also include T1, T2 relaxation.

$$\mathbf{M}_4 = \mathbf{G}\mathbf{C}_g\mathbf{M}_3 + \mathbf{D}_g$$

$$\text{where } \mathbf{G} = \begin{bmatrix} \cos \theta_g & \sin \theta_g & 0 \\ -\sin \theta_g & \cos \theta_g & 0 \\ 0 & 0 & 1 \end{bmatrix}, \mathbf{C}_g = \begin{bmatrix} e^{-\frac{T_g}{T_2}} & 0 & 0 \\ 0 & e^{-\frac{T_g}{T_2}} & 0 \\ 0 & 0 & e^{-\frac{T_g}{T_1}} \end{bmatrix},$$

$$\mathbf{D}_g = (\mathbf{I} - \mathbf{C}_g) \begin{bmatrix} 0 \\ 0 \\ M_0 \end{bmatrix}.$$

4.  $\mathbf{M}_4$  to  $\mathbf{M}_1$  : The tip-down pulse rotates  $\mathbf{M}$  about the x axis by  $\alpha$ .

$$\mathbf{M}_1 = \mathbf{R}_d \mathbf{M}_4$$

$$\text{where } \mathbf{R}_d = \begin{bmatrix} 1 & 0 & 0 \\ 0 & \cos \alpha & \sin \alpha \\ 0 & -\sin \alpha & \cos \alpha \end{bmatrix}.$$

Combining these steps and requiring that the magnetization reaches a steady-state, we obtain:

$$\begin{aligned} \mathbf{M}_1 &= \mathbf{R}_d(\mathbf{G}\mathbf{C}_g(\mathbf{R}_u(\mathbf{P}\mathbf{C}_f\mathbf{M}_1 + \mathbf{D}_f)) + \mathbf{D}_g) \\ \Rightarrow \mathbf{M}_1 &= (\mathbf{I} - \mathbf{R}_d\mathbf{G}\mathbf{C}_g\mathbf{R}_u\mathbf{P}\mathbf{C}_f)^{-1}(\mathbf{R}_d\mathbf{G}\mathbf{C}_g\mathbf{R}_u\mathbf{D}_f + \mathbf{R}_d\mathbf{D}_g) \end{aligned}$$

We obtain an expression for the transverse part of  $\mathbf{M}$ , i.e., Eq. (3.1), by simplifying the above expression using symbolic math software (MATHEMATICA 8, Wolfram, Champaign, Illinois, USA). The MATHEMATICA code is available on our website (<http://www.umich.edu/~sunhao>)

## APPENDIX B

### Derivation of Hessian matrix with respect to k-space trajectory

We derived the Hessian of the cost function (7.1) with respect to  $\mathbf{k}$  here. Let us define the excitation error term  $\mathbf{e} = \mathbf{d} - \mathbf{S}\mathbf{A}(\mathbf{k}_x, \mathbf{k}_y, \mathbf{k}_z)\mathbf{b}$ . and the  $N_t \times 1$  temporal vector:

$$\mathbf{p}_x = \nabla_{\mathbf{k}_x} f = \nabla_{\mathbf{k}_x} \|\mathbf{e}\|_{\mathbf{W}}^2, \quad (\text{B.1})$$

then the  $j$ th element of  $\mathbf{p}_x$  is

$$p_{xj} = 2\text{Re} \{ \mathbf{e}' \mathbf{W} \mathbf{q}_{xj} \} \quad (\text{B.2})$$

where

$$\begin{aligned} \mathbf{q}_{xj} &= \frac{\partial \mathbf{e}}{\partial k_{xj}} \\ &= -i2\pi \mathbf{S} \mathbf{X} \mathbf{a}_j b_j \end{aligned} \quad (\text{B.3})$$

Then, the  $(i, j)$ th elements of the Hessian matrix are:

$$\begin{aligned} \frac{\partial^2 f}{\partial k_{xi} \partial k_{xj}} &= \frac{\partial p_{xj}}{\partial k_{xi}} \\ &= 2\text{Re} \left\{ \frac{\partial \mathbf{e}'}{\partial k_{xi}} \mathbf{W} \mathbf{q}_{xj} + \mathbf{e}' \mathbf{W} \frac{\partial \mathbf{q}_{xj}}{\partial k_{xi}} \right\} \\ &= 2\text{Re} \left\{ \mathbf{q}'_{xi} \mathbf{W} \mathbf{q}_{xj} + \mathbf{e}' \mathbf{W} \frac{\partial \mathbf{q}_{xj}}{\partial k_{xi}} \right\} \end{aligned} \quad (\text{B.4})$$

For the second term, when  $i \neq j$ ,

$$\frac{\partial \mathbf{q}_{xj}}{\partial k_{xi}} = 0. \quad (\text{B.5})$$

When  $i = j$ ,

$$\frac{\partial \mathbf{q}_{xj}}{\partial k_{xi}} = i2\pi \mathbf{S} \mathbf{X} \mathbf{X} \mathbf{a}_j b_j. \quad (\text{B.6})$$

Then we substitute equation (B.3) (B.5) (B.6) into (B.4), and obtain the elements of the Hessian matrix

$$\begin{aligned} \frac{\partial^2}{\partial k_{xi} \partial k_{xj}} f &= 8\pi^2 \text{Re}\{b_j^* \mathbf{a}'_j \mathbf{X} \mathbf{S}' \mathbf{W} \mathbf{S} \mathbf{X} \mathbf{a}_i b_i\}, \quad i \neq j; \\ \frac{\partial^2}{\partial k_{xi} \partial k_{xj}} f &= 8\pi^2 \text{Re}\{b_j^* \mathbf{a}'_j \mathbf{X} \mathbf{S}' \mathbf{W} \mathbf{S} \mathbf{X} \mathbf{a}_i b_i\} \\ &\quad - 2(2\pi)^2 \text{Re}\{\mathbf{e}' \mathbf{W} \mathbf{S} \mathbf{X} \mathbf{X} \mathbf{a}_i b_i\}, \quad i = j. \end{aligned}$$

In the parallel transmission case, we can modified the above derivation and obtain the following results. Equation B.3 is changed to:

$$\begin{aligned} \mathbf{q}_{xj} &= \frac{\partial \mathbf{e}}{\partial k_{xj}} \\ &= -i2\pi \sum_{r=1}^R \mathbf{S} \mathbf{X} \mathbf{a}_j b_{jr}, \end{aligned} \quad (\text{B.7})$$

where  $N_c$  is the number of coils. Then Equation B.6 becomes:

$$\frac{\partial \mathbf{q}_{xj}}{\partial k_{xi}} = i2\pi \sum_{m=1}^{N_c} \mathbf{S} \mathbf{X} \mathbf{X} \mathbf{a}_j b_j. \quad (\text{B.8})$$

Then we substitute equation (B.7) (B.5) (B.8) into (B.4), and obtain the elements of the Hessian matrix for parallel transmit case:

$$\begin{aligned} \frac{\partial^2}{\partial k_{xi} \partial k_{xj}} f &= 8\pi^2 \text{Re}\left\{ \sum_{m=1}^{N_c} \sum_{n=1}^{N_c} b_{mj}^* \mathbf{a}'_j \mathbf{X} \mathbf{S}'_m \mathbf{W} \mathbf{S}_n \mathbf{X} \mathbf{a}_i b_{ni} \right\}, \quad i \neq j; \\ \frac{\partial^2}{\partial k_{xi} \partial k_{xj}} f &= 8\pi^2 \text{Re}\left\{ \sum_{m=1}^{N_c} \sum_{n=1}^{N_c} b_{mj}^* \mathbf{a}'_j \mathbf{X} \mathbf{S}'_m \mathbf{W} \mathbf{S}_n \mathbf{X} \mathbf{a}_i b_{ni} \right\} \\ &\quad - 2(2\pi)^2 \text{Re}\left\{ \sum_{n=1}^{N_c} \mathbf{e}' \mathbf{W} \mathbf{S}_n \mathbf{X} \mathbf{X} \mathbf{a}_i b_{ni} \right\}, \quad i = j. \end{aligned}$$

## APPENDIX C

### Instructions for STFR experiments

The STFR experiments are not trivial, since there are so many combinations in the settings of RF and gradients. Here are some introductions.

#### **Epic file**

For most of my STFR experiments, I used `stfr*.e`, where `*` means number 1 to 5. Recently, I started using `sos3d.e`. The settings on the console are quite conventional. I used Left/Right as my acquisition direction, to be consistent with my field map and pulse design code, otherwise, the x and y gradients may need to be switched.

#### **B0 field map**

We used two SPGR acquisitions with different TEs to obtain the field map. I usually set the TE difference to be 2.3 ms, so the on-resonance fat spins have the same phase for those two scans. If using different TE differences, the B0 field map reconstruction code has to be checked since I hard code the difference to be 2.3 ms in some of my reconstruction code. Also, Feng Zhao mentioned the B0 map acquired using Doug's sequence and code is negative to the B0 map from Jon's code, so check the source of your code.

#### **Tailored pulse design**

I have three main files for STFR pulse design in the `pulseDesign/stfr/` directory: `m1_main.m`, `bt_main.m`, and `joint_main.m`.

'm1' stands for method 1, meaning only the tip-up pulse is pre-phasing pulse, and the tip-down pulse is just a slice/slab selective pulse. This code was not often used in my work, since most of my work used pre-phasing pulse for both tip-down and tip-up to increase the target BW.

'joint' stands for joint design of tip-down and tip-up (Chapter III).

'bt' stands for both tailored. This code is the mostly used code for both spatial-STFR and spectral-STFR. I implemented 7 different pulse design methods for tip-down and tip-up as listed below.

`spinsrf.m`: spatial-STFR using SPINS trajectory; used in III.

`spectralRF.m`: spectral-STFR using small-tip-angle pulse design; used in V.

`spectralRF_large.m`: spectral-STFR using large-tip-angle pulse design.

`spectralRF_spsp.m`: spectral-STFR using spatial spectral pulse; my old code, not Sydney's code used in [101].

`ktpointsRF.m`: spatial-STFR using KT-points method for tailored pulse.

`ktpoints_contrRF.m`: spatial-STFR using KT-points method with continuous trajectory and RF.

`ktContrRF_greedy2.m`: spatial-STFR using my proposed joint design of excitation k-space and RF VII.

The last 5 code in the list worked correctly for single shot excitation, but have not been fully evaluated and compared to the first two in STFR.

When writing the output gradient waveform from my pulse design code to .wav file, gx has to be negated.

**Data processing** The *in vivo* experiment data used in Chapter III and corresponding processing code can be found in `lab/SPINS_data/`.

## APPENDIX D

### Bloch simulations for steady-state sequences

The core of my Bloch simulation is a mex file `blochCim.c`, that can be found in `mtools/others/BlochSimulator` directory, and can be used directly. I had an interface file named `parallel_blochCim.m` that may be more convenient to use. The `blochCim` function has a steady-state simulation mode that can fast simulate the steady-state. However, this mode is not applicable to pseudo steady-state (e.g., RF spoiled).

The main script for STFR Bloch simulation is in `simulations/ssfp_cim`, named `main_stfr_blochCim.m`. It can simulate spoiled/unspoiled STFR with different pulse and tissue parameters. You can use the same code to simulate bSSFP and SPGR by simply setting proper tip-up angle, gradient crusher cycle, and RF phase increment.

## APPENDIX E

### Data and code for STFR-fMRI

#### Simulations of STFR, BOLD and bSSFP in fMRI

The following 3 main files for simulating STFR, bSSFP, and BOLD in fmri (Chapter IV) can be found in my `simulations/stfr_fmri/` directory.

`monte_carlo_parfor.m`: STFR in fmri.

`bssfp_fmri_parfor.m`: bSSFP in fmri.

`BOLD_SteadyState_parfor.m`: Conventional long TE BOLD in fmri.

`generate_voxel_2d.m` generated the field map of the simulated voxel.

`makefigure_simu.m` generated the plots in Chapter IV.

#### Experimental data and processing

The data and processing code are in my `lab/fmri/resubmission/data/` directory. See README file there for more detail.

## APPENDIX F

### Selected source code for Chapter VI to IX

In this appendix, I summarized the main files for generating the results in minimax pulse design (Chapter VI), joint design of k-space trajectory and RF pulse (Chapter VII), inner volume STFR imaging (Chapter VIII), and regularized B1 map estimation (Chapter IX). Only main files are listed here, and supporting functions can be found in the corresponding folder. Jeffrey Fessler's image reconstruction toolbox must be installed (<http://www.eecs.umich.edu/~fessler>). All other supporting utility functions can be found in my `mtools` folder.

#### Minimax pulse design

The code can be found in `pulseDesign/minimax`. The main files are:

`main_compare.m`: compare minimax design with  $l_2$  norm based design for single coil and fast-kz trajectory.

`main_b0_ptx.m`: minimax pulse design with B0 field map, parallel transmit, and fast-kz trajectory.

`main_minimax_general.m`: minimax pulse design for arbitrary k-space trajectory. RF power is regulated using Tikhonov regularization.

#### Joint design of excitation k-space trajectory and RF pulse

The code can be found in `pulseDesign/kTraj`. The main files are:

`main_ktpoints.m`: main script for KT-points pulse design.

`main_ktCont.m`: main script for my proposed joint design.

`main_compareAll.m`: main script for comparing all the initialization methods.

`main_makeFigurePaper_compareAll.m` main script for generating the figures in Chapter VII.

### **Inner-volume STFR imaging**

The code to generate inner volume excitation pulses are in `pulseDesign/kTraj`, as mentioned above. The code to simulate the stack-of-spiral rFOV acquisition is `simuRFOV.m`, which can be found in `pulseDesign/kTraj/rFOV`. There are three files to simulate the steady-state inner/outer volume signal in `simulations/rFOV` folder: `STFR_IV_OV_blochCim.m`, `bSSFP_IV_OV_blochCim.m`, `SPGR_IV_OV_blochCim.m`

### **Regularized Bloch-Siegert B1 mapping**

The code can be found in `b1PL`. The code to generate B1 encoding pulses (e.g., Fermi pulse) are in `pulseGenCode` subdirectory.

The reconstruction code are in `reconCode` subdirectory:

- `main_b1PL_demo.m`: demo code for the proposed regularized B1 mapping.
- `main_figures.m`: generates simulation results in Chapter IX.
- `main_figures_allCoil_human.m`: generates figures based on human experimental data using parallel transmit coil in Chapter IX.

## BIBLIOGRAPHY

## BIBLIOGRAPHY

- [1] M. J. Allison and J. A. Fessler. Accelerated computation of regularized field map estimates. In *Proc. Intl. Soc. Magn. Reson. Med.*, page 0413, 2012.
- [2] J. Asslander and J. Hennig. Spin echo formation with a phase pre-winding pulse. In *Proc. Intl. Soc. Magn. Reson. Med.*, page 4249, 2013.
- [3] J. Asslander, S. Kocher, S. Glaser, and J. Hennig. Spin echoes in the weak dephasing regime. In *Proc. Intl. Soc. Magn. Reson. Med.*, page 0030, 2014.
- [4] N. K. Bangerter, B. A. Hargreaves, S. S. Vasanaawala, J. M. Pauly, G. E. Gold, and D. G. Nishimura. Analysis of multiple-acquisition SSFP. *Magn. Reson. Med.*, 51:1038–1047, 2004.
- [5] O. Bieri, M. Markl, and K. Scheffler. Analysis and compensation of eddy currents in balanced SSFP. *Magn. Reson. Med.*, 54:129–137, 2005.
- [6] O. Bieri and K. Scheffler. SSFP signal with finite RF pulses. *Magn. Reson. Med.*, 62(5):1232–41, November 2009.
- [7] O. Bieri and K. Scheffler. Extended chimera SSFP. In *Proc. Intl. Soc. Magn. Reson. Med.*, page 76, 2010.
- [8] C.V. Bowen, R.S. Menon, and J.S. Gati. High field balanced-SSFP FMRI: a BOLD technique with excellent tissue sensitivity and superior large vessel suppression. In *Proc. Intl. Soc. Magn. Reson. Med.*, page 119, 2005.
- [9] S. Boyd, N. Parikh, E. Chu, B. Peleato, and J. Eckstein. Distributed optimization and statistical learning via the alternating direction method of multipliers. *Found. & Trends in Machine Learning*, 3(1):1–122, 2010.
- [10] D. Chen, F. Bornemann, M. Vogel, L. Sacolick, G. Kudielka, and Y. Zhu. Sparse parallel transmit pulse design using orthogonal matching pursuit method. In *Proc. Intl. Soc. Magn. Reson. Med.*, page 171, 2009.
- [11] MA Cloos, N Boulant, M Luong, G Ferrand, E Giacomini, D Le Bihan, and A Amadon. kt-points: Short three-dimensional tailored rf pulses for flip-angle homogenization over an extended volume. *Magnetic Resonance in Medicine*, 67(1):72–80, 2012.

- [12] T. Çukur, M. Lustig, and D. G. Nishimura. Improving non-contrast-enhanced steady-state free precession angiography with compressed sensing. *Magn. Reson. Med.*, 61(5):1122–31, May 2009.
- [13] T. Cukur and D. G. Nishimura. Multiple rePETition time balanced steady-state free precession imaging. *Magn. Reson. Med.*, 62(1):193–204, 2009.
- [14] M. Davids, B. Guerin, L.R. Schad, and L.L. Wald. Optimization of fast k-space trajectories for 3d spatially selective parallel excitation. In *Proc. Intl. Soc. Magn. Reson. Med.*, 2014.
- [15] R Deichmann, CD Good, and R Turner. Rf inhomogeneity compensation in structural brain imaging. *Magnetic Resonance in medicine*, 47(2):398–402, 2002.
- [16] DA Feinberg, JC Hoenninger, LE Crooks, L Kaufman, JC Watts, and M Arakawa. Inner volume mr imaging: technical concepts and their application. *Radiology*, 156(3):743–747, 1985.
- [17] J. A. Fessler, S. Lee, V. T. Olafsson, H. R. Shi, and D. C. Noll. Toeplitz-based iterative image reconstruction for MRI with correction for magnetic field inhomogeneity. *IEEE Trans. Sig. Proc.*, 53(9):3393–402, September 2005.
- [18] J. A. Fessler and B. P. Sutton. Nonuniform fast Fourier transforms using min-max interpolation. *IEEE Trans. Sig. Proc.*, 51(2):560–74, February 2003.
- [19] J.A. Fessler. Image reconstruction toolbox. <http://web.eecs.umich.edu/~fessler/code/index.html>.
- [20] S. D. Forman, J. D. Cohen, M. Fitzgerald, W. F. Eddy, M. A. Mintun, and D. C. Noll. Improved assessment of significant change in functional magnetic resonance imaging (fMRI): Use of a cluster size threshold. *Magn. Reson. Med.*, 33(5):636–47, May 1995.
- [21] A. K. Funai, J. A. Fessler, D. T. B. Yeo, V. T. Olafsson, and D. C. Noll. Regularized field map estimation in MRI. *IEEE Trans. Med. Imag.*, 27(10):1484–94, October 2008.
- [22] C. R. Genovese, D. C. Noll, and W. F. Eddy. Estimating test-retest reliability in functional MR imaging I: Statistical methodology. *Magn. Reson. Med.*, 38(3):497–507, September 1997.
- [23] W. Grissom, C. Yip, Z. Zhang, V. A. Stenger, J. A. Fessler, and D. C. Noll. Spatial domain method for the design of RF pulses in multi-coil parallel excitation. *Magn. Reson. Med.*, 56(3):620–9, September 2006.
- [24] W. A. Grissom, M-M. Khalighi, L. I. Sacolick, B. K. Rutt, and M. W. Vogel. Small-tip-angle spokes pulse design using interleaved greedy and local optimization methods. *Magn. Reson. Med.*, 2012.

- [25] W. A. Grissom, D. Xu, A. B. Kerr, J. A. Fessler, and D. C. Noll. Fast large-tip-angle multidimensional and parallel RF pulse design in MRI. *IEEE Trans. Med. Imag.*, 28(10):1548–59, October 2009.
- [26] W. A. Grissom, C-Y. Yip, S. M. Wright, J. A. Fessler, and D. C. Noll. Additive-angle method for fast large-tip-angle RF pulse design in parallel excitation. In *Proc. Intl. Soc. Magn. Reson. Med.*, page 1689, 2007.
- [27] E.M. Haacke, S.Lai, J.R. Reichenbach, K. Kuppusamy, F.G.C. Hoogenraad, H. Takeichi, and W. Lin. In vivo measurement of blood oxygen saturation using magnetic resonance imaging: A direct validation of the blood oxygen level-dependent concept in functional brain imaging. *Human Brain Mapping*, 5:341–346, 1997.
- [28] E. Han, G. Gold, J. Stainsby, G. Wright, C. Beaulieu, and J. Brittain. In-Vivo T1 and T2 Measurements of Musculoskeletal Tissue at 3T and 1.5T. *Proc. Intl. Soc. Magn. Reson. Med.*, page 450, 2003.
- [29] C. J. Hardy, P. A. Bottomley, M. O’Donnell, and P. Roemer. Optimization of two-dimensional spatially selective NMR pulses by simulated annealing. *J. Mag. Res.*, 77(2):233–50, February 1988.
- [30] C. J. Hardy and H. E. Cline. Spatial localization in two dimensions using NMR designer pulses. *J. Mag. Res.*, 82(3):647–54, May 1989.
- [31] B. A. Hargreaves, S. S. Vasanawala, J. M. Pauly, and D. G. Nishimura. Characterization and reduction of the transient response in steady-state MR imaging. *Magn. Reson. Med.*, 46(1):149–58, July 2001.
- [32] J. A. Heilman, J. J. Derakhshan, M. J. Riffe, N. Gudino, J. Tkach, C. A. Flask, J. L. Duerk, and M. A. Griswold. B0 and B1 correction using the inherent degrees of freedom of a multi-channel transmit array. In *Proc. Intl. Soc. Magn. Reson. Med.*, page 251, 2009.
- [33] J Hennig. Multiecho imaging sequences with low refocusing flip angles. *Journal of Magnetic Resonance (1969)*, 78(3):397–407, 1988.
- [34] N. Hollingsworth, K. Moody, J-F. Nielsen, D. Noll, M. McDougall, and S. Wright. An eight channel transmit system for transmit SENSE at 3T. In *Proc. IEEE Intl. Symp. Biomed. Imag.*, pages 0775–0778, 2011.
- [35] Andres Hoyos-Idrobo, Pierre Weiss, Aurélien Massire, Alexis Amadon, and Nicolas Boulant. On variant strategies to solve the magnitude least squares optimization problem in parallel transmission pulse design and under strict sar and power constraints. *Medical Imaging, IEEE Transactions on*, 33(3):739–748, 2014.
- [36] P. J. Huber. *Robust statistics*. Wiley, New York, 1981.

- [37] E. K. Insko and L. Bolinger. Mapping of the radiofrequency field. *J. Mag. Res. A*, 103(1):82–5, June 1993.
- [38] M. W. Jacobson and J. A. Fessler. An expanded theoretical treatment of iteration-dependent majorize-minimize algorithms. *IEEE Trans. Im. Proc.*, 16(10):2411–22, October 2007.
- [39] Marcin Jankiewicz, John C Gore, and William A Grissom. Improved encoding pulses for Bloch-Siegert  $|B_1^+|$  mapping. *Journal of Magnetic Resonance*, 226:79–87, 2013.
- [40] Christian Kanzow, Nobuo Yamashita, and Masao Fukushima. Levenberg–marquardt methods with strong local convergence properties for solving nonlinear equations with convex constraints. *Journal of Computational and Applied Mathematics*, 172(2):375–397, 2004.
- [41] Peter William Kassakian. *Convex approximation and optimization with applications in magnitude filter design and radiation pattern synthesis*. PhD thesis, University of California, Berkeley, 2006.
- [42] U. Katscher, P. Bornert, C. Leussler, and J. S. van den Brink. Transmit SENSE. *Magn. Reson. Med.*, 49(1):144–50, January 2003.
- [43] Ulrich Katscher, Dong-Hyun Kim, and Jin Keun Seo. Recent progress and future challenges in mr electric properties tomography. *Computational and mathematical methods in medicine*, 2013, 2013.
- [44] Mohammad Mehdi Khalighi, Brian K Rutt, and Adam B Kerr. Adiabatic RF pulse design for Bloch-Siegert  $B_1^+$  mapping. *Magnetic Resonance in Medicine*, 70(3):829–835, 2013.
- [45] T. S. Kim, J. Lee, J. H. Lee, G. H. Glover, and J. M. Pauly. Analysis of the BOLD characteristics in pass-band bSSFP fMRI. *International Journal of Imaging Systems and Technology*, 22(1):23–32, 2012.
- [46] J. Kirk. Traveling salesman program - genetic algorithm. [http://www.mathworks.com/matlabcentral/files/13680/tsp\\_ga.m](http://www.mathworks.com/matlabcentral/files/13680/tsp_ga.m).
- [47] Jin Hyung Lee, Serge O. Dumoulin, Emine U. Saritas, Gary H. Glover, Brian A. Wandell, Dwight G. Nishimura, and John M. Pauly. Full-brain coverage and high-resolution imaging capabilities of passband b-SSFP fMRI at 3T. *Magn. Reson. Med.*, 59(5):1099–1110, 2008.
- [48] Jongho Lee, Michael Lustig, Dong-hyun Kim, and John M Pauly. Improved shim method based on the minimization of the maximum off-resonance frequency for balanced steady-state free precession (bssfp). *Magnetic Resonance in Medicine*, 61(6):1500–1506, 2009.

- [49] J. Leupold, J. Hennig, and K. Scheffler. Alternating repetition time balanced steady state free precession. *Magn. Reson. Med.*, 55(3):557–565, 2006.
- [50] Y. S. Levin, L. J. Pisani, D. M. Spielman, and J. M. Pauly. Trajectory optimization for variable-density spiral two-dimensional excitation. In *Proc. Intl. Soc. Magn. Reson. Med.*, page 3012, 2006.
- [51] Michael Lustig, Seung-Jean Kim, and John M Pauly. A fast method for designing time-optimal gradient waveforms for arbitrary-space trajectories. *Medical Imaging, IEEE Transactions on*, 27(6):866–873, 2008.
- [52] Haas M., Snyder J., Buchenau S., Kokorin D., Schneider J. T., Ullmann P., Hennig J., and Zaitsev M. Selective excitation of arbitrary three-dimensional targets in vivo using parallel transmit. In *Proc. Intl. Soc. Magn. Reson. Med.*, page 3476, 2012.
- [53] C. Ma, D. Xu, K. F. King, and Z. P. Liang. Joint design of spoke trajectories and RF pulses for parallel excitation. *Magn. Reson. Med.*, 65(4):973–85, April 2011.
- [54] S. J. Malik and J. V. Hajnal. 3d-fse inner volume imaging using 3d selective excitation. In *Proc. Intl. Soc. Magn. Reson. Med.*, page 0948, 2014.
- [55] S. J. Malik, S. Keihaninejad, A. Hammers, and J. V. Hajnal. Tailored excitation in 3D with spiral nonselective (SPINS) RF pulses. *Magn. Reson. Med.*, 67(5):1303–15, 2012.
- [56] Chang-Sheng Mei, Lawrence P Panych, Jing Yuan, Nathan J McDannold, Lisa H Treat, Yun Jing, and Bruno Madore. Combining two-dimensional spatially selective rf excitation, parallel imaging, and unfold for accelerated mr thermometry imaging. *Magnetic Resonance in Medicine*, 66(1):112–122, 2011.
- [57] K. L. Miller, B. A. Hargreaves, J. Lee, D. Ress, R. C. deCharms, and J. M. Pauly. Functional brain imaging using a blood oxygenation sensitive steady state. *Magn. Reson. Med.*, 50(4):675–83, October 2003.
- [58] K. L. Miller and P. Jezzard. Modeling SSFP functional MRI contrast in the brain. *Magn. Reson. Med.*, 60(3):661–73, September 2008.
- [59] Karla L Miller, Stephen M Smith, Peter Jezzard, Graham C Wiggins, and Christopher J Wiggins. Signal and noise characteristics of SSFP fMRI: a comparison with GRE at multiple field strengths. *Neuroimage*, 37(4):1227–1236, 2007.
- [60] V. De. Moortele, J. Pfeuffer, G.H. Glover, K. Ugurbil, and X. Hu. Respiration-induced b0 fluctuations and their spatial distribution in the human brain at 7 tesla. *Magnetic resonance in medicine*, 47(5):888–895, 2002.

- [61] E. R. Muir and T. Q. Duong. Layer-specific functional and anatomical MRI of the retina with passband balanced SSFP. *Magn. Reson. Med.*, 66(5):1416–1421, 2011.
- [62] K. S. Nayak, H. L. Lee, B. A. Hargreaves, and B. S. Hu. Wideband SSFP: alternating repetition time balanced steady state free precession with increased band spacing. *Magn. Reson. Med.*, 58(5):931–938, 2007.
- [63] J. F. Nielsen and K. S. Nayak. Interleaved balanced SSFP imaging: Artifact reduction using gradient waveform grouping. *J. Magn. Reson. Imaging*, 29(3):745–50, 2009.
- [64] J-F. Nielsen, H. Sun, J. A. Fessler, and D. C. Noll. Steady-State Functional MRI Using Small-Tip Fast Recovery (STFR) Imaging. In *Proc. Intl. Soc. Magn. Reson. Med.*, page 3333, 2013.
- [65] J-F. Nielsen, D. Yoon, and D. C. Noll. Small-tip fast recovery imaging using non-slice-selective tailored tip-up pulses and radiofrequency-spoiling. *Magn. Reson. Med.*, 69:657 – 666, 2013.
- [66] Jon-Fredrik Nielsen, Daehyun Yoon, and Douglas C Noll. Small-tip fast recovery imaging using non-slice-selective tailored tip-up pulses and radiofrequency-spoiling. *Magnetic Resonance in Medicine*, 69(3):657–666, 2013.
- [67] D. C. Noll, C. R. Genovese, L. E. Nystron, A. L. Vazquez, S. D. Forman, W. F. Eddy, and J. D. Cohen. Estimating test-retest reliability in functional MR imaging II: Application to motor and cognitive activation studies. *Magn. Reson. Med.*, 38(3):508–17, September 1997.
- [68] S. Ogawa, D. W. Tank, R. Menon, J. M. Ellermann, S-G. Kim, H. Merkle, and K. Ugurbil. Intrinsic signal changes accompanying sensory stimulation: Functional brain mapping with magnetic resonance imaging. *Proc. Natl. Acad. Sci.*, 89(13):5951–5, July 1992.
- [69] W. R. Overall, D. G. Nishimura, and B. S. Hu. Steady-state sequence synthesis and its application to efficient fat-suppressed imaging. *Magn. Reson. Med.*, 50(3):550–559, 2003.
- [70] S. Patterson, E. Mazerolle, S. Beyea, and C. Bowen. Whole-brain artifact-suppressed SSFP fMRI in a single paradigm run: Alternating SSFP. In *Proc. Intl. Soc. Magn. Reson. Med.*, page 2309, 2012.
- [71] J. Pauly, P. Le Roux, D. Nishimura, and A. Macovski. Parameter relations for the Shinnar-Le Roux selective excitation pulse design algorithm. *IEEE Trans. Med. Imag.*, 10(1):53–65, March 1991.
- [72] J. Pauly, D. Nishimura, and A. Macovski. A k-space analysis of small-tip-angle excitation. *J. Mag. Res.*, 81(1):43–56, January 1989.

- [73] W. H. Press, B. P. Flannery, S. A. Teukolsky, and W. T. Vetterling. *Numerical recipes in C*. Cambridge Univ. Press, New York, 2 edition, 1992.
- [74] S. Rieseberg, J. Frahm, and J. Finsterbusch. Two-dimensional spatially-selective rf excitation pulses in echo-planar imaging. *Magnetic resonance in medicine*, 47(6):1186–1193, 2002.
- [75] L. I. Sacolick, F. Wiesinger, I. Hancu, and M. W. Vogel. B1 mapping by Bloch-Siegert shift. *Magn. Reson. Med.*, 63(5):1315–22, May 2010.
- [76] S. Saekho, F. E. Boada, D. C. Noll, and V. A. Stenger. Small tip angle three-dimensional tailored radiofrequency slab-select pulse for reduced  $B_1$  inhomogeneity at 3 T. *Magn. Reson. Med.*, 53(2):479–84, February 2005.
- [77] S. Saekho, C. Yip, D. C. Noll, F. E. Boada, and V. Andrew Stenger. Fast- $k_z$  three-dimensional tailored radiofrequency pulse for reduced  $B_1$  inhomogeneity. *Magn. Reson. Med.*, 55(4):719–24, April 2006.
- [78] K. Scheffler. A pictorial description of steady-states in rapid magnetic resonance imaging. *Concepts in Magnetic Resonance*, 11(5):291–304, 1999.
- [79] K. Scheffler and S. Lehnhardt. Principles and applications of balanced SSFP techniques. *Eur. Radiology*, 13(11):2409–18, November 2003.
- [80] Klaus Scheffler, Erich Seifritz, Deniz Bilecen, Ramesh Venkatesan, Jürgen Hennig, Michael Deimling, and E Mark Haacke. Detection of bold changes by means of a frequency-sensitive truefisp technique: preliminary results. *NMR in Biomedicine*, 14(7-8):490–496, 2001.
- [81] Johannes T Schneider, Raffi Kalayciyan, Martin Haas, Sarah R Herrmann, Wolfgang Ruhm, Jürgen Hennig, and Peter Ullmann. Inner-volume imaging in vivo using three-dimensional parallel spatially selective excitation. *Magnetic Resonance in Medicine*, 69(5):1367–1378, 2013.
- [82] K. Setsompop, L. L. Wald, V. Alagappan, B. A. Gagoski, and E. Adalsteinsson. Magnitude least squares optimization for parallel radio frequency excitation design demonstrated at 7 Tesla with eight channels. *Magn. Reson. Med.*, 59(4):908–15, April 2008.
- [83] Tingting Shao, Ling Xia, Guisheng Tao, Jieru Chi, Feng Liu, and Stuart Crozier. Advanced three-dimensional tailored rf pulse design in volume selective parallel excitation. *Medical Imaging, IEEE Transactions on*, 31(5):997–1007, 2012.
- [84] Piechnik SK, Chiarelli PA, and Jezzard P. Modelling vascular reactivity to investigate the bias of the relationship between cerebral blood volume and flow under  $CO_2$  manipulation. *Neuroimage*, 39:107–117, 2008.

- [85] G.J. Stanisz, E.E. Odobina, J. Pun, M. Escaravage, S.J. Graham, M.J. Bronskill, and R.M. Henkelman.  $T_1$ ,  $T_2$  relaxation and magnetization transfer in tissue at 3T. *Magn. Reson. Med.*, 54:507–512, 2005.
- [86] V Andrew Stenger, Marius S Giurgi, Fernando E Boada, and Douglas C Noll. Excitation unfold (xunfold) to improve the temporal resolution of multishot tailored rf pulses. *Magnetic resonance in medicine*, 56(3):692–697, 2006.
- [87] H. Sun, J. A. Fessler, , D.C. Noll, and J. F. Nielsen. Strategies for Improved 3D Small-Tip Fast Recovery (STFR) Imaging. In *Proc. Intl. Soc. Magn. Reson. Med.*, page 2362, 2013.
- [88] H. Sun, J. A. Fessler, , D.C. Noll, and J. F. Nielsen. Joint design of continuous excitation k-space trajectory and rf pulse for 3d tailored excitation. In *Proc. Intl. Soc. Magn. Reson. Med.*, 2014.
- [89] H. Sun, J. A. Fessler, , D.C. Noll, and J. F. Nielsen. Small-tip Fast Recovery (STFR) imaging Using Spectrally Tailored Pulse. In *Proc. Intl. Soc. Magn. Reson. Med.*, 2014.
- [90] H. Sun, J. A. Fessler, , D.C. Noll, and J. F. Nielsen. Steady-state Functional MRI Using Spoiled Small-tip Fast Recovery (STFR) Imaging. In *Proc. Intl. Soc. Magn. Reson. Med.*, 2014.
- [91] H. Sun, J. A. Fessler, and J. F. Nielsen. Analytic description of steady-state imaging with dual RF pulses and gradient spoiling. In *Proc. Intl. Soc. Magn. Reson. Med.*, page 4183, 2012.
- [92] H. Sun, J. A. Fessler, D. C. Noll, and J.-F Nielsen. Balanced ssfp-like steady-state imaging using small-tip fast recovery with a spectral prewinding pulse. *Magnetic resonance in medicine*, page DOI: 10.1002/mrm.25682.
- [93] H. Sun, J. A. Fessler, D.C. Noll, and J-F. Nielsen. Strategies for Improved 3D Small-Tip Fast Recovery (STFR) Imaging. *Magn. Reson. Med.*, 72(2):389–398, 2014.
- [94] H. Sun, J.A. Fessler, D.C. Noll, and J-F Nielsen. Steady-state imaging with 3d inner volume excitation. In *Proc. Intl. Soc. Magn. Reson. Med.*, 2015. To appear.
- [95] H. Sun, W. A. Grissom, and J. A. Fessler. Regularized estimation of bloch-siegert b1+ maps in mri. In *Proc. IEEE Intl. Conf. on Image Processing*, 2014.
- [96] H. Sun, D. S. Weller, A. Chu, S. Ramani, D. Yoon, J-F. Nielsen, and J. A. Fessler. Spoke pulse design in magnetic resonance imaging using greedy minimax algorithm. In *Biomedical Imaging (ISBI), 2013 IEEE 10th International Symposium on*, pages 696–699. IEEE, 2013.

- [97] Hao Sun, Jeffrey A Fessler, Douglas C Noll, and Jon-Fredrik Nielsen. Steady-state functional mri using spoiled small-tip fast recovery imaging. *Magnetic Resonance in Medicine*, 73(2):536–543, 2015.
- [98] B. P. Sutton, D. C. Noll, and J. A. Fessler. Fast, iterative image reconstruction for MRI in the presence of field inhomogeneities. *IEEE Trans. Med. Imag.*, 22(2):178–88, February 2003.
- [99] J. A. Tropp. Algorithms for simultaneous sparse approximation, Part II: convex relaxation. *Signal Processing*, 86(3):589–602, March 2006.
- [100] S. Vaziri and M. Lustig. The fastest gradient waveforms for arbitrary and optimized k-space trajectories. In *Biomedical Imaging (ISBI), 2013 IEEE 10th International Symposium on*, pages 708–711. IEEE, 2013.
- [101] S.N. Williams, H. Sun, J-F Nielsen, J.A. Fessler, and D.C. Noll. A spectral-spatial pulse for improved signal recovery in the small-tip fast recovery (STFR) sequence. In *Proc. Intl. Soc. Magn. Reson. Med.*, page To appear., 2015.
- [102] V. L. Yarnykh. Actual flip-angle imaging in the pulsed steady state: A method for rapid three-dimensional mapping of the transmitted radiofrequency field. *Magn. Reson. Med.*, 57(1):192–200, January 2007.
- [103] C. Yip, J. A. Fessler, and D. C. Noll. Iterative RF pulse design for multidimensional, small-tip-angle selective excitation. *Magn. Reson. Med.*, 54(4):908–17, October 2005.
- [104] C. Yip, J. A. Fessler, and D. C. Noll. Advanced three-dimensional tailored RF pulse for signal recovery in  $T_2^*$ -weighted functional magnetic resonance imaging. *Magn. Reson. Med.*, 56(5):1050–9, November 2006.
- [105] C. Yip, W. A. Grissom, J. A. Fessler, and D. C. Noll. Joint design of trajectory and RF pulses for parallel excitation. *Magn. Reson. Med.*, 58(3):598–604, September 2007.
- [106] C. Yip, D. Yoon, V. Olafsson, S. Lee, W. A. Grissom, J. A. Fessler, and D. C. Noll. Spectral-spatial pulse design for through-plane phase precompensatory slice selection in  $T_2^*$ -weighted functional MRI. *Magn. Reson. Med.*, 61(5):1137–47, May 2009.
- [107] C-Y. Yip, J. A. Fessler, and D. C. Noll. A constrained minimization approach to designing multi-dimensional, spatially selective RF pulses. In *Proc. Intl. Soc. Magn. Reson. Med.*, page 188, 2004.
- [108] D. Yoon, J. A. Fessler, A. C. Gilbert, and D. C. Noll. Simultaneous signal loss correction from B1 and B0 field inhomogeneity in BOLD fMRI with parallel excitation. In *ISMRM Workshop on Parallel MRI*, page 38, 2009.

- [109] D. Yoon, J. A. Fessler, A. G. Gilbert, and D. C. Noll. Fast joint design method for parallel excitation RF pulse and gradient waveforms considering off-resonance. *Magn. Reson. Med.*, 68(1):278–85, July 2012.
- [110] Jing Yuan, Tzu-Cheng Zhao, Yi Tang, and Lawrence P Panych. Reduced field-of-view single-shot fast spin echo imaging using two-dimensional spatially selective radiofrequency pulses. *Journal of Magnetic Resonance Imaging*, 32(1):242–248, 2010.
- [111] A. C. Zelinski, L. L. Wald, K. Setsompop, V. K. Goyal, and E. Adalsteinsson. Sparsity-enforced slice-selective MRI RF excitation pulse design. *IEEE Trans. Med. Imag.*, 27(9):1213–29, September 2008.
- [112] F. Zhao, J. A. Fessler, S Wright, and D. C. Noll. Regularized estimation of magnitude and phase of multi-coil b1 field via bloch-siegert b1 mapping and coil combination optimizations. *Medical Imaging, IEEE Transactions on*, 2014.
- [113] F. Zhao, J-F. Nielsen, and D.C. Noll. Four dimensional spectral-spatial fat saturation pulse design. *Magnetic Resonance in Medicine*, 2013.
- [114] F. Zhao, J-F. Nielsen, S.D. Swanson, J.A. Fessler, and D.C. Noll. Simultaneous fat saturation and magnetization transfer contrast imaging with steady-state incoherent sequences. *Magnetic Resonance in Medicine*, page DOI: 10.1002/mrm.25475, 2014.
- [115] F. Zhao, H. Sun, J-F. Nielsen, J. A. Fessler, and D.C. Noll. Balanced ssfp-like imaging with simultaneous water-fat separation and band reduction using small-tip fast recovery. In *Proc. Intl. Soc. Magn. Reson. Med.*, page 2403, 2013.
- [116] L. Zhao, B. Madore, and L. P. Panych. Reduced field-of-view MRI with two-dimensional spatially-selective RF excitation and UNFOLD. *Magn. Reson. Med.*, 53(5):1118–25, May 2005.
- [117] H. Zheng, T. Zhao, Y. Qian, T. S. Ibrahim, and F. E. Boada. Improved large tip angle parallel transmission pulse design through a perturbation analysis of the bloch equation. *Magn. Reson. Med.*, 66(3):687–96, 2011.
- [118] Kai Zhong, Jochen Leupold, Juergen Hennig, and Oliver Speck. Systematic investigation of balanced steady-state free precession for functional MRI in the human visual cortex at 3 Tesla. *Magnetic Resonance in Medicine*, 57(1):67–73, 2007.
- [119] Y. Zhu. Parallel excitation with an array of transmit coils. *Magn. Reson. Med.*, 51(4):775–84, April 2004.
- [120] Y. Zur, M. L. Wood, and L. J. Neuringer. Spoiling of transverse magnetization in steady-state sequences. *Magn. Reson. Med.*, 21(2):251–263, 1991.